Design and Evaluation of Microwave Antennas for Abdominal Fat Measurement Systems

by

Siamak Sarjoghian

A thesis submitted in partial fulfillment of the requirements for the degree of Doctor of Philosophy

School of Electronic Engineering and Computer Science

Queen Mary University of London

May 2019

Statement of originality

I, SIAMAK SARJOGHIAN, confirm that the research included within this thesis is my own work or that where it has been carried out in collaboration with, or supported by others, that this is duly acknowledged below and my contribution indicated. Previously published material is also acknowledged below.

I attest that I have exercised reasonable care to ensure that the work is original, and does not to the best of my knowledge break any UK law, infringe any third party's copyright or other Intellectual Property Right, or contain any confidential material.

I accept that the College has the right to use plagiarism detection software to check the electronic version of the thesis.

I confirm that this thesis has not been previously submitted for the award of a degree by this or any other university.

The copyright of this thesis rests with the author and no quotation from it or information derived from it may be published without the prior written consent of the author.

Signature: [ ]

Date:

Details of collaboration and publications:

[1] S. Sarjoghian, Y. Alfadhl, and X. Chen, "On the limitation of ultra-wideband technique for medical scanning systems," *in Loughborough Antennas & Propag. Conf. (LAPC)*, pp. 1–4, Nov. 2016.

[2] S. Sarjoghian, Y. Alfadhl, and X. Chen, "Compact ultra-wideband double-ridged horn antennas for medical imaging*," in Loughborough Antennas & Propag. Conf. (LAPC)*, pp. 1–4, Nov. 2016.

[3] S. Sarjoghian, Y. Alfadhl, and Xiaodong Chen, "A novel wide-band reflection-based system for measuring abdominal fat in humans," *in URSI Int. Symp. Electromag. Theory (EMTS)*, pp. 586–589, Aug. 2016.

[4] S. Sarjoghian, Y. Alfadhl, X. Chen, and C. Parini "A 3D-printed high-dielectric materials-filled pyramidal double-ridged horn antenna for abdominal fat" *IEEE Transactions on Antennas and Propagation*, Submitted, Dec. 2018.

[5] S. Sarjoghian, M. Sagor, Y. Alfadhl, and X. Chen, "A 3D-printed high-dielectric filled elliptical double-ridged horn antenna for biomedical monitoring applications" *IEEE Access*, Submitted, Feb. 2019.

ABSTRACT

Availability of accurate, low cost and non-invasive devices for the measurement of abdominal fat is an important factor for early diagnosis of the obesity-related diseases.

To achieve this, a wideband (WB) system was developed that includes the advantages of high range resolution due to the wide bandwidth (BW ≥ 0.5 GHz) and acceptable penetration depth due to the low centre frequency (1 – 3.5 GHz).

For the pulse transmission, double-ridged horn (DRH) antennas were proposed because of their wide bandwidth, high gain, and impedance matching capability. Simulation studies suggested that optimal pulse focus and minimal interference to be introduced into the system by pyramidal- and elliptical-DRH, especially when extended to locate the antenna in the far-field region. Since these shapes are complex to manufacture, 3D printing was employed to fabricate low-cost antennas with high resolution.

A further improvement in system performance as well as a reduction in system size was achieved by embedding the antenna in a high dielectric material, which further reduced the reflections caused by impedance differences. Previously proposed high dielectric materials such as Barium Titanate-based ceramics and canola oil were characterised during this study and combined with different percentages of Titanium Oxide to increase their dielectric constant, while retaining good conductivity. In addition, Paraffin was preferred over oil, as it has the same dielectric properties but solidifies at room temperature.

Analyses were conducted based on a three-layer dielectric tissue model mimicking human tissue thicknesses. To measure the extent of the fat layer, a parameterised WB pulse was transmitted through the tissue model and its reflections were recorded. Evaluation metrics including the reflection coefficient were employed to investigate the pulse magnitude reduction and time of arrival at the fat layer. Results indicate that the proposed system is able to measure fat thickness with the accuracy within ±1 mm.

ACKNOWLEDGMENTS

Firstly, I would like to express my sincere gratitude to my advisor Dr. Yasir Alfadhl for the continuous support of my PhD study and related research, for his patience, motivation, and immense knowledge. His guidance helped me in all the time of research and writing of this thesis. I could not have imagined having a better advisor and mentor for my PhD study.

Besides my advisor, I would like to thank the rest of my thesis committee: Prof. Xiaodong Chen, and Dr. Akram Alomainy, for their insightful comments and encouragement, but also for the hard question, which encouraged me to widen my research from various perspectives.

My sincere thanks also goes to Dr. Max Munoz Torrico, who gave access to the laboratory and research facilities. Without they precious support it would not be possible to conduct this research.

I thank my fellow mates in for the stimulating discussions, for the sleepless nights we were working together before deadlines, and for all the fun, we have had in the last five years. In particular, I am also grateful to Prof. Clive Parini and Dr. Md Hasanuzzaman Sagor for their support and guidance.

Last but not the least; I would like to thank my family for supporting me spiritually throughout writing this thesis and my life in general.

Table of Contents

List of Tables

Chapter 2:

Chapter 3:

Chapter 5:

List of Figures

Chapter 1:

Chapter 2:

Chapter 3:

Chapter 4:

Chapter 5:

List of Abbreviations

RF	Radio Frequency
EM	Electromagnetic
UWB	Ultra Wide-Band
WB	Wide-Band
GP	Gaussian Pulse
FMCW	Frequency-modulated continuous wave
Ofcom	Office of Communications (UK)
FCC	Federal Communications Commission (US)
SF	Subcutaneous Fat
VF	Visceral Fat
PH	Pyramidal Horn
CH	Conical Horn
DRH	Double-Ridged Horn
PDRH	Pyramidal Double-Ridged Horn
EDRH	Elliptical Double-Ridged Horn
DRGH	Double-Ridge Guide Horn
3D	Three-Dimensional
SAR	Specific Absorption Rate
TDR	Time Domain Reflectometry
VNA	Vector Network Analyser
FPGA	Field-programmable gate array
ADC	Analog-to-digital Converter
VCO	Voltage Control Oscillator
PA	Power Amplifier
LNA	Low Noise Amplifier
BPF	Band Pass Filter
SLL	Side Lobe Level

CHAPTER 1

1.1. INTRODUCTION

Obesity is considered as a widespread disease attributing to a number of other health effects. A recent study involving 19.2 million contributors from 200 countries have indicated that by 2025, global obesity will reach an average of 18% in men and exceed 21% in women [1].

Within the body, fat or adipose tissue is generally initiated in two forms: white adipose tissue (WAT) and brown adipose tissue (BAT). These two tissues have opposite roles in whole-body energy metabolism. WAT has the ability to store energy contained in glucose and fatty acids in the form of triacylglycerol and release the energy in the form of free fatty acids. While BAT has the aptitude to scatter energy in the form of heat by oxidation of fatty acids and of glucose. Research indicates that both of these tissue types are playing important roles in the fat mass storage in different area of the body [2, 3].

Early diagnosis of fat accumulation inside the human body, especially around abdomen area, is very important to prevent the development of related diseases. The upsurge of fat inside the human body may result in unwanted fatty deposition within various parts of the body, most predominantly around areas such as the hips, thighs, abdomen and other internal organs. Recent research has shown that abdominal fats are associated with higher health risks to humans compared with other type of fats [4, 5]. This is because abdominal fats are typically associated with other types of adipose tissues accumulating around and within organs such as the liver, kidneys and the heart [6].

Accurate measurements of the fat deposition within the body can be a great assistance for health watchers and has many other uses such as by beauty surgeons to monitor the fat thickness before they start any liposuction or other type of operation on the patient [7].

Nowadays, general practitioners and dieticians reply heavily on measuring waist size to determine the fat level in the abdomen using the body mass index (BMI) [8]. However, the method is very susceptible to human errors and lacks accuracy.

In order to reduce these errors, techniques have been developed such as magnetic resonance imaging (MRI) scanning (shown in Fig. 1.1a), computed tomography (CT) scanning (in Fig. 1.1b), ultrasound (in Fig. 1.1c), and the traditional waist measurement (in Fig. 1.1d) [9−12].

(a) [9] (b) [10] (c) [11] (d) [12]

Fig 1. 1: Available technologies employed by the health professionals to determine the amount of abdominal fat.

The main advantage of the newer techniques over the traditional waist measurement technique is the capability to distinguish normal skin cells from fat cells. However, some of these methods are not established as routine practices for medical testing and diagnosis, due to some issues such as their cost-effectiveness and side effects on the health [13, 14].

Other recent equipment designs rely on checking the biological electrical impedance of the human body to determine the amount of body fat with respect to weight using an electric current flowing through the body, as shown in Figs. 1.2 (a, b) [15, 16].

This technique was found to be unreliable based on the fact that the body water content can play a critical role in changing the impedance of the body. Moreover, the device was designed to measure overall body fat spread throughout the entire human body, and not just the abdomen [17].

(a) (b)

Fig 1. 2: Frequency bio-impedance analysis devices [15].

The research emphasises detection of fat through pulse discontinuity technique using a probe. The method suffers from weaknesses such as hazards of attaching the device to the patient's body and a small scanning area. Small scanning area means that more time is required to cover the entire area of interest [18].

Review of literature on existing techniques and methods, employed for this purpose, indicates that the ultra-wideband (UWB) method with large bandwidth (and therefore high accuracy) has been selected and employed widely by researchers for a similar

application. This technique has other excellent features such as being inexpensive due to using low power pulses and therefore is low cost, not having dangerous side effects for patients such as the ionising effect, which can be caused by most of the screening techniques such as X-ray and CT scanning.

Considering this technique's features and benefits, it has been the technique of choice for a great number of researchers, who employed it for different medical applications such as breast cancer detection (Fig. 1.3 (a)), head stroke detection (Fig. 1.3 (b)), heartbeat figure and respiratory motion detection (Fig. 1.3 (c)), and more [19–21].

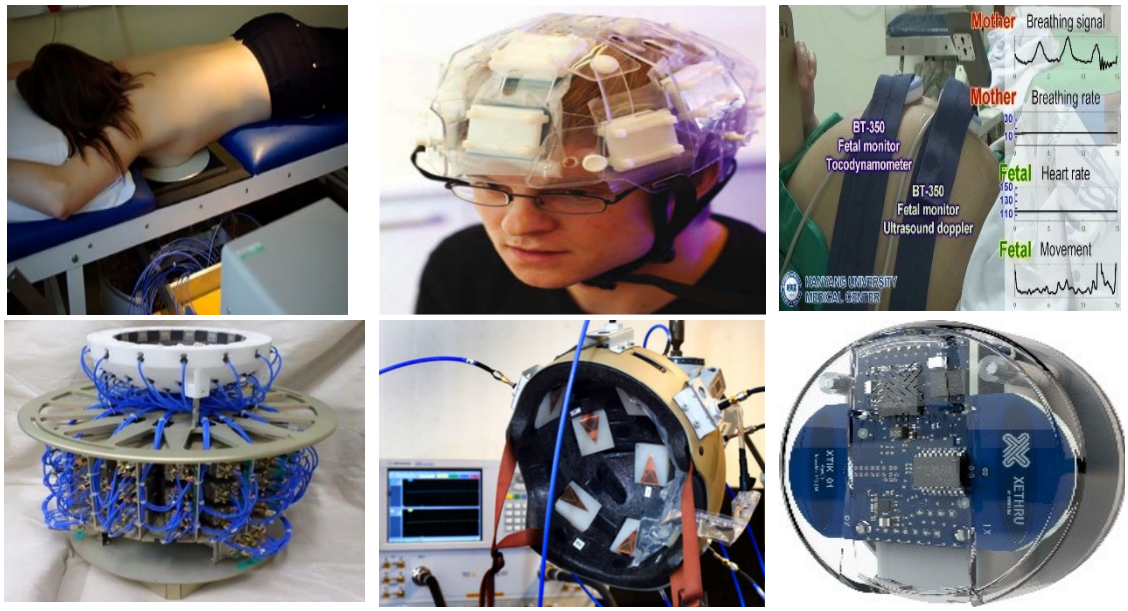

(a) [19] (b) [20] (c) [21]

Fig. 1.3: Developed medical systems using the UWB technique.

Other recent research has also demonstrated the use of UWB methods for different applications such as distinguishing fat cells from the other cells based on the cells' dielectric properties [22, 23]. Moreover, a number of UWB imaging techniques, which were investigated by various research groups for detecting breast cancer, employed different types of antennas and signal processing techniques to retrieve information [24–27].

The term UWB is an industry standard, which refers to specific range of frequency (3.1–10.6 GHz). For unlicensed use of this band, the signal strength must be less than −41.3 dBm/MHz [28]. In this thesis, the wideband (WB) term introduced to refer to pulses with frequency spectra that can be either within or outside the UWB range.

1.2. CHALLENGES

Challenges for the system development can be broken down to the following:

- To select an appropriate pulse based on required penetration depth and range resolution.
- To design and fabricate a compact WB antenna, which has optimum performance in the operating frequency with a suitable shape for the system.
- To devise a scheme for extraction of the necessary information from the reflection.

1.3. AIMS

Aim of this research is to design, develop and implement a device that is capable of measuring the thickness of abdominal fat layer underneath the human skin (subcutaneous fat), which is related to the internal fat (visceral fat), in order to ease the monitoring of human health for the health watchers. The WB technique has been selected as a satisfactory method based on its exceptional features. An alternative WB antenna has to be designed for the system to transmit a pulse and collect the reflected pulse. Then, the data could be analysed later to extract information such as the thickness of the fat layer and possibly to construct an image.

1.4. OBJECTIVES

Objectives for the system can be broken down to the following:

- Using a wide-band technique.
- Achieving good data accuracy.
- Providing a flexible and compatible system for future modifications.
- Minimising the computation and financial costs of the developed method.
- Simplifying the measurement output.
- Providing a wider knowledge base of the methodologies involved, and highlight any associated advantages and/or limitations.

1.5. ORGANISATION OF THE THESIS

The rest of this thesis is organised as follows:

Chapter 2 presents the background knowledge of UWB pulses, human abdominal fat, theory of dielectric materials, key system parameters, transmission reflection method and relevant antenna design process.

Chapter 3 presents, the material characterisation for the design process.

Chapter 4 presents, the wide band antenna design and development process.

Chapter 5 provides the development procedures and analysis of the abdominal fat measurement system.

Chapter 6 that concludes the thesis with the future extension to the work.

1.6. CHAPTER SUMMARY

Accumulation of fat tissues in different body areas, especially in the abdomen, was found to have great impacts on the ability of other diseases to further develop in the body.

Literature review has shown that there is a demand for new techniques and equipment in order to increase the resolution as well as decrease the hazards and costs of the equipment being used by health specialists.

The UWB/WB techniques can be promoted as promising methods for body fat measurement considering their advantages, which can be summarised by their lower-cost, higher-accuracy, elimination of the ionising hazard, increasing of the resolution, and other factors explained in Chapter 1.

REFERENCES (CHAPTER 1)

[1] Trends in adult body-mass index in 200 countries from 1975 to 2014: a pooled analysis of 1698 population-based measurement studies with 192 million participants. *Lancet* 2016;387:1377-1396.

[2] Cannon B, Nedergaard J. , "Brown adipose tissue: function and physiological significance," *Physiol Rev*. 2004;84:277-359.

[3] B.P. Leitner *et al.,* "Mapping of human brown adipose tissue in lean and obese young men," *Proc. Natl. Acad. Sci. U. S. A*. 114 (2017) 8649–8654.

[4] D. Canoy *et al.* , "Body fat distribution andrisk of coronary heart disease in men and women in the EuropeanInvestigation into Cancer and Nutrition in Norfolk cohort: a popula-tion-based prospective study," *Circulation.* 2007;116:2933–2943.

[5] Y. Saito, O. Takahashi, H. Arioka, D. Kobayashi, "Associations between body fat variability and later onset of cardiovascular disease risk factors," *PLoS One.* 2017;12(4):e0175057.

[6] G. De Pergola and F. Silvestris, "Obesity as a major risk factor for cancer," *J. Obes.* , Jul. 2013, 291546.

[7] M. S. Mohammed *et al.* , "Systems and WBANs for controlling obesity," *Journal of Healthcare Engineering*, vol pp. 1–21, Feb. 2018.

[8] GA Bray *et al.* , "The science of obesity management: an Endocrine Society scientific statement," *Endocr Rev*, Vol. 39, pp. 79–132, Mar. 2018.

[9] MA. Staten*, et al.* , "Measurement of fat distribution by magnetic resonance imaging," *Invest Radiol*., vol. 24, pp. 345–9, May 1989.

[10] T. Yoshizumi*, et al.* , "Abdominal fat: Standardized technique for measurement at CT," *Radiology*, vol. 211, pp. 283-286, Apr. 1999.

[11] H. R. Atta, Ophthalmic Ultrasound—A Practical Guide. Edinburgh: Churchill Livingstone, Feb. 1996.

[12] R. Ramírez-Vélez, JE. Correa-Bautista, J. Martínez-Torres, *et al.* , "LMS tables for waist circumference and waist–height ratio in Colombian adults: analysis of nationwide data," *Eur J Clin Nutr*., 2010. 70, 1189–1196.

[13] M. D. Jensen, J. A. Kanaley, J. E. Reed, and P. F. Sheedy, "Measurement of abdominal and visceral fat with computed-tomography and dual-energy X-Ray absorptiometry," *American Journal of Clinical Nutrition*, vol. 61, pp. 274-278, Feb. 1995.

[14] A. K. Karlsson *et al.* , "Measurements of total and regional body composition in preschool children: A comparison of MRI, DXA, and anthropometric data," *Obesity*, vol. 21, pp. 1018-1024, May 2013.

[15] B. Yang, "Body fat detection using radio frequency," *Ph.d Thesis*, EECS, Queen Mary University of London, Jun. 2009.

[16] U. G. Kyle, E. P. Soundar, L. Genton, and C. Pichard, "Can phase angle determined by bioelectrical impedance analysis assess nutritional risk? A comparison between healthy and hospitalized subjects," *Clinical Nutrition*, vol. 31, pp. 875-881, Dec. 2012.

[17] M. Tengvall *et al.* , "Body composition in the elderly: Reference values and bioelectrical impedance spectroscopy to predict total body skeletal muscle mass," *Clinical Nutrition*, vol. 28, pp. 52-58, Feb. 2009.

[18] K. W. Washburn and P. A. Stewart, “Use of a fat probe to assess variation in abdominal fat in broilers,” *Poultry Sci.* , vol. 66, pp. 1911-1917, Dec. 1987.

[19] A. W. Preece *et al.* , “clinical evaluation of a prototype ultra wideband radar scanner for breast cancer detection.,” *J. Med. Imag.,* vol. 3, no. 3, Jul. 2016.

[20] M. Persson *et al.* , “Microwave-based stroke diagnosis making global prehospital thrombolytic treatment possible,” *IEEE Trans. on Biomed. Eng.,* vol. 61, pp. 2806-2817, Nov. 2014.

[21] E. Pittella, S. Pisa, and M. Cavagnaro, “Breath activity monitoring with wearable UWB radars: measurement and analysis of the pulses reflected by the human body,” *IEEE Trans. Biomed. Eng.*, vol. 63, no. 7, pp. 1147–1154, Jul. 2016.

[22] K. Naishadham, J. E. Piou, L. Y. Ren, and A. E. Fathy, “Estimation of cardiopulmonary parameters from ultra wideband radar measurements using the state space method,” *IEEE Transacs. on Biomed. Circs. and Sys.,* vol. 10, pp. 1037-1046, Dec. 2016.

[23] A. E. C. Tan and M. Y. W. Chia, “Measuring human body impulse response using UWB radar,” *Electronics Letters*, vol. 41, pp. 1193-1194, Oct. 2005.

[24] M. Klemm, I. Craddock, J. Leendertz, A. Preece, and R. Benjamin, “Experimental and clinical results of breast cancer detection using UWB microwave radar,” *presented at the IEEE Antennas and Propag. Society Int. Symp.*, San Diego, CA, Jul. 7–12, 2008.

[25] I. J. C. Y. Chen Y, P. Kosmas, M. Ghavami, and P. Rapajic, “Multiple-input multiple-output radar for lesion classification in ultra-wideband breast imaging,” *IEEE Journal of Selected Topics in Signal Processing*, vol. 4, pp. 1217-1225, Jun. 2010.

[26] X. Yong, L. Yinghua, Z. Hongxin, and W. Yeqiu, B, “An overview of ultra wideband technique application for medical engineering,” *in Proc. Int. Conf. Complex Med. Eng.*, pp. 408–411, Beijing, China, May 2007.

[27] J. D. Kim, *et al.* , “Non-contact respiration monitoring using impulse radio ultrawideband radar in neonates,” R. Soc. open sci., vol. 6, Jun. 2019.

[28] Federal Communications Commission, “Revision of part 15 of the commission’s rules regarding ultra-wideband transmission systems,” *First Report and Order*, FCC 02-48, Washington, DC, 2002.

CHAPTER 2

2. BACKGROUND

In this part of the thesis, more literature research is described on the UWB technique and its characteristics, in order to enable one to design a system that can measure the abdominal fat accurately. Some important factors should be considered during the system design carefully, summarised as the pulse parameters (such as required centre frequency and bandwidth), the compatible transceiver, the medium characteristics (tissue modelling), the employed method to determine the pulse behaviour in the medium, and the suitable technique to determine the fat thickness.

A number of topics have been investigated to gain a wider understanding of the types of techniques as well as the diverse nature of the fat tissues involved. The Chapter also focuses on the available WB techniques such as UWB technology, which was selected as a good candidate for localised scanning of patients. The technique offers different advantages such as elimination of ionizing effect on human's cells, lower cost, and wide bandwidth, which provides better resolution.

There has been considerable research conducted in the past few years on monitoring and scanning inside human tissues using UWB technique. This research has led to ways to diagnose breast cancer and head stroke, to measure heart rate and to provide other critical health information [1–3]. This research has been broken down to following segments:

2.1. UWB SIGNALS

Ultra wideband (UWB) technology uses radio waves for transferring information over a high bandwidth (typically<500MHz), and was originally aimed for short-range wireless communication channels [4]. The technology requires low power levels and is used mainly for short range or indoor applications. It utilises a large segment of the radio frequency spectrum and can improve the speed and reduce interference compared with other available technologies. The independent regulator and competition authority for the UK communications industries (Ofcom) and the Federal Communications Commission (FCC) in the US has regulated the UWB technology allowing unlicensed operation within the range of 3.1 GHz to 10.6 GHz and 41.3dBm/MHz transmitted power that is illustrated in Fig. 2.1 [5].

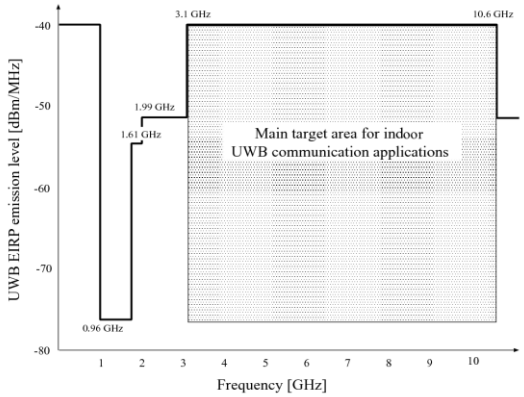

Fig 2. 1: Spectral mask mandated by FCC 15.517(b, c) for indoor UWB systems [5].

In this technique, the signals are transmitted across a wide range of frequencies to detect a subject accurately. The technique provides a high data rate in comparison to the other technologies.

In this method, one sends trains of pulses containing hundreds of millions of pulses per second. As it can be implemented in a physically small and very low power system, it fits the requirements for use in indoor application. In the last few years, the UWB has been selected as a good candidate for medical purposes compared to other scanning technologies due to its unique properties, such as [6]:

- **Wide bandwidth:** The large bandwidth occupied by the UWB pulse (<500MHz) and therefore higher resolution.
- **Low cost:** UWB method is a low power and a low-cost technique.
- **Multipath immunity:** Use of the UWB pulse can provide for satisfactory resolution of the reflected pulse at the receiver end of the system due to the narrow shape of the pulse, which offers a better pulse separation capability compared with other pulses.
- **Ranging:** The UWB technique can provide the user with direction and distance information for a target object.
- **Eliminating ionising effect:** The UWB has the advantage over X-ray based methods, such as CT scan that there is no ionization of atoms of biological structures.

The pulse used here is the basic Gaussian pulse (GP), which has the mathematical definition given by equation (2-1) below. σ is the standard deviation:

$$G(x) = \frac{1}{\sqrt{2\pi\sigma^2}} e^{-x^2/2x\sigma^2} \qquad \text{Eq. (2-1)}$$

The basic GP and its first derivative (monocycle) and second derivative (doublet) presented in Fig. 2.2, have been used by research conducted to monitor the body [6].

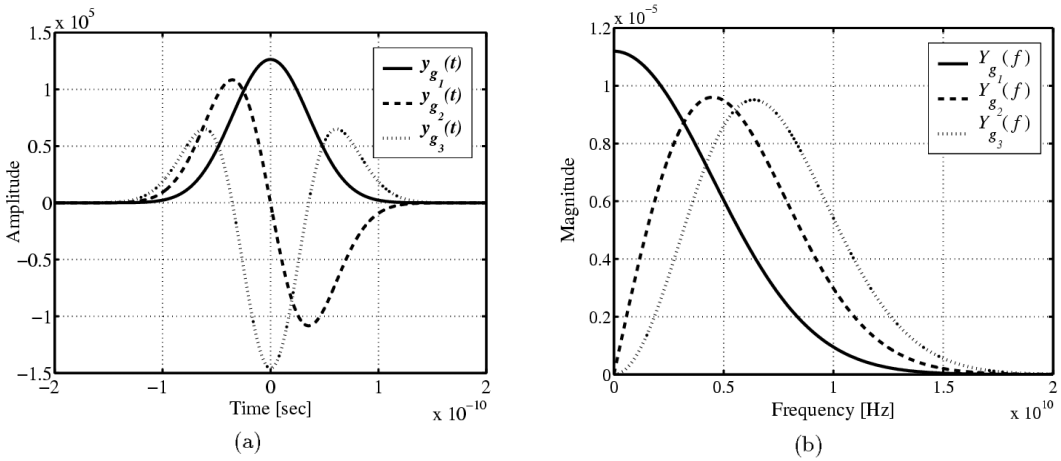

Fig 2. 2: Basic, first and second derivatives of Gaussian pulses in time and frequency domains [6].

Higher order derivatives can be taken from basic pulse equation, which results in different wave shapes and characteristics than lower order derivative pulses, and can be used for different applications.

Orthogonal pulses such as Hermite pulse are mainly employed for communications purposes. Therefore, more attention is required, in order to choose the right UWB pulse for the system. Some important factors have to be taken into account in order to decide a correct pulse for the system, therefore the pulse parameters are summarised as follows:

- Pulse shape: each UWB pulse has its own shape used for different applications based on requirements such as data rate, resolution, etc.
- Pulse centre frequency: the pulse centre frequency is important, as it can determine the penetration depth of pulse through the medium.
- Pulse Bandwidth: Another pulse property that is essential to identify for the system is pulse bandwidth, this parameter can determine the system resolution.

In this thesis, the base-band GP is chosen, as it is easy to generate and identify, however, the pulse has to be modulated with a sinewave carrying a high-frequency in order to be able to move the pulse frequency band up to required band of interest. The FCC and Ofcom regulation on the restricted region of the UWB technique (3.1−10.6 GHz) for medical applications is ignored due to the low penetration depth [7].

2.1.1. UWB CHIRP PULSE MODELING

The chirped-pulse (CP) amplification method has been introduced by Strickland and Mourou (in 1985) to solve or at least mitigate the problem of high peak powers in amplifier systems. The method uses the compressing technique to amplify the pulse over the frequency spectrum [8]. MATLAB code was written to generate the GP, Chirp pulse, and their combination using the pulses multiplication method, in order to modulate the pulses linearly. The results have been generated in the time domain as well as frequency domain as it has been illustrated in Fig. 2.3.

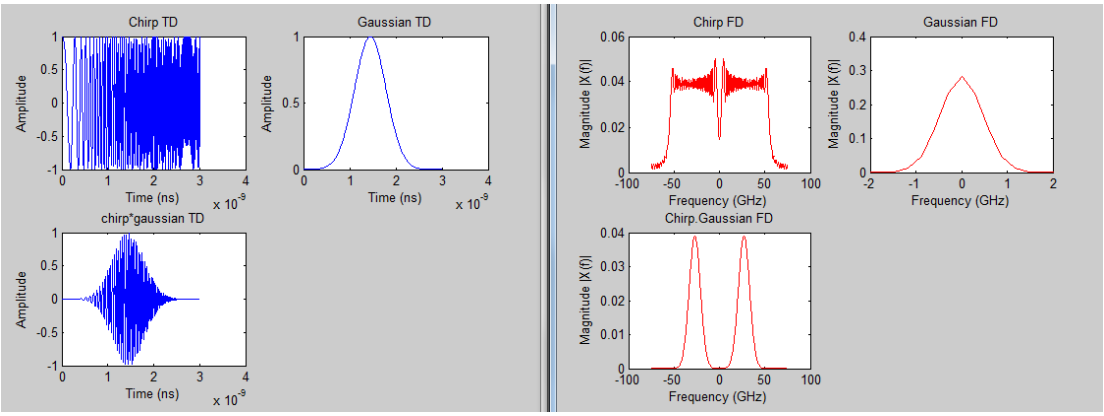

(a) Time Domain (b) Frequency Domain

Fig 2. 3: Time and Frequency domain representation of the Gaussian, chirp pulse, and their modulation.

Fig. 2.3 show that achieving broad bandwidth and transferring the pulses' frequency to the frequency of interest is easy using this technique. The frequency domain results indicates the large increase of the band in the GP and CP modulated graph compared to the GP graph.

However, sampling the reflected pulse will introduce high hardware cost to the system as the analogue to digital converter (ADC), field programmable gate arrays (FPGA) for such a system will cost thousands of pounds, and this might make the design not affordable.

2.2. HUMAN ABDOMINAL FAT

With aging, the human body suffers from increased fat contents as mentioned earlier. Large amount of these fat cells accumulate and are stored in upper body parts over the abdomen, waist, thighs and other parts of the body [9]. Increasing waistline and therefore gaining weight, largely due to a thickening fat layer in the human abdomen can raise the risk of a range of health dilemmas such as metabolic disorders, hyperlipidaemia, hypertension, diabetes mellitus and cardiovascular disease [10].

2.2.1. TISSUE TYPES

From the healthcare perspective, superfluous fats are closer to internal abdominal organs such as liver, spleen, gallbladder, intestines and other organs [11]. These fats can act as a gland or endocrine organ that produces hormones and other substances like leptin, which is released after a meal to dampen appetite, adiponectin that influence the response of cells to insulin and substances like cytokines [12].

The excessive release of these biological substances boosts the risks of cardiovascular disease by promulgating insulin resistance and increasing the level of chronic inflammation and having other detrimental effects, which scientists are still discovering these roles. Regarding human aesthetics, superfluous fats can play critical roles in the human's self-esteem and confidence [13].

The abdominal fat has been subdivided into two major types based on their location in the body. This is presented in Fig. 2.4:

- Visceral: surrounding the abdominal organs.
- Subcutaneous: Lying between the skin and abdominal barrier.

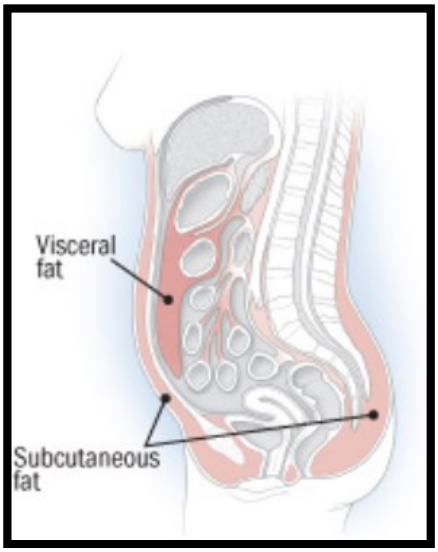

Fig 2. 4: Two types of Abdominal Fat [8].

The female and male are believed to store the fat at different sites, based on their unambiguous physiological preference for the pattern and location of the fat storage [14]. The distribution pattern of fat in the body for males is labelled generally as Android (apple-shape), where the fat largely is stored in the abdominal area [15].

However, in females the distribution is labelled as Gynoid (pear-shape), where fat is spread out in thighs, hips, and buttocks. Research illustrates that in general, there are more subcutaneous fat (SF) than visceral fat (VF) in females, whereas the trend is opposite in men. Generally, men's bodies are more metabolically active [16].

2.3. ABDOMEN FAT TYPES AND TISSUE MODELLING

The aim of this research is to detect and measure amount of the VF tissue attached to the organs inside the human's abdomen. This fat has a direct relation to the growth of the risk of a range of health dilemmas as briefly discussed in Chapter 1 [17].

Research in this area, has revealed that there is a direct relationship between the thickness of VF tissue and the thickness of SF tissue. This means that as the thickness of VF tissue increases, the thickness of the SF tissue will increase accordingly [18, 19].

This makes the measurement of the fat thickness easier as the SF is attached to the skin, and it is close to the outer area of the body. Therefore, the monitoring area is mainly involved with three tissue layers (i.e. Skin, SF, and muscle).

The thickness of each tissue type for normal people has been retrieved from previous research and found to be approximately 1.5 to 2.5 mm for skin, 16 mm for SF and 20 to 30 mm for muscle, for normal average age humans [20, 21]. The preliminary abdomen tissue is modelled to have the tissues type thicknesses: 2 mm Skin, 30 mm SF and infinite muscle.

These thicknesses have been chosen to model an obese candidate, however knowing the muscle thickness is not as essential as measuring the thickness of the SF tissue is the main objective of this research. Each layer of the modelled tissue is represented based on its characteristics such as the dielectric properties and dimensions. These parameters are affected by factors such as the person's age and skin dryness.

2.3.1. THEORY OF DIELECTRIC MATERIALS

The dielectric properties of tissues can be defined by the complex relative permittivity (ε*) [22]. The complex relative permittivity of a tissue in free space can be determined by equation (2-2) as follows;

$$\varepsilon^* = \varepsilon' - j\varepsilon'' \qquad \text{Eq. (2-2)}$$

The real part ε' is referred to as the dielectric constant and represents stored energy when the material is exposed to an electric field, the dielectric loss factor ε'', which is the imaginary part, influences energy absorption and attenuation, and $j = \sqrt{-1}$. In addition, the dielectric loss factor ε'' can be obtain by equation (2-3) [23] as:

$$\varepsilon'' = \frac{\sigma}{\varepsilon_0 \omega} \qquad \text{Eq. (2-3)}$$

where the relative conductivity of the layer is represented by σ, $\omega = 2\pi f$ is angular frequency and $\varepsilon_0 = \frac{1}{\mu_0 c^2} = 8.85 \times 10^{-12}\ {}^{F}/_{m}$ is the permittivity of free space. Here, the permeability of free space $\mu_0 = 4\pi \times 10^{-7}\ {}^{web}/_{(A.m)}$ and $c = 3 \times 10^{8}\ {}^{m}/_{s}$ is the speed of light in free space. One more important parameter used in electromagnetic (EM) theory is a loss tangent angle [24]:

$$tan\,\delta = {}^{\varepsilon''}/_{\varepsilon'} \qquad \text{Eq. (2-4)}$$

Mechanisms that contribute to the dielectric loss in heterogeneous mixtures include polar response, electronic response, atomic response, and Maxwell–Wagner response [25]. Moreover, in material processing, these equations are also used to describe RF and microwave frequency response [26]. With respect to equation (2-3), we can see that the imaginary part of permittivity will decrease when frequency is increasing, however; in practice, constant conductivity increases as frequency increases [27].

The ε'' in the case of biological tissue represents the ionic conductivity and the absorption during relaxation process, which embraces both the friction related to the alignment of the electric dipoles and also the vibration and rotation of molecules. The reaction of any material to a voltage disparity comprises physical shift of charge and the kinetics of this shift launches the frequency response of the substance properties.

In natural surroundings, this voltage disparity could appear in either resonance forms or relaxation. This relaxation reaction in materials can be defined by the physical procedures

involved, and can be denoted in terms of the relaxation time constant (τ). Moreover, there are many materials whose dielectric oscillation procedures are known to have more than one relaxation time constant. For example, biological materials permit several relaxation procedures to proceed simultaneously hence, the total electrical reaction of the material can be considered using several time constant.

The Debye relaxation theory developed by scientist to consider the dielectric properties of materials in terms of the relaxation time τ is presented in the equation (2-5). The first and second order Debye equations are given in equations (2-6, 7) as they are used later in this thesis to analyse the dielectric properties of biological tissues against different range of frequencies [28].

$$\varepsilon^* = \varepsilon_\infty + \frac{\varepsilon_S - \varepsilon_\infty}{1+\omega^2\tau^2} - j\frac{(\varepsilon_S - \varepsilon_\infty)\omega\tau}{1+\omega^2\tau^2} \quad \text{Eq. (2-5)}$$

$$\varepsilon' = \varepsilon_\infty + \frac{\varepsilon_S - \varepsilon_\infty}{1+j\omega\tau} \quad \text{Eq. (2-6)}$$

$$\varepsilon' = \varepsilon_\infty + \frac{\varepsilon_{S1} - \varepsilon_\infty}{1+j\omega\tau_1} + \frac{\varepsilon_{S2} - \varepsilon_\infty}{1+j\omega\tau_2} \quad \text{Eq. (2-7)}$$

Here the complex permittivity is represented by ε' , ε_{s1} and ε_{s2} are the relative static permittivity at low frequencies and ε_∞ is the relative optical permittivity at high frequencies.

The relaxation spectrum of biological tissue extends over the electromagnetic (EM) spectrum to four different dispersion regions bound to the coverage frequencies ($\alpha, \beta, \delta, \gamma$). These regions represent the relaxation processes for the frequency range of a few hertz to a few Giga hertz as summarised in Table 2.1 [29]:

Table 2. 1: Frequency characterisation of the main biological tissue relaxation regions [29].

Region	Frequency Range (Hz)
α	$1 - 10^4$
β	$10^4 - 10^8$
δ	$10^8 - 10^9$
γ	$\sim 10^{10}$

The second order Debye model within the δ, γ regions will be used later in this work to model the tissue.

2.4. DETECTION PARAMETERS

In this section, two main and important parameters in any radar system, which is expected to detect an object in a medium, are defined: The **penetration depth** and the **range resolution**.

2.4.1. PENETRATION DEPTH

The propagation constant of each model layer can be defined as $\gamma = \alpha + j\beta$, where α is the attenuation constant, β is the phase constant and the δ is the skin depth constant. The three parameters are defined by equations (2-9, 2-10 and 2-11) [30, 31]:

$$\alpha = \omega\sqrt{\mu_0\varepsilon_0\varepsilon_r}\left[\frac{1}{2}\left(\sqrt{1+\left(\frac{\sigma}{\omega\varepsilon_0\varepsilon_r}\right)^2}-1\right)\right]^{\frac{1}{2}} \quad Neper/m \qquad \text{Eq. (2-9)}$$

$$\beta = \omega\sqrt{\mu_0\varepsilon_0\varepsilon_r}\left[\frac{1}{2}\left(\sqrt{1+\left(\frac{\sigma}{\omega\varepsilon_0\varepsilon_r}\right)^2}+1\right)\right]^{\frac{1}{2}} \quad rad/m \qquad \text{Eq. (2-10)}$$

$$\delta = \frac{1}{\alpha} = \frac{1}{\omega\sqrt{\mu_0\varepsilon_0\varepsilon_r}\left[\frac{1}{2}\left(\sqrt{1+\left(\frac{\sigma}{\omega\varepsilon_0\varepsilon_r}\right)^2}+1\right)\right]^{\frac{1}{2}}} \quad m \qquad \text{Eq. (2-11)}$$

Considering the dielectric properties of materials, the three modelled tissue types used to describe the abdomen tissue (skin, fat and muscle) have large differences in permittivity that can lead to recognition of each of the three kinds of tissue. In regards to the tissue dielectric properties, some factors lead to variations of tissue properties from one individual to the next such as age and sex. The major effects caused by frequency differences can be ignored at this stage of design [32].

Once an electric field is applied to a dielectric material, it takes a finite extent of time to become polarized. When this electric field fluctuates in time, it causes the material polarization to become out of phase with the introduced field. The polarization of the complex permittivity can be broken down to the polarization of the real part of the permittivity in phase with the field and the polarization of the imaginary part of the permittivity in quadrature to the field. This phase difference can attenuate the wave as it travels through the material.

The attenuation properties of a dielectric material can be defined by a property known as the skin depth (δ), the depth at which the amplitude of a penetrating signal is attenuated

to 1/e of its initial value. The skin depth can be referred to as penetration depth and calculated by equation 2.12.

$$\delta = \sqrt{\frac{2}{\omega\mu\sigma}} \qquad \text{Eq. (2-12)}$$

where ω represents the angular frequency, μ represents the permeability of the material, and σ is the material conductivity. The penetration depth for the three main tissue types (Skin, Fat, and Muscle) of the human body were defined later by Gregory Connor Richard Melia using the measured dielectric properties and using the Gabriel's Cole-Cole model [27, 33].

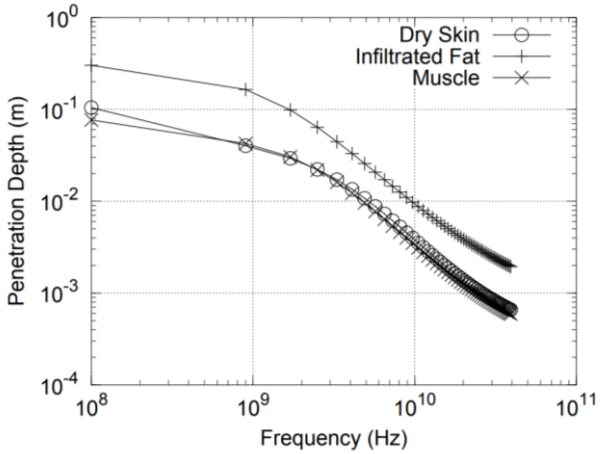

Fig 2. 5. Log-log plot of penetration depth from 100 MHz to 40 GHz of dry skin, infiltrated fat, and muscle by Gabriel's Cole-Cole model [33].

The initial centre frequency for the design was selected to be 3.2 GHz to have acceptable penetration depth in this region and to fit within the UWB licence-free band set by FCC. However, later a GP with the centre frequency of 1.5 GHz (i.e. WB pulse) was chosen for the system as it benefits from better penetration and resolution. Tables 2.2 and 2.3 present the dielectric properties, loss tangents, wavelengths and penetration depths for each of these tissues in 1.5 and 3.2 GHz frequencies [34].

Table 2. 2: Penetration parameters of three type of human tissues in 1.5 GHz.

Tissue Name	Frequency (GHz)	Conductivity (S/m)	Relative Permittivity	Loss tangent	Wavelength (mm)	Penetration depth (mm)
Skin Dry	1.5	1.071	39.4	0.326	31.4	31.5
Skin Wet	1.5	1.089	44.4	0.297	29.7	32.8
Fat	1.5	0.068	5.4	0.151	85.9	181.6
Muscle	1.5	1.188	53.9	0.264	27	33.1

Table 2. 3: Penetration parameters of three type of human tissues in 3.2 GHz.

Tissue Name	Frequency (GHz)	Conductivity (S/m)	Relative Permittivity	Loss tangent	Wavelength (mm)	Penetration depth (mm)
Skin Dry	3.2	1.850	37.3	0.279	15.2	17.7
Skin Wet	3.2	2.087	41.8	0.280	14.3	16.6
Fat	3.2	0.14	5.2	0.151	40.9	86.7
Muscle	3.2	2.303	51.8	0.25	12.9	16.7

The parameters shown in Tables 2.2 and 2.3 indicate that the penetration depth has inverse relation to the centre frequency. This means by reducing the centre frequency by half, the penetration depth will be increased to double. Therefore, comparing the penetration depth factor in the modelled tissue types defined at two different frequencies (1.5 and 3.2 GHz) suggests use of lower frequency (1.5 GHz) is better to obtain the higher penetration depth in the modelled tissue.

2.4.2. RANGE RESOLUTION

One important factor in any stationary radar system that has to detect different targets close or bound to each other is Range Resolution. Range resolution is defined as the capability of any radar system to differentiate between two or more targets that are very close to each other on the same altitude but different ranges.

Degree of range resolution is related to the width of transmitted pulse, which should be selected to correspond, the types and sizes of targets and the efficiency of the receiver.

In the 19th century, the English physicists Baron Rayleigh and John Strutt produced a criterion that later was named Rayleigh Criterion. This criterion identifies that in order to detect two targets in the same altitude, crossing of two reflected scattering should be 9 dB below their maximum value as shown in Fig. 2.6 [35].

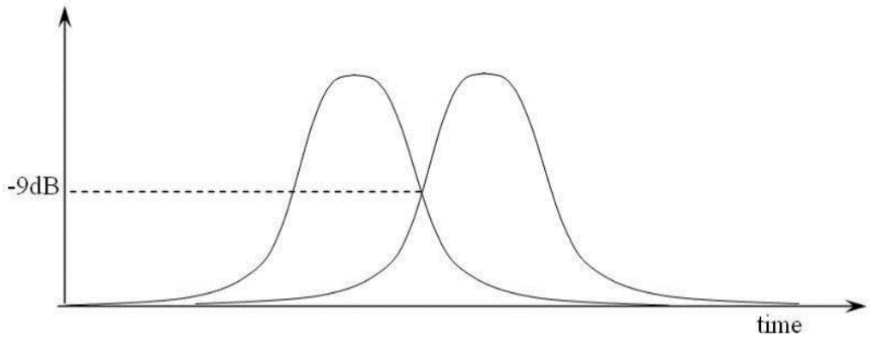

Fig 2. 6: Rayleigh criterion: limit of resolution for two point-scatters [35].

Pulse width is the key factor in range resolution. An ingenious radar system, with all other elements at maximum efficiency, should be able to distinguish targets separated by one-half the pulse width time; Therefore, theoretical range resolution of a radar system can be defined as [36]:

$$\Delta R = R_{n-1} - R_n = \frac{c.\tau}{2} \text{ (m)} \qquad \text{Eq. (2-13)}$$

Where $c = 3 \times 10^8 (^m/_s)$ represents the speed of light in free space, τ (s) is the pulse width in second and ΔR is the distance between two targets in meters. This means that by increasing the pulse bandwidth results in reduction of the pulse width in time domain, smaller targets can be resolved by the system.

When there is a limitation in increasing the width of the pulse (due to sampling and down conversion issues), the pulse compression technique can be applied in order to increase the bandwidth of the pulse.

The range resolution of the radar can be defined by the bandwidth of the transmitted pulse (B) instead of its pulse width, as shown in equation (2-14). This allows very high resolution to be obtained with long pulses, requiring higher average power.

$$\Delta R \geq \frac{c}{2B\sqrt{\varepsilon_r}} \text{ (m)} \qquad \text{Eq. (2-14)}$$

Based on the findings in the previous part of this thesis, for designing a radar system that is capable of detecting the abdominal fat layer attached to another thin skin layer (with thickness of 2 mm), the suitable pulse bandwidth can be derived from (2-14) as:

$$B \geq \frac{c}{2\Delta R\sqrt{\varepsilon_r}} \text{ (Hz)} \qquad \text{Eq. (2-15)}$$

Considering the initial estimation of thicknesses of different layers in the tissue model, the required bandwith is generated for the free space and for the high dielectric ceramic using equation (2-15) in Table 2.4;

Table 2. 4: The human tissue thickness and related bandwidth required for detection in free space and the ceramic environment.

Tissue types	Thickness [mm]	Required BW in free space ($\varepsilon_r = 1$) [GHz]	Required BW in the ceramic ($\varepsilon_r = 41$) [GHz]
Skin	2	75	11.7
Fat	16	9.4	1.46
Muscle	30	5	0.78

Table 2.4 represents the minimum required bandwidth for the system in the free space and high dielectric medium (ceramic ε_r=41) to avoid the overlapping issue. The results represent that by increasing the permittivity of the environment in which the system operates by a factor of 41, the required bandwidth will reduce by 6.4 times. To achieve this, a signal technically requires a very wide bandwidth that exceeds the UWB bandwidth region. There are a number of techniques proposed by researchers to increase the bandwidth, but they are not employed because of their limitations, such as:

- For the licence-free UWB technique, regulations restrict the bandwidth from the extreme bandwidth required when the antenna has to be located in free space.
- In order to be able to penetrate inside the lossy material such as human tissues, there is a need for using a centre frequency of less than 4 GHz, as indicated from equation (2-11). This low centre frequency is another limitation that can make the project more problematic.

In order to have a better understanding of the effects of increasing the bandwidth and the generated errors, different techniques to increase the pulse bandwidth are reviewed here briefly:

Pulse compression is a common method, which is a process to shape a propagating pulse by modifying the electrical network properties of the transmission line. This process is conducted by frequency or phase modulation. As a result, we will have a high-energy long pulse, or a high-resolution short pulse. This process is carried out in order to increase the detection and range resolution of the system at a lower peak power.

By modulating the pulse, a timing reference is produced within the pulse, similar to frequency-modulated continuous wave (FMCW) radar systems. Several different modulation techniques can be employed. The most common ones are:

- FM (Frequency Modulation)
  - Linear Frequency Modulation (Chirp Radar)
  - Non-Linear Frequency Modulation
  - Time-Frequency Coded Modulation (e.g. Costas code)
- PM (Phase Modulation)
  - Encoded phase modulation (e.g. Barker code)
  - Polyphase modulation

Although the pulse compression technique has various benefits such as low pulse power with good range and distance resolution, it suffers from the significant disadvantage that the minimum measurement range is degraded depending on the pulse length, since the radar receiver is blocked during transmission of the pulse. This is a major disadvantage for the radar systems used for the air traffic control as well, therefore typically both techniques are employed to minimise the effects. The frequency-modulated pulses for the shorter range are small (very short) pulses, which only have to cover the nearby area and do not require very high pulse power.

Linear FM (Chirp) is a most common technique that is being used in many radar systems based on its simplicity; however, it can introduce the problem of producing jamming pulses within the system by the so-called sweeper [37].

In past and recent years, various researchers have considered the chirp technique, and more techniques have been developed for generating and processing a pulse using this technique, compared to other modulating techniques. The radar requirements influence the type of pulse and the method of generating and processing the pulse. As the aim of this radar system is to scan human tissue layers as thin as 2 mm, radar system sitting close to the scanning area of the tissue. Furthermore, two relevant methods, which both use a voltage-controlled oscillator (VCO) are chosen and will be discussed here:

- In the first method, a linear voltage ramp is used to alter the voltage of a VCO gradually, which results in varying the frequency generated by the VCO. This technique is used to generate of a linear-FM waveform that more likely adds a linearity error of ±1% to the system (the VCO is a device that generates a

frequency with respect to an applied voltage). There are different approaches to generate a linear voltage ramp such as the bootstrap ramp generator circuit based on a bipolar junction transistor (BJT) differential pair amplifier [38] or simply applying a voltage step to an analogue integrator, however, the integrator must be reset each time when pulse generation gets to its end [39].

- The second approach is to apply a composite right left-handed transmission line (CRLH-TL) after modulation of our VCO frequency with an intermediate pulse [40].

2.4.2.1. SUPER RESOLUTION ALGORITHM

Researchers have developed many processing algorithms in these last few decades that can be used to increase the range resolution without extending pulse bandwidth, at the cost of some limitations to the design such as complexity and cost. Many of these methods referred to as super-resolution techniques. The main algorithms can be summarized as the maximum entropy method (Burg), the covariance method (Prony), CLEAN, Matrix pencil, ESPRIT, MUSIC, Root-MUSIC.

In 1997, the Lincoln Laboratory established a method to use the WB radar signature to detect an object by using sparse sub-band measurements. This method expands the range resolution of the reflected pulses by increasing the operative bandwidth through a bandwidth extrapolation algorithm (BWE) [41, 42].

The BWE algorithm intends to expand the effective bandwidth of the radar employing the prediction of the object's response at specific frequencies that lie outside the measurement bands. This technique increases the range resolution by a factor of two to three and can improve the quality of images dramatically. Although this improves the resolution of the image developed by the system, it introduces some limitations such as [43]:

- The algorithm works mainly on signal processing models, which characterise a complex target as a collection of points, with each point hits own independent function for scattering amplitude versus frequency.
- The method is satisfactory for typical wideband signal processing where the waveforms have a small fractional bandwidth compared with the centre frequency of the radar system. However, the scattering amplitude of the discrete scattering centres can fluctuate significantly with frequency.

2.5. TRANSMISSION AND REFLECTION

In this section, two kinds of transmission and reflection of the pulse are described for an EM wave propagating from one medium into another medium (i.e. direct and diagonal incidence).

2.5.1. NORMAL INCIDENT:

In the case when the direct pulse penetrates through mediums, it splits into transmitted and reflected portions as shown in Fig. 2.7.

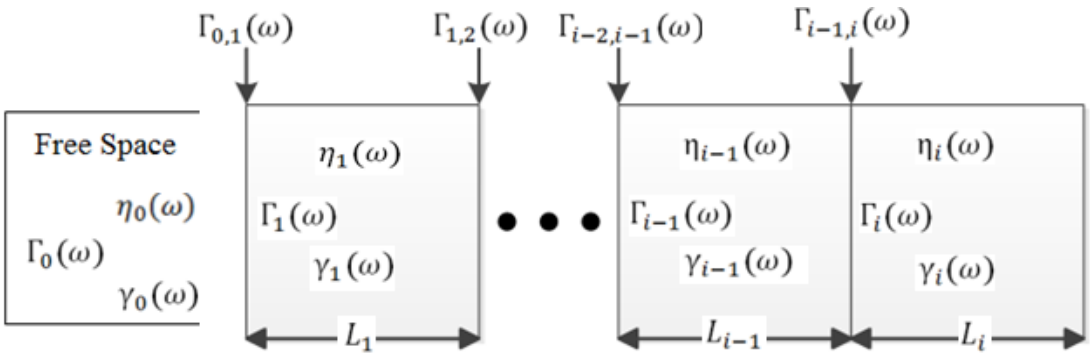

Fig 2. 7: Transmission line model of a multilayer structure [32].

Here Γ_i is the total reflected field by the i^{th} layer and can be found by equation (2-16) [44, 45]:

$$\Gamma_{i-1}(\omega) = \frac{\Gamma_{i-1,i}(\omega)+\Gamma_i(\omega).e^{(-2\gamma_i(\omega)d_i)}}{1+\Gamma_{i-1,i}(\omega)+\Gamma_i(\omega).e^{(-2\gamma_i(\omega)d_i)}} \qquad \text{Eq. (2-16)}$$

where $\Gamma_{i-1,i}(\omega)$, the reflection coefficient seen at the interface between two layers, is defined by equation (2-17):

$$\Gamma_{i-1,i}(\omega) = \frac{\eta_i-\eta_{i-1}}{\eta_i+\eta_{i-1}} = \frac{\sqrt{\frac{\mu_{r\_i}}{\varepsilon_{r\_i}}}-\sqrt{\frac{\mu_{r_{i-1}}}{\varepsilon_{r_{i-1}}}}}{\sqrt{\frac{\mu_{r\_i}}{\varepsilon_{r\_i}}}+\sqrt{\frac{\mu_{r_{i-1}}}{\varepsilon_{r_{i-1}}}}} = \frac{\sqrt{\varepsilon_{r_{i-1}}}-\sqrt{\varepsilon_{r_i}}}{\sqrt{\varepsilon_{r_{i-1}}}+\sqrt{\varepsilon_{r_i}}} \qquad \text{Eq. (2-17)}$$

Starting at the total reflection coefficient of the model $\Gamma_0(\omega)$ can be calculated (i=n), where n is the number of layer's performing successive calculations and decreasing (i) successfully until we reach one layer.

In the case of the multilayer model with n layers of infinite width or unit we reach the case of a reflector, we can set $\Gamma_n(\omega)$ to zero or to -1 for all frequencies. To calculate $\Gamma_{0,1}(\omega)$, the layer zero should be assigned to intrinsic properties of free space.

In equation (2-17), d_i is the thickness of i^{th} layer and $\gamma_i(\omega)$ is the propagation constant, which is derived according to equation (2-18):

$$\gamma_i(\omega) = j\omega\sqrt{\mu\varepsilon} = j\omega\sqrt{\mu_0\varepsilon_0}\sqrt{\mu_{r\_i}(\omega).\varepsilon_{r\_i}(\omega)} = j\omega\sqrt{\mu_0\varepsilon_0}\sqrt{\varepsilon_{r\_i}(\omega)} = j\omega\frac{\sqrt{\varepsilon_{r\_i}(\omega)}}{c} \qquad \text{Eq. (2-18)}$$

The complex relative permittivity of each layer can be calculated using equation (2-19), which was proposed in 1996 by Gabriel [27] to analyse the quantity of data in different types of tissue.

$$\varepsilon_{r_i}(\omega) = \varepsilon_\infty + \sum_{m=1}^{4}\frac{\Delta\varepsilon_m}{1+(j\omega.\tau_m)^{1-\alpha_m}} + \frac{\sigma_{static}}{j\omega.\varepsilon_0} \qquad \text{Eq. (2-19)}$$

ε_∞ is permittivity if $\omega\tau \gg 1$, $\Delta\varepsilon_m$ is magnitude of the dispersion, τ_m is relaxation time, $\propto_m$is distribution parameter and σ_{static} is static conductivity.

2.5.2. PULSE REPETITION AND TRANSMISSION REFLECTION

Pulse repetition frequency (PRF) is defined as the number of pulses generated by a radar system in a one-second interval, which has an inverse relation with respect to the pulse repetition time (PRT) as shown in equation (2-20). The PRT is defined using the total amount of time from the start of one pulse to the start of next pulse generated by the system:

$$PRF = \frac{1}{PRT} \qquad \text{Eq. (2-20)}$$

In order to increase the accuracy of a radar system and distinguish the pulses reflected from the human tissue model, it is important to determine the PRF of the system.

The multilayer human tissue model has different specification not only in electric properties but in the thickness of each layer, which causes several echo traveling pulse time with respect to each layer of the system.

In order to define the PRT, the traveling time of the reflected pulse has to be determined in advance. The traveling time has a direct relation to the distance through which the echo pulses will travel as shown in equation (2-21):

$$t = \frac{d}{v} \qquad \text{Eq. (2-21)}$$

where *t* stands for the time taken for the pulse to travel from the transmitter to the target and reflect back to the receiver, d is the distance from the transmitter to the target and

back to the receiver, as shown in equation (2-22), and finally *v* is the velocity of the wave in the medium:

$$d = 2\frac{l}{sin\theta} \quad \text{Eq. (2-22)}$$

where l represents the distance and θ is the angle of the pulse from/to the transmitter/receiver to the target. The velocity of an EM wave through any medium can be determined using equation (2-23) [46]:

$$v = \frac{c}{\sqrt{\varepsilon_r}} \quad \text{Eq. (2-23)}$$

where ν is the velocity of the wave in the specific medium, $c \cong 3 \times 10^8\, {}^{m}/_{S}$ is the velocity of the wave in free space (the same as light) and ε_r is the relative permittivity of the medium at a specific frequency.

Table 2.5: Time taken for the signal to penetrate through the medium.

Tissue types	Speed V(m/s)	Thickness (mm)	Time taken (ns)
Skin	0.49 x 10^8	2	0.08
Fat	0.13 x 10^8	16	0.08+0.106=0.186
Muscle	0.04 x 10^8	30	0.186+0.2=0.386

Table 2.5 provides the time taken by the pulse to pass through each layer in the medium with respect to its thickness and the signal speed in each layer. However, in the case that the pulse also reflects back to the receiver this has to be multiplied by two as shown in equation (2-22).

For a wave with a frequency of f, the wavelength in any medium can be defined by equation (2-24):

$$\lambda = \frac{\upsilon}{f} \quad \text{Eq. (2-24)}$$

where υ can be calculated by equation (2-23). Since $\varepsilon_r > 1$, λ is smaller than the wavelength in vacuum. The wave phase constant (β) for EM wave is:

$$\beta = \frac{2\pi}{\lambda} \quad \text{Eq. (2-25)}$$

The wave can be stated as $Ae^{j(\omega t - \beta z)}$ where ω=2πf is the angular frequency. The propagation constant measures the amount of phase accumulated per unit length. The phase velocity is shown in equation (2-26):

$$v_p = \frac{\omega}{\beta} = \lambda f \qquad \text{Eq. (2-26)}$$

In practice, every single EM signal holds multiple frequency components. The superposition of a group of plane waves is called a wave packet.

Group velocity (v_g) is the propagation velocity of a wavepacket which is different from phase velocity (v_p). It is a function of frequency and is defined by (2-27).

$$v_g = \frac{d\omega}{d\beta} \qquad \text{Eq. (2-27)}$$

2.6. TIME DOMAIN METHODS

2.6.1. TIME DOMAIN REFLECTOMETRY (TDR)

TDR measurement has been widely used by previous researchers to indicate the time at which the pulse moves from one medium to the other medium with different dielectric properties, based on the reflections. Understanding of some fundamentals, which are summarized in the following can help us to determine the behaviors at different time, the signature of the TDR pulse from any transmitter is recognised as the propagation of EM waves in any medium. The plane Maxwell equations can be employed to provide a simple solution for the electric field vector E_0 of a time-harmonic wave. Propagation of a pulse in the z-direction can be expressed as follows [47, 48]:

$$E = E_0 \cdot e^{-i(\omega t - k^* z)} \qquad \text{Eq. (2-28)}$$

where ω is the angular frequency and k^* is the complex wave number that can be defined by equation (2-29) :

$$k^* = \frac{\omega}{c^*} = \omega\sqrt{\mu\varepsilon^*} \qquad \text{Eq. (2-29)}$$

In addition, c^* is the complex velocity of the pulse propagating in the medium, μ is the permeability and ε^* is the complex permittivity. As the non-ferromagnetic medium is being used throughout, therefore the permeability of vacuum (μ_0) will be used.

$$c^* = \frac{1}{\sqrt{\mu_0\varepsilon^*}} = \frac{1}{\sqrt{\mu_0\varepsilon_0\varepsilon_r^*}} = \frac{c_0}{\sqrt{\varepsilon_r^*}} \qquad \text{Eq. (2-30)}$$

where ε_r^* is the complex relative permittivity, ε_0 is the permittivity of vacuum and c_0 is the velocity of wave propagation in vacuum.

Combining Equations (2-29 and 2-30), we obtain:

$$k^* = \frac{\omega}{c_0}\sqrt{\varepsilon_r^*} \quad \text{Eq. (2-31)}$$

Moreover, using the notation $k^* = k' + ik''$, $\varepsilon_r^* = \varepsilon_r' + i\varepsilon_r''$ then,

$$k' = \frac{\omega}{c_0}\sqrt{\varepsilon_{r1}} \quad \text{Eq. (2-32)}$$

$$k'' = \frac{\omega}{c_0}\sqrt{\varepsilon_{r2}} \quad \text{Eq. (2-33)}$$

where,

$$\varepsilon_{r1} = \frac{1}{2}\left(\sqrt{(\varepsilon_r')^2 + (\varepsilon_r'')^2} + \varepsilon_r'\right) \quad \text{Eq. (2-34)}$$

$$\varepsilon_{r2} = \frac{1}{2}\left(\sqrt{(\varepsilon_r')^2 + (\varepsilon_r'')^2} - \varepsilon_r'\right) \quad \text{Eq. (2-35)}$$

Substituting Eq. (2-32) and Eq. (2-35) into Eq. (2-28) by equation (2-36) can be obtained:

$$E = E_0 \cdot e^{-k''z} \cdot e^{-i(\omega t - k'z)} = E_0 \cdot e^{-z.\frac{\omega}{c_0}\sqrt{\varepsilon_{r2}}} \cdot e^{-i\omega\left(t - \frac{z}{c_0}\sqrt{\varepsilon_{r1}}\right)} = A(z).e^{-i\omega(t - \frac{z}{c_f})} \quad \text{Eq. (2-36)}$$

Where A (z) is the real pulse amplitude value and defined by equation (2-37):

$$A(z) = E_0 \cdot e^{-z.\frac{\omega}{c_0}\sqrt{\varepsilon_{r2}}} \quad \text{Eq. (2-37)}$$

In addition, c_f is the phase velocity of a pulse propagating in a non-absorbing medium.

$$c_f = \frac{c_0}{\sqrt{\varepsilon_{r1}}} \quad \text{Eq. (2-38)}$$

Based on the previous equations, if an EM pulse is propagating through an absorbing medium with a known thickness of Δz, two quantities can be defined. The traveling time (Δt) of the pulse that passes the distance Δz, and the attenuation A that can be defined as follows:

$$A = \frac{A(\Delta z)}{A(0)} \quad \text{Eq. (2-39)}$$

Using Eq. (2-37) & Eq. (20-38), by equations can be obtained:

$$lnA = -\frac{\omega}{c_0}\sqrt{\varepsilon_{r2}}.\Delta z \quad \text{Eq. (2-40)}$$

$$\frac{\Delta z}{\Delta t} = \frac{c_0}{\sqrt{\varepsilon_{r1}}} \quad \text{Eq. (2-41)}$$

Substituting (2-34) and (2-35) into (2-40) and (2-41) we obtain a system with two algebraic equations for unknown real and imaginary parts of the complex relative permittivity ($\varepsilon_r', \varepsilon_r''$):

$$\frac{1}{2}\left(\sqrt{(\varepsilon_r')^2+(\varepsilon_r'')^2}+\varepsilon_r'\right)=\left(\frac{c_0\Delta t}{\Delta z}\right)^2 \quad \text{Eq. (2-42)}$$

$$\frac{1}{2}\left(\sqrt{(\varepsilon_r')^2+(\varepsilon_r'')^2}-\varepsilon_r'\right)=\left(\frac{c_0.lnA}{\omega\Delta z}\right)^2 \quad \text{Eq. (2-43)}$$

This leads to definitions for the $\varepsilon_r', \varepsilon_r''$:

$$\varepsilon_r'=\left(\frac{c_0}{\Delta z}\right)^2.[\Delta t^2-\left(\frac{lnA}{\omega}\right)^2] \quad \text{Eq. (2-44)}$$

$$\varepsilon_r''=-2\left(\frac{c_0}{\Delta z}\right)^2.\frac{\Delta t}{\omega}.lnA \quad \text{Eq. (2-45)}$$

For the case of very low attenuation of an EM wave into the material, the equation can be redefined by $lnA \to 0$ and the equations (2-44 and 2-45) can be simplified further into the equations (2-46 and 2-47) as follows:

$$\varepsilon_r'=\left(\frac{\Delta t c_0}{\Delta z}\right)^2 \quad \text{Eq. (2-46)}$$

$$\varepsilon_r''=-2\frac{c_0}{\omega\Delta z}.\sqrt{\varepsilon_r'}.lnA \quad \text{Eq. (2-47)}$$

The velocity of an EM wave through each medium could be shown by equation (2-48):

$$v=\frac{c}{\sqrt{\varepsilon_r}} \quad \text{Eq. (2-48)}$$

2.6.2. GROUP DELAY

Group delay is described as the negative derivative of phase response with respect to a frequency; this is another useful parameter to describe phase response of the pulse. The group delay changes during propagation through each medium and reflection from each medium back to the receiving antenna. The group delay is indicating the time delay the signal suffers at each exact frequency in a specific medium. However, if the antennas have non-linear phase response, the group delay differs with frequency and this causes the pulse to experience different delays at different frequencies. Therefore, the pulse is likely to get distorted [46]. The group delay is defined as the rate of change of total phase shift with respect to angular frequency, going through a driven medium and is given by equation (2-49):

$$\tau_g=-\frac{d\emptyset}{d\omega} \quad \text{Eq. (2-49)}$$

where Ø is a total phase shift in radians and ω is the angular frequency in radians per unit of time.

2.7. REVIEW ON RELEVANT ANTENNA DESIGNS

In order to design an antenna for a system, the selected design has to satisfy the system requirements such as to have good directivity, gain, and wide bandwidth. There are a number of WB antennas with high directivity designed and built by previous researchers for detecting an object [49]. The new design has to comply with the needs of this application such as compact size, having large bandwidth, and having centre frequency of less than 3 GHz, with good directivity and gain over the bandwidth.

The review on existing UWB antennas for the system reveals there are different types of WB antenna designs that have been used in past for the human scanning by different research groups. In this part, a few important designs will be considered and their advantage, to be chosen as the ideal design for the system, will be declared.

A compact double-layer on-body matched bowtie antenna has been designed using mixture of a polyethylene glycol (PEG) 400 and a distilled water dielectric liquid that has a permittivity of 45 and conductivity of 0.5 S/m at 2 GHz. The liquid is placed in a cubic box located at the back cavity of the design.

The group of researchers in the Institut für Hochfrequenztechnik und Elektronik (IHE), KIT, Germany [50], have published many antenna designs, which have used high dielectric materials. The antenna design shown in Fig. 2.8 (a) operates in acceptable wide bandwidth around 1.5 GHz from 0.5 to 2 GHz in simulation and experiment, however, the design suffers from insufficiently high gain and can achieve a maximum gain of 6 dBi in the frequency range of 1 to 2 GHz.

Three-dimensional folded antenna with the UWB performance, directional radiation and compact size was designed using two parallel slabs of GIL GML 1032 substrate (dielectric constant ε_r = 3.2, thickness h_s = 1.52 mm) by the group of researchers in the University of Queensland, Australia [51]. The design represented in Fig. 2.8 (b) qualifies as wide bandwidth covering from 1.27–2.57 GHz with a maximum gain of up to 6 dBi. The lower frequency chosen for this system was expected to improve the penetration depth at lower centre frequency.

A directional double-ridged horn (DRH) antenna in a matching liquid for microwave radar imaging was designed, with canola oil as the liquid as shown in Fig. 2.8 (c). The canola oil has a measured permittivity of 3 at 2 GHz, conductivity 0.03 S/m. An ultra-wide bandwidth of 3.75 GHz (1.54 to 5.29 GHz), equalling 110% was achieved with the

maximum gain of 7.8 dBi at a frequency of 2.4 GHz. The joint groups at University of South Alabama, USA and University of Manitoba, Canada published this work [52]. These groups later published another design, using the distilled water with permittivity of 76 and low conductivity of 10 μS/cm, that reduced the size of the antenna significantly, however the bandwidth of the design decreased to 260 MHz (1.28 to 1.54 GHz) at −10 dB point, which was ignored and −5 dB point was selected at first [53]. Miniature DRH antennas composed of solid high-permittivity sintered ceramics (LF085 with $\varepsilon_r = 75$) for biomedical ultra-wideband radar applications were designed by the group of researchers in the Ilmenau University of Technology, Germany. The first approach by this group was using pure water with permittivity of 76 however because of the mismatching and low gain they were motivated to design the antenna made from a high dielectric ceramic that has a permittivity of 75 and very low conductivity. The design provides a very wide bandwidth of around 4 GHz and acceptable gain of around 15 dBi. The design is represented in Fig. 2.8 (d) [54].

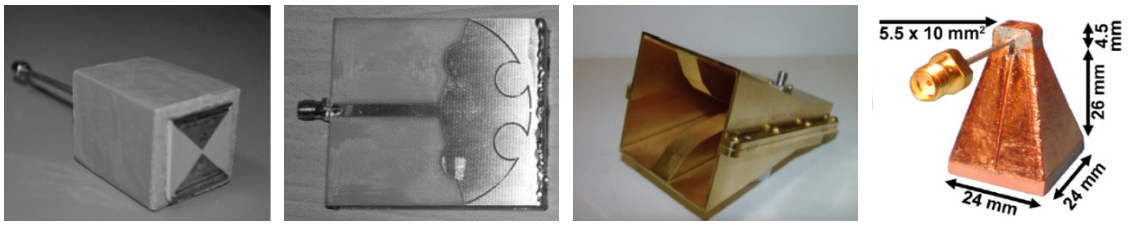

(a) [50] (b) [51] (c) [52] (d) [54]

Fig 2. 8: The relevant antennas designed by different research group for on-body medical applications.

Comparing these designs, the DRH found more suitable for the abdomen fat measurement system based on its innovative parameters such as good directivity, gain, wide bandwidth, easy of fabrication. The antenna can be filled with different high dielectrics, in order to be miniaturised and matched to human body to minimise the large mismatched reflection.

2.7.1. HORN ANTENNA DESIGN PROCESS

The most universal and elementary microwave antenna being used in any microwave field is the horn antenna. The horn antenna advantages are factors such as the design simplicity, ease of excitation, high bandwidth and high gain. These factors make the antenna an exceptional design compared to others. However, miniaturising the antenna size for different applications is one of the main challenges for the antenna designers. The horn antenna has different types that are named based on their shapes and radiation patterns such as the pyramidal horn (PH) and conical horn (CH) geometry in the Figs. 2.9 [54].

2.7.1.1. PYRAMIDAL HORN ANTENNA DESIGN

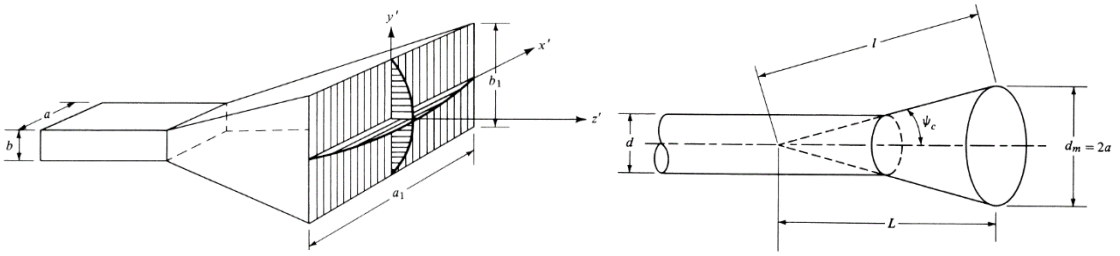

(a) Geometry of the PH. (b) Geometry of the CH.

Fig 2. 9: Pyramidal and Cylindrical horn antenna geometry.

The PH antenna is widely used in microwave applications compared to others because of its satisfactory radiation characteristics, which are attained by the combination of the E- and H-plane sectional horns as shown in Figs. 2.10 (a) and (b).

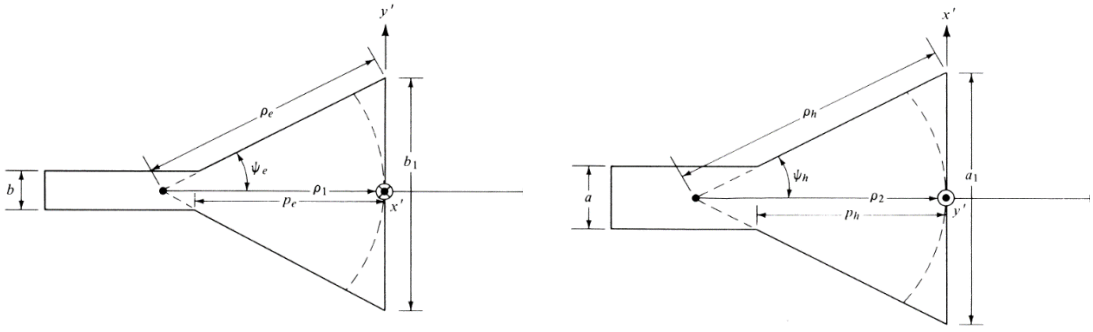

(a) Geometry of the E-plane horn. (b) Geometry of the H-plane horn.

Fig 2. 10: E and H-plane geometry of the PH antenna.

In order to construct a PH, the given dimensions in Figs 2.10 for E- and H- plane should be determined. The values for the p_e and p_h can be calculated using by equations (2-50 a–b):

$$p_e = (b_1 - b)[\left(\frac{\rho_e}{b_1}\right)^2 - \frac{1}{4}]^{1/2} \qquad \text{Eq. (2-50a)}$$

$$p_h = (a_1 - a)[\left(\frac{\rho_h}{a_1}\right)^2 - \frac{1}{4}]^{1/2} \qquad \text{Eq. (2-50b)}$$

The directivity of the design is optimised by use of equations (2-50 c–d), [55]:

$$a = \frac{a_1}{\lambda}\sqrt{\frac{50}{\rho_h/\lambda}} \qquad \text{Eq. (2-50c)}$$

$$b = \frac{b_1}{\lambda}\sqrt{\frac{50}{\rho_e/\lambda}} \qquad \text{Eq. (2-50d)}$$

The standard PH parameters usually are calculated based on the desired gain G_0 by using the equation (2-50e) and the dimensions of a, b of the rectangular feed waveguide that were calculated using equations (2-50 c–d).

$$\chi = \frac{G_0}{2\pi\sqrt{2\pi}}$$ Eq. (2-50e)

Once χ is determined from eq. (2-50e), then the p_e and p_h can be calculated by equations (2-50f, g).

$$\frac{\rho_e}{\lambda} = \chi$$ Eq. (2-50f)

$$\frac{\rho_h}{\lambda} = \frac{G_0^2}{8\pi^3}\left(\frac{1}{\chi}\right)$$ Eq. (2-50g)

Finally, the corresponding values of a_1 and b_1 can be evaluated using eq. (2-50 h–i):

$$a_1 = \sqrt{3\lambda\rho_2} \sim \sqrt{3\lambda\rho_h} = \frac{G_0}{2\pi}\sqrt{\frac{3}{2\pi\chi}}\lambda$$ Eq. (2-50h)

$$b_1 = \sqrt{2\lambda\rho_1} \sim \sqrt{2\lambda\rho_e} = \sqrt{2\chi\lambda}$$ Eq. (2-50i)

where λ represents the wavelength of the frequency of interest [54].

2.7.1.2. CONICAL HORN ANTENNA DESIGN

The physical construction of a conical horn CH involves the determination of the dimensions given in Fig. 2.9(b) that can be obtained by calculating waveguide diameter (d) and length (h) for the matching circuit, and then optimising the horn aperture (d_m) and its length (L) for maximum directivity. The directivity of the CH that has known aperture efficiency of ε_{ap} and aperture circumference of (c) can be determined using eq. (2-51a):

$$D_c(dB) = 10log_{10}^{[\epsilon_{ap}\frac{4\pi}{\lambda^2}(\pi a^2)]} = 10log_{10}^{(\frac{c}{\lambda})^2} - L(s)$$ Eq. (2-51a)

where a is the horns radius at the aperture, and L(s) can determined by Eq. (2-51b):

$$L(s) = -10log_{10}^{\epsilon_{ap}}$$ Eq. (2-51b)

The directivity of the CH optimised by the diameter length can determined by equation (2-51c):

$$d_m \approx \sqrt{3l\lambda}$$ Eq. (2-51c)

The next phase of the work focuses on mixing the structures of the two designs (pyramidal and conical) to produce a new design named elliptical horn, which benefits from the high bandwidth and gain. This new design can increase the directivity and therefore the gain and bandwidth compared to each individual design type [54].

2.7.1.3. DRH ANTENNA DESIGN IMPEDANCE MATCHING

There are different types of horn antenna designs developed and employed by researchers, and among all of these, double-ridged horns are most attractive for the task of matching the impedance in the monitoring area. Therefore, the pyramidal double-ridged horn (PDRH) antenna design is selected and redesigned for our system. Desirable aspects of this type of horn antenna such as the upgraded directivity, gain and widened impedance-matched bandwidth are necessary for the specific application of biomedical scanning. The impedance matching factor can be highly improved by using the ridges in the waveguide and in the flared part of the antenna. The coaxial connection is used to feed and excite the field into the design; however, the impedance matching of the coaxial connection to the double-ridged waveguide is an important factor as mismatch leads to the return loss. This degrades the performance of the antenna and should be considered in advance for the best outcome. Better match was achieved by lowering the voltage standing wave ratio (VSWR) of the design since it has a direct relation to the back cavity length, the initial distance between ridges in the rectangular waveguide, and the probe spacing from the ridged edge. An antenna in free space experiences the free space wave impedance of 377 Ohms that is determined by the equation (2-52a) presented next [52]:

$$z = \sqrt{\frac{\mu_0}{\varepsilon_0}} \qquad \text{Eq. (2-52a)}$$

where, $\varepsilon_0 = 8.854 \times 10^{-12}(\frac{F}{m})$ is the free space permittivity and $\mu_0 = 4\pi \times 10^{-7}(\frac{V.s}{A.m})$ is the free space permeability. However, if the antenna is built in or immersed within any dielectric material, the impedance will be different and can be calculated by equation (2-52b);

$$z_m = \sqrt{\frac{\mu_0}{\varepsilon_0 \varepsilon_r}} \qquad \text{Eq. (2-52b)}$$

where ε_r is the permittivity of a dielectric material that the antenna is built within, which has to be considered during the design process in order to achieve the highest performance for the antenna. It is universally accepted that one should construct the pyramidal back cavity to achieve the lower return loss from resonant points between the coaxial cable and the double-ridged waveguide demonstrated in Fig. 2.11 (a) [57, 58].

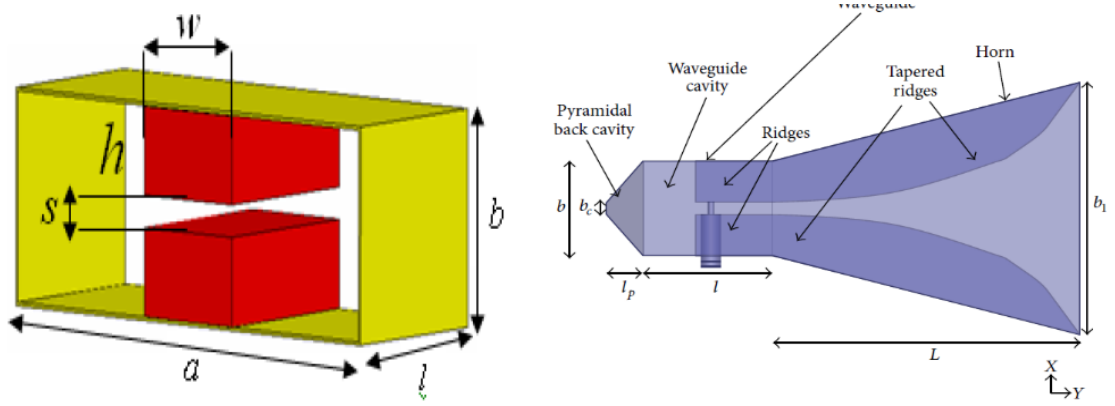

(a) Geometry of waveguide and ridges. (b) Geometry of a DRH Antenna.

Fig 2. 11: Geometry of the ridges in a DRH antenna.

Design of exponentially tapered section is the most crucial part of the design, as it has varying reference impedance, going from the 50 Ω coaxial connection to the free space impedance of 377 Ω at the antenna's aperture. The reference impedance is given by Eq. (2-53a), [57].

$$z(y) = z_0 e^{-ky}, (0 \leq y \leq L) \qquad \text{Eq. (2-53a)}$$

where y is the distance from the waveguide aperture and L is the axial length of the antenna from the opening along the exponential tapered part represented in Fig. 2.10 (b), and k is determined by Eq. (2-53b) [52].

$$k = \frac{1}{L}\ln\left(\frac{Z_L}{Z_0}\right) \qquad \text{Eq. (2-53b)}$$

Z_L and Z_0 are the characteristic impedance of the medium and of free space respectively. In order to synthesize the exponential tapered part of the antenna, different approaches have been taken by researchers such as dividing the tapered ridge to smaller ridges and corresponding each ridge to a characteristic impedance then adding these individual ridges together. The corresponding characteristic impedance gradually increases from 50 Ω to 377 Ω at the aperture in the case of the horn in free space [52].

2.7.1.4. ELLIPTICAL DOUBLE-RIDGED HORN ANTENNA DESIGN

The concept of an elliptical double-ridged horn (EDRH) antenna was developed by combining the PH and CH structure. The new design offers improved directivity, gain, and bandwidth factors. To determine dimensions of each section of the antenna, the same equations as for determining the PDRH antenna dimensions can be applied.

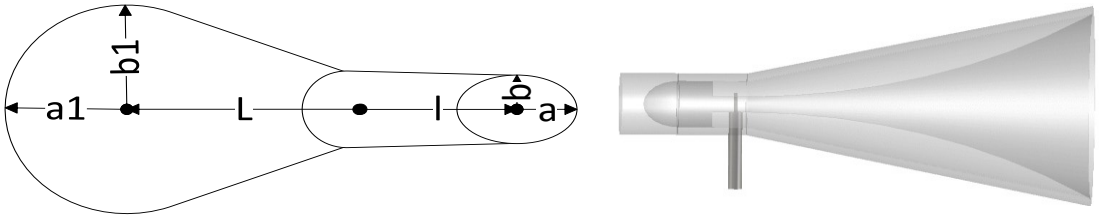

(a) (b)

Fig 2.12: Geometry of the EDRH antenna.

The EDRH antenna design presented in Fig. 2.12 improves the directivity and the bandwidth factors, compared to the PDRH antenna due to the smoother transition in all sections of the antenna. However, the complex structure of the design may raise the cost of the fabrication compared to the PDRH antenna, and should be considered. Recently, different techniques were developed to fabricate such an antenna at reduced cost like three-dimensional (3D) printing. However, there are always disadvantages for such methods. For example, another objective would be to considered using a dense metal with high conductivity for an acceptable system performance. The vertical and horizontal radius of the waveguide can be determined by the equations (2-49c and d) and the horn aperture's radius can be defined by the equations (2-49 h and i). Moreover, the length of the design that governs the impedance matching can be determined by equation (2-51, and 2-52) of the PDRH antenna design section [59].

2.7.2. SYSTEM REQUIREMENTS SUMMARY

After careful consideration of specification parameters, such as range resolution and penetration depth required for the system to be able to measure the abdominal fat. A GP with estimated minimum bandwidth of 500 MHz was selected to satisfy the system accuracy and centre frequency within the range of 1.5 to 3.5 GHz was chosen to fulfil the penetration depth for this application. Moreover, a number of antenna design was investigated and among all, the pyramidal and elliptical DRH antennas filled with high dielectric material were chosen as prime antennas for this application. The DRH antenna has the advantages over other types such as high gain and directivity, large bandwidth, impedance matching capability and miniaturisation ability with the high dielectric embedded inside the design.

2.8. CHAPTER SUMMARY

In this Chapter of the thesis, the following parameters have been reviewed and investigated:

- The human tissue dielectric properties.
- The suitable UWB pulse for this project and pulse parameters such as centre frequency, Bandwidth, and shape, based on the important factors for instance penetration depth and range resolution.
- The penetration depth mathematically calculated for the case of the 3.2GHz centre frequency, which is found to be appropriate for the case in which transmitter and receiver have been placed in free space.
- The range resolution mathematically is calculated for the free space case. The techniques, which widen the bandwidth of the pulse such as FM and PM were investigated. Furthermore, the pulse has been regenerated with the linear FM technique using MATLAB software and finally, super-resolution algorithms have been investigated in the case that the very wideband pulse needs to be produced. However, the technique may decrease the resolution.
- The hardware components for the system selected and their functionality have been investigated and will be designed, built, and tested, in the future.
- The transmission and reflection within the system have been inspected using the mathematical equations for the two cases of a direct incidence and a diagonal incidence; however, only direct incidence will be covered in this thesis.
- PRF of the system is studied in order to eliminate any error in the system by estimating the time of arrival for the reflected pulse from each specific target layer.
- The time domain results such as TDR and group delay were introduced to use for extracting information.
- A literature review was accomplished on various types of UWB directional antennas that are developed and used for the biomedical applications in which one needs to scan inside the human body.
- The pre-defined equations were introduced and employed for different types of horn antenna such as PH and CH antennas. In addition, the impedance matching equation was introduced and the antennas ridges dimensions were determined.

REFERENCES (CHAPTER 2)

[1] I. Amdaouch, *et al.,* "Breast tumor detection system based on a compact UWB antenna design," *Prog. Electromagn. Res. M*, vol. 64, pp. 123–133, Feb. 2018.

[2] S. Baskar, *et al.,* "Detection of brain stroke and brain tumour using UWB pentagon antenna," *in IJISRT*, Apr. 2019.

[3] H. S. Cho,Y. J. Park, "Detection of heart rate through a wall using UWB impulse radar," *Journal of Healthcare Engineering.,* Apr. 2018.

[4] R. Aiello and A. Batra, *Ultra Wideband Systems, Technologies and Applications*. London, U.K.: Newnes Publication, 2006.

[5] Federal Communications Commission, "Revision of part 15 of the commission's rules regarding ultra-wideband transmission systems," *First Report and Order*, FCC 02-48, Washington, DC, 2002.

[6] M. Ghavami, L. B. Michael, and R. Kohno, *Ultra Wideband Signals and Systems in Communication Engineering*, 2nd Edition, John Wiley & Sons, Inc., Jan. 2007.

[7] S. Sarjoghian, Y. Alfadhl, and X. Chen, "On the limitation of ultra-wideband technique for medical scanning systems," *in Loughborough Antennas & Propag. Conf. (LAPC)*, pp. 1–4, Nov. 2016.

[8] D. Li, *et al.,* "Evolution of the frequency chirp of Gaussian pulses and beams when passing through a pulse compressor," *Opt. Express*, Vol. 17, pp. 17070–17081, Sep. 2009.

[9] AH. Kissebah, *et al.,* "Relation of body fat distribution to metabolic complications of obesity.," *J Clin Endocrinol Metab*, vol. 54, no. 2, pp. 60-254, Feb. 1982.

[10] B. Larsson, K. Svardsudd, L. Welin, L. Wilhelmsen, P. Bjorntorp, G. Tibblin, "Abdominal adipose-tissue distribution, obesity, and risk of cardiovascular-disease and death - 13 year follow up of participants in the study of men born in 1913," *British Medical Journal*, vol. 288, pp. 1401-1404, May 1984.

[11] SH. Scheuer*, et al.,* "Abdominal fat distribution and cardiovascular risk in men and women with different levels of glucose tolerance," *J Clin Endocrinol Metab*. , vol. 100, pp. 3340–7, Sep. 2015.

[12] H. M. School. (2005). *Abdominal fat and what to do about it.* Available: https://www.health.harvard.edu/staying-healthy/abdominal-fat-and-what-to-do-about-it

[13] M S. Mirza, *et al.,* "Obesity, visceral fat, and NAFLD: Querying the role of adipokines in the progression of nonalcoholic fatty liver disease." *in ISRN Gastroenterology*, Aug. 2011.

[14] Karastergiou K, Smith SR, Greenberg AS, Fried SK. , "Sex differences in human adipose tissues-the biology of pear shape," *Biol Sex Differ.*, vol. 3, May 2012.

[15] BF. Palmer, DJ. Clegg, "The sexual dimorphism of obesity," *Mol Cell Endocrinol.* , vol. 402, pp. 113–9, Feb. 2015.

[16] D. Royall, "Nutrition for exercise and sport," *Canadian Journal of Dietetic Practice and Research*, vol. 77, pp. 2-2, Feb 2016.

[17] J.P. Despres and I. Lemieux, "Abdominal obesity and metabolic syndrome," *Nature,* vol. 444, pp. 881–887, Dec. 2006.

[18] LJ. Andrade*, et al.,* "Grading scale of visceral adipose tissue thickness and their relation to the nonalcoholic fatty liver disease.," *Arq Gastroenterol*, vol. 51, pp. 22-118, Jul. 2014.

[19] B. L. Wajchenberg, “Subcutaneous and visceral adipose tissue: Their relation to the metabolic syndrome,” *Endocrine Reviews*, vol. 21, pp. 697-738, Dec 2000.

[20] M. A. Gibney, *et al.,* “Skin and subcutaneous adipose layer thickness in adults with diabetes at sites used for insulin injections: implications for needle length recommendations,” *Current Medical Research and Opinion*, vol. 26, pp. 1519-1530, Jun. 2010.

[21] G. Rankin, M. Stokes, and D. J. Newham, “Abdominal muscle size and symmetry in normal subjects,” *Muscle & Nerve*, vol. 34, pp. 320-326, Sep. 2006.

[22] J. Baker-Jarvis and S.Kim, “The interaction of radio-frequency fields with dielectric materials at macroscopic to mesoscopic scales,” *J Res Inst Stand Technol*, vol. 117, pp. 1–60, Feb. 2012.

[23] V. Komarov, S. Wang, and J. Tang, “Permittivity and measurements,” *Encyclopaedia RF Microw. Eng.,* vol. 308, pp. 1–20, 2005.

[24] C. Alabaster, “The microwave properties of tissue and other lossy dielectrics,” Ph.D. dissertation, College of Defence Technol., Dep. Aerosp., Power and Sensors, Cranfield Univ., Cranfield, U.K., Mar. 2004.

[25] A. C. Metaxas, Roger J. Meredith, *Industrial Microwave Heating*. London: Peter Peregrinus, 1983.

[26] S. Ryynanen, “The electromagnetic properties of food materials - a review of the basic principles,” *Journal of Food Engineering*, vol. 26, pp. 409-429, 1995.

[27] S. Gabriel, R. W. Lau, and C. Gabriel, “The dielectric properties of biological tissues .3. Parametric models for the dielectric spectrum of tissues,” *Physics in Medicine and Biology*, vol. 41, pp. 2271-2293, Nov 1996.

[28] P. Debye, Polar Molecules, *the Chemical Catalog Co*. New York: The Chemical Catalog Company, Inc, 1929.

[29] Y. Alfadhl, “Numerical evaluations on the interaction of electromagnetic fields with animals and biological tissues,” Ph.d Thesis, Department of Electronic Engineering, Queen Mary University of London, 2005.

[30] A. V. Hippel, *Dielectrics and Waves*. New York: Wiley and Sons, 1954.

[31] G. Kang and O. P. Gandhi, “Effect of dielectric properties on the peak 1- and 10-g SAR for 802.11 a/b/g frequencies 2.45 anal 5.15 to 5.85 GHz,” *Ieee Transactions on Electromagnetic Compatibility*, vol. 46, pp. 268-274, May. 2004.

[32] A. Peyman*, et al.,* “Dielectric properties of porcine cerebrospinal tissues at microwave frequencies: in vivo, in vitro and systematic variation with age,” *Physics in Medicine and Biology,* vol. 52, pp. 2229-2245, Apr 21 2007.

[33] G. Melia, “Electromagnetic absorption by the human body from 1-15 GHz,” Ph.D. dissertation, Univ. York, U.K., 2013.

[34] D. A. e. R.Fossi, “Dielectric properties of human tissues: definitions, parametric model, And computer codes,” *IFAC-CNR*, Firenze, Italy, 2000.

[35] S. Q. Simon Kingsley, *Understanding Radar Systems*. Sheffield SciTech Publishing, 1999.

[36] M. A. Richards, *Fundamentals of Radar Signal Processing*, 2nd ed., New York, NY, USA: McGraw-Hill, 2014.

[37] C. Wolff, “*Basic Radar Book*,” ed, 2009.

[38] T. Elganimi, “Design and analysis of a bootstrap ramp generator circuit based on a bipolar junction transistor (BJT) differential pair amplifier,” *Proc. of the World Cong. on Eng. and Comp. Sci*., vol. 1, pp. 22-24, Sep. 2014.

[39] G. H. S. Edward C. Farnett, “*Pulse Compression Radar*,” in Radar Handbook, 2end, Ed., ed New york: GE Aerospace, 1990.

[40] R. S. a. V. Lal, KJ, “Generation of a short-duration ultrawideband chirped-pulse using CRLH transmission lines,” *presented at the National Conference on Communications (NCC),* Bangalore, 2011.

[41] K. Cuomo , “A bandwidth extrapolation technique for improved range resolution of coherent radar data.,” *Revision 1. Defense Technical Information Center*,1992.[Online].Available:https://books.google.it/books?id=I0ujNwAACAAJ

[42] S. B. B. S.L. Borison, and K.M. Cuomo, “Super-resolution methods for wideband radar,” *Lincoln Laboratory Journal*, vol. 5, pp. 441–461, 1992.

[43] J. E. P. Kevin M. Cuomo, and Joseph T. Mayhan, “Ultra-wideband coherent processing,” *Lincoln Laboratory Journal*, vol. 10, Jun. 1999.

[44] E. Taoufik, S. Nabila, and B. Ridha, “The reflection of electromagnetic field by body tissue in the UWB frequency range,” IEEE Radar Conference, pp. 1403-1407, Washington, DC, USA, May 2010.

[45] E. D. A. G. V. M. Strackx, P. Reynaert, P. Leroux, “Measuring material/tissue permittivity by UWB time-domain reflectometry techniques,” *presented at the Int. Sympo. Applied Scie. in Biomed. and Communica. Tech. (ISABEL)*, Leuven, Belgium, Nov. 2010.

[46] Y. Wang, “UWB pulse radar for human imaging and doppler detection applications,” *Ph.d Thesis*, University of Tennessee, Tennessee, 2012.

[47] M. Born, E. Wolf, *Principles of Optics*, sixth ed., Pergamon Press, Oxford, 1991. p. 613.

[48] W.R. Smythe, *Static and Dynamic Electricity*, third ed., Hemisphere, New York, 1989. p. 415.

[49] Borja, B., J. A. Tirado-Mendez, and H. Jardon-Aguilar, “An overview of UWB antennas for microwave imaging systems for cancer detection purposes,” *Progress In Electromagnetics Research B*, vol. 80, pp. 173–198, 2018.

[50] X. Y. Li, *et al.,* “A compact double-layer on-body matched bowtie antenna for medical diagnosis,” *IEEE Trans. on Antennas and Propag.*, vol. 62, pp. 1808-1816, Apr. 2014.

[51] A. T. Mobashsher and A. Abbosh, “Three- dimensional folded antenna with ultra- wideband performance, directional radiation and compact size,” *IET Microwaves Antennas & Propagation*, vol. 8, pp. 171-179, Feb. 2014.

[52] S. I. Latif, *et al.,* “A directional antenna in a matching liquid for microwave radar imaging,” *Int. J. Antennas Propag.*, vol. 2015, no. 751739, pp. 1-8, Nov. 2015.

[53] S. I. Latif, *et al.,* “Design and performance analysis of the miniaturised water-filled double-ridged horn antenna for active microwave imaging applications,” *IET Microwaves Antennas & Propagation*, vol. 9, pp. 1173-1178, Aug. 2015.

[54] U. Schwarz, R. Stephan, and M. A. Hein, “Miniature double-ridged horn antennas composed of solid high-permittivity sintered ceramics for biomedical ultra-wideband radar applications,” *IEEE Antennas and Propag. Soci. Int. Sympo.,* Toronto, ON, Canada, Jul. 2010.

[55] C. A. Balanis, “*Antenna theory - a review*,” Proceedings of the Ieee, vol. 80, pp. 739-805, Jan. 1992.

[56] W. H. Emerson and H. B. Sefton, “An improved design for indoor ranges,” *Proceedings of the IEEE is the leading journal abbreviation*, vol. 53, pp. 1079-1081, Aug. 1965.

[57] A. R. Mallahzadeh and A. Imani, “Double-ridged antenna for wideband applications,” *Progress in Electromagnetics Research-Pier*, vol. 91, pp. 273-285, Jan. 2009.

[58] M. A. Saed, “Broadband CPW-FED planar slot antennas with various tuning stubs,” *Progress in Electromagnetics Research-Pier*, vol. 66, pp. 199-212, Jan. 2006.

[59] C. Bruns, P. Leuchtmann, and R. Vahldieck, “Analysis and simulation of a 1-18-GHz broadband double-ridged horn antenna,” *IEEE Transac. on Electromag. Compat.*, vol. 45, pp. 55-60, Feb. 2003.

CHAPTER 3

3. MATERIAL CHARACTERISATION FOR THE DESIGN PROCESS

In this Chapter, different types of the high dielectric materials were considered that have the potential to be employed during the system design process. In addition, these materials were characterised by various dielectric properties measurement methods such as open-ended probe technique.

3.1. HIGH DIELECTRIC FOR ANTENNA DESIGN

Use of low conductive materials with high permittivity in the EM field (antenna) has drawn the attention of various research groups. These high dielectric materials are mainly used to miniaturise the antenna size and to reduce the reflections resulted from the impedance mismatches of the medium (i.e. free space, and human skin) in the system [1, 2]. A German research group in the Ilmenau University of Technology [3] first purposed the use of ceramic for antenna design to be used in medical applications, such as scanning inside the human body. In their first attempt, they used water and then the VLF-085 dielectric ceramic due to its high permittivity, miniaturisation and impedance matching. They measured the permittivity of the ceramic sample as high as 73.5 at the frequency region of interest (0.3−3.3 GHz), within which the ceramic's permittivity was claimed to be 80 to 85, according to datasheets. This difference can be due to various factors, such as fabrication process.

The barium titanate (BaTiO3) based ceramic powder (VLF-440) was supplied by the MRA Laboratories, lnc. This ceramic mainly is composed form mixture of different types of high dielectric ceramics including $BaTiO_3$, and Titanium Oxide (TiO_2). [4]. In this experiment, the VLF-440 powder was porposed for the antenna design based on its approximate permittivity value close to the human skin, which is in the range of 45 to 40 for the frequency range of interest (1.5−3.5 GHz). The manufacturer confirmed that the permittivity for the ceramic would be promising (45−40). However, the German group's experiment has clarified that its measured value (75) would be a bit lower than the manufacturer's datasheet (85).

3.1.1. EXPERIMENTAL PROCEDURES

First step in experimental process was to fabricate the sample using the provided information in the ceramic's datasheet. The limited information about fabrication procedures (i.e. pressure) in the datasheet, forced us to extend the design procedure to characterisation and deployment of the superlative parameters. To this point, different pressures values were applied and tested during fabrication process in order to obtain the best pressure value, before sintering procedure (the process of compacting and forming a solid mass of material by heat without melting it to the point of liquefaction). For this purpose, a cylindrical shape metal mould with 30 mm diameter was employed.

Two and four tons/sqm pressure were found to be optimal and the sample was cold pressed uniaxially by an automatic hydraulic press machine (i.e. Specac, Atlas, T40, U.K.). Furthermore, the samples were sintered using the sintering program given by the material data sheet presented in Figs. 3.1 (a, b, c) and summarised in Table 3.1. The sintering process was applied to the sample by a box furnace (i.e. Nabertherm, p300, 1300℃, Germany) [4].

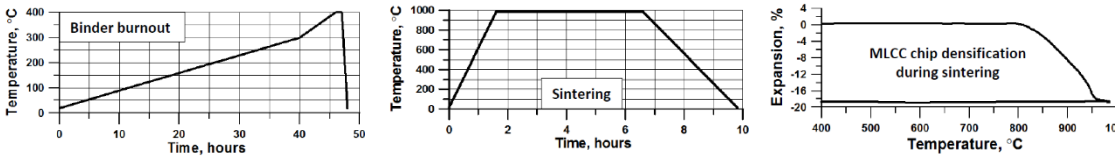

(a): Binder burnout up to 400°C in the air. (b): Sintering 985°C ± 10°C for 5 hours in the air. (c): Heating rate 10°C/min.

Fig 3. 1: Sintering procedures for the VLF-440 ceramic powder [4].

Figs. 3.1(a, b, c) can be interpreted by Table 3.1, which is divided into two-part procedures to program the sintering machine.

Table 3. 1: Oven programming temperature against time for sintering the ceramic.

Part 1		
$20°c \rightarrow 300°c \; at \; 0.1 \; \frac{°c}{min}$	$= \rangle$	$300°c \rightarrow 400°c \; at \; 0.3 \; \frac{°c}{min}$
Part 2		
$300°c \rightarrow 985°c \; at \; 10 \; \frac{°c}{min}$ $= \rangle$	$985°c \rightarrow Hold \; for \; 5 \; hour = \rangle$	$985°c \rightarrow 20°c \; at \; 5 \; \frac{°c}{min}$

Both sintered samples are represented in Figs. 3.2 (a, b), the results verify two tons/sqm sample shown in Fig 3.2 (a) to have enough pressure, concerning the sample's cracks and homogeneity after compressing and sintering procedures for the given size. Hence, the

sample prepared by 4 tons/sqm of pressure shown in Fig 3.2 (b) has suffered from significant amount of cracks and inhomogeneity.

(a) (b)

Fig 3. 2: (a) The 2 tons/sqm and (b) 4 tons/sqm of the pressure applied to the samples using cold press method.

The next experiment considered different techniques to increase the density of the sample; techniques such as increasing both the pressure and temperature [5].

The raw powder was mixed homogeneously with a 5% of polyvinyl alcohol binder by a mortar machine. Then the mixture was placed into a 30 mm diameter mould and cold-pressed by automatic hydraulic press machine under 5 tons for 6 min find to be sufficient pressure to produce raw pellets.

The raw pellets were sintered later by box furnace in air at 600℃ for 4 hours for binder burnout, and then the temperature was increased to 1100℃ for 2 hours sintering. The final pellets presented homogeneous quality with light brown colour.

The sintering temperature of the raw powder was tested by the spark plasma sintering (SPS) with its default load at 5 KN and temperature-increasing rate of 100℃/min by 30 mm diameter graphite mould. It was noticed that the temperature corresponding to the shrinkage rate maxima was around 1000℃. This temperature was defined normally as the sintering point for the SPS, as shown in Fig. 3.3.

During box furnace sintering, the sintering temperature was normally 75-100 ℃ higher than SPS due to the load applied during the SPS sintering [6]. Therefore, the final sintering temperature range was decided between 1075℃ and 1100℃ for box furnace sintering.

In addition, the final temperature of 1100℃ was chosen after several times of sintering attempts by box furnace starting from 1075℃ with 5℃-10℃ increments and ending up at 1100℃ at which sintering temperature presented the highest density and most reasonable dielectric permittivity.

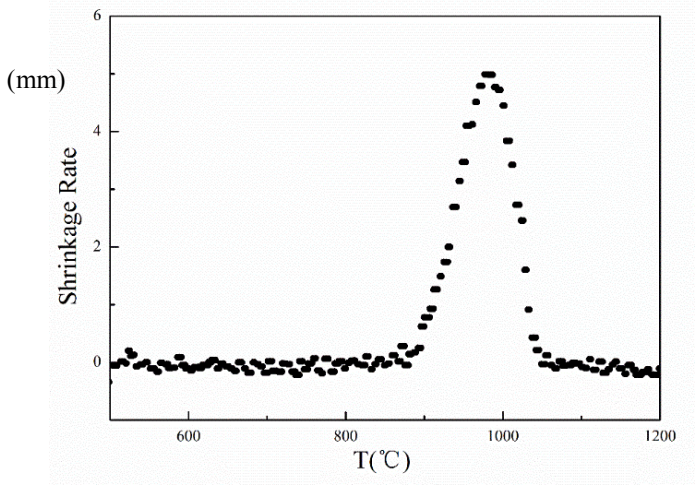

Fig 3. 3: The shrinkage rate during Spark Plasma Sintering.

A density measurement equipment (Archimedes principle) was used to measure the density of the pellet, and appeared to have 4.493 g/cm density through measurement.

3.1.2. DIELECTRIC MEASUREMENT

The dielectric properties of any dielectric material can be measured using different techniques, e.g. open-ended probe. In this method, the transmission and reflection method is employed to measure the dielectric properties of the samples. For this purpose, a signal is transmitted through the ceramic using a vector network analyser (VNA), which has a high temperature probe for frequencies up to 20 GHz and analyses the reflections properly. Different dielectric material measurement methods such as the resonant cavity based on resonant frequency and quality factor at 2 GHz, LCR meters, and impedance analyser for low frequencies up to 100 MHz have been performed for the pellets to validate the results [7, 8].

All the pellets for dielectric measurements were coated with silver paste (Gwent Electronic Materials Ltd., C2011004D5, Pontypool, U.K.) as the electrodes with the edges have been polished off to prohibit the current short during tests. The dielectric properties of the samples were measured by using an LCR meter (Agilent, 4284A) in the frequency range of 40 Hz to 100 MHz at room temperature of 20℃, as represented in Figs. 3.4 (a, b).

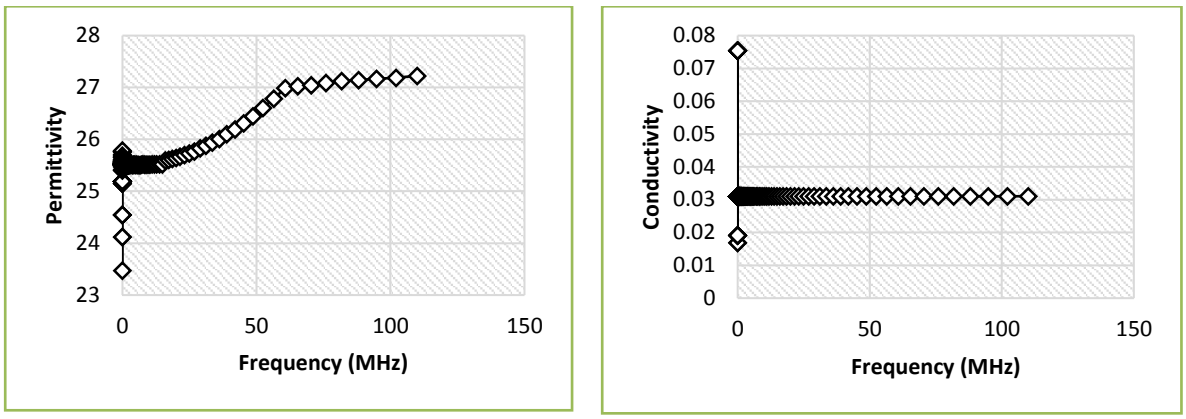

(a) (b)

Fig 3. 4 (a) Permittivity and (b) Conductivity of the sample measured in megahertz using an LCR meter.

Fig. 3.4 (a) represents the measured permittivity of 25.5 using LCR meter at very low frequencies that increases to 27.3 at a 110 MHz. Fig. 3.4 (b) represents the conductivity of 0.03S/m for the entire range of frequencies up to 110 MHz. The fluctuating at lower frequencies are due to the measurement errors.

The resonant cavity was the next technique used to determine the dielectric properties of the sample at room temperature of 20°C. In this technique, the sample is placed into the cavity, which affects the resonant frequency and quality factor of the cavity compared with the empty cavity and based on this information the dielectric properties can be calculated. The results recorded for 1.92 GHz had a permittivity of 28 and conductivity of 0.275 mS/cm as presented in Table 3.2 [9, 10].

Table 3. 2 Resonant cavity measurement of the ceramic sample.

Sample	*F (GHz)*	*Qu*	*h (mm)*	*Diameter (mm)*	*R (mm)*	ε'	ε''	σ(S/m)
Mode 1 TM010	1.92	3654.45	9.930	27.100	13.550	28.010	0.00258	0.000275

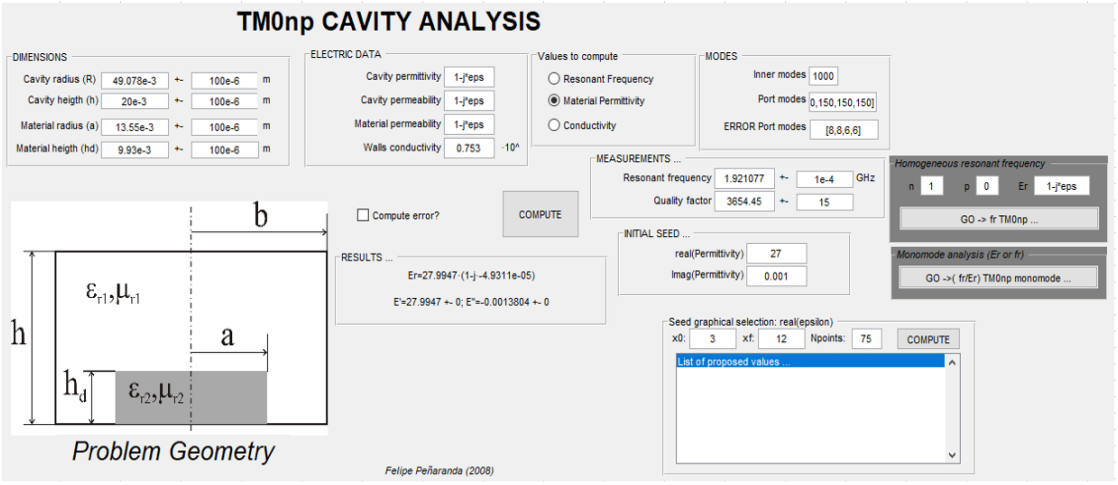

Fig 3.5: The resonant cavity dielectric measurement analysis software snap.

The open-ended coaxial probe technique is performed by cutting off a section of transmission line for the last measurement and touching the ceramic sample to the probe and then pressure is applied using the finger to eliminate air gaps. In the measurement process the fringing field is excited into the sample, the reflected signal (S_{11}) is measured and the permittivity is defined based on the reflections. The general measurement system requirements for such an assessment are; a network analyser (ENA or PNA network analysers series), a software to calculate the dielectric properties from the reflected signal result, a coaxial probe, a stand, and cables. The high-temperature probe used for the measurement is shown in Fig. 3.6.

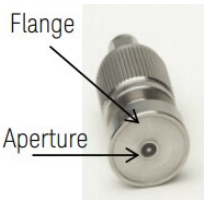

Fig 3. 6: High temperature open-ended coaxial probe.

It is worth noting that the probe should be in direct contact with the sample with no air gap in order to get the satisfactory measurement. This was performed during the experiment by simply pushing the ceramic sample toward the probe using the finger at the room temperature of 20°C. The process repeated a few times to maintain the highest data value and the data recorded and employed for a purpose later in the system design process. The calibration was performed using the standard free space, blocking the probe using metal and distilled water. The measurements set up and the captured data results on the screen is presented in Fig. 3.7(a) [11-13].

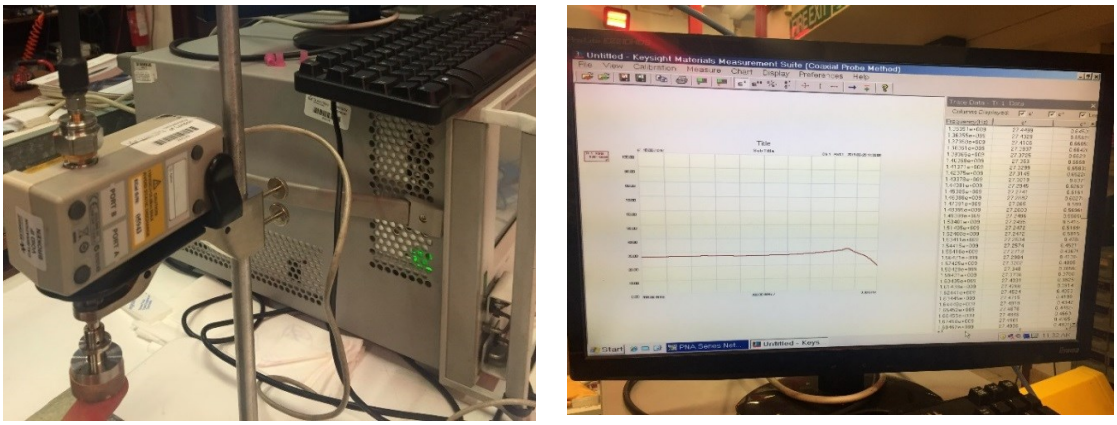

Fig 3.7 (a): Dielectric measurement experiment set up using the open-ended coaxial probe technique.

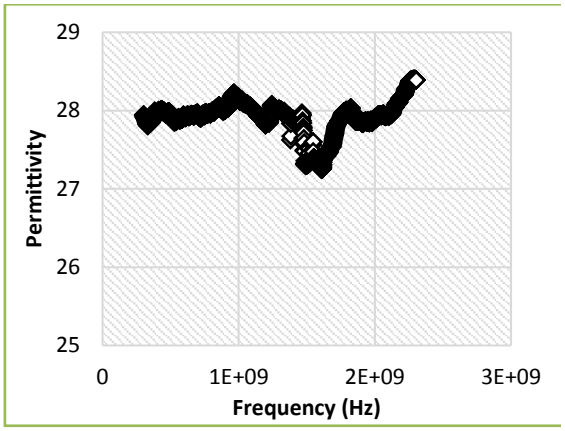

(b): Open-ended probe measurement permittivity of the sample in Hertz.

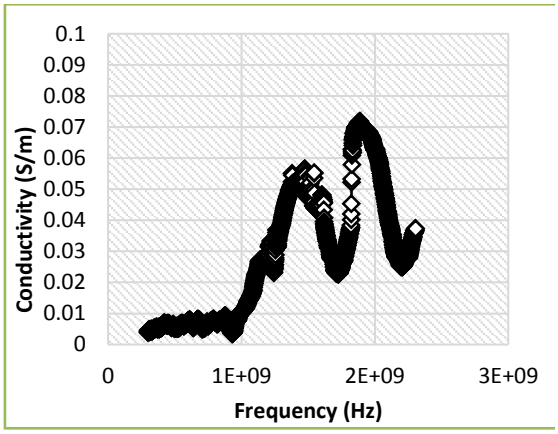

(c): Open-ended probe measurement conductivity of the sample in Hertz.

Fig 3. 7: Dielectric measurement of the 5 tones pressured using the open-ended coaxial probe technique.

The results presented in Figs. 3.7 (b, c), extracted from the experimental measurement of the sample, which represents the permittivity and conductivity of the sample at the frequency range of 0.3 to 2.3GHz. The results taken using different characterisation methods are in good agreement with each other in terms of the sample dielectric properties with a minor ignorable difference. The sample was cold-pressed earlier using 2 tons/sqm press and sintered according to datasheet instruction and characterised using the probe measurement technique at the room temperature of 20°C. The results of measurement were confirmed by other accurate measurement techniques such as resonant cavity and the dielectric properties of the sample are shown in Fig. 3.8 (a, b).

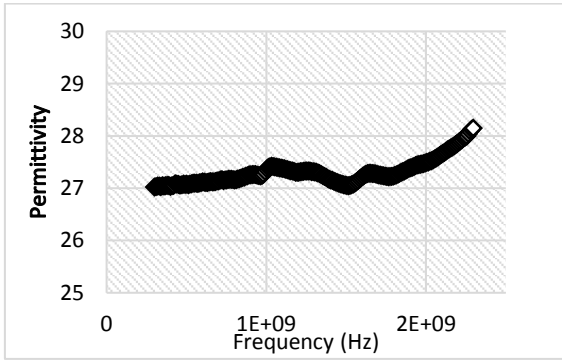

(a)

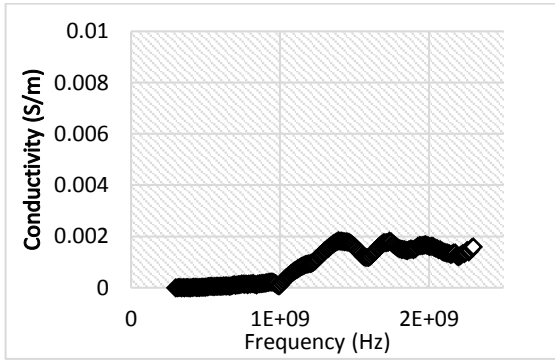

(b)

Fig 3. 8: (a) Permittivity and (b) Conductivity of 2 tones pressured sample using an open-ended probe.

The dielectric properties results present a slight reduction in the permittivity, in this case, compared to high pressure and temperature case, which is used to increase the density. Finally, a larger sample with a diameter size of 90 mm was constructed using the 65 bar/sqm cold press followed by sintering using the data sheet instruction given in Table 3.1 result of which is shown in Figs. 3.9 (a, b).

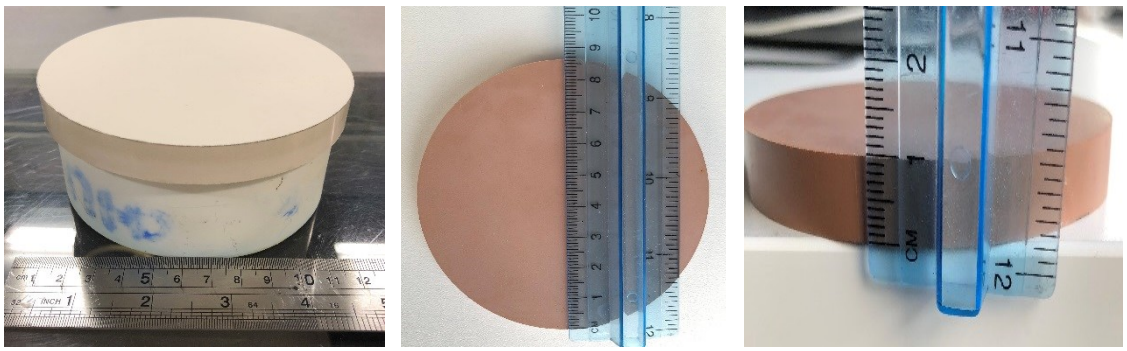

(a) The cold pressed 90 mm diameter ceramic sample. (b) The sintered 90 mm diameter ceramic sample.

Fig 3. 9: Compressed and sintered 90 mm sample ceramic.

The open-ended probe method was employed to measure the dielectric properties of the 90 mm sample shown in Fig. 3.9 (b), and the results of measurement are demonstrated in Figs. 3.10 (a, b). The results indicate that the dielectric properties of the sample are slightly lower than previous samples but overall, the results are more or less complying with the 30 mm sample measurement.

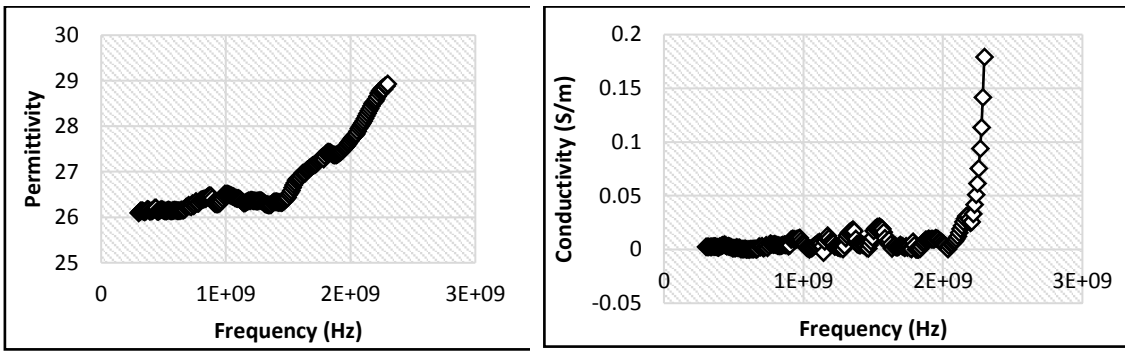

(a) (b)

Fig 3. 10: (a) Permittivity and (b) Conductivity of the 90 mm sample using the open-ended probe technique.

Then sintered ceramic samples were attached to each other using high temperature super glue and were cut to the shape of the PDRH antenna using the laser cut and milling machine. The antenna shaped sample were painted using high conductive silver paint and finally, the SAM connector was attached.

3.1.3. MODIFIED HIGH DIELECTRIC SOLID MIXTURE

In the previous section, the VLF-440 ceramic powder supplied by the MRA Laboratories was characterised to determine the dielectric properties in the frequency region of interest. Different approaches such as increase and decrease of the pressure and the sintering temperature were applied in order to increase the dielectric constant of the sample; however, none of these parameters had a considerable effect. The new approach of mixing the ceramic powder with more portion of the titanium dioxide (which is an ingredient of

VLF-440) was taken, to increase the ceramic's dielectric constant (approx. 27) and bring it as close as possible to the human skin dielectric constant (40-45). Based on trace metal analysis (having minimum amount of the metal) the rutile-TiO_2(r-TiO_2) powder with an average particle size of ≤100 nm and a purity of 99.5% (by Sigma Aldrich) was chosen. The selection r-TiO_2 in this work, was due to its features such as higher permittivity and melting points, as well as lower conductivity compared to other types (e.g. anatase and brookite) [19–20]. The white powder r-TiO_2 was sintered using the spark plasma sintering (SPS) technique at 1100ºC. The sintered VLF-440 and r-TiO_2 dielectric properties were measured using the open-ended probe method in the frequency region of interest and results are presented in the Figs. 3.11 [14, 15].

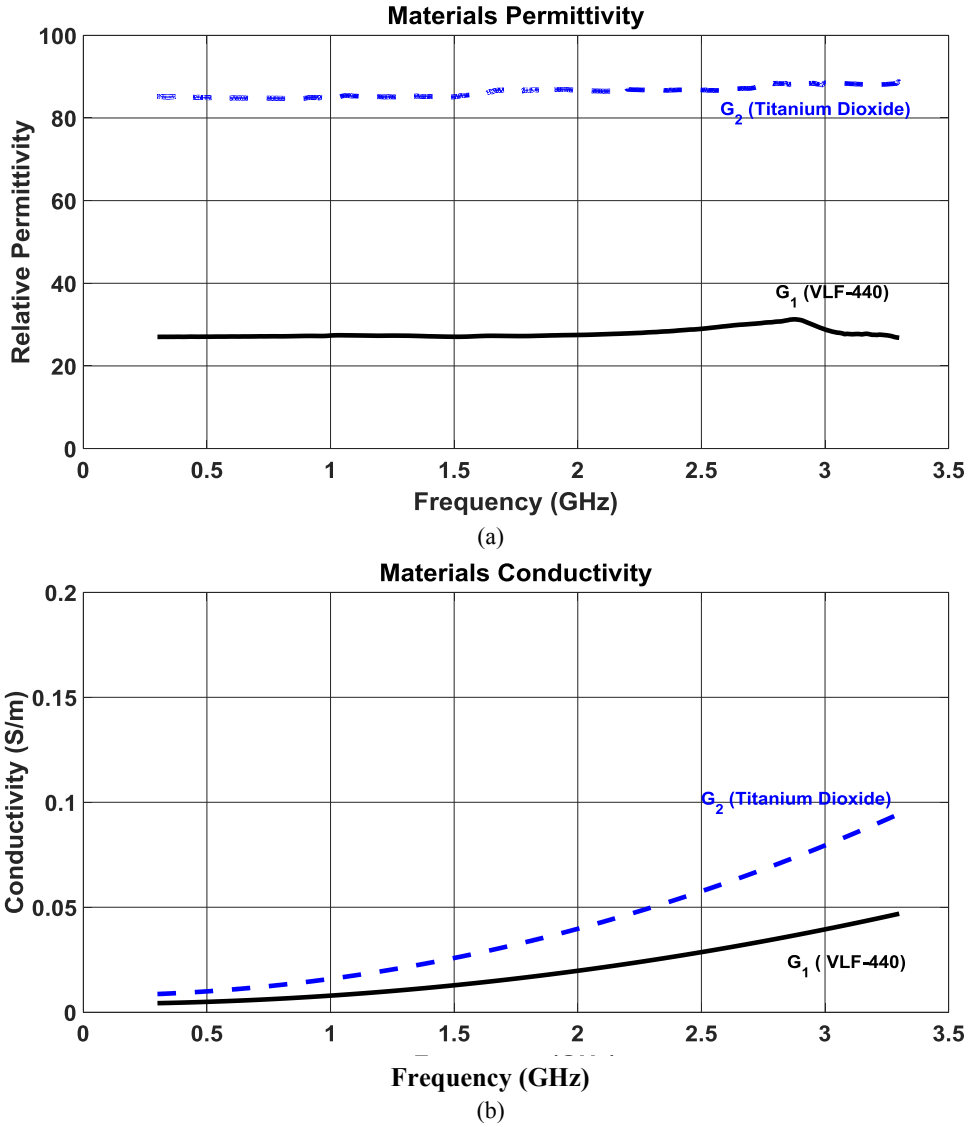

Fig 3. 11: (a) Permittivity and (b) Conductivity of the VLF-440 and r-TiO_2 measured using the open-ended probe technique.

The results indicate the approximate permittivity of 27 for the VLF-440 and 85 for the r-TiO_2 at 1.5 GHz centre frequency (which was chosen as operating frequency for on body application).

The measured permittivity of the r-TiO2 sample shown in Fig. 3.11 (a), shows minor fluctuation at higher frequencies. It is casued by the unavoidable air-gap that developed during the experiment between the sample and probe. The small air-gap error can be detected at higher frequencies and could be ignored at lower frequencies as expected. Fig. 3.11(b) indicates that both ceramics benefit from low conductivity, however the r-TiO_2 has higher conductivity compared to the VLF-440 ceramic. But it is well below the acceptable specified range in whicn less energy is absorbed due to high conductivity.

The next approach was mixing two ceramics with chosen different portions followed by sinter process and finally measuring thier dielectric properties. In the first attempt, four portions of the VLF-440 and one portion of the r-TiO2 were mixed together which provide the measured permittivity of 36.6 at 1.5 GHz.

Next, same portions of each material were mixed which resulting in a ceramic with raised permittivity of 53.7 at 1.5 GHz. Finally, two portions of the VLF-440 were mixed with one portion of the r-TiO_2, and the measured permittivity was 43.7 at 1.5 GHz, which is closest approximation of human skin dielectric constant (41-45).

Fig 3.12 (a) shows the measured permittivty for different miture while Fig. 3.12 (b) illustrates the conductivity of different mixtures, which implies that increasing the share of the r-TiO_2 in the mixture would result in increased conductivity [16, 17].

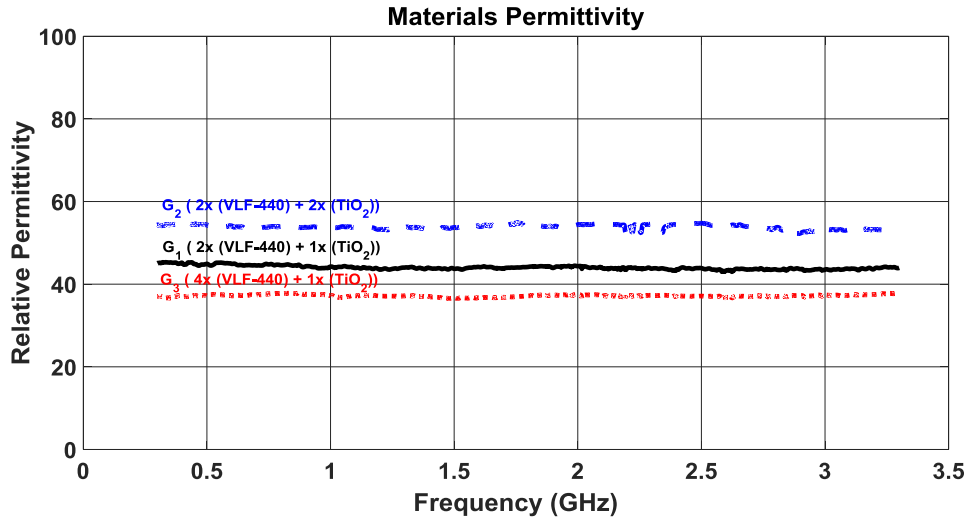

(a)

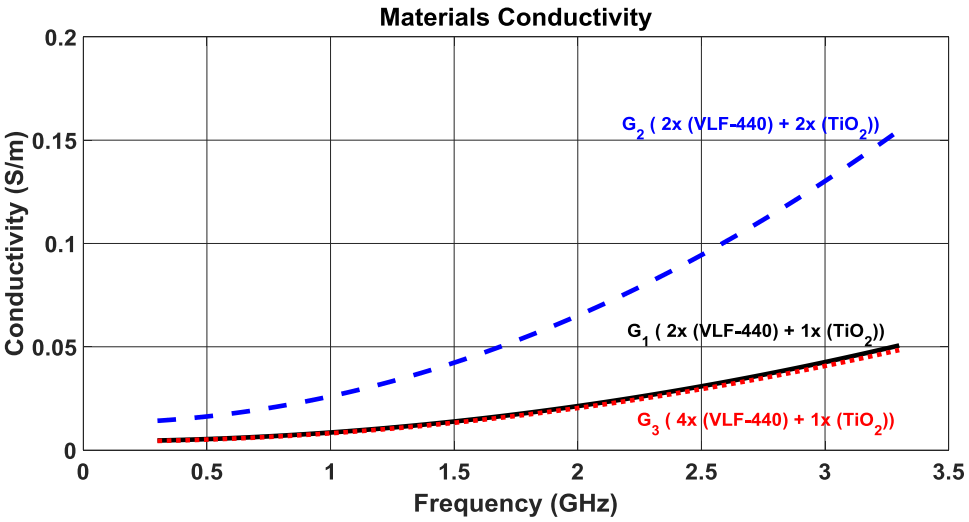

(b)

Fig 3. 12: (a) Permittivity and (b) Conductivity of different mixtures of the VLF-440 and r-TiO_2 samples, measured using the open-ended probe technique.

3.2. HIGH DIELECTRIC LIQUIDS

The open-ended coaxial probe is an established principal method for measurement of the dielectric properties of a liquid, semisolid, or solid. The VNA, dielectric probe and Agilent electronic calibration module (ECal) were employed for the calibration and increasing the accuracy for the measurement of the dielectric properties of the material under test, at the room temperature (i.e. 20°C). The arrangement is shown in Fig. 3.13.

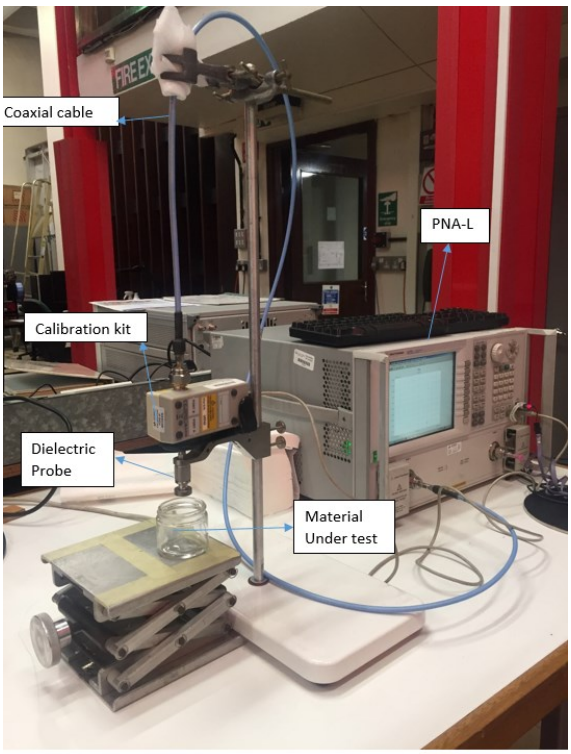

Fig 3. 13: The open-ended coaxial probe method for a dielectric measurement.

The default calibration process is leaving the open-ended probe in free space, then blocking it with a metal conductor, and finally immersing the probe into a measurement beaker filled with distilled water. The distilled water could be replaced with a dielectric material with closer dielectric properties to that of the material under test to enhance the accuracy of the measurement.

There are two different types of pure water; distilled and deionised. These two types of pure water are prepared from tap water in different ways, and the product can be used for different purposes. Distilled water is produced by the process of boiling normal tap water to evaporation point and then recondensing the vapour, leaving most impurities behind, that did not evaporate with the water. Deionised water is produced through filtering (physical filters, carbon filters) processes, followed by reverse osmosis membrances to remove all ions and dissolved mineral salts. Distilled water and deionised water were purchased from the market, and their dielectric properties were measured at room temperature (i.e. 20°C), using the dielectric probe method within the frequency range of 400 MHz to 3 GHz. The results are shown in Fig. 3.14;

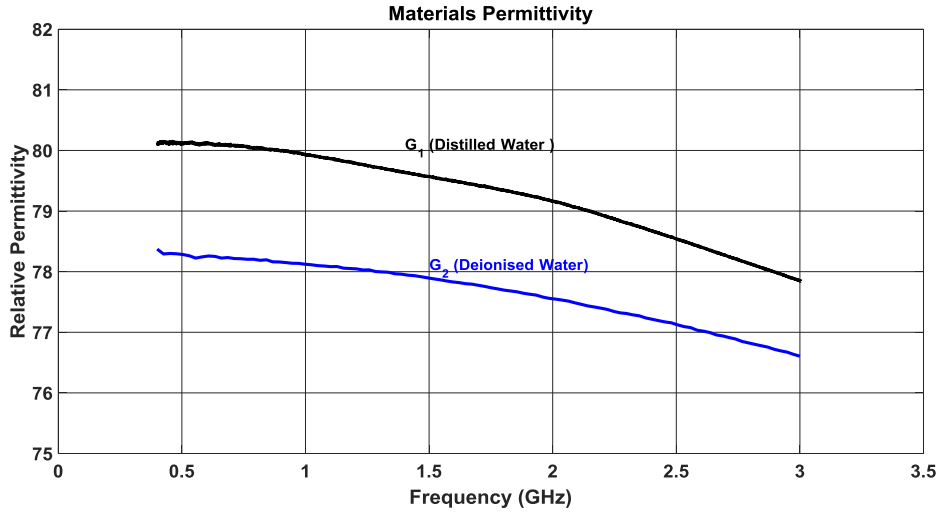

(a)

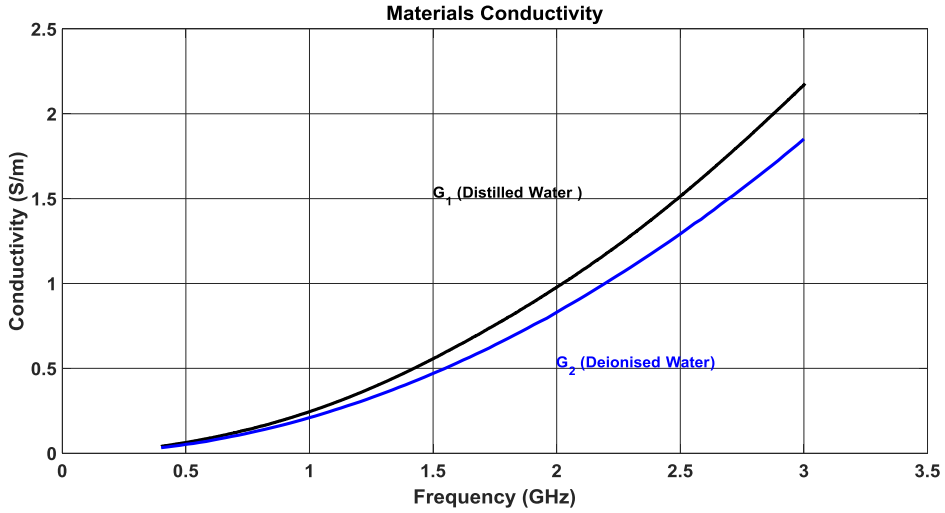

(b)

Fig 3. 14: (a) Permittivity and (b) Conductivity of *distilled and deionised water* using high-temperature probe method at 0.3 to 3.3 GHz.

The results shown in Fig. 3.14 indicate that the dielectric properties of distilled water is slightly higher than that of deionised water, which were expected due to the presence of ions. Dielectric properties of the distilled water were recorded to be as high as 79.5 for the permittivity, and 0.55 S/m for the conductivity, at 1.5-GHz where deionised water has a value of 77.9 for the permittivity, and 0.47 S/m for conductivity [18].

The next step was dissolving different additive food materials into distilled water to increase the permittivity of the composite. Different materials were selected based on their high dielectric constant and being harmless in the case of probable contact with human skin. Edible material such as glycerol and xylitol sweetener, and detergents such as tween 20 (polysorbate 20), Triton X-100 and various types of oils were considered for this purpose. First dielectric properties of the glycerol were measured at its own and then different mixtures with distilled water that increases the permittivity closer to the human

skin permittivity (i.e. 41-45) in the frequency of interest (i.e. 1.5 GHz). The same procedure was perfomed for the xylitol and the distilled water at the chosen frequency region (i.e. 0.3 to 3.3 GHz), presented in Fig. 3.15. The glycerol was measured using open-ended probe method, and were found to have the permittivity of approx. 8 with the conductivity of 0.5 S/m at the centre frequency of 1.5 GHz. The distilled water with measured permittivity of approx. 79.5 was mixed with the glycerol at the rate of 45 milliliters (ml) to 20 ml, which increased the permittvity of the mixture to 40.5 and conductivity to 2 S/m [19]. Moreover, 100 ml of Xylitol was mixed with 60 ml of distilled water and the permittivity of the mixture rose to 41 and conductivity to 1.8 S/m at the 1.5 GHz centre frequency.

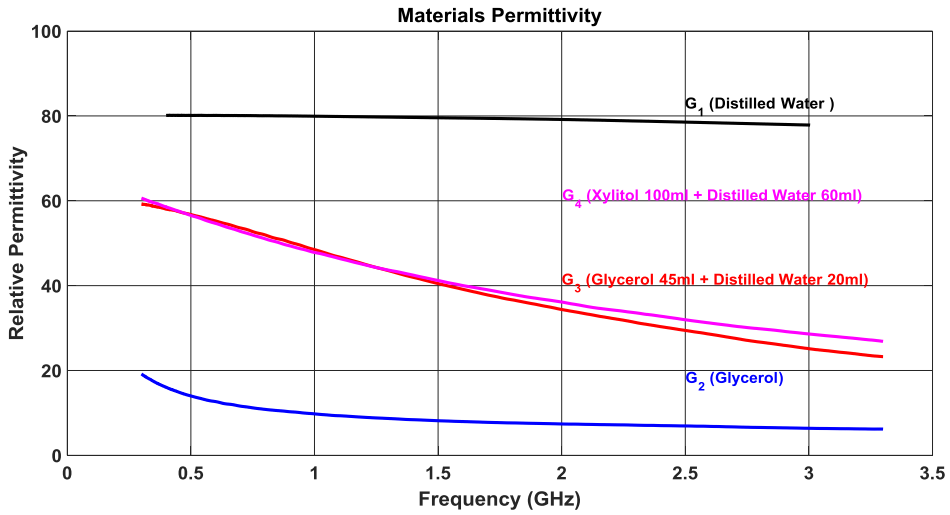

(a)

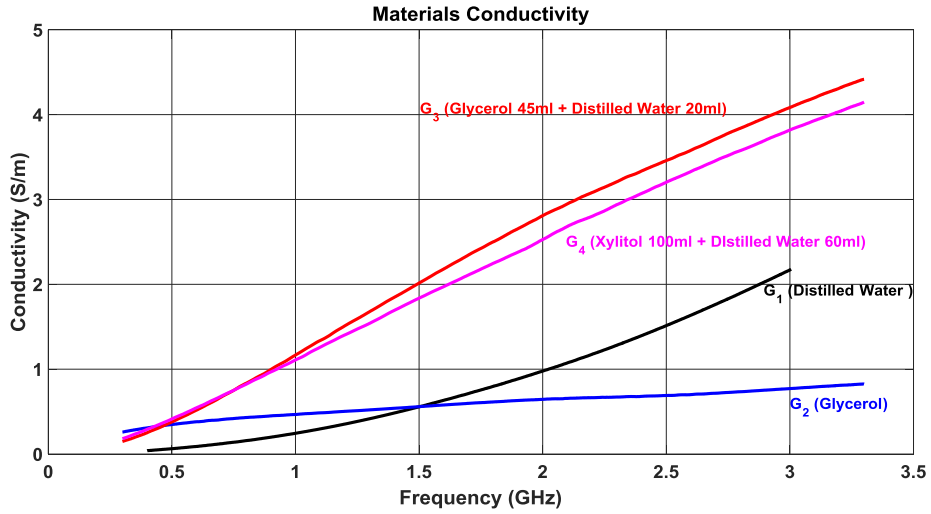

(b)

Fig 3. 15: (a) Permittivity and (b) Conductivity of the distilled water, glycerol, xylitol and their mixture have measured using high-temperature probe technique at 0.3-3.3 GHz.

In the next stage, detergents such as Tween 20 (i.e. polysorbate 20) and Triton X-100 were measured for their dielectric properties at 0.3 to 3.3 GHz. The distilled water was then added to the solutions in order to increase their permittivity to the skin permittivity (i.e. 41-45) at room temperature (i.e. 20°C). The 50 ml of distilled water was added to 17-ml of Tween 20 and mixed well while 60-ml of distilled water was added to 17 ml of the Triton x100 and the dielectric properties of both mixtures were measured.

Figs. 3.16 (a, b) presents the measured dielectric properties of both detergents and their mixtures with distilled water. The results show that the permittivity of Tween 20 and Triton x100 is 2.9, and 2.2, and their conductivity is 0.095 and 0.067 S/m, respectively. These values rose to 39.7 and 39.5 for permittivity, and 0.86 and 0.84 S/m for conductivity when they were mixed with distilled water at 1.5 GHz [20].

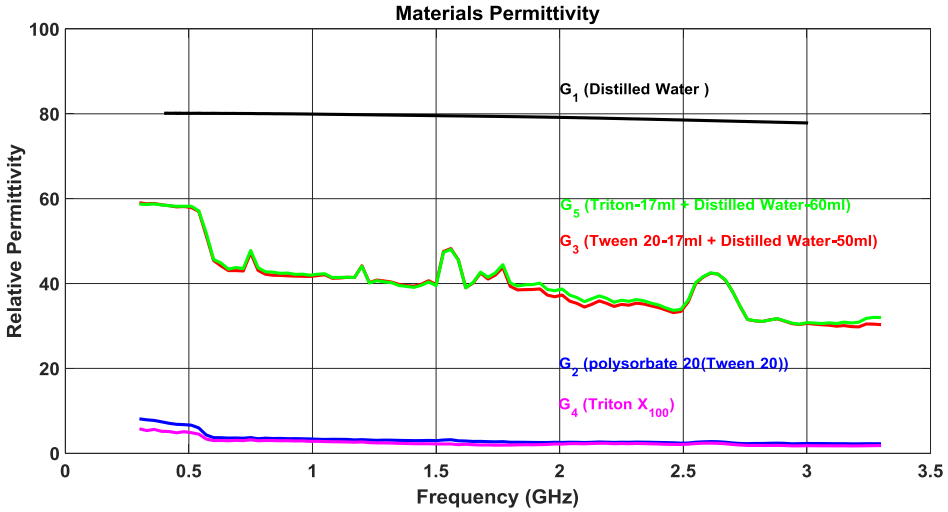

(a)

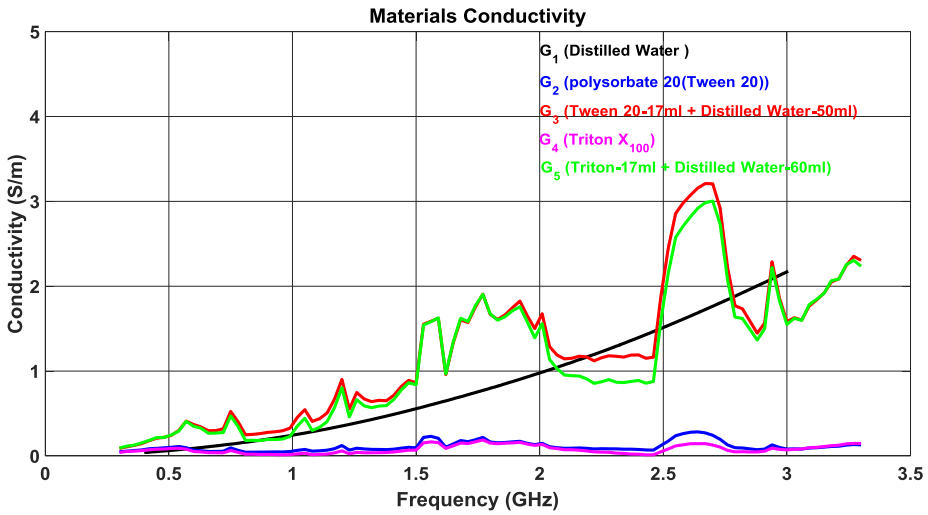

(b)

Fig 3. 16: (a) Permittivity and (b) Conductivity of the tween 20, triton x 100, distilled water and their mixture were measured using high temperature probe technique at 0.3 to 3.3 GHz.

The dielectric properties of sugar alcohol and detergents indicate that mixing these materials with distilled water not only increases their permittivity significantly, but also raises their conductivity extremely. Rise in the material conductivity is a result of high absorption rate factor, which make the material a profligate element to get employed in an EM system. Therefore, employing a liquid with lower conductivity such as different types of oils is crucial. Hence, different types of oils such as linseed, extra virgin olive, avocado, duck, and salmon oils were employed, and their dielectric properties were measured using the open-ended probe technique.

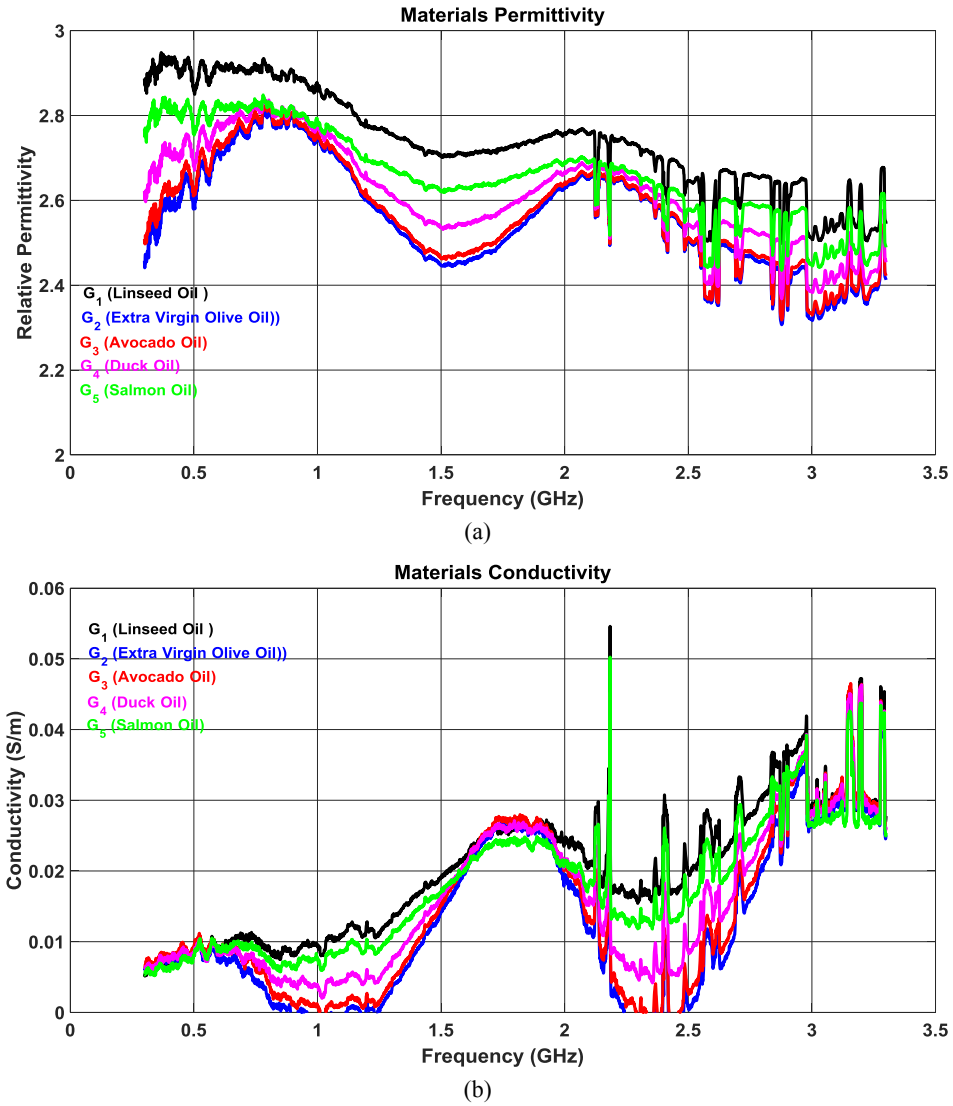

Fig 3. 17: (a) Permittivity and (b) Conductivity of the linseed, olive, avocado, duck, and salmon oils using high temperature probe technique.

Figs. 3.17 (a) and (b) represent the measured permittivity and conductivity of different oils. It is noted that the linseed oil has higher dielectric properties (i.e. $\varepsilon_r = 2.7$ and $\sigma = 0.019$ S/m at 1.5 GHz) among all different types of oils, and extra virgin olive oil has the lowest dielectric properties (i.e. $\varepsilon_r = 2.4$ and $\sigma = 0.014$ S/m at 1.5 GHz) among all [21].

Therefore, the linseed oil was chosen as an alternative liquid to be employed in the system during design process.

3.3. HIGH DIELECTRIC SEMI-SOLID MIXTURES

In this section, the high dielectric semi solid mixture produced using the r-TiO_2 white powder with the low conductive liquid oil or semi-solid paraffin is tested.

The proposed mixture can not only increase the material permittivity, it also enables users to modify the material shape. Commercial paraffin wax (by Candles Company), which has a density of app. 0.83−0.86 g/cm^3 at 15°C and melting point of 45°C was chosen for this purpose.

The linseed oil was found to have the highest permittivity among all other tested oils. Therefore, the linseed oil was chosen to be mixed with r-TiO_2 ceramic powder in different portions. The r-TiO_2 was added to the linseed oil up to the saturation point where the mixture turn into semi solid. The mixture was shaken well to remove the airgap and have homogeneous mixture.

Four portions of r-TiO_2 (40 g) was mixed with three portions of the linseed oil (30 g),which produced a white flexible shape material. The dielectric properties of the mixture was measured using the open-ended probe method at 0.3 – 3.3 GHz, and shown in Figs. 3.18; The measured permittivity of the mixture is almost equal to the permittivty of linseed oil, with higher conductivity (i.e. $\varepsilon_r = 5.26$ and $\sigma = 0.019$ at 1.5 GHz).

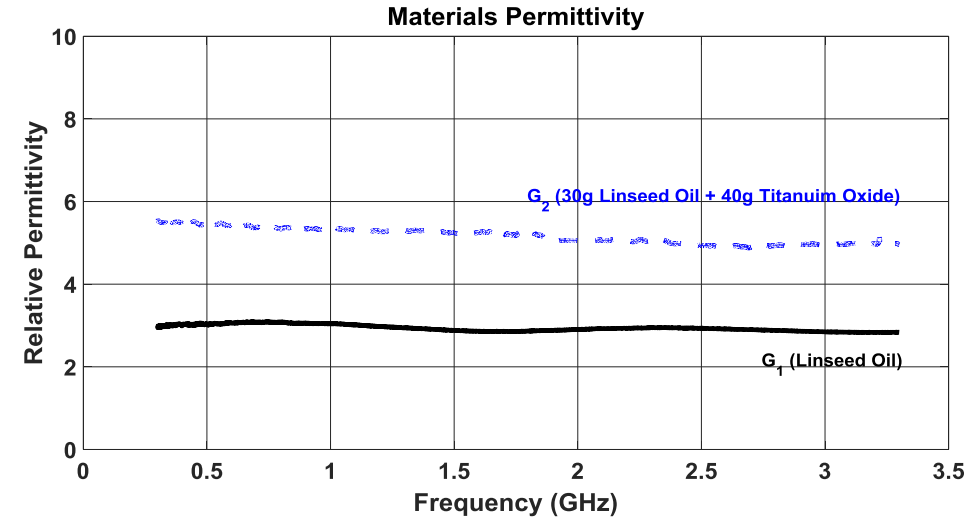

(a)

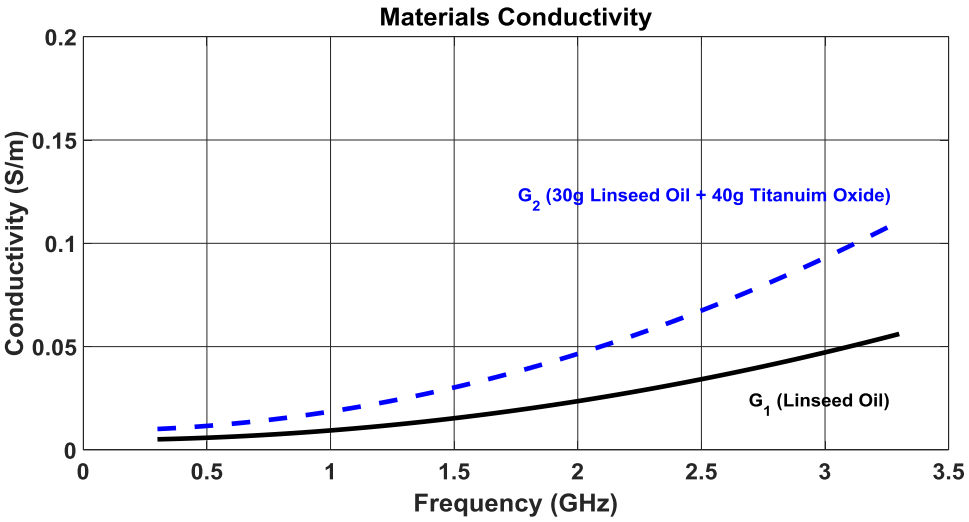

(b)

Fig 3. 18: (a) Permittivity and (b) Conductivity of the linseed oil and its mixture with the r-TiO_2 measured using high temperature probe technique at 0.3 to 3.3 GHz.

In addition, we chose the paraffin as the preliminary dielectric material because of its outstanding properties such as better solubility, flexible fixed shape, and lower conductivity, compared to other materials.

The measured dielectric properties of the paraffin, as shown in Figs. 3.19 (a) and (b) presents the low conductivity and a moderate permittivity at 1.5 GHz (i.e. ε_r=1.97 and σ=0.005).

In order to increase the permittivity of the paraffin, it was mixed with the r-TiO_2, which has a high permittivity and low conductivity (i.e. see Figs. 3.19 (a) and (b)). The conductivity of the mixture was increased to some extent thanks to higher conductivity of the r-TiO_2, which was in the acceptable range, in terms of EM field absorption rate.

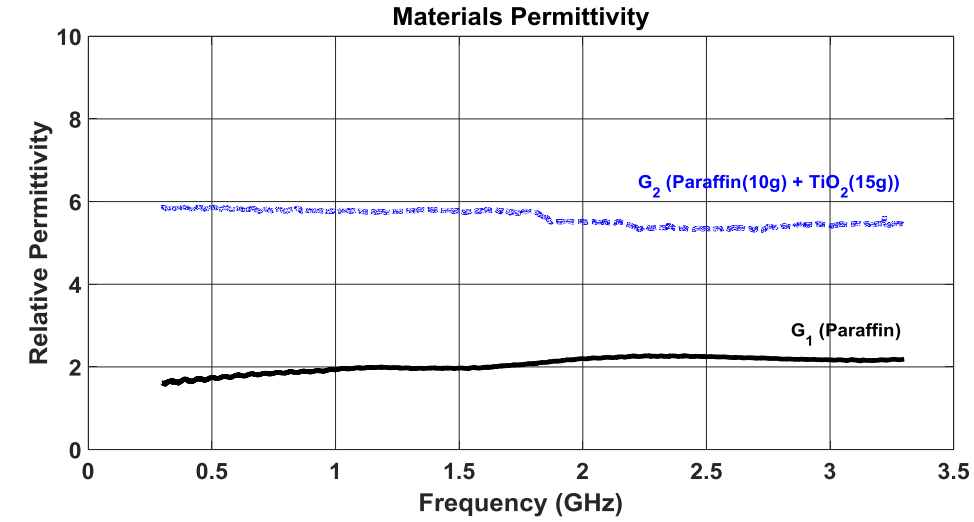

(a)

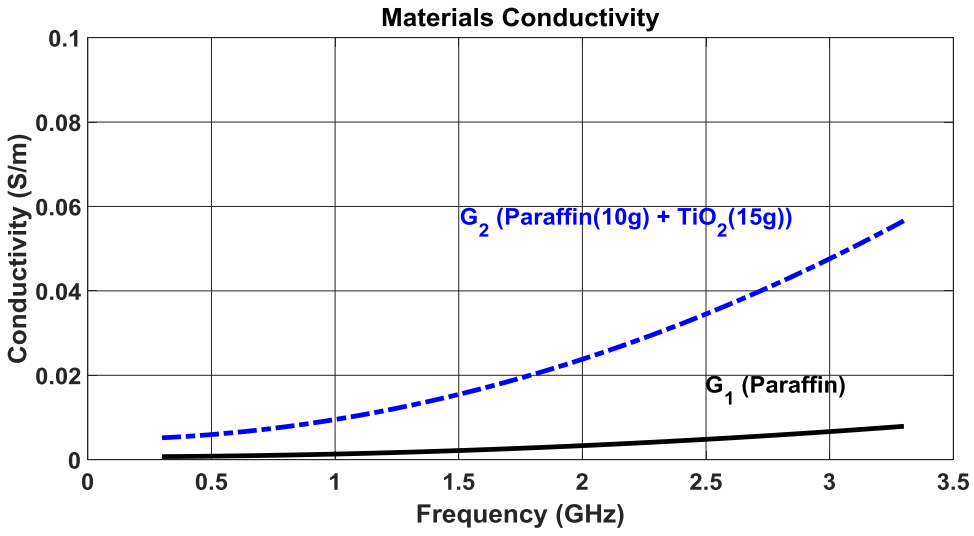

(b)

Fig 3. 19: (a) Permittivity and (b) Conductivity of the paraffin and its mixture with the r-TiO_2 measured using high temperature probe technique at 0.3 to 3.3 GHz.

Figs 3.19 (a) and (b) depicts the dielectric properties of the paraffin and its mixture with the r-TiO_2 (i.e. 10g of the paraffin with 15g of the r-TiO_2) measured through the open probe technique (i.e. $\varepsilon_r = 5.7$ and $\sigma = 0.02$ at 1.5 GHz).

This mixing rate was selected considering the saturation point of r-TiO_2 in paraffin. The mixture was shaken well to remove the bubbles and left to cool down to turn into a solid form. Furthermore, to check the homogeneity of the mixture, the dielectric properties measurement were obtained from different parts of the sample using the open-ended probe method. The obtained results were taken from different section of the sample confirmed the homogeneity of the sample. The measured dielectric properties of the sample in the frequency range of 0.3–3.3 GHz are shown in Fig. 3.19.

3.4. ABSORBER SHEET

A thin, flexible, and magnetically loaded silicone microwave absorbing material sheet (i.e., ECCOSORB FGM-40) was selected to be used as part of the high-performance design of the proposed antenna. The dielectric properties of absorber sheet were characterised using the open-ended probe technique at 0.3-3.3 GHz, as shown Fig. 3.20 (a) and (b). The measured permittivity of the material at the centre frequency of interest is approximately 21 and the conductivity is 0.075 S/m [22].

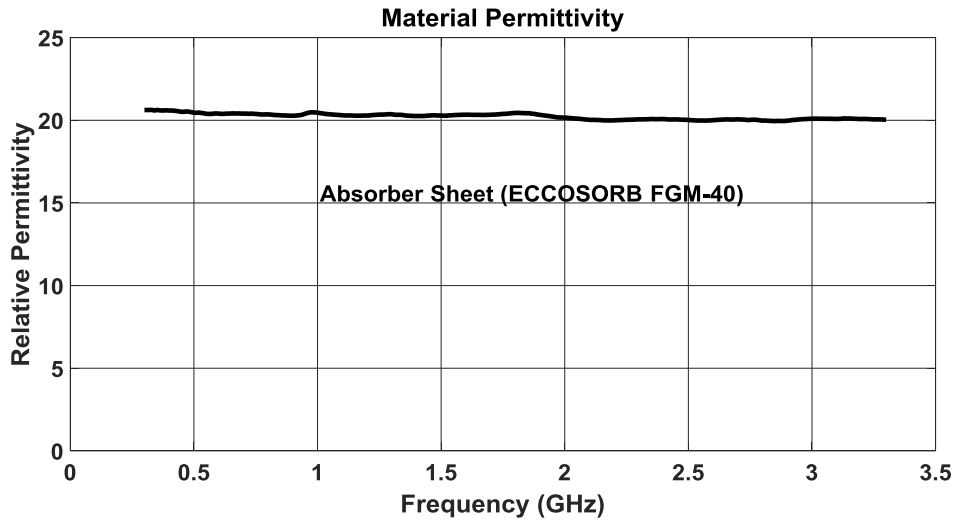

(a)

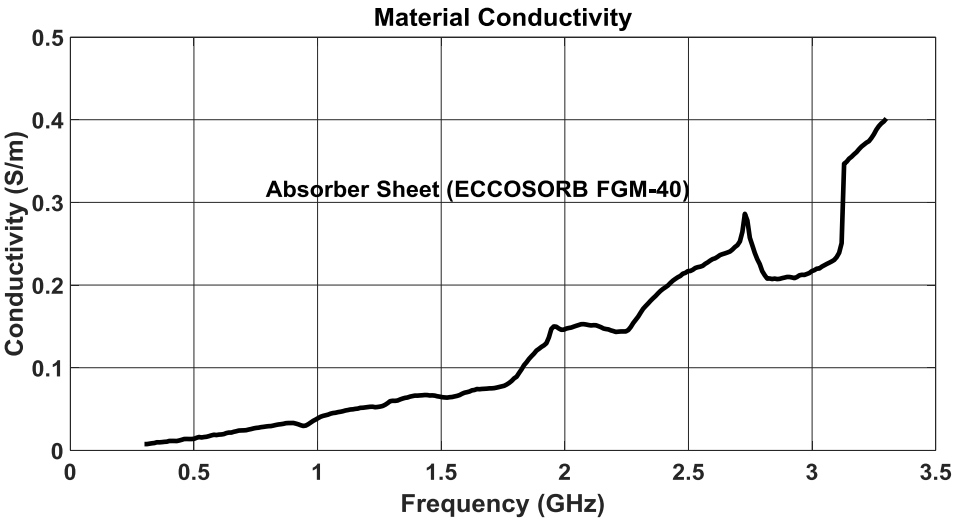

(b)

Fig 3. 20: (a) Permittivity and (b) Conductivity of the absorber sheet (ECCOSORB FGM-40) measured using high temperature probe technique at 0.3 to 3.3 GHz.

3.5. CHAPTER SUMMARY

In this Chapter, different high dielectric materials were characterised, which will be used in the system design process in following Chapters.

The barium titanate (BaTiO3) based ceramic powder (VLF-440) was compressed, and further sintered according to the data sheet. The dielectric properties of the samples were measured using a different method such as an open-ended probe, resonant cavity and capacitance plates within the frequency range of the interest (i.e. 0.3−3.3 GHz) and the results were recorded to be used for the system design process.

The dielectric properties of distilled and deionised water were measured using the open-ended probe method. The deionised water has lower dielectric properties. However, the conductivity was found to be quite high and therefore they cannot be used in the system due to its high absorption rate.

The dielectric properties of food additive materials such as glycerol and xylitol, and their mixture with the distilled water were measured using the general open-ended probe method. The reason of mixing these materials with distilled water was to increase the permittivity of the mixture to approximately human skin permittivity (i.e. 40-45) in the centre frequency of interest (i.e. 1.5GHz). The detergent materials such as tween 20, Triton x-100, and their mixtures with the distilled water were measured next. The concept of using these types of materials in the system design process was the fact that these materials can be in contact with human skin without any hazardous effect, therefore can be used for any channel modeling and impedance matching.

The dielectric properties of different types of liquid oils were measured next, using open-ended probe technique. The linseed oil appeared to have highest dielectric properties among all. Moreover, the linseed oil was mixed with the r-TiO_2 in order to increase the permittivity of the material. This method increased the permittivity of the mixture, approximately twice. In addition, paraffin was chosen as an alternative material suitable for being formed to the desired shape. Due to high permittivity and low conductivity of r-TiO_2, it was considered as a good candidate to be mixed with paraffin. The outcome increased the permittivity of mixture, nearly twice that of paraffin itself, while preserving the low conductivity.

Finally, the absorber sheet that will be used later in the antenna design process was characterized using the conventional open-ended probe technique.

REFERENCES (CHAPTER 3)

[1] A. La Gioia *et al.,* "Open-ended coaxial probe technique for dielectric measurement of biological tissues: challenges and common practices," *Diagnostics* , vol. 8, no. 40, pp. 1–38, Jun. 2018.

[2] F. Di Clemente, R. Stephan and M. Hein, "Ultra-wideband miniaturised high permittivity-matched antennas for biomedical diagnostic," *7th Eu Conf. on Antennas and Propag. (Eucap)*, pp. 2896-2899, Apr. 2013.

[3] U. Schwarz *et al.,* "Design and application of dielectrically scaled double-ridged horn antennas for biomedical UWB radar applications," *IEEE Int. Conf. on Ultra-wideband (Icuwb)*, pp. 150-154, Sep. 2009.

[4] MRA Laboratories, product catalog [Online]. Available: www.mralabs.com.

[5] Z. A. Munir, U. Anselmi-Tamburini and M. Ohyanagi, "The effect of electric field and pressure on the synthesis and consolidation of materials: A review of the spark plasma sintering method," *Journal of Materials Science*, vol. 41, no. 3, pp. 763-777, Feb. 2006.

[6] M. Omori, "Sintering, consolidation, reaction and crystal growth by the spark plasma system (SPS)," *Materials Science and Engineering: A,* vol. 287, no. 2, pp. 183-188, Agu. 2000.

[7] M. T. Jilani *et al.,* "A brief review of measuring techniques for characterization of dielectric materials," *Int. J. Inf. Technol. Electr. Eng.* , vol. 1, no. 1, pp. 1–5, Dec. 2012.

[8] P. P. Bobrov, A. V. Repin, and O. V. Rodionova, "Wideband Frequency Domain Method of Soil Dielectric Property Measurements," *IEEE Trans. Geosci. Remote Sens.*, vol. 53, pp. 2366–2372, May. 2015.

[9] Q. R. Marksteiner *et al.,* "Cavity resonator for dielectric measurements of high-epsilon, low loss materials, demonstrated with barium strontium zirconium titanate ceramics," *Rev Sci Instrum*, vol. 88, no. 6, Jun. 2017.

[10] Mailadil T. Sebastian, *Dielectric Materials for Wireless Communication*, 1st Edition, Elsevier, 2008.

[11] J. Baker-Jarvis, M. Janezic, and D. C. DeGroot, "High-frequency dielectric measurements," *IEEE Instrum. Meas. Mag.*, vol. 13, no. 2, pp. 24–31, Apr. 2010.

[12] D. L. Gershon *et al.,* "Open-ended coaxial probe for high-temperature and broad-band dielectric measurements," *IEEE Trans. Microw. Theory Tech.,* vol. 47, no. 9, pp. 1640–1648, Sep. 1999.

[13] P. M. Meaney, T. Rydholm, and H. Brisby, "A transmission-based dielectric property probe for clinical applications," *Sensors (Basel, Switzerland),* vol. 18, no. 10, pp. 3484, Oct. 2018.

[14] S. Marinel *et al.,* "Broadband dielectric characterization of TiO2 ceramics sintered through microwave and conventional processes," *Ceramics International,* vol. 39, pp. 299–306, Jun. 2013.

[15] A. Wypych *et al.,* "Dielectric Properties and Characterisation of Titanium Dioxide Obtained by Different Chemistry Methods," *J. Nanomater.* , pp. 1−9, Mar. 2014.

[16] U. Schwarz, R. Stephan, M. A. Hein, "Miniature double-ridged horn antennas composed of solid high-permittivity sintered ceramics for biomedical ultra-wideband radar applications," *IEEE Antennas and Propagation Society International Symposium (APSURSI), Toronto*, pp. 1-4. Jul. 2010.

[17] F. S. di Clemente *et al.,* "Permittivity-matched compact ceramic ultra-wideband horn antennas for biomedical diagnostics," *5th Eur. Conf. Antennas Propag., Rome, Italy*, pp. 2386–2390, Apr. 2011.

[18] Z. O. Rodríguez-Moré *et al.,* "Complex dielectric permittivity of rum and its mixtures with methanol, ethanol, and water at frequencies up to 15GHz,"*Journal of Microwave Power and Electromagnetic Energy* , vol. 52, no. 1, pp. 16-30, Jan. 2018.

[19] R. Behrends *et al.,* "Dielectric properties of glycerol/water mixtures at temperatures between 10 and 50 C," *J. Chem. Phys.,* vol. 124, no. 14, p. 144512, Apr. 2006.

[20] K. Asami, "Dielectric properties of water in Triton X-100 (nonionic detergent)- water mixtures," *J Phys Condens Matter*, 19, 376102−376106, Jul. 2007.

[21] S. Latif, S. Pistorius, and L. Shafai, "A double-ridged horn antenna design in canola oil for medical imaging," *in 2nd Int. Conf. Advances in Elect. Eng. (ICAEE)*, pp. 421–424, Dec. 2013.

[22] H. Balegh, B. A. Arand, and L. Yousefi, "Side lobe level reduction in horn antennas using graphene," *24th Iranian Conf. Elect. Eng. (ICEE),* pp. 1937–1941, May 2016.

CHAPTER 4

4. WIDE BAND ANTENNA DESIGN

In order to be able to transmit the chosen WB pulse through the mediums and receiving the reflected pulses, the device is needed to behave as a transmission line, for the pulse propagation. This transmitter could be an antenna, a probe, or any metal conductor that carries a pulse to the end-point for propagation. A UWB antenna was found to be a good candidate for propagation through human body, because of its advantages such as wide bandwidth, small size and capability to direct the pulse to any direction. However, the frequency region allowed by the FCC has limited this technique and therefore WB antenna purpose. Moreover, considering other transmitting techniques such as probes could be rewarding.

4.1. DRH ANTENNA DESIGN

Based on the literature review and system needs consideration, a DRH antenna is preferred over other designs due to its advantages such as high gain, directivity, and bandwidth, for a biomedical application where antenna placed on the human tissue to monitor a specific area [1]. Different types of the DRH antennas in free space and the high dielectric mixtures are investigated and purposed for the system. The first approach was to design a PDRH antenna in free space within the frequency range of interest (i.e. 1-3.5 GHz).

4.1.1. PDRH ANTENNA DESIGN IN FREE SPACE

In this part, two different types of PDRH antennas are designed in free space and investigated. More attention is needed in the antenna simulation using CST microwave studio (CST-MWS) in order to be able to analyse the antenna operation before moving to experimentally fabricating the antenna and testing it.

4.1.1.1. INITIAL PDRH ANTENNA DESIGN IN FREE SPACE:

The initial PDRH antenna designed in free space has two thick ridges to manage the impedance matching by escalating the EM energy throughout the ridges. The PDRH antenna dimensions were calculated using equations given in Chapter 2. Fig. 4.1 presents the calculated design dimensions, satisfying the bandwidth and centre frequency required for the design to operate in free space [2-4].

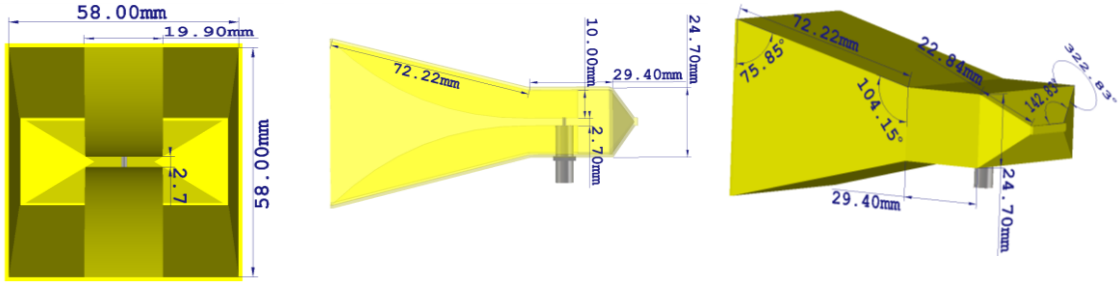

(a) Front view perspective (b) Inside view perspective (c) Back view perspective

Fig. 4.1: A double-ridge horn antenna in the free space.

The antenna has a length of L = 110 mm and width and height of W_x = 60 mm, W_y = 60 mm in the outer aperture of the horn, the angle of 104.15 degrees. Fig. 4.2 represents, the S_{11} response of the PDRH antenna design showing at −10dB point which provide 2.5 GHz bandwidth. Moreover, the graph presents two resonant points within the operating frequency band (2.94 and 5.5 GHz).

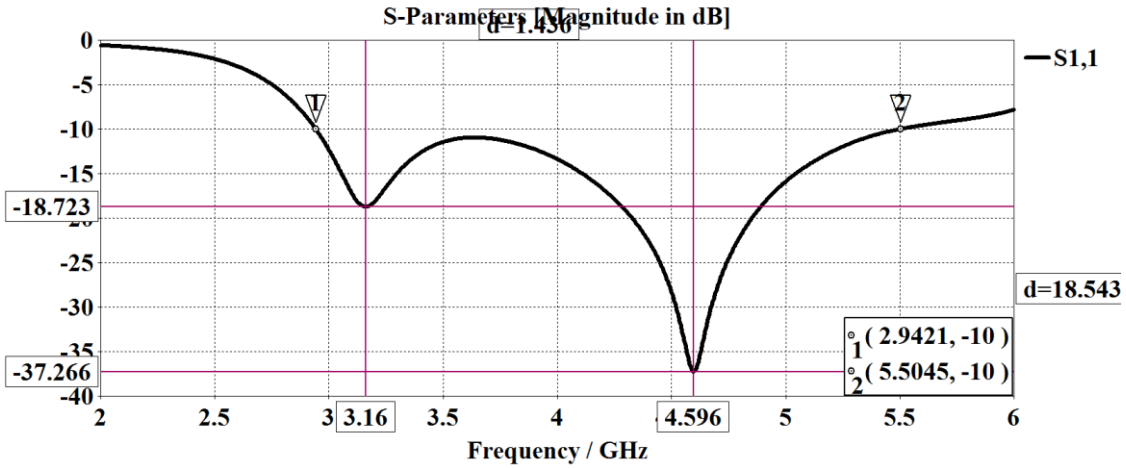

Fig. 4.2: S_{11} parameters that stand below -10dB between 3.22 - 5.23 GHz.

The design offers a relative gain of approximately 7.5 dB at the first resonant frequency (3.16 GHz), and 9.35 dB at the second resonant frequency (4.59 GHz), as given in Fig. 4.3. The gain rapidly increases from 7.08 to 10.61 dB over the frequency range of 2.94 to 5.5 GHz.

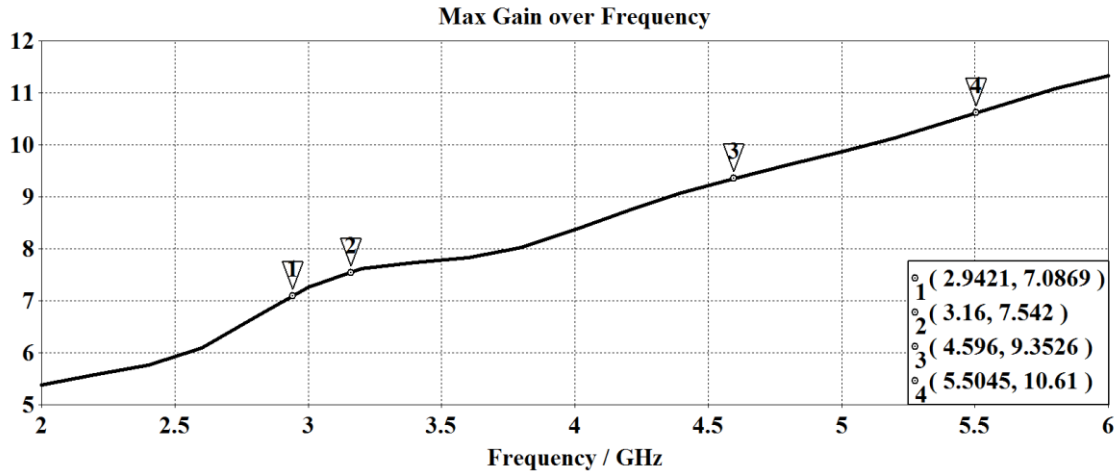

Fig. 4.3: the initial antenna design gain over the frequencies of 2−6 GHz.

The E and H-plane radiation patterns of the antenna are presented in Fig. 4.4, for both resonant frequencies (3.16, 4.59 GHz). High directionality and focused radiation with low side lobes levels (SLLs) and relative gains of 7.54 and 9.36 dB are evident.

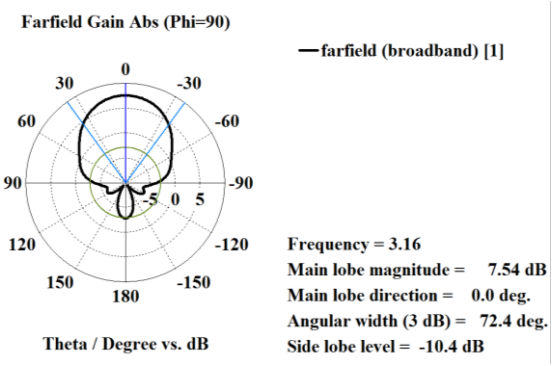

(a) E-plane Far-field radiation pattern at 3.16GHz.

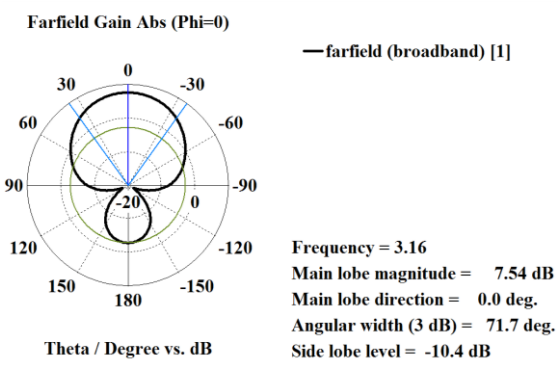

(b): H-plane Far-field radiation pattern at 3.16GHz.

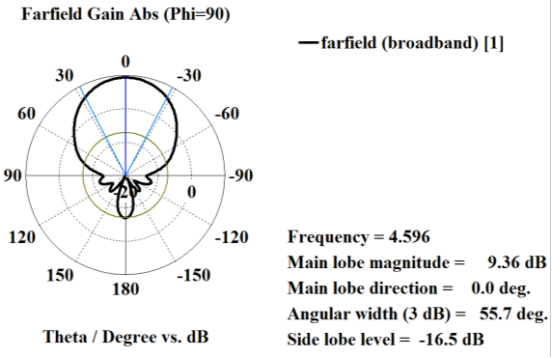

(c) E-plane Far-field radiation pattern at 4.6 GHz.

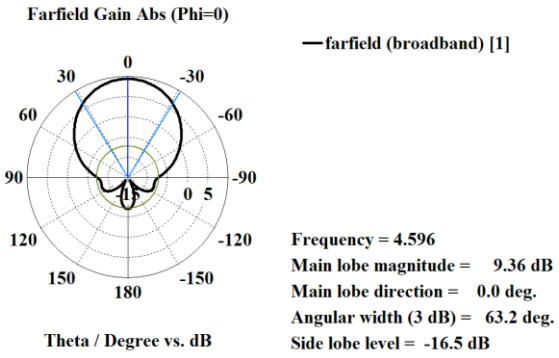

(d): H-plane Far-field radiation pattern at 4.6 GHz.

Fig. 4.4: The E and H-plane polar radiation patterns in the resonant regions.

The antenna design benefits from the high bandwidth and gain. It makes the design reliable for the systems, as good directivity, gain, and wide bandwidth are the main requirements. However, the antenna size is bulky and the pulse penetration would be another major concern of the system design.

4.1.1.2. IMPROVED PDRH ANTENNA DESIGN IN FREE SPACE

The improved PDRH antenna design was further optimised in free space to increase the bandwidth and gain as well as reducing the ridges thickness and outer aperture of the antenna, resulting in the improved design.

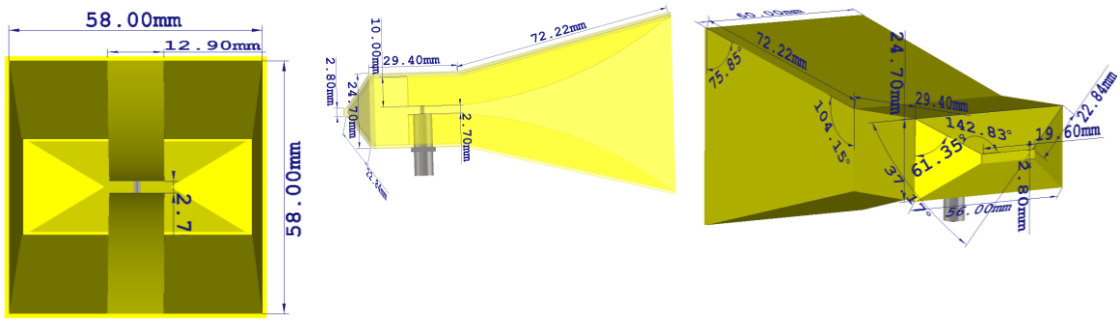

(a): Front view perspective (b): Inside view perspective (c): Back view perspective

Fig. 4.5: An improved DRH antenna design in the free space.

The antenna has a length of L = 110 mm and width and height of W_x = 58 mm, W_y = 58 mm in the outer aperture of the design. The design aperture also is opened with an angle of 104.15 degrees and the other dimensions are provided in Fig. 4.5. This PDRH antenna design has 3.6 GHz of bandwidth at -10 dB point and it is resonating at two frequencies (3.22, and 5.23 GHz), as shown in Fig. 4.6.

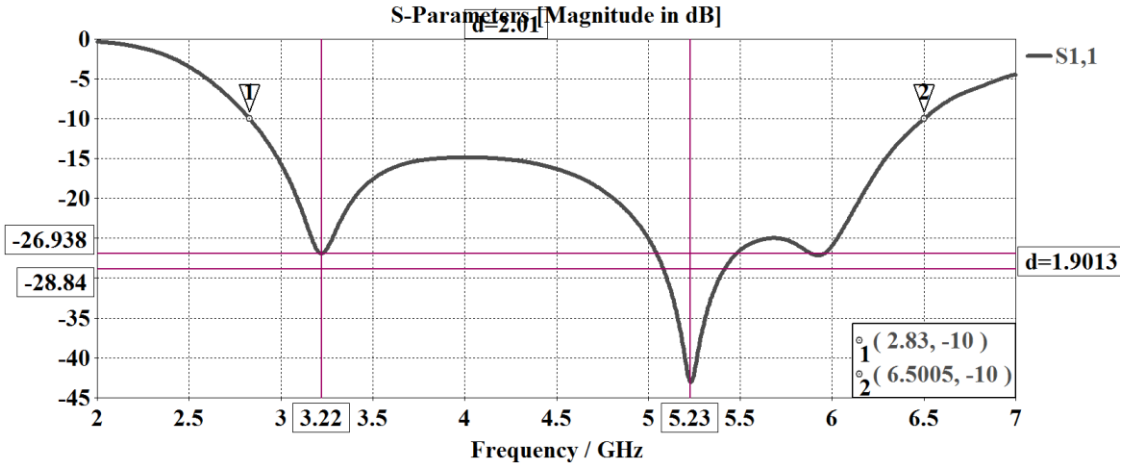

Fig. 4.6: S_{11} parameters that stand below -10dB between 2.83 – 6.49 GHz.

The design also benefits from a gain of 7.69 dB at the first resonant frequency (3.22 GHz), and 10.28 dB at the second resonant (5.23 GHz), presented in Fig. 4.6.

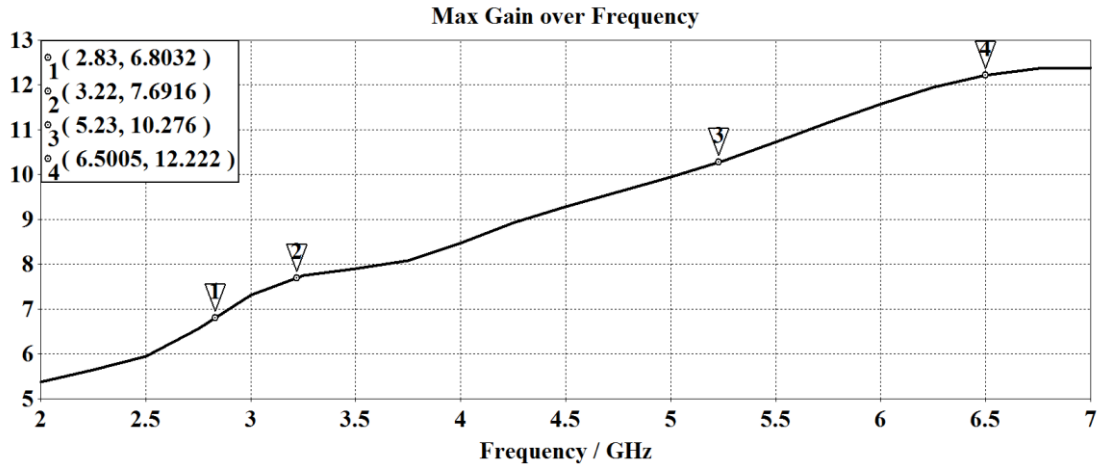

Fig. 4.7: Improved antenna design gain over the frequencies of the 2 - 6GHz.

The gain over the antenna's operating frequency of 2.83 to 6.5 GHz, rapidly increases from 6.8 dB to 12.2 dB as is shown in Fig 4.7. The E-plane and H-plane radiation patterns of the antenna are shown in Fig. 4.8, for resonant frequencies (3.22 and 5.23 GHz), which depict good directionality with low SLLs and relative gains of 7.69 dB and 10.27 dB.

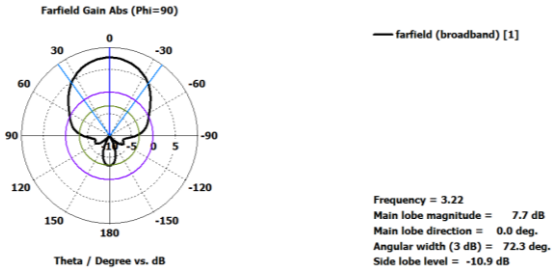

(a) E-plane Far-field radiation pattern at 3.22 GHz.

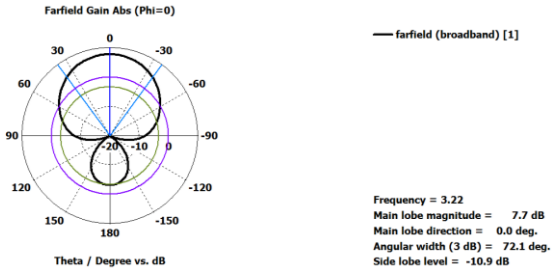

(b): H-plane Far-field radiation pattern at 3.22 GHz.

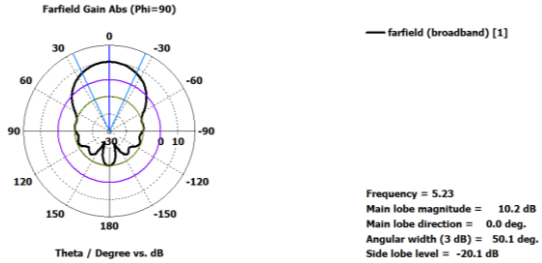

(c) E-plane Far-field radiation pattern at 5.23 GHz.

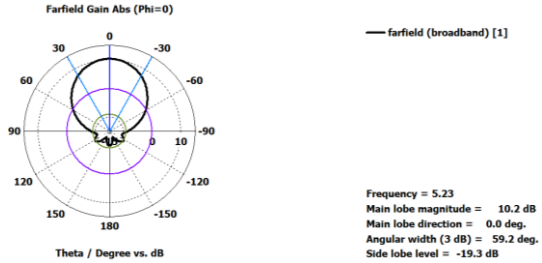

(d): H-plane Far-field radiation pattern at 5.23 GHz.

Fig. 4.8: E and H-plane polar radiation patterns in the resonant regions.

This PDRH antenna design improved the bandwidth by more than 1 GHz and the gain and directivity were enhanced slightly too. However, the dimensions of the antenna are still large and operating centre frequency is high. Employing a high dielectric material in the antenna design shrink the size and reduce the operating frequency to lower frequencies (considering skin depth and absorption rate of the pulse in the human tissue). The other motivation of using such a high dielectric medium was to match the permittivity of the antenna to the skin (which is around 41), and to reduce the large reflections resulting from

the dielectric difference between two mediums. Therefore, different materials with high dielectric properties are employed in the design process in order to achieve these goals. The initial optimised antenna was designed using the ideal high dielectric material that has a permittivity of 41 and conductivity of 0.1 S/m.

4.1.2. IDEAL HIGH DIELECTRIC FILLED DRH ANTENNA

Previous research on the DRH antenna design indicates that use of dielectric material inside the antenna not only miniaturise the design, but also can match the medium, eliminating the reflections in the system [5]. The design parameters for the antenna when it is filled with a high dielectric material (i.e. a permittivity of 41 and a conductivity 0.1 S/m) were calculated based on equations that given earlier in section 2.7.1 of Chapter 2.

4.1.2.1. INITIAL IDEAL HIGH DIELECTRIC PDRH ANTENNA

This PDRH antenna design has aperture dimensions of L = 33.24, A = 34.44, B = 28.48 mm with the opened angle of 108.08 degrees and waveguide dimensions of a = 11.70, b = 5.85, l = 8 mm having rectangular cavity in the back that has a length of 5.31 mm. The ridges' dimensions are given in the side view perspective with a thickness of 3 mm, the height of 1.92 mm and length of 2.86 mm are presented in Fig. 4.9 [5], [6].

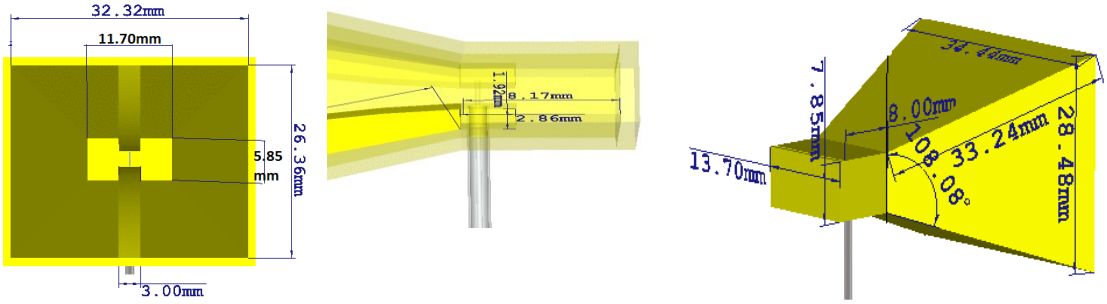

(a): Front view perspective (b): Inside view perspective (c): Back view perspective

Fig 4. 9: Initial DRH antenna design perspective dimensions.

The antenna designed in the ideal high dielectric medium with a permittivity of 41 and conductivity of 0.1 S/m. The miniaturisation of the antenna was possible due to an increase in the material permittivity as well as reduction of the bulky reflection due to the mismatched medium.

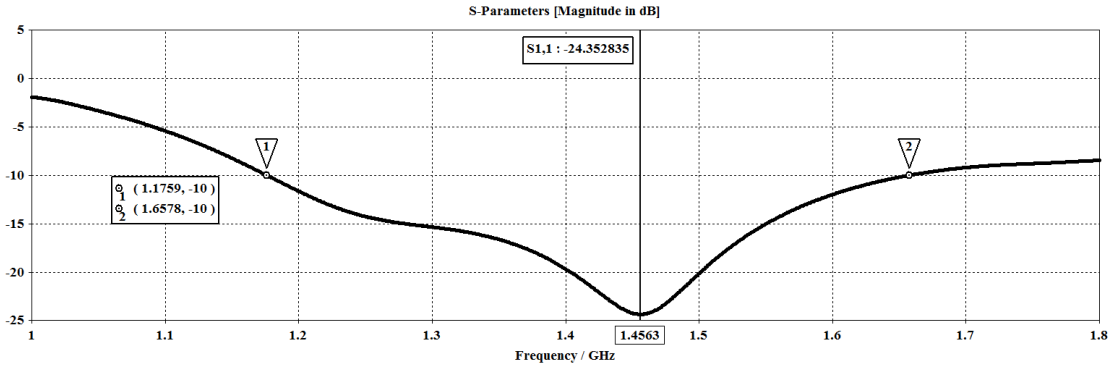

Fig 4. 10: S_{11} graph of the antenna design.

Fig. 4.10 shows the reflection coefficient graph and indicates the -10 dB bandwidth of 482 MHz and the resonant frequency of 1.45 GHz.

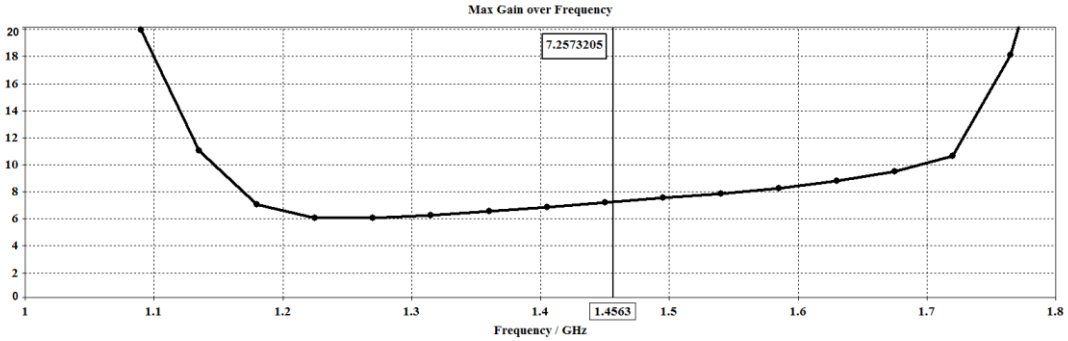

Fig 4. 11: Gain over the frequency range of 1.15 to 1.7 GHz.

The gain of the designed antenna is shown in Fig. 4.11 decays from the onset frequency of 1.15 GHz from 10 dB to 6 dB and starts increasing at 1.25 GHz rapidly to 10 dB. The gain at the resonant frequency (1.45 GHz) is 7.26 dB.

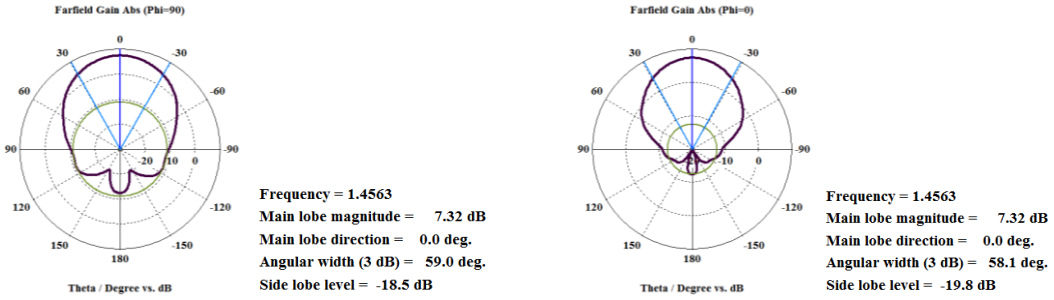

(a): E-plane polar radiation pattern at 1.45 GHz. (b): H-plane polar radiation pattern at 1.45 GHz.

Fig 4. 12: The E and H-plane polar radiation patterns in the resonant region.

The electric and magnetic fields polar radiation pattern for the resonant frequency are givens in Figs. 4.12 (a), and (b). The radiation patterns demonstrate a high directive design with very low SLLs, as expected.

4.1.2.2. IMPROVED IDEAL HIGH DIELECTRIC PDRH ANTENNA

The improved antenna designed and presented in Fig. 4.13, has the pyramidal back shape (compared to initial design) to analyse the back effect on the design. The antenna design has aperture dimensions of L = 33.24, A = 38.44 and B = 32.48 mm with the opened angle of 108.08 degrees and waveguide dimension of l = 8, a = 11.7, and b = 5.85 mm. The gap of 6.65 mm is added at the end of waveguide ridge and a 2 mm gap between the waveguide ridges were obtained where the feeding line is connected, to enhance the performance in the background material with permittivity of 41 [6]. This means all environment around the antenna called background material, has been assumed to have the permittivity of 41 and conductivity of 0.1 S/m.

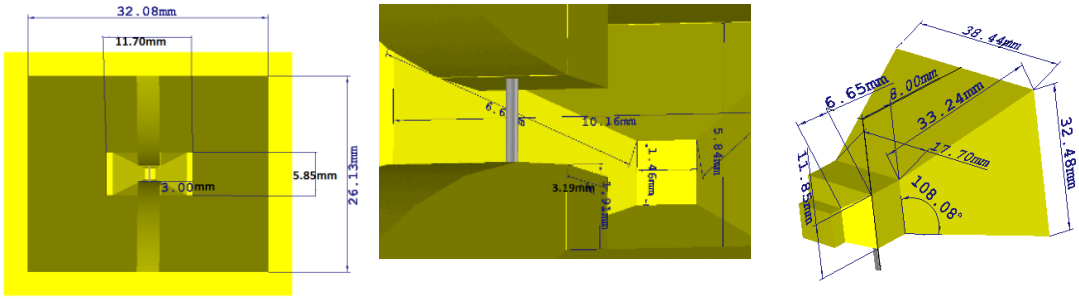

(a): Front view (b): Inside view (c): Back view

Fig 4. 13: Improved DRH antenna in the high dielectric material.

The reflection coefficient graph presented in Fig. 4.14 for the PDRH antenna design illustrates the antenna performance such as the operating bandwidth at −10 dB, and centre frequency of the antenna where it has satisfactory performance.

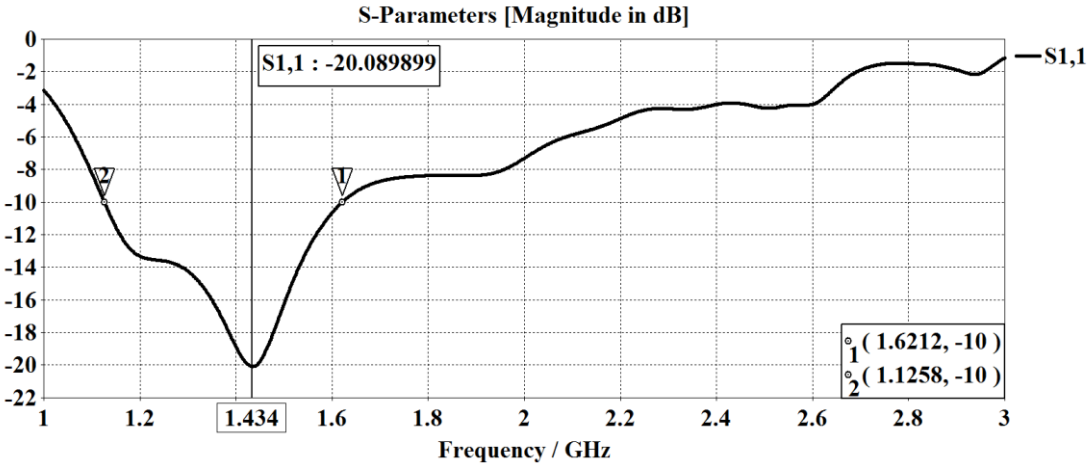

Fig 4. 14: S_{11} graph the improved DRH antenna design.

Figure 4.14 represents the S_{11} graph, which indicates that the antenna has -10 dB badwidth of 500 MHz, starting at 1.12 GHz and ending at 1.62 GHz. The resonant frequency of the design is at 1.43 GHz.

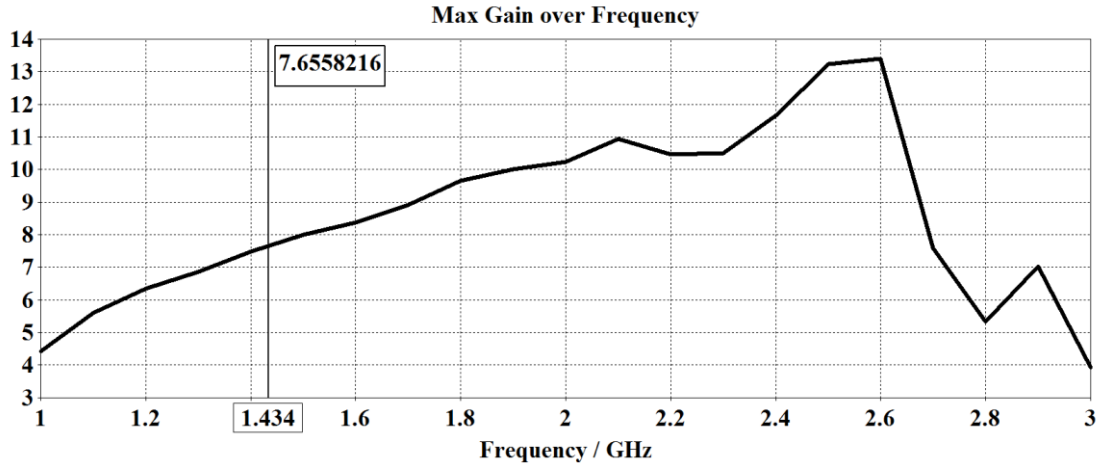

Fig 4. 15: Gain over the frequency of interest (1−3 GHz) of the improved DRH antenna design.

Fig. 4.15 represents the maximum gain over the frequency region of interest. The design exhibits high directivity and gain of 7.6 dB at the resonant frequency (1.43 GHz), which satisfies the system requirement. The gain proportionally increases over the frequency range with a value of 5.8 dB at 1.12 GHz and 8.5 dB at 1.62 GHz.

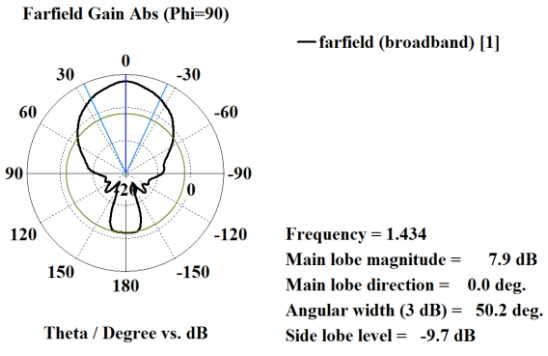

(a): E-plane polar radiation pattern at 1.43 GHz.

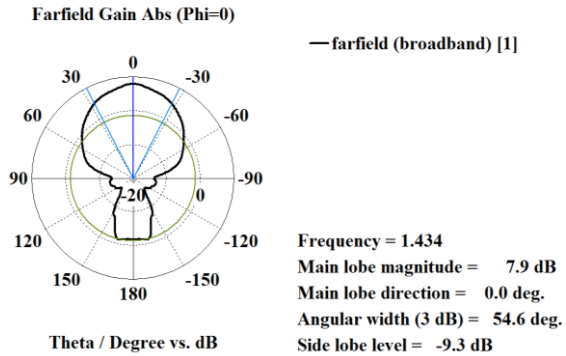

(b): H-plane polar radiation pattern at 1.43 GHz.

Fig 4. 16: E and H-plane polar radiation patterns in the resonant region.

The E and H-plane far-field radiation patterns are presented in Fig. 4.16 (a) and (b), which indicate the high directivity for the design with a gain of 7.9 dB at the resonant frequency (1.434 GHz). The bandwidth and gain have improved in this design, but the SLLs were increased slightly compare to the initial design.

4.1.2.3. DOUBLE-RIDGED GUIDE HORN ANTENNA

The third design, named as Double-Ridge Guide Horn (DRGH) antenna has been designed for the case where the antenna is embedded inside the medium with the permittivity of 41 and the conductivity of 0.1 S/m [7-8]. Figs. 4.17 represents the design dimensions that has aperture dimensions of L = 33.24, A = 35.44, B = 26.41 mm and waveguide pyramidal dimension of l = 8, a = 11.50, b = 8 mm. The waveguide ridges have dimensions of height = 1.58, length = 5, and thickness of 2.2 mm and the gap size of 0.925 mm between two ridges of the design.

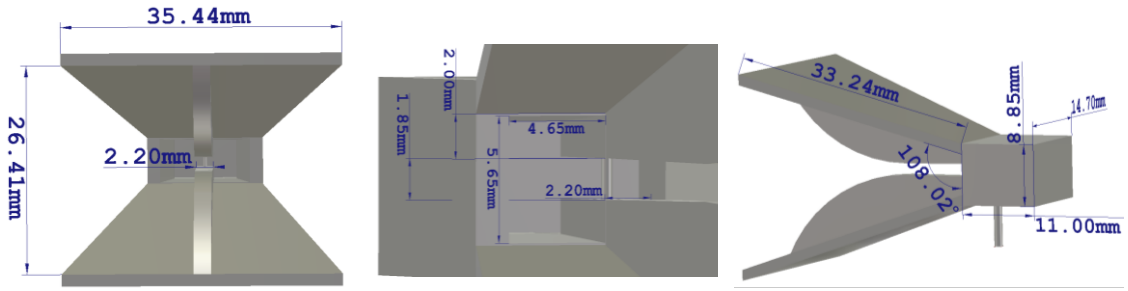

(a): Front view (b): Inside view (c): Back view

Fig 4. 17: Double-Ridged Guide Horn Antenna dimensions in the high dielectric material.

Inside and at the back end of the waveguide aperture, four flaps have been located on the four corner and two edges were placed between them that creates a pyramidal shape on the back of waveguide aperture, which can increase the directivity of the wave. The pyramidal back has dimensions of $l_1 = 3$, $a_1 = 8$, and $b_1 = 5$ mm as shown in Fig. 4.17.

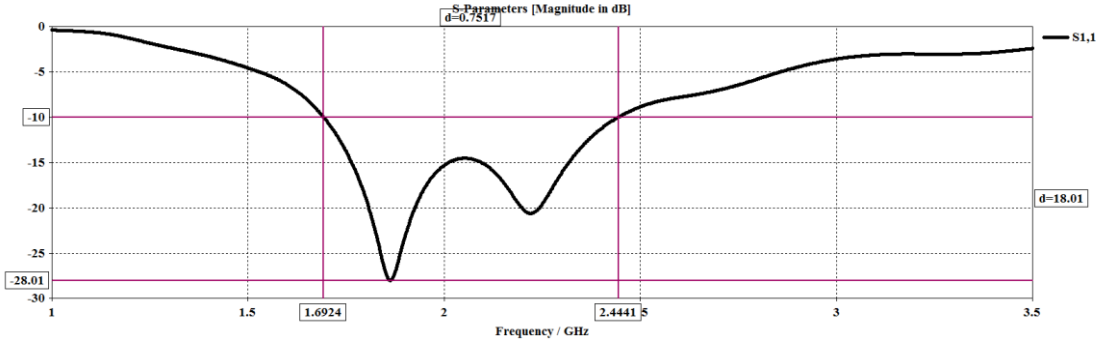

Fig 4. 18: S_{11} graph of the DRGH antenna design.

The S_{11} graph demonstrated in Fig. 4.18, specifies the antenna operating bandwidth of approximately 0.75 GHz ($f_l = 1.69\ GHz\ \&\ f_h = 2.44\ GHz$) and two resonant frequencies at 1.86 and 2.22 GHz. In this design however the centre frequency has been moved to higher frequencies compared to the previous design which was at 1.43 GHz and

therefore reduce the penetration depth, but on the other hand it has increased the design's bandwidth enormously to around twice as the previous design.

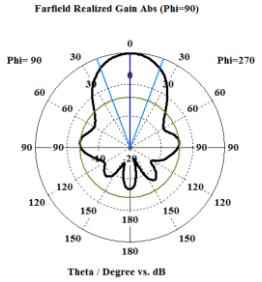

Frequency = 1.8625
Main lobe magnitude = 9.76 dB
Main lobe direction = 0.0 deg.
Angular width (3 dB) = 41.3 deg.
Side lobe level = -13.9 dB

(a) E-plane polar pattern at 1.86 GHz.

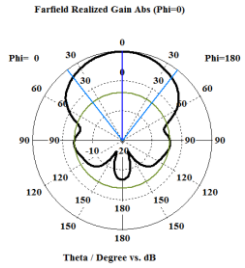

Frequency = 1.8625
Main lobe magnitude = 9.76 dB
Main lobe direction = 0.0 deg.
Angular width (3 dB) = 75.7 deg.
Side lobe level = -13.7 dB

(b): H-plane polar pattern at 1.86 GHz.

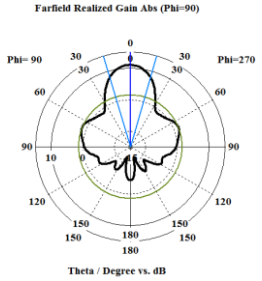

Frequency = 2.22
Main lobe magnitude = 11 dB
Main lobe direction = 0.0 deg.
Angular width (3 dB) = 32.7 deg.
Side lobe level = -9.5 dB

(c): E-plane polar pattern at 2.22 GHz.

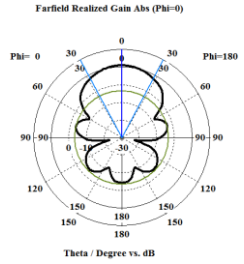

Frequency = 2.22
Main lobe magnitude = 11 dB
Main lobe direction = 0.0 deg.
Angular width (3 dB) = 56.1 deg.
Side lobe level = -14.3 dB

(d): H-plane polar pattern at 2.22 GHz.

Fig 4. 19: E and H-plane polar radiation patterns in the resonant regions.

Figs. 4.19 (a) and (b) presented the far-field graphs of the design that demonstrates a good directivity with low SLLs and gain as high as 9.49 dB at 1.8 GHz centre frequency at E and H field region. Moreover, Figs. 4.19 (c), and (d) illustrates more SLLs with less directivity due to side open aperture and higher gain of 11 dB in the centre frequency of 2.2 GHz in the E and H field region that verifies an acceptable operation for the design.

4.1.2.4. EDRH ANTENNA IN HIGH DIELECTRIC

The novel EDRH antenna was carefully designed with respect to the previously defined pyramidal design dimensions as shown in Figs. 4.20. Furthermore, the cavity at the back of the design was decided to be a half sphere as is presented in Fig. 4.20 (b).

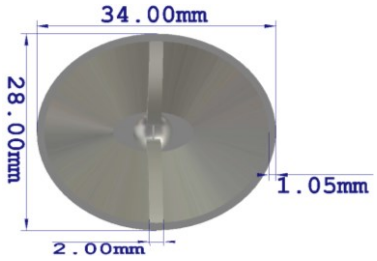

(a): Front view

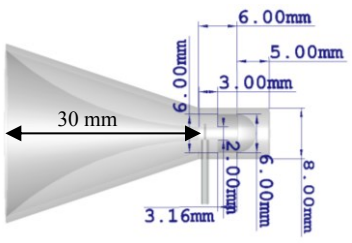

(b): Inside view

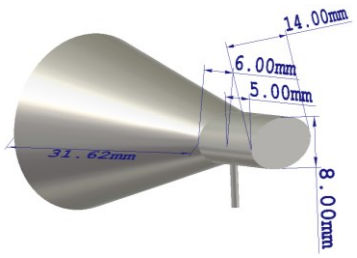

(c): Back view

Fig 4. 20: EDRH antenna design dimension.

The S_{11} results of the antenna shown in Fig. 4.21 represents the bandwidth is 1 GHz of operating bandwidth and the resonant frequency at 2.04 GHz that is almost double the bandwidth of the PDRH antenna design.

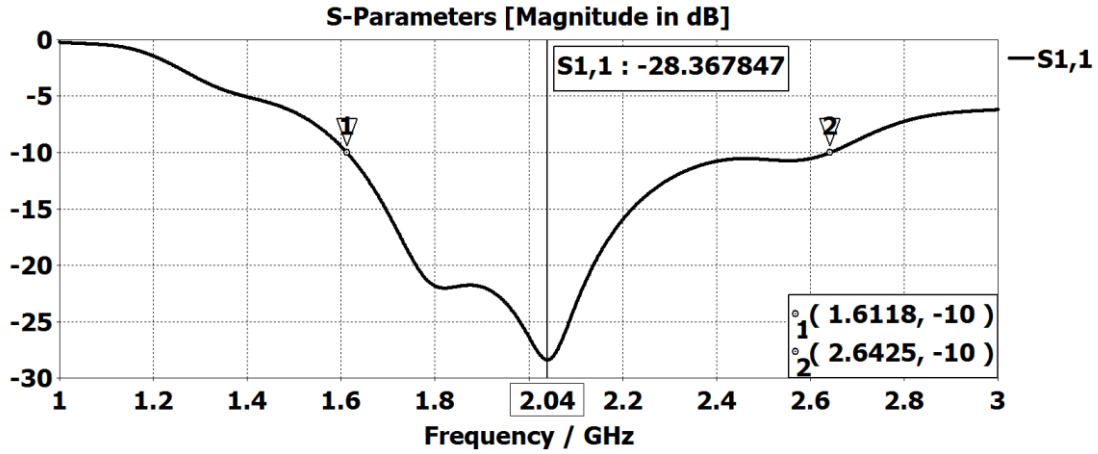

Fig 4. 21: S_{11} graph for the EDRH Antenna.

Fig. 4.22 demonstrates the maximum gain over the frequency range of interest (1–3 GHz) for the antenna design. The gain increases from zero to around 12.5 dB, which is optimum for this design type.

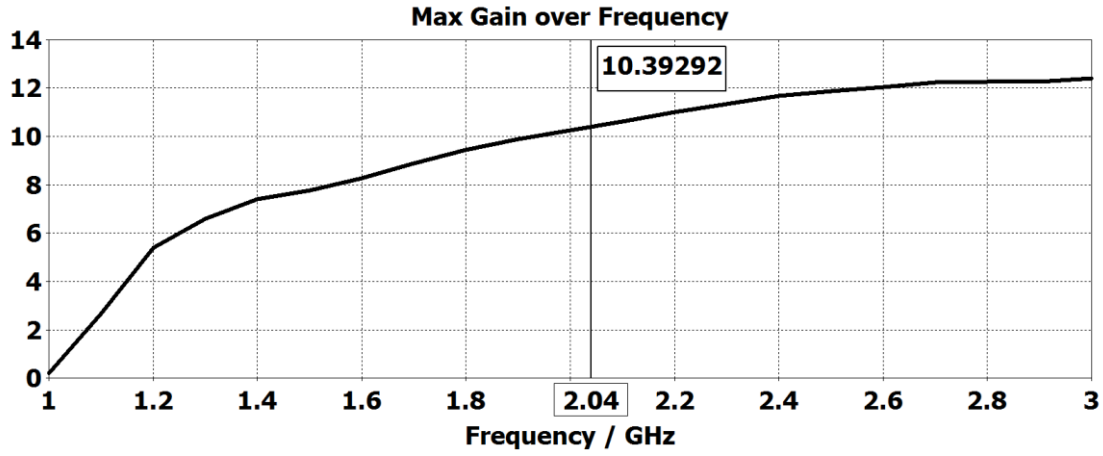

Fig 4. 22: Gain over the frequency range of 1 to 3 GHz.

The gain of the EDRH antenna at 2.04 GHz resonant frequency is 10.4 dB that is close to the previously designed PDRH antenna.

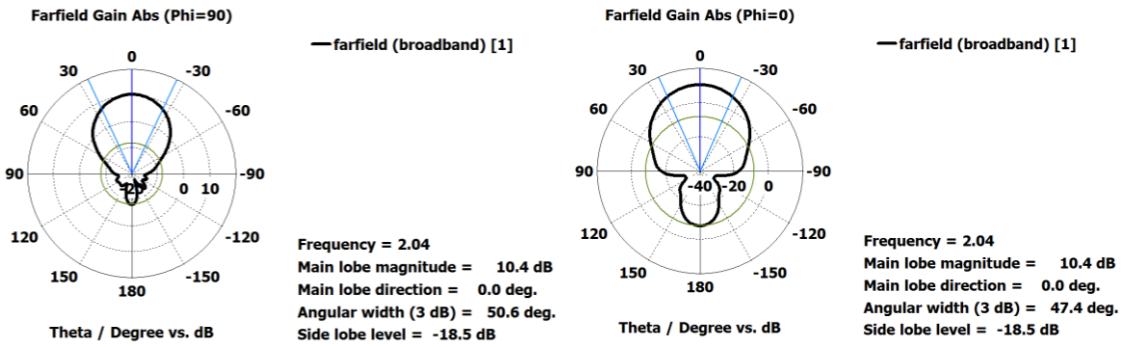

(a): E-plane polar pattern at 2.04GHz. (b): H-plane polar pattern at 2.04 GHz.

Fig 4. 23: E and H-plane polar radiation patterns in the resonant region.

Figs 4.23 (a) and (b) show the polar far-field radiation patterns of the EDRH antenna design in E and H-plane regions for 2.04 GHz resonant frequency. The gain of 10.4 dB was obtained at 2.04 GHz, which is slightly higher than the PDRH antenna design with less SLLs compared to the previous designs.

The simulation results for EDRH antenna design were compared to the previous PDRH antenna design and indicated that in the new design, not only the antenna bandwidth has slightly increased. The gain has also improved to some extent. However, the fabrication process needs more attention.

4.1.3. EXTENSION TO THE OPTIMAL DESIGNS

In this stage, to place the design at a distance from the scanning area to produce a delay and avoid pulse overlapping, and having plane wave propagating through the monitoring medium, an extension was added to the design with a determined length that can be calculated by the equations (4-1a, b).

$$\lambda = {}^{c}/_{f\sqrt{\varepsilon_r}} \qquad \text{Eq. (4-1a)}$$

$$d_f = {}^{2 \times D^2}/_{\lambda} \qquad \text{Eq. (4-1b)}$$

where f is the selected centre frequency for of operation ε_r is the relative permittivity of the dielectric material that is embedded within the design and D is the biggest aperture dimension of the design. Placing antenna close to far-field region would improve the design in such as having plane wave propagation into the scanning area as well as avoiding overlapping and protecting the path from noises added to the received pulse. But it also has some drawbacks such as adding more distance to the wave path and therefore, causing more energy loss within this path as well as adding complexity and more

fabrications cost to the design. In order to define the outer aperture dimensions of the design where the extension is added, the equations (4-2a, and b) developed.

$$w_{a2} = 2 \times [\frac{w_{a0}}{2} + \frac{w_{a1} - w_{a0}}{2 \times l_1} \times (l_2 + l_1)] \quad \text{Eq. (4-2a)}$$

$$w_{b2} = 2 \times [\frac{w_{b0}}{2} + \frac{w_{b1} - w_{b0}}{2 \times l_1} \times (l_2 + l_1)] \quad \text{Eq. (4-2b)}$$

where w_a is width of the horn aperture, w_b is height of the horn aperture and l is length of the aperture. The aperture dimensions expand with respect to the increased length.

4.1.3.1. EXTENDED PDRH ANTENNA IN IDEAL HIGH DIELECTRIC

In this section, an extension was added to the PDRH antenna that was designed previously in order to satisfy both delay and far field approach, by placing the antenna at a distance from the scanning area. The wavelength can be determined by equation (4-1a) to be $\lambda = 31.2\ mm$. And the far-field region for the design, d_f defined by equation (4-1b), $d_f \geq 65\ mm$. Therefore, there is need of a minimum of 30 mm extension to the outer aperture of the design. The outer dimensions of the aperture of this design can be determined using equations (4-2a, and b).

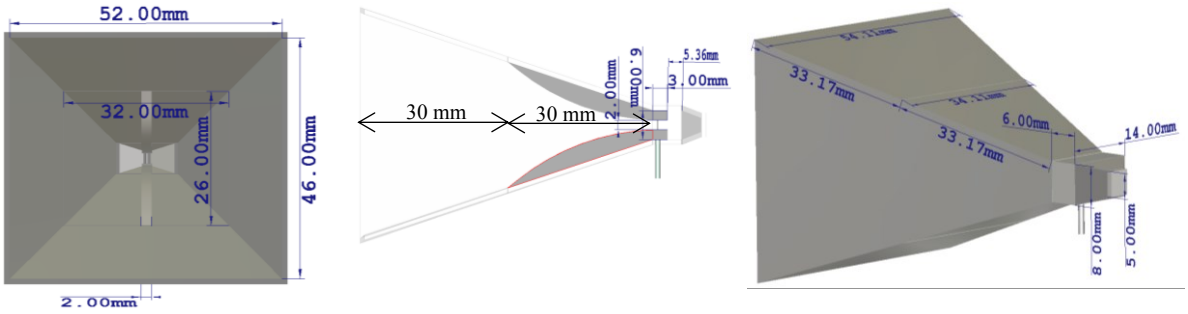

(a): Front view (b): Inside view (c): Back view

Fig 4. 24: Extended PDRH antenna with the dimensions.

The initial PDRH antenna was redesigned with an extension that has dimensions of l = 30, a_2 = 52, and b_2 = 46 mm as shown in Fig. 4.24, in order to locate the antenna close to far field region of scanning area of the human body.

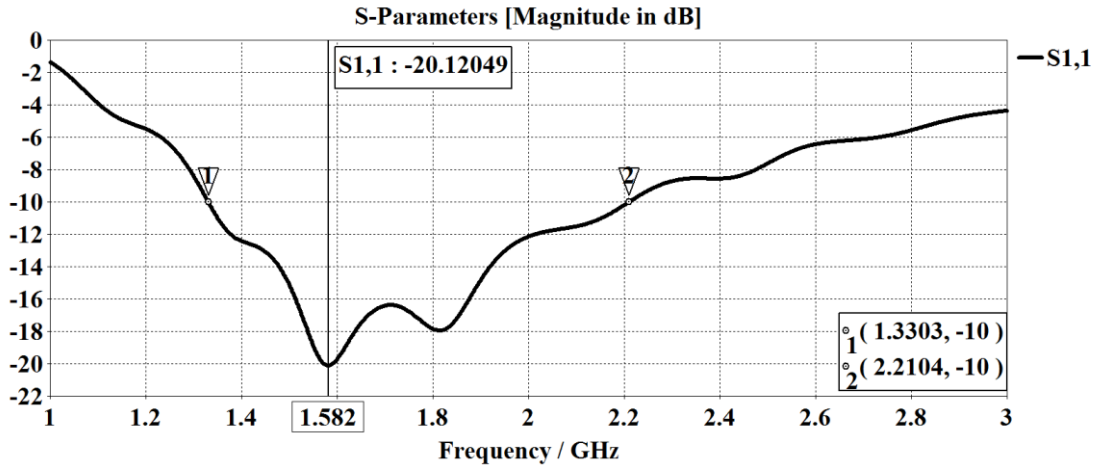

Fig 4. 25: S_{11} graph for the extended PDRH antenna design.

Fig. 4.25 represents the S_{11} graphs, which defines the operating bandwidth of 880 MHz covering frequencies from 1.3 GHz to 2.2 GHz. The graph demonstrates two resonant frequencies of 1.58 and 1.81 GHz.

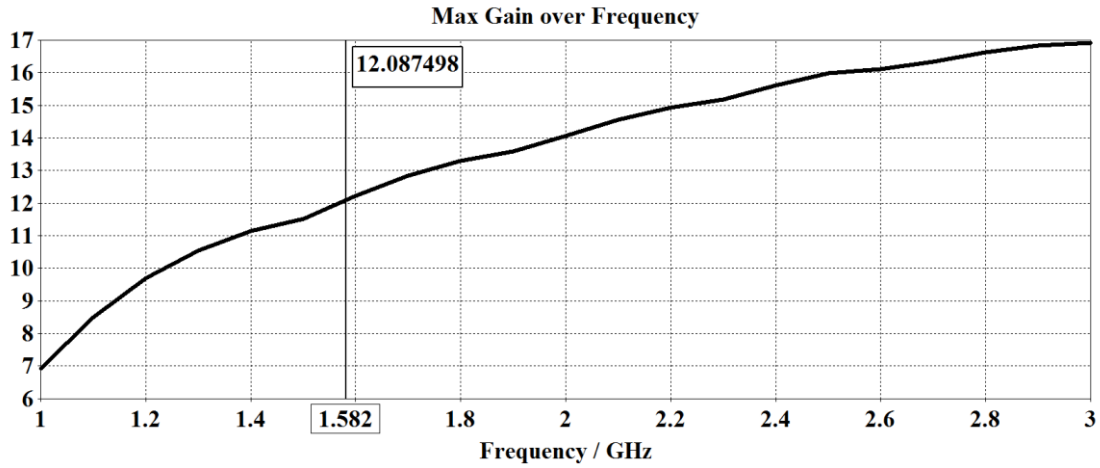

Fig 4. 26: Extended PDRH antenna gain over the frequency range of 1 to 3 GHz.

Fig. 4.26 represents the gain of the design over a frequency range of 1 to 3 GHz. that indicates increase rate from 7 dB to 17 dB. Concerning the two resonant frequencies of 1.58 and 1.81 GHz, which have gain of 12.09 dB and 13.33 dB.

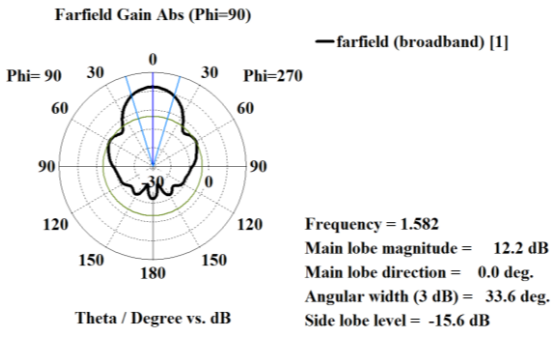

(a): E-plane polar pattern at 1.58 GHz.

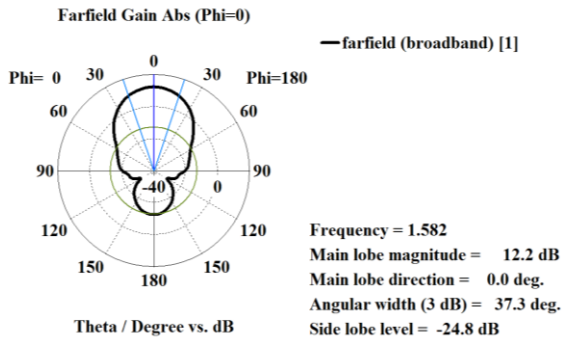

(b): H-plane polar pattern at 1.58 GHz.

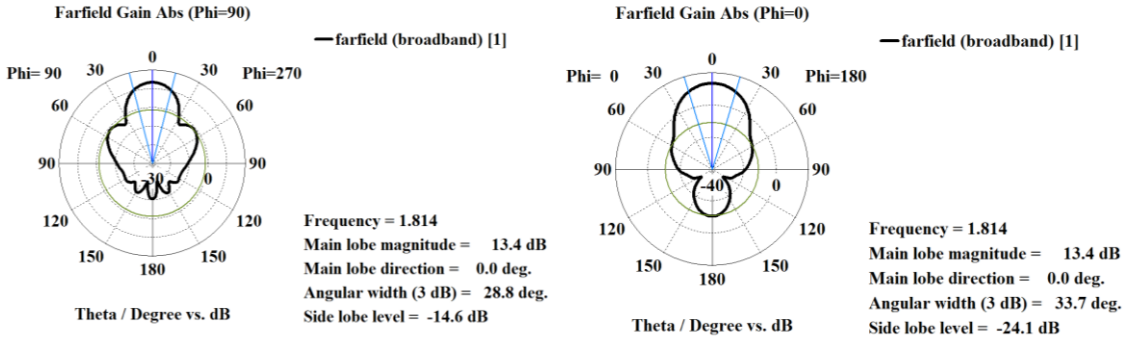

(c): E-plane polar pattern at 1.81 GHz. (d): H-plane polar pattern at 1.81 GHz.

Fig 4. 27: E and H-plane polar radiation patterns in the resonant regions.

Figs. 4.27 (a) and (b) show the polar electric and magnetic far-field patterns at 1.58 GHz representing the gain of 12.2 dB and low SLLs. The far field radiation patterns at 1.81 GHz demonstrate a higher gain of 13.4 dB and increase in the SLLs.

4.1.3.2. EXTENDED EDRH ANTENNA IN IDEAL HIGH DIELECTRIC

In this section, the EDRH antenna designed in previous part is modified with an extension to the outer aperture in order to satisfy the far field region approach for avoiding overlapping issue. The extended EDRH antenna design filled with the dielectric material of 41 is purposed as shown in Figs 4.28. The design has been analysed with respect to previous design with no extension and the results were discussed.

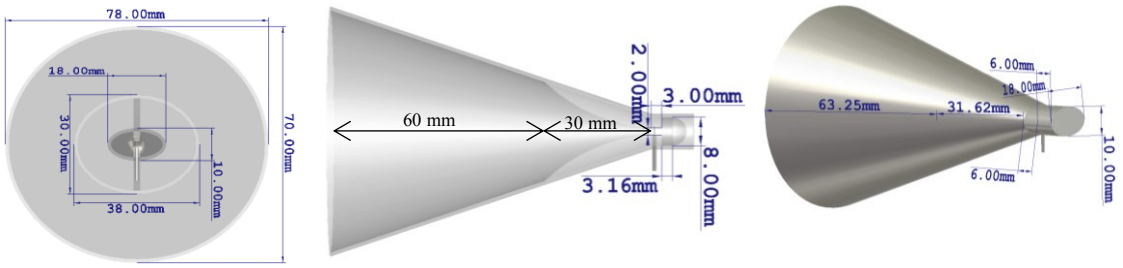

(a): Front view (b): Inside view (c): Side view

Fig 4. 28: Extended EDRH antenna design dimensions.

Figs. 4.28 represents the design dimensions and the length of the antenna extension determined using equations (4-1a, b). The wavelength of this design can be defined by equation (4-1a) and is calculated to be $\lambda = 31.2\ mm$ and the far-filed distance defined by (4-1b) is calculated to be $d_f = 83.1\ mm$.

The length of the extension part selected is 60 mm as shown in Fig. 4.28 (c). This length plus 33 mm length of the antenna to the port is adding a gap of 93 mm, which should satisfies the far field placement equipment.

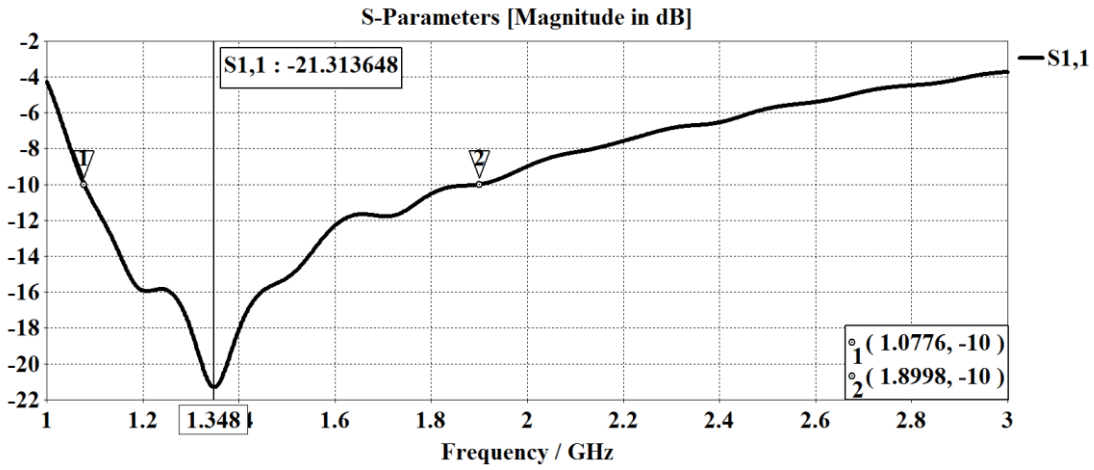

Fig 4. 29: S_{11} graph of the antenna design with an extension.

The resonant frequency of the design shifted to 1.37 GHz and the -10 dB bandwidth reduced to 882 MHz shown in Fig. 4.29.

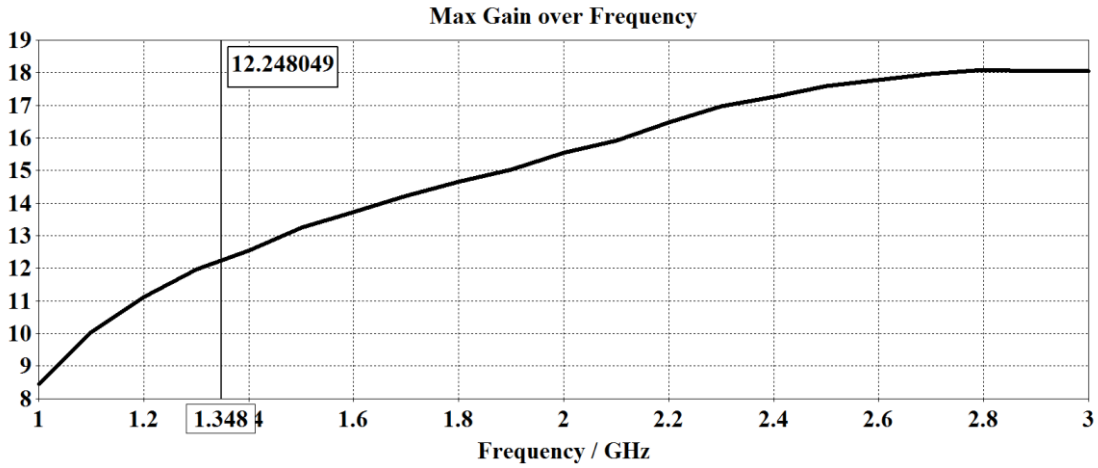

Fig 4. 30: Extended design gain over the frequencies of interest (1 to 3 GHz).

The extended design gain over the frequency range of interest (1 to 3 GHz) is shown in Fig. 4.30. The graph presents a gradual increase in the gain from 8.5 dB to 18 dB. The gain at resonant frequency recorded a gain of 12.37 dB.

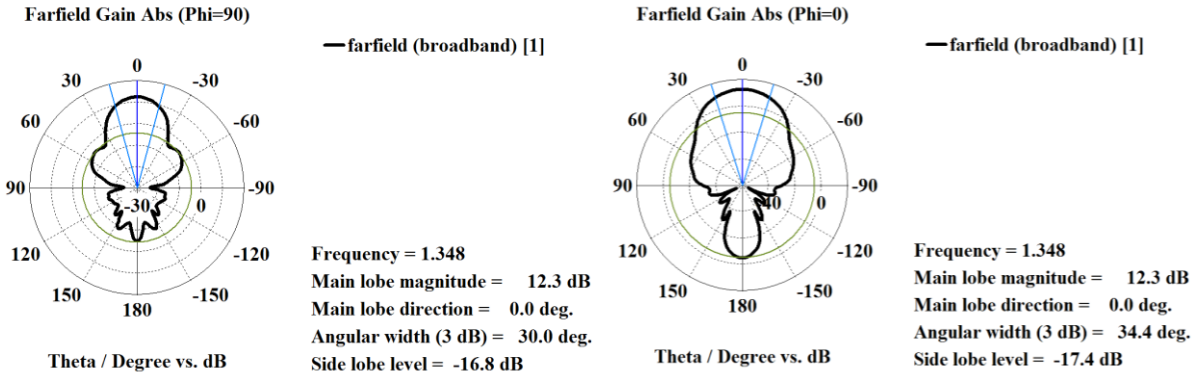

(a): E-plane polar radiation pattern at 1.37 GHz. (b): H-plane polar radiation pattern at 1.37 GHz.

Fig 4. 31: E and H-plane Far-field radiation patterns at 1.37 GHz frequency, main lobe magnitude is 12.4 dB, main lobe direction is 0 degree, angular width (3 dB) is 27.6 degree and side lobe level is −16.6 dB.

Figs 4.31 (a) and (b) represent the electric and magnetic far-field radiation patterns of the antenna with the extension. The results indicate that the gain has improved slightly to 12.4 dB and the SLLs decreased in the new design result of removing the medium mismatched due to increase of the permittivity of the material to the skin permittivity.

4.1.3.3. EXTENDED PDRH ANTENNA DESIGN IN CERAMIC

The extended PDRH antenna was redesigned and modified for the high dielectric ceramic (VLF-440) that has permittivity of around 30 and conductivity of 0.04 S/m at the frequency of interest. The ceramic was characterised in Chapter 3 of this thesis, and the data was employed. In order to place the antenna in the far field, the gap is calculated using equation (4-1a, b) [9, 10]. The wavelength of this design can be defined by equation (4-1a) and is calculated to be $\lambda = 36.5\ mm$ and the far-filed distance defined by (4-1b) is calculated to be $d_f = 71\ mm$.

Concerning the far field distance, the length of the extended aperture of the antenna has to be increased to at least 70 mm. This means that the extended part should have minimum length of 40 mm. The width and height of aperture should be redefined also by equations (4-2a, b) to 66 and 58 mm respectively. The ceramic material was modelled using the data characterised previously and was fed into the CST Studio software deploying the dispersion Debye 1st order dispersion model and the measured data shown in Fig. 4.32.

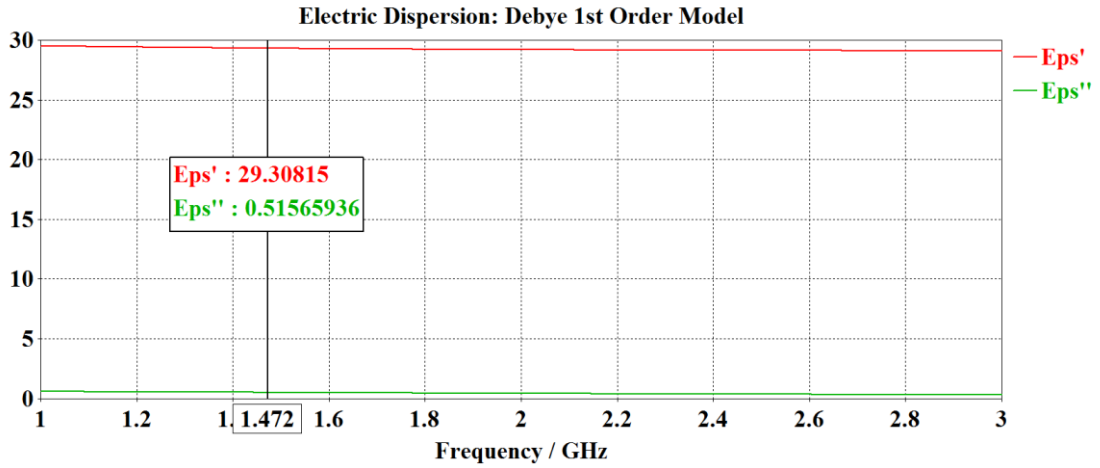

Fig 4. 32: Ceramic data created using debye 1st order from the real data in CST Studio software.

The extended PDRH antenna was designed based on these dielectric properties as shown in Figs. 4.33.

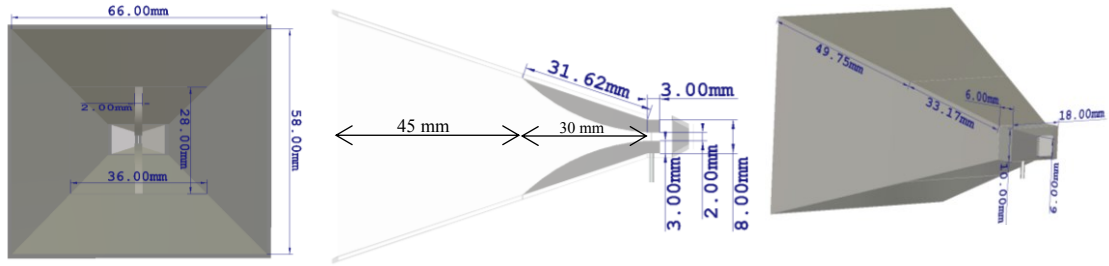

(a): Front view (b): Inside view (c): Back view

Fig 4. 33: Extended PDRH antenna with the dimensions in the ceramic created using the Debye 1st order.

The design parameters were changed and compared to the previous design, based on the ideal 41 permittivity and 0.1 S/m conuctivity.

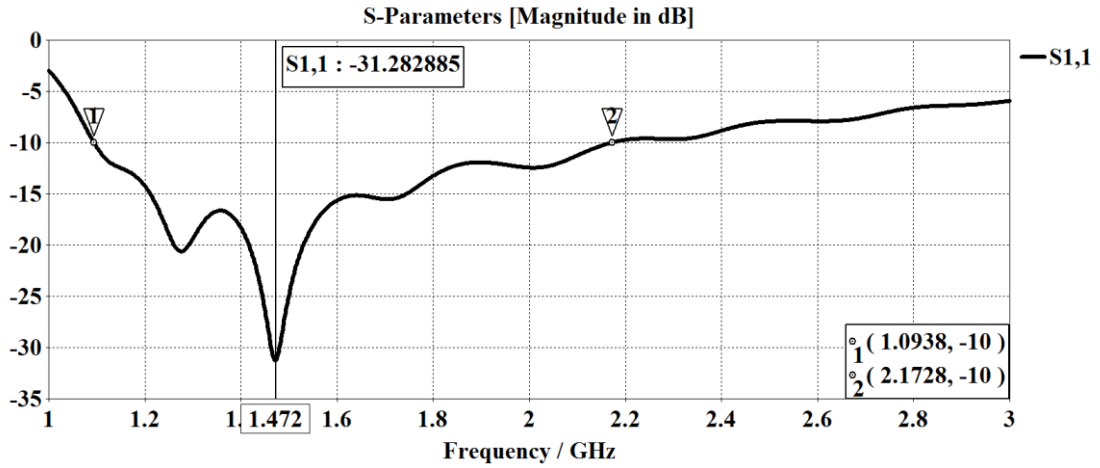

Fig 4. 34: S_{11} graph of the EPDRH antenna design with an extension in the real Debye 1st order.

The S_{11} graph represented in Fig. 4.34, for the extended PDRH antenna offers more than 1 GHz of bandwidth and two resonant frequencies at 1.27, and 1.47 GHz (The highest dip recorded for 1.47 GHz was −31.3 dB).

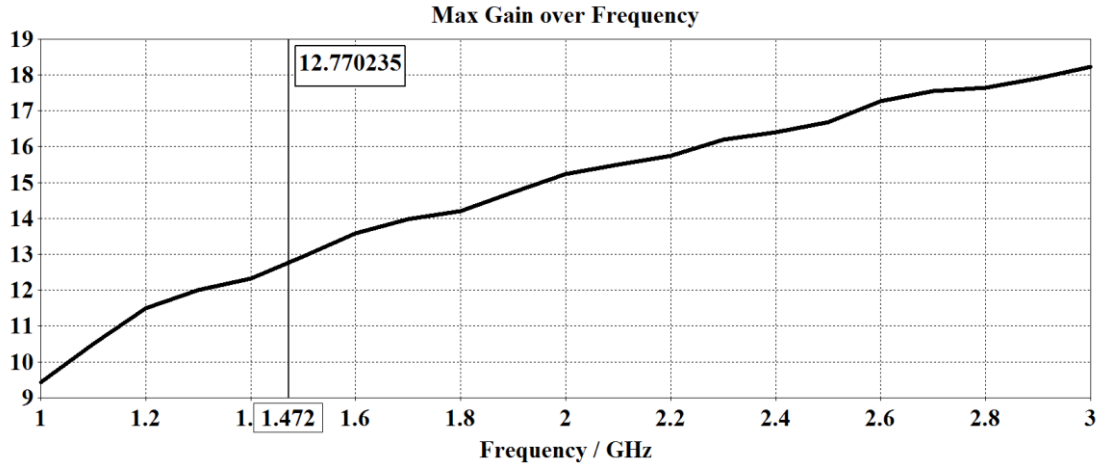

Fig 4. 35: EPDRH antenna gain over the frequency range of 1 to 3 GHz.

The antenna gain increased gradually from 9.5 dB at 1 GHz to 18.3 dB at 3 GHz. The gain at resonant frequencies (1.28 and 1.47 GHz) is recorded as 11.8 dB and 12.7 dB as shown in Fig. 4.35.

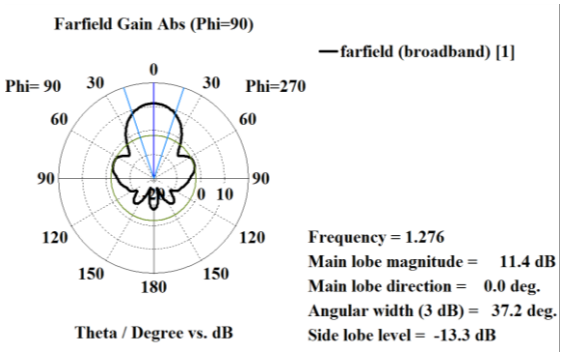

(a): E-plane polar pattern at 1.28 GHz.

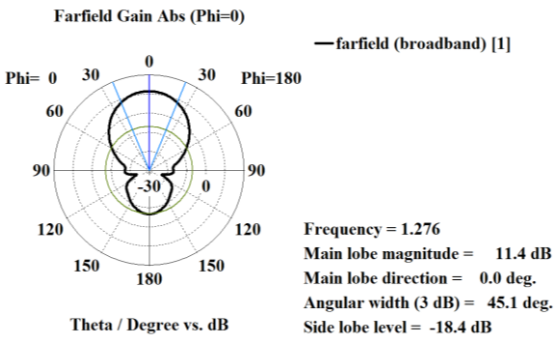

(b): H-plane polar pattern at 1.28 GHz.

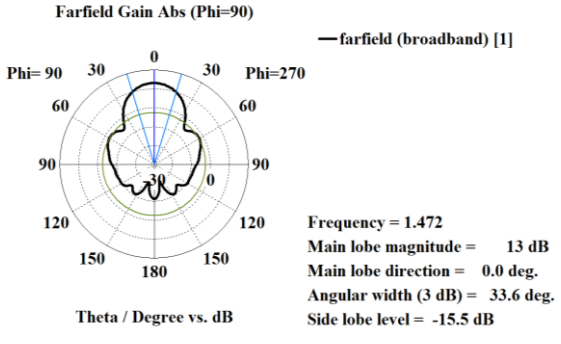

(c): E-plane polar pattern at 1.47 GHz.

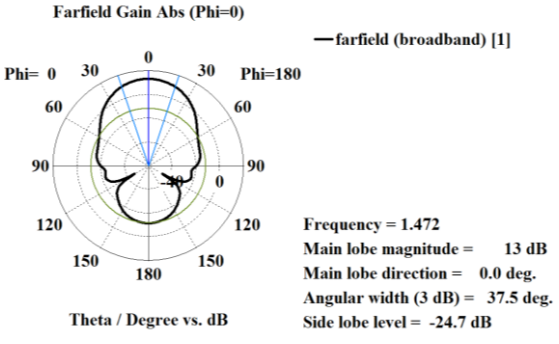

(d): H-plane polar pattern at 1.47 GHz.

Fig 4. 36: E and H-plane polar radiation patterns in the resonant regions.

Figs. 4.36 (a) and (b) represents the polar E and H field radiation patterns at 1.28 GHz, which provides acceptable directivity and gain of 11.4 dB with the slight SLLs. Furthermore, the Figs. 36 (c) and (d) expressed the same patterns at 1.47 GHz with a higher gain of 13 dB and less SLLs due to better matching.

4.1.3.4. EXTENDED EDRH ANTENNA DESIGN IN CERAMIC

The extended EDRH antenna was redesigned and modified to move the centre frequency and operating band to lower frequencies using the high dielectric ceramic (VLF-440) for better penetration depth.

The ceramic measured permittivity was 29.2 and conductivity of 0.04 S/m as characterised in Chapter 3. In order to achieve the goal of placing the antenna in the far field and producing a delay, an extension was added to the design with a length that can be calculated using the equations (4-1a, b). The wavelength of this design can be defined by equation (4-1a) and is calculated to be $\lambda = 36.5\ mm$ and the far-filed distance defined by (4-1b) is calculated to be $d_f = 87.7\ mm$.

Concerning, the far field distance; length of the extended aperture of the antenna has to be increased to 60 mm as the EDRH antenna had more than 30 mm length up to the connector points used to excite the wave. Therefore, the width and height of the aperture was defined to 80 and 70 mm by defined equations (4-2a, b) at the start of this chapter.

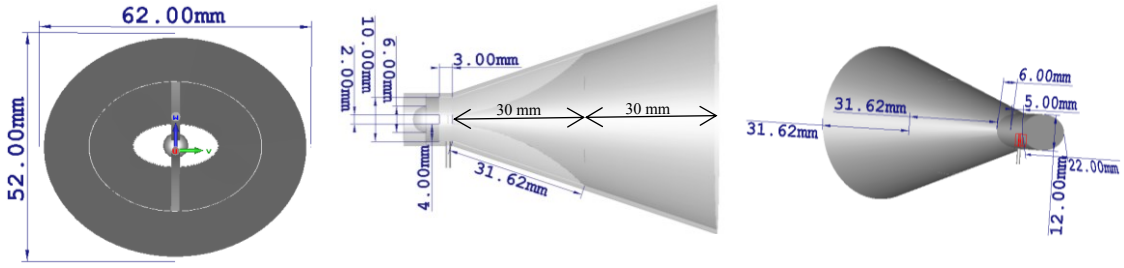

(a): Front view (b): Inside view (c): Back view

Fig 4. 37: Extended PDRH antenna with the dimensions in the ceramic created using the Debye 1st order.

The dimensions of the extended EDRH antenna shown in Fig. 4.37, were determined based on the real measured ceramic dielectric properties that was plotted in the CST software employing the Debye 1st order dispersion modeling method.

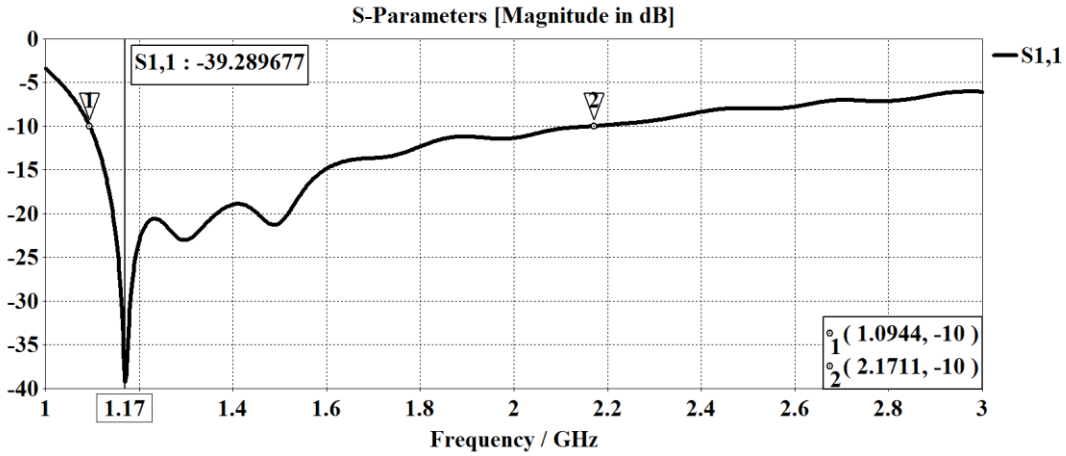

Fig 4. 38: S_{11} graph of the EDRH antenna design with an extension in the real Debye 1st order.

Fig. 4.38 represents the S_{11} graph showing a high resonant frequency at 1.17 GHz and two standard resonant frequencies at 1.3 and 1.49 GHz. The graph shows more than 1 GHz of bandwidth with reference to −10 dB.

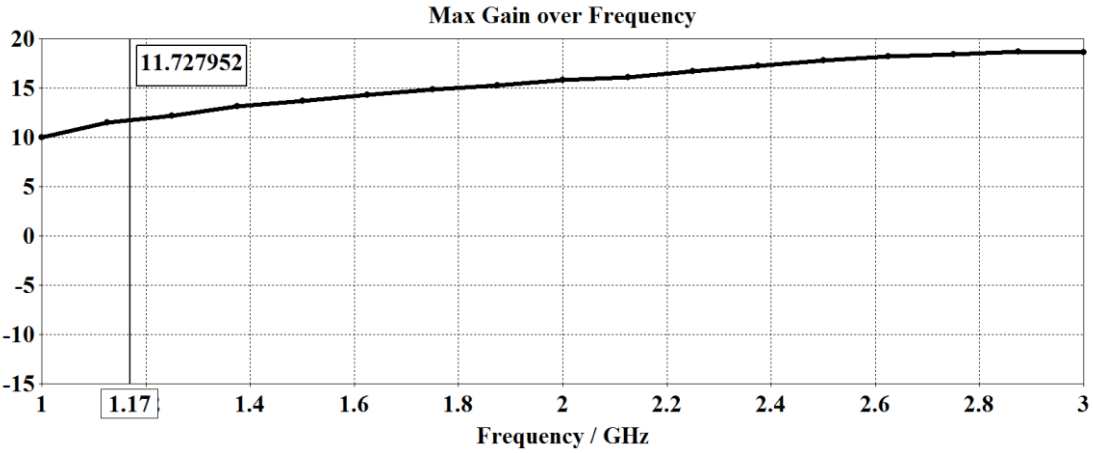

Fig 4. 39: EDRH antenna gain over the frequency range of 1 to 3 GHz.

Fig. 4.39 represents the maximum gain of the extended EDRH antenna, specifying gradual increase of the gain from 10 dB to around 20 dB over the frequency range of 1 to 3 GHz.

The gain at two resonant frequencies of 1.3 and 1.49 GHz is recorded to be 12.5 dB and 13.6 dB, which is premium in this design types.

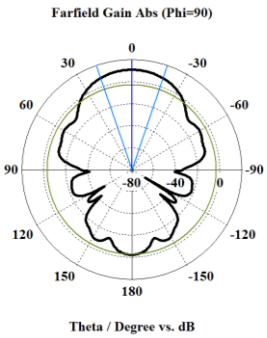

(a): E-plane polar pattern at 1.17 GHz.

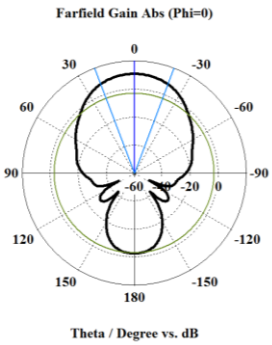

(b): H-plane polar pattern at 1.17 GHz.

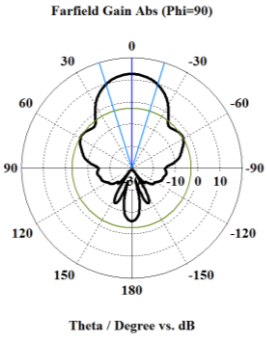

(c): E-plane polar pattern at 1.3 GHz.

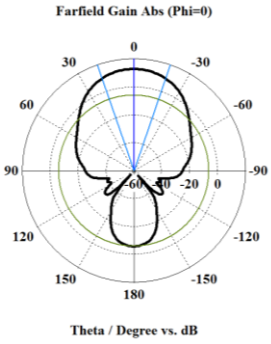

(d): H-plane polar pattern at 1.3 GHz.

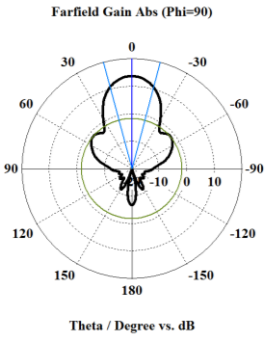

(e): E-plane polar pattern at 1.49 GHz.

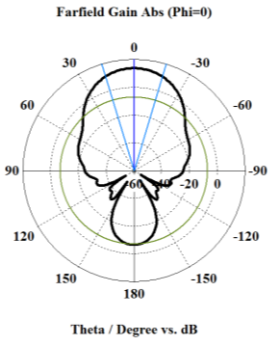

(f): H-plane polar pattern at 1.49 GHz.

Fig 4. 40: E and H field polar radiation patterns in the resonant regions.

Figs. 4.40 (a-f) represents the polar E and H field radiation patterns at all three resonant frequencies of the design, indicating high directivity and gain as the frequency increases and less SLLs.

4.1.3.5. PDRH ANTENNA DESIGN IN OPTIMISED CERAMIC

The dielectric properties of the r-TiO_2 was characterised in Chapter 3 and it was mixed with the VLF-440 ceramic powder with different ratios, to increase the permittivity of the material to the skin permittivity (41-45). The mixture of two portions of VLF-440 with one portion of the r-TiO_2 was found to match perfectly to the dielectric properties at the region of interest. The dielectric properties of the mixture at 1.8 GHz was measured to be

$\varepsilon_r = 44.1$ and $\sigma = 0.002$ S/m. Furthermore, the PDRH antenna was redesigned with modified dimensions shown in Fig 4.41; In addition, the extension dimension was determined using equations (4-2a) and (4-2b) and was added to the design in order to place the antenna in the far-field region of monitoring area presented in Fig. 4.42 [11].

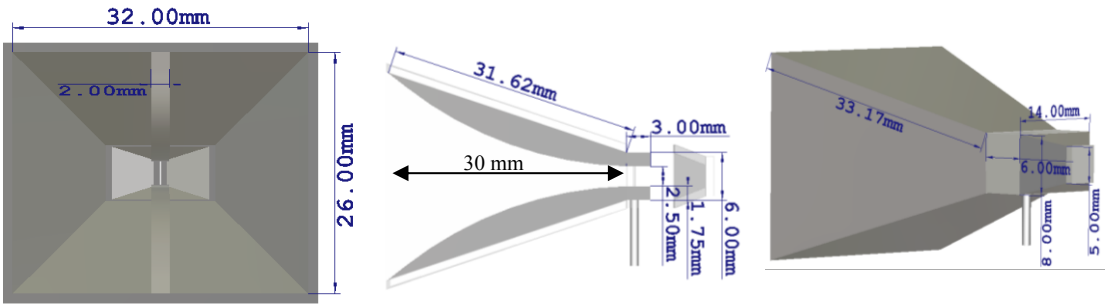

(a): Antenna front veiw (b): Antenna side veiw (c): Antenna Back veiw

Fig 4. 41: PDRH antenna dimensions in the mixture of the VLF-440 and r-TiO_2.

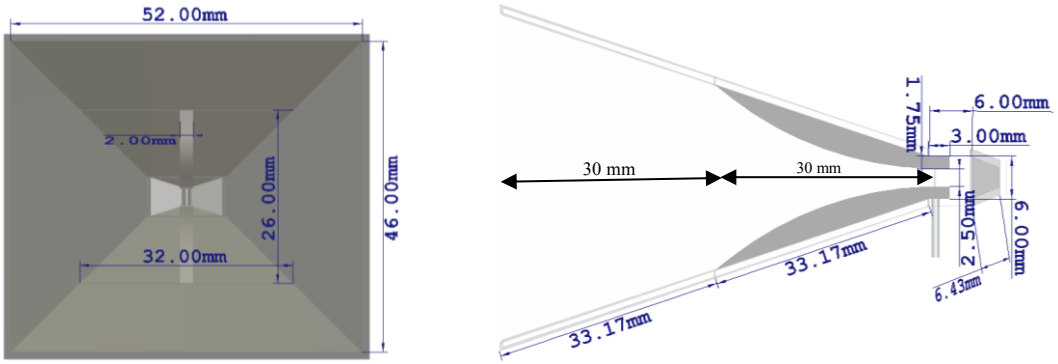

(a): The antenna front veiw (b): The antenna side veiw

Fig 4. 42: Extended PDRH antenna dimensions in the mixture of the VLF-440 and r-TiO_2.

The high dielectric mixture sample made and measured in Chapter 3 was fed in the CST software and was selected as background material in order to determine the design operation as shown in Fig. 4.43.

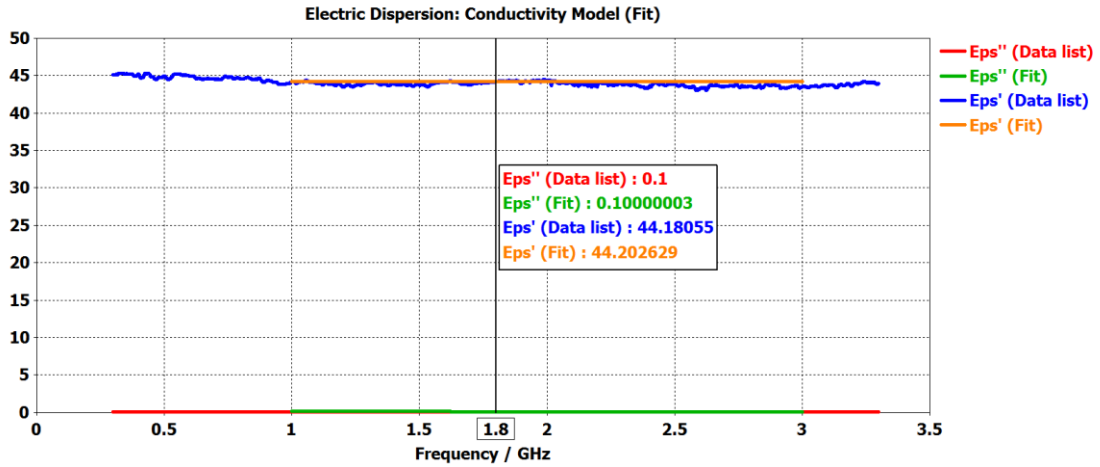

Fig 4. 43: Measured sample made of mixture of the VLF-440 and r-TiO_2 was fed into the CST software.

The reflection coefficient of the both designed antennas are determined using CST software and presented in Fig. 4.44 as follows.

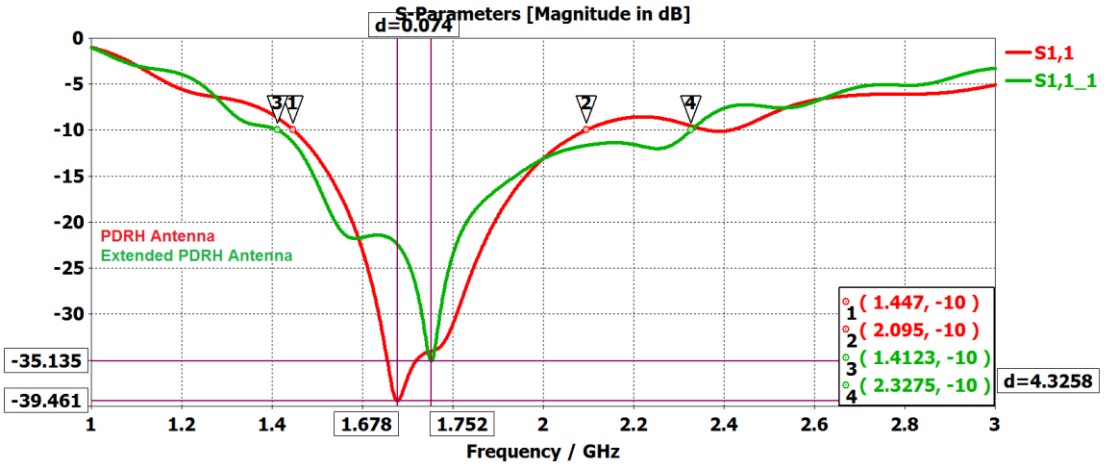

Fig 4. 44: Reflection coefficient results of the PDRH and extended designs in a mixture of the VLF-440 and r-TiO_2.

Fig. 4.44 represents the reflection coefficient results of the antennas (with and without the extension), which demonstrates that the bandwidth of the design with the extension increased by 267 MHz having a shift in the resonant point from 1.6 GHz to 1.75 GHz. Fig. 4.45 represents maximum gain over the interested frequency region. The extended design at 1.8 GHZ has approximately 4.5 dB higher gain as compare to the design with no extension.

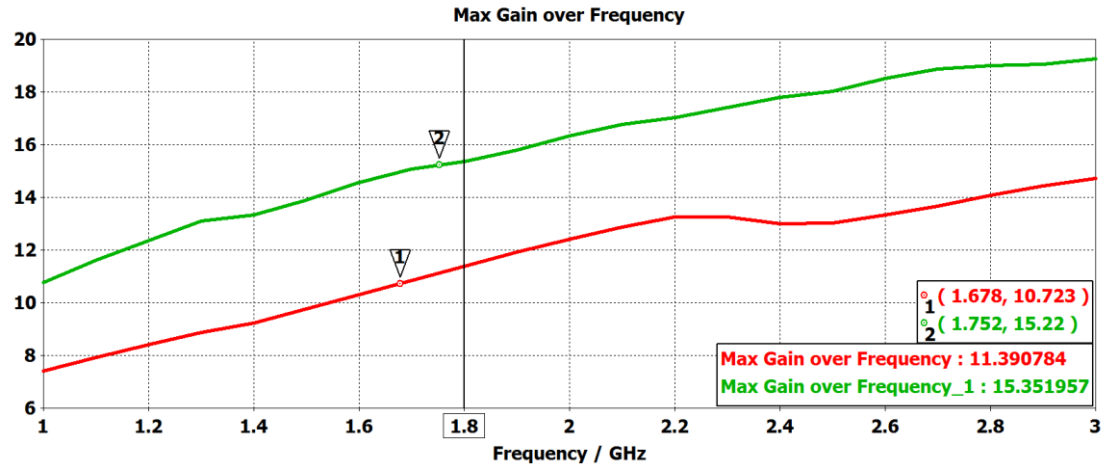

Fig 4. 45: Maximum gain results of the PDRH and extended antennas in the mixture of the VLF-440 and r-TiO_2.

Finally, the H and E-plane polar far field radiation patterns are presented in Fig. 4.46. they show the main lobe magnitude of 10.7 dB in the PDRH antenna case, which is increased to 15.2 dB in the extended design. Moreover, the main lobe direction for both the antennas are zero degree. The angular width at 3 dB point reduced in the case of the PDRH antenna compared to the extended case. All the results indicate the increase of

directivity in the extended case at the cost of increasing the SLLs, compared to the PDRH antenna design.

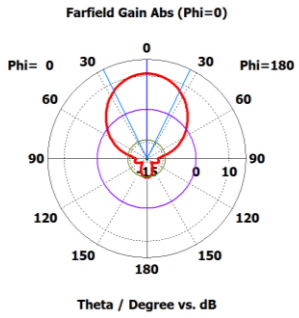

Frequency = 1.678
Main lobe magnitude = 10.7 dB
Main lobe direction = 0.0 deg.
Angular width (3 dB) = 51.9 deg.
Side lobe level = -20.0 dB

(a): H-plane polar pattern at 1.68 GHz.

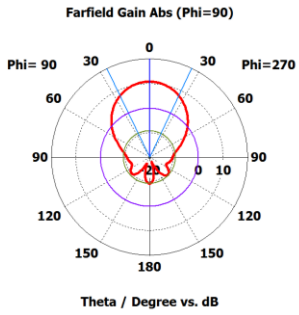

Frequency = 1.678
Main lobe magnitude = 10.7 dB
Main lobe direction = 0.0 deg.
Angular width (3 dB) = 51.0 deg.
Side lobe level = -20.0 dB

(b): E-plane polar pattern at 1.68 GHz.

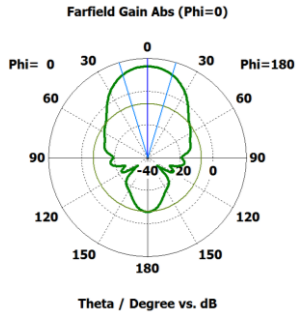

Frequency = 1.752
Main lobe magnitude = 15.2 dB
Main lobe direction = 0.0 deg.
Angular width (3 dB) = 33.4 deg.
Side lobe level = -22.4 dB

(c): H-plane polar pattern at 1.8 GHz.

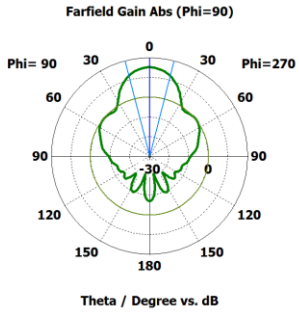

Frequency = 1.752
Main lobe magnitude = 15.2 dB
Main lobe direction = 0.0 deg.
Angular width (3 dB) = 29.0 deg.
Side lobe level = -15.1 dB

(d): E-plane polar pattern at 1.8 GHz.

Fig 4. 46: H and E-plane polar radiation patterns in the resonant regions.

4.1.3.6. EDRH ANTENNA DESIGN IN OPTIMISED CERAMIC

The EDRH antennas was designed and developed within the VLF-440 and r-TiO_2 mixture that has the same permittivity as of human skin, using CST software with the given dimensions shown in Fig 4.47.

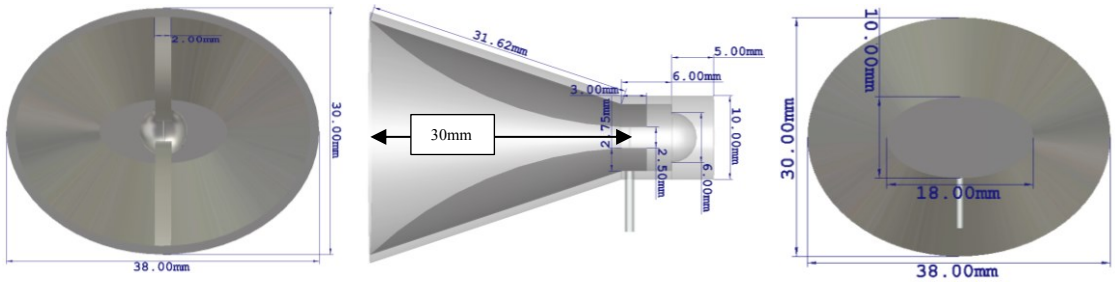

(a): Front veiw (b): Side veiw (c): Back veiw

Fig 4.47: EDRH antenna dimensions in the mixture of the VLF-440 and r-TiO_2.

The EDRH design was extended using equations 4-1a and 4-1b, which have been developed previously in this Chapter in order to place the antenna in the far field region of scanning modelled tissue, as presented in Fig. 4.48;

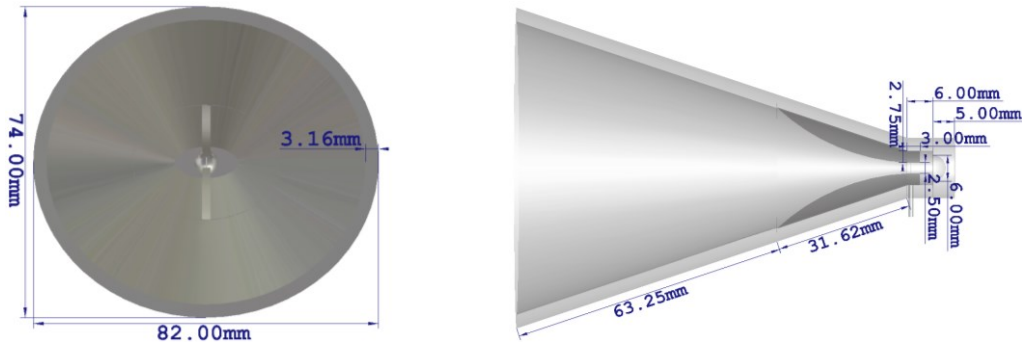

(a): Front veiw of the extended antenna (b): Side veiw of the extended antenna

Fig 4.48: Extended EDRH antenna dimensions in the mixture of the VLF-440 and r-TiO_2.

The next step was to feed the mixture data as background material and generate the S_{11} results using CST software.

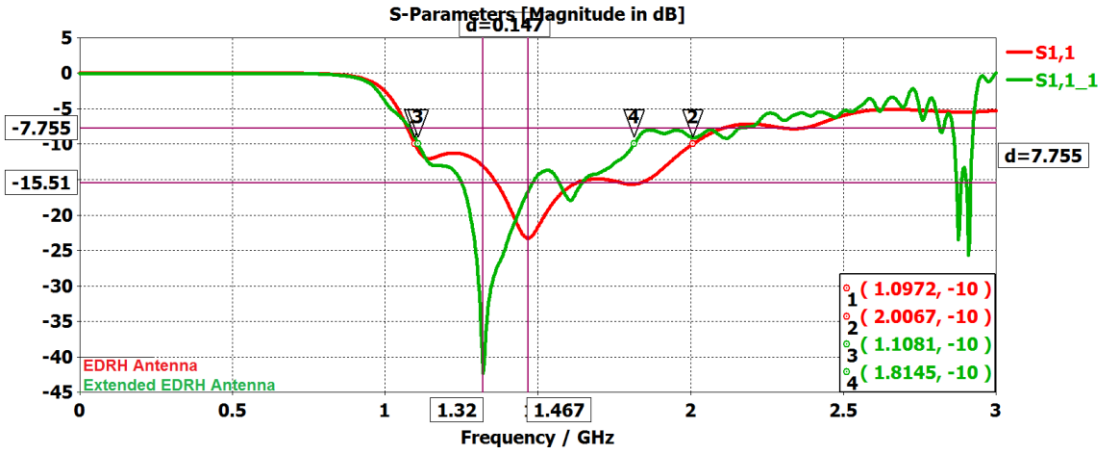

Fig 4. 49: Reflection coefficients of the EDRH and extended antennas in a mixture of the VLF-440 and r-TiO_2.

Fig. 4.49 represents the S_{11} results of both antennas, which indicates that the extended antenna has higher resonance point as well as reduced operation bandwidth by 203 MHz. Moreover, Fig. 4.50, which illustrates the gain of both designs over the frequency region of interest, indicates higher gain for the extended design compared to the design with no extension. This means that although the bandwidth of the antenna with extension is reduced, it has higher gain.

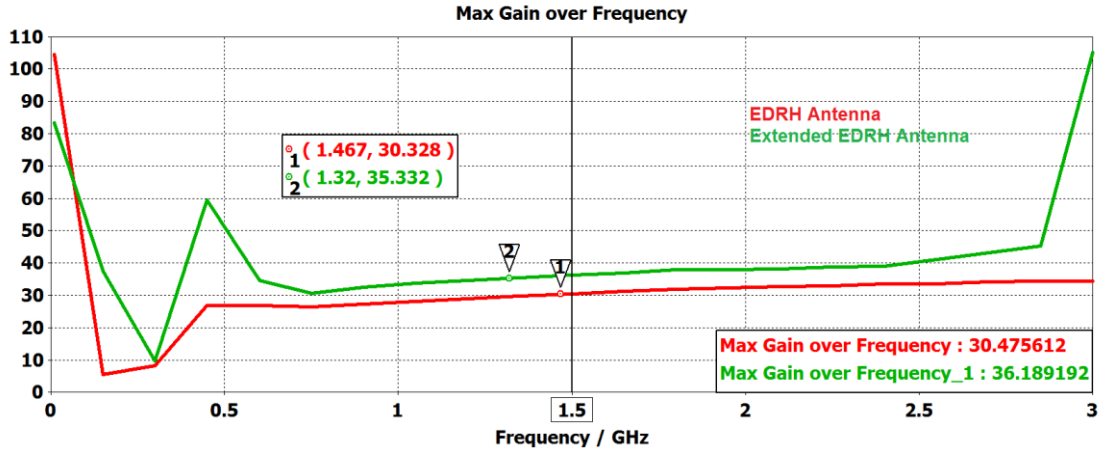

Fig 4. 50: Maximum gain results of the EDRH and extended antennas in the mixture of the VLF-440 and r-TiO_2.

The polar far field radiations of both designs in electric and magnetic field planes directions have been defined and shown in Fig. 4.51, which indicates the extended design has better directivity and gain due to its elliptical shape.

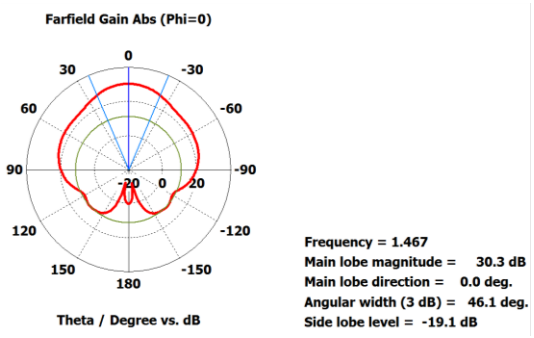

(a): H-plane polar pattern at 1.467-GHz.

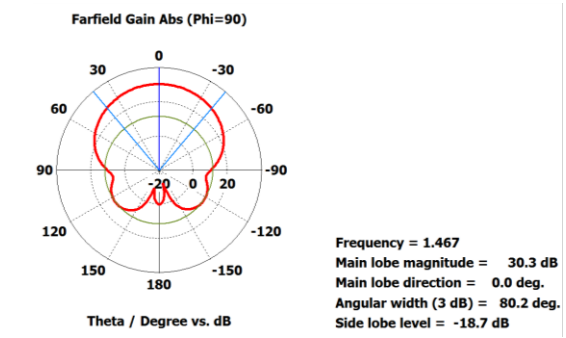

(b): E-plane polar pattern at 1.467-GHz.

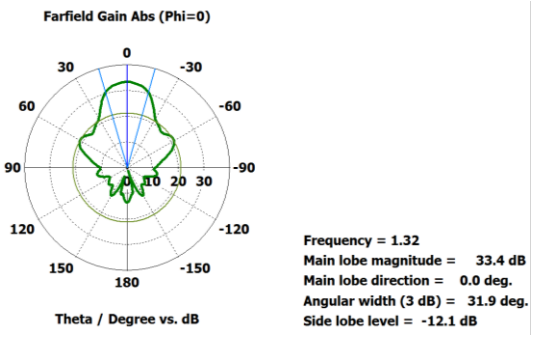

(c): H-plane polar pattern at 1.32-GHz.

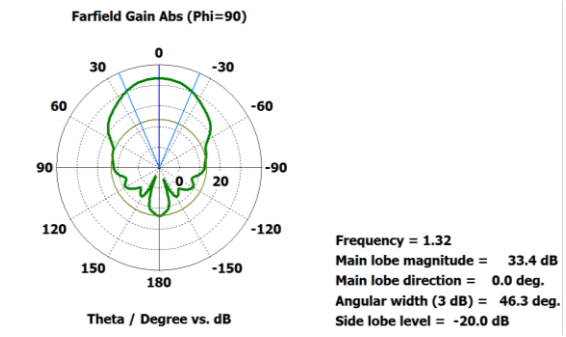

(d): E-plane polar pattern at 1.32-GHz.

Fig 4. 51: H and E-plane field polar radiation patterns in the resonant regions.

4.1.3.7. EXTENDED PDRH ANTENNA DESIGN IN DISTILLED WATER:

The EDRH antenna was redesigned in the distilled water with real measured dielectric properties given in Chapter 3. The distilled water created inside the CST software using the dispersion option from the real data as presented in Fig. 4.52 [12].

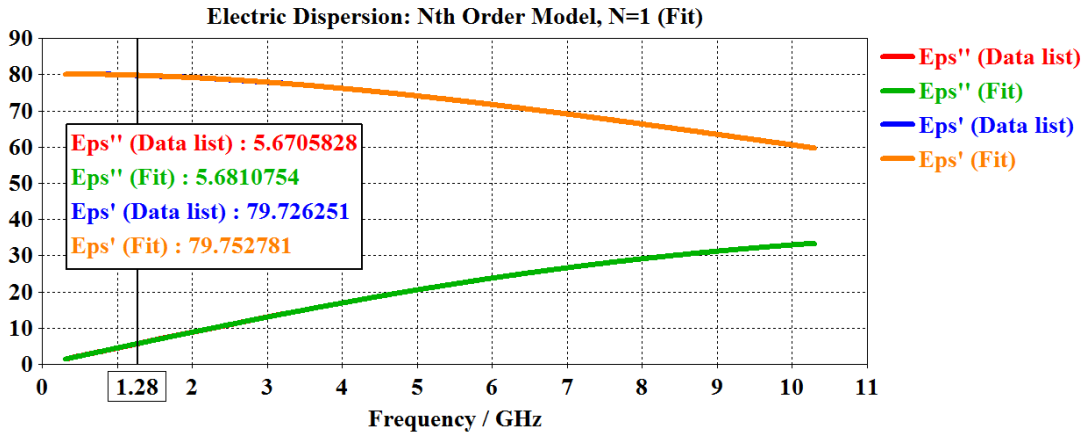

Fig 4. 52: The distilled water material created in the CST studio using the real distilled water data.

In order to avoid over-lapping and propagating plane wave to the scanning region by placing the antenna in the far field region, equations (4-1a, b) were redefined and employed. The wavelength of this design can be defined by equation (4-1a) and is calculated to be $\lambda = 22.4\,mm$ and the far-filed distance defined by (4-1b) is calculated to be $d_f = 91.4\,mm$.

Considering the far field distance, length of the extended aperture of the antenna should be increased to 60 mm. Therefore, the width and height of aperture were recalculated to be 72 and 66 mm by equation (4-2a, b) given early in this Chapter.

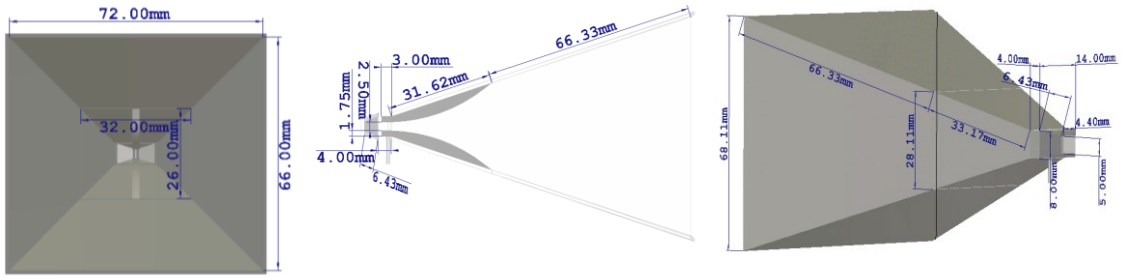

(a): Front view (b): Inside view (c): Back view

Fig 4. 53: PDRH antenna design dimensions using the real distilled water data.

Fig. 4.53 represents the design dimensions from all perspective viewes when the PDRH antenna design was extended and embedded in the distilled water with the permittivity of almost 80 within the frequency range (1−3.5 GHz) chosen for this design.

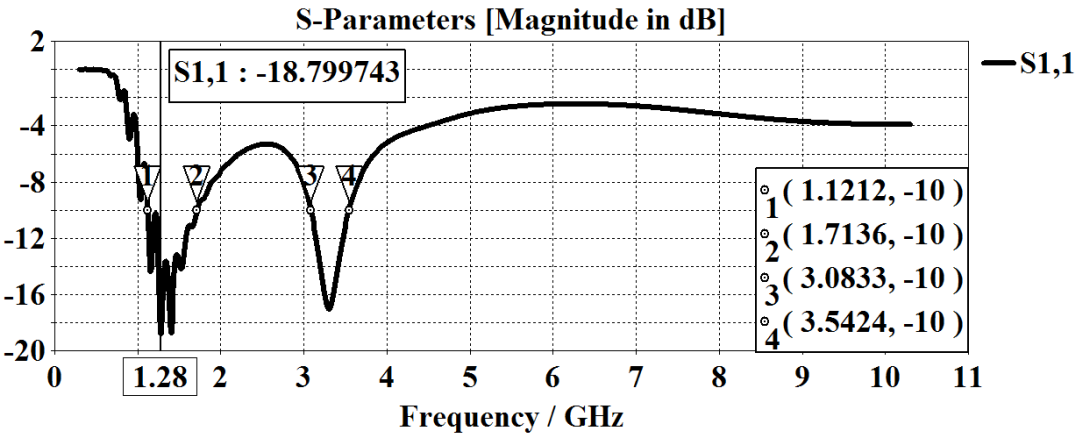

Fig 4. 54: S_{11} graph of the PDRH antenna design with an extension in the real distilled water data.

The S_{11} result as shown in Fig. 4.54 represents two resonant frequencies. The first resonant frequency, which takes place at 1.28 GHz, has provided a bandwidth of almost 600 MHz at −10 dB point. The other resonant frequency appears at 3.3 GHz and provides a bandwidth of 460 MHz at −10 dB.

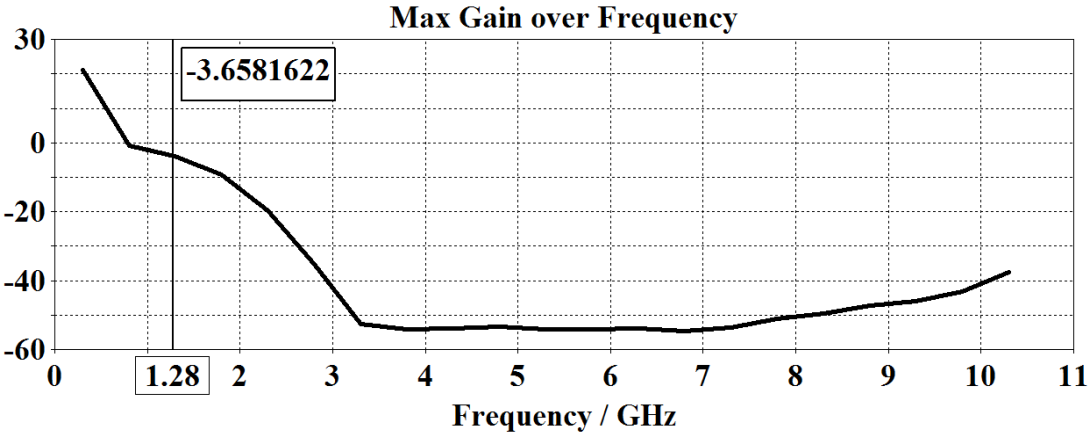

Fig 4. 55: PDRH antenna gain designed in distilled water over the frequency range of 0.5 to 10.5 GHz.

Fig. 4.55 represents the gain over the frequency range of interenst for the extended PDRH antenna design, which has been designed to operate within the distilled water. The results indicate that the antenna has acceptable gain for the frequencies below 500 MHz, which means the antenna dose not radiate above 500 MHz and the energy absorb within the antenna structure. This is due to the high conductivity of the distilled water that cause the system not operating within the frequency of interest.

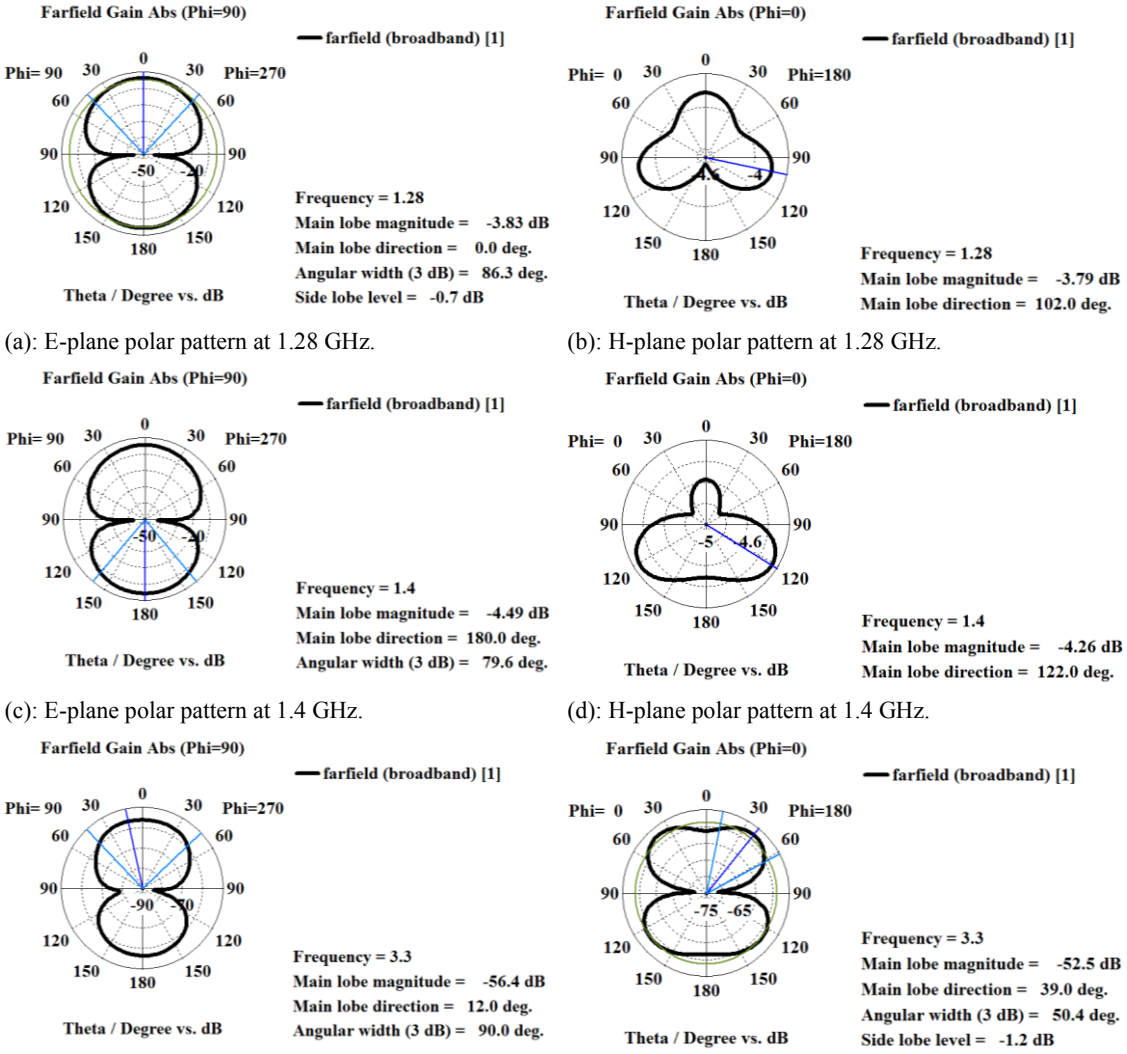

(a): E-plane polar pattern at 1.28 GHz.

(b): H-plane polar pattern at 1.28 GHz.

(c): E-plane polar pattern at 1.4 GHz.

(d): H-plane polar pattern at 1.4 GHz.

(e): E-plane polar pattern at 3.3 GHz.

(f): H-plane polar pattern at 3.3 GHz.

Fig 4. 56: E and H-plane field polar radiation patterns in the resonant regions.

The far-field polar radiation patterns shown in Figs. 4.56 (a-f), represent the directivity of the extended PDRH antenna design in distilled water for all the resonant frequencies. This indicates that the E and H-plane field radiation patterns are not directional and energy is radiated in both the front and back direction as well as side in the H-plane field patterns. This confirms that distilled water approach is not satisfactory and the design was not employed due to high conductivity and therefore high-energy absorption.

4.1.3.8. EXTENDED PDRH ANTENNA DESIGN IN DEIONISED WATER:

In this part, the functionality of the extended PDRH antenna in the deionised water that has lower conductivity compared to distilled water is investigated. The deionised water dielectric properties measured in Chapter 3 are employed to create the deionised water in the CST studio using dispersion user define data as represented in Fig. 4.57 [12].

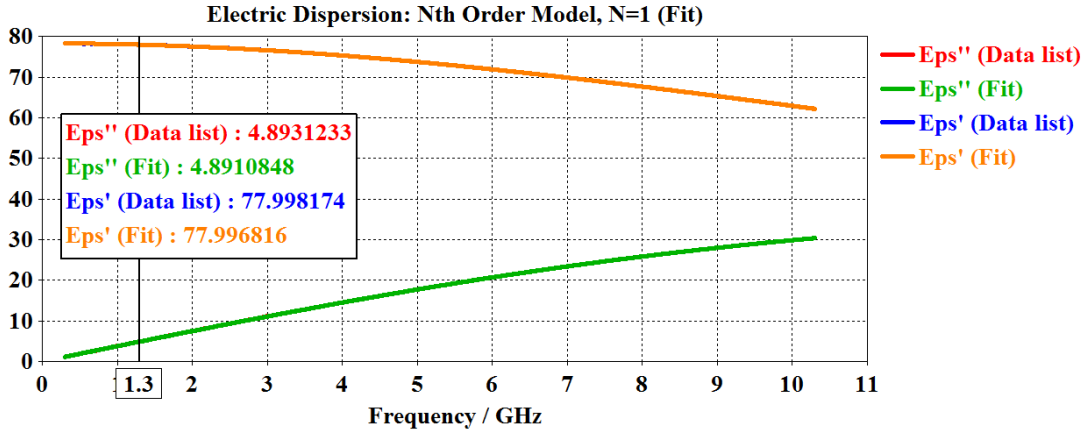

Fig 4. 57: The deionised water material created in the CST studio using the real deionised water data.

The data for the deionised water represents lower permittivity of 78. Moreover the conductivity of deionised water is reduced by 0.1 S/m compared to the distilled water in the frequency range of interest. Concerning the permittivity of the deionised water, it has not much difference compared to the distilled water using the same design as shown in Figs. 4.57, where the background material is replaced with deionised water and functionality is obtained and observed.

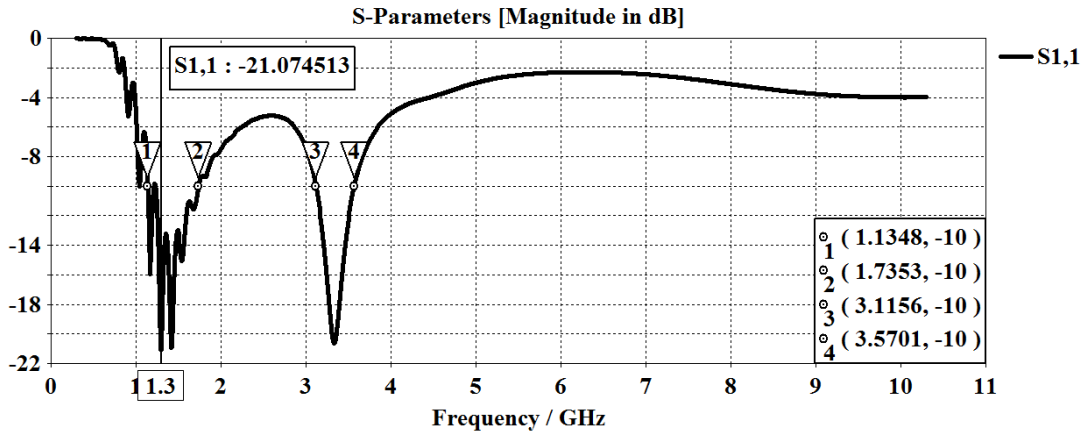

Fig 4. 58: S_{11} graph of the PDRH antenna design with an extension in the real deionised water data.

The S_{11} results shown in Fig. 4.58, represents no improvement when the deionised water used, compared to the previous design where the distilled water employed in the design. The results represents unstable reflection coefficient that may be resulted to the high conductivity and absorption rate of the deionised water.

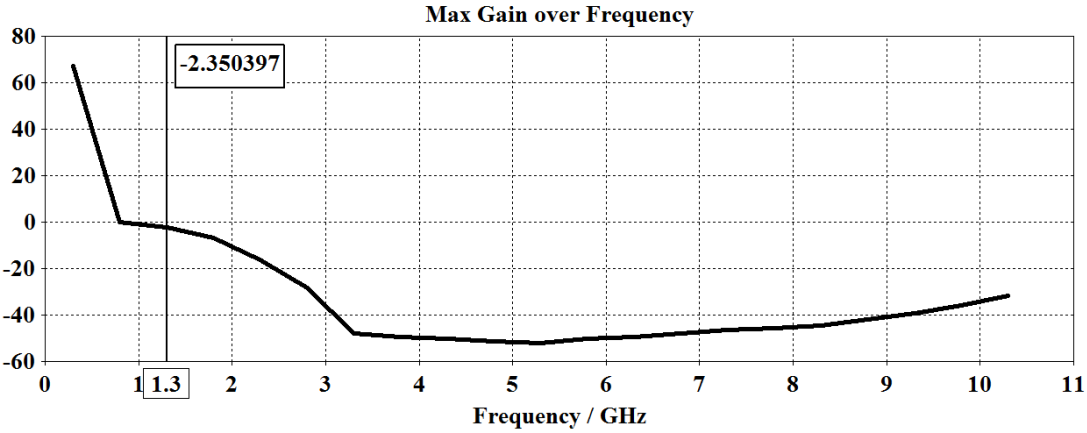

Fig 4. 59: PDRH antenna gain designed in the deionised water over the frequency range of 0.5 to 10.5 GHz.

The maximum gain over the frequency region (i.e. 0.3-10.3 GHz) for the deionized water design was improved as shown in Fig. 4.59. This indicates that the design is not operated in the frequency range of interest due to energy absorption within the design structure, however, there is a slight increase in the operational band to 750 MHz compared to the distilled water design.

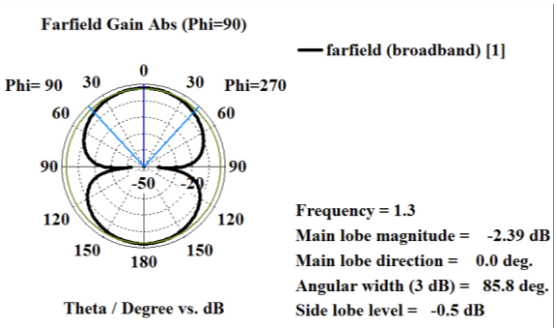

(a): E-plane polar radiation pattern at 1.3 GHz.

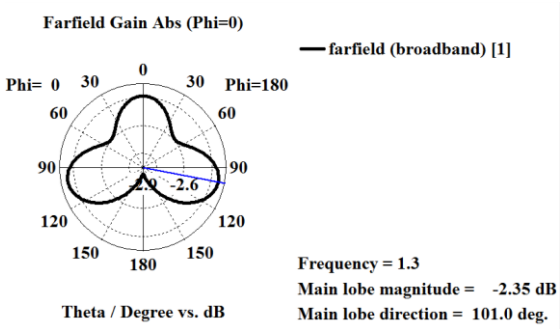

(b): H-plane polar radiation pattern at 1.3 GHz.

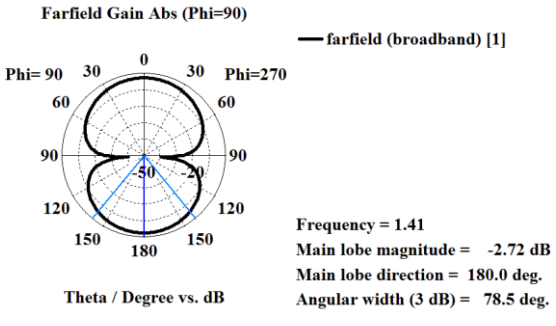

(c): E-plane polar radiation pattern at 1.41 GHz.

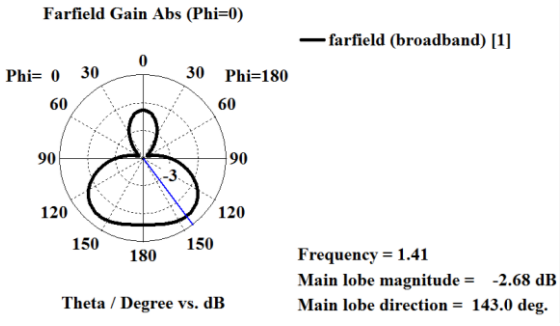

(d): H-plane polar radiation pattern at 1.41 GHz.

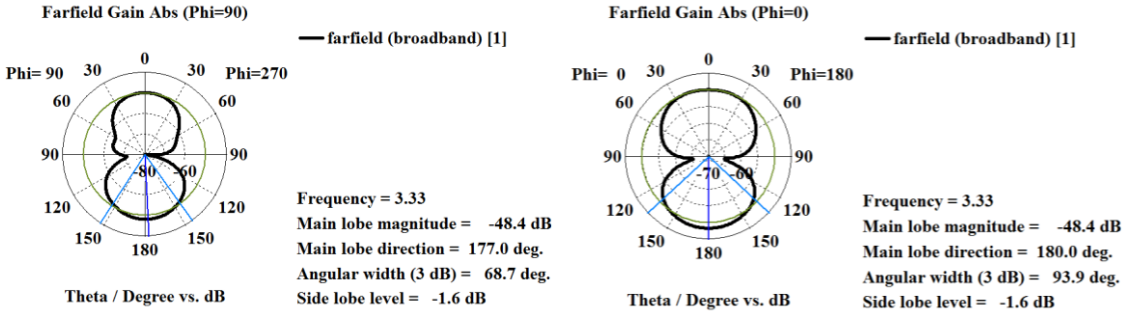

(e): E-plane polar radiation pattern at 3.33 GHz. (f): H-plane polar radiation pattern at 3.33 GHz.

Fig 4. 60: E and H field polar radiation patterns in the resonant regions.

The E and H field radiation patterns in the resonant frequencies demonstrated in Figs. 4.60 (a-f) represent a poor directive pattern same as the previous design in the distilled water. The results presented here prove that by removing ions from the water, the conductivity reduces slightly, but not enough for the wave to radiate through.

Therefore, the water is not a good choice for this system design. Different types of the detergents and glycerol characterised in Chapter 3, were used to develop the antennas in the mixtures. However, they failed to operate because of their high conductivity and energy absorption within the antenna region after the wave excited.

4.1.3.9. EXTENDED PDRH ANTENNA DESIGN IN THE MIXTURE OF LINSEED OIL AND TITANUIM OXIDE:

The next phase of the investigation was to use liquid oil for the antenna design due to low conductivity of the oil [13]. Various types of liquid oils were characterised in Chapter 3 and linseed oil was selected based on its high permittivity. Moreover, the linseed oil was mixed with the r-TiO_2 in order to increase the permittivity and keep the conductivity as low as possible. Furthermore, the best mixture ratio chosen, which enabled to easily remove the air bubbles by shaking the mixture was found to be 30 ml of the linseed oil and 40 mg of the r-TiO_2.

The permittivity of the mixture measured by conventional open-ended probe was found to be almost twice that of the linseed oil (i.e. ε_r~5.26 at 1.8-GHz), and slightly higher conductivity. The dimensions of *E*- and *H*- planes of a PH have been determined based on the dielectric material and the equations presented in the seminal antenna textbook [3]. The antenna has been designed based on the calculated parameters, in order to operate within the desired frequency of operation (1 to 8 GHz).

Fig. 4.61 presents the modelling of the proposed antenna based on the measured mixture of the material data (i.e., linseed and r-TiO_2) loaded into the software as a new material by using the user dispersion option, as well as the time-domain transient solver. The next stage of the antenna design is to propose a solution for the device to be located in the far-field EM region of the targeted area of the body. This has been performed for the plane-wave to penetrate more into the tissue.

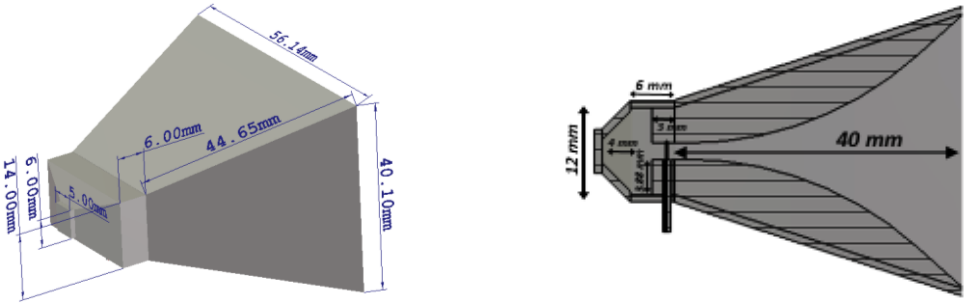

(a): Outside view perspective (b): Inside view perspective

Fig 4. 61: Dimensions of the modelled PDRH design, when immersed in a mixture of the linseed oil and the r-TiO_2.

In addition, equations (4-1a and b) have been used to define the design wavelength followed by the far-field distance of the system (i.e., d_f). The calculated wavelength is 74 mm and is obtained based on the operating frequency of 1.8 GHz, and the measured material permittivity properties. The far field distance is also calculated according to Fig. 4.62 (a) and (b), which are defined based on the obtained wavelength (λ) and largest section of the design dimensions. The high-dielectric PDRH antenna has been extended with the pyramidal aperture length of 40 mm, based on the equations (4-2a and b), in order to maintain the primary design antenna objectives, as shown in Fig. 4.62. This was to define the outer aperture of extended part, when the length of the extension changes.

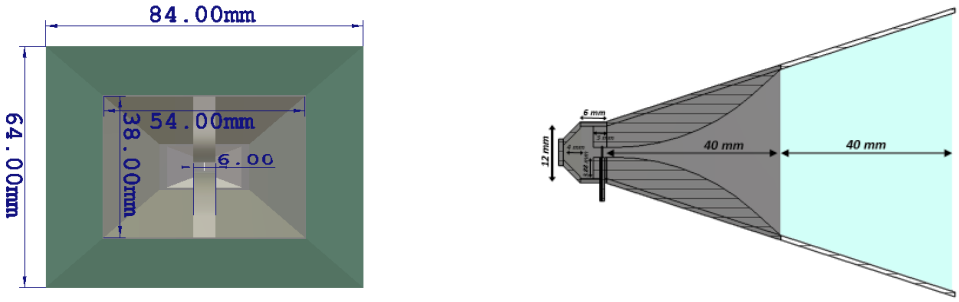

(a): Outside view perspective (b): Inside view perspective

Fig 4. 62: Dimensions of the extended PDRH design, when immersed in a mixture of the linseed oil and the r-TiO_2.

The developed mixed material has also been chosen as the background material in the CST software, in order to effectively evaluate the antenna performance inside the dielectric medium. As such, the primary figures of merit for the evaluation of the

proposed antenna, including the reflection coefficients based on the scattering (S)-parameters, gain, and EM radiation patterns, have been obtained.

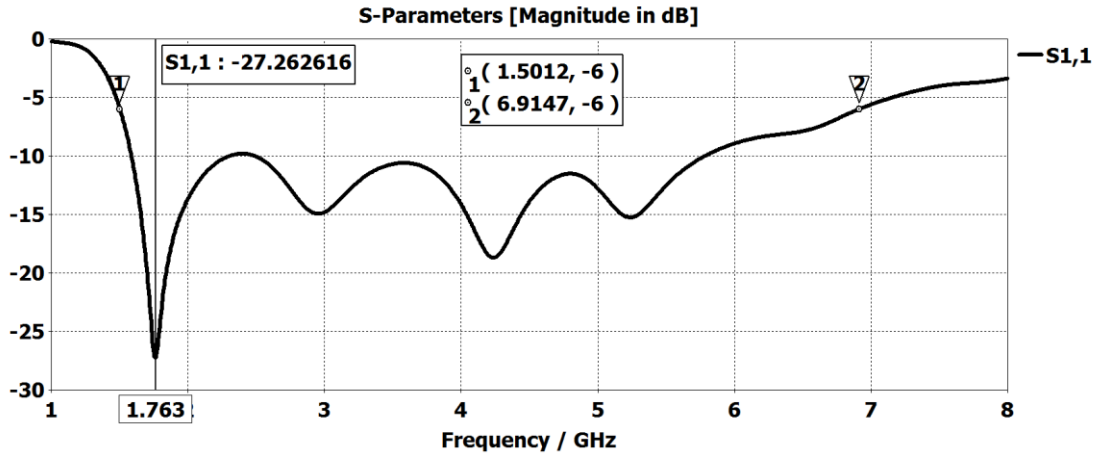

Fig 4. 63: Simulated S_{11} when the antenna is inside the proposed material (Linseed oil and r-TiO_2).

The reflection coefficient (i.e., S_{11}) results shown in Fig. 4.63 present the wide operating bandwidth of 5.41 GHz from 1.5 to 6.91 GHz, taking –6 dB as a reference; commonly defined for the on-body applications, as well as the large resonant at a low frequency of 1.77 GHz . Fig 4.64 represents the maximum gain over the frequency region of interest (1 - 8 GHz) generated by the CST software that indicates the gain of 5.7 dB at first large resonant point (1.763-GHz).

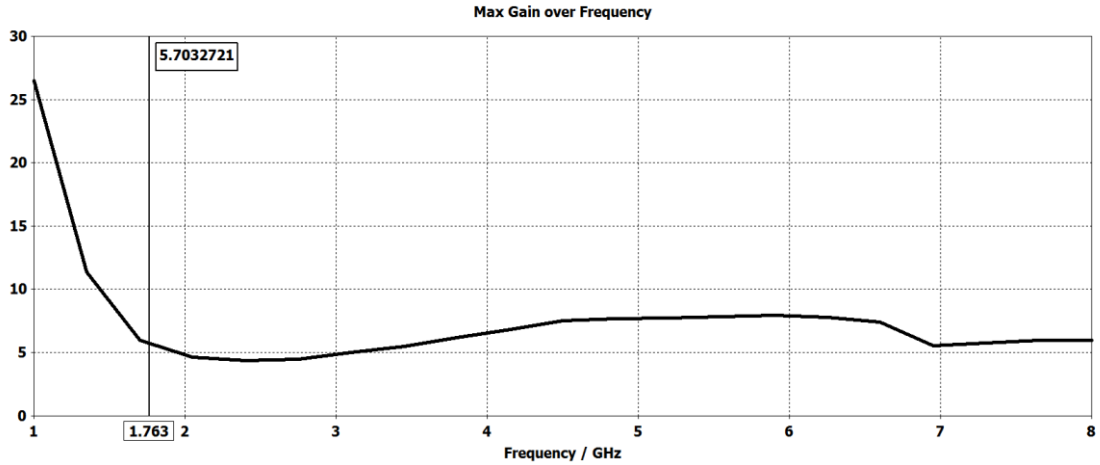

Fig 4. 64: Simulated S_{11} when the antenna is inside the proposed material (Linseed oil and r-TiO_2).

In addition, Fig. 4.65 shows the H and E radiation patterns, in polar form, and the gain at the resonant point (i.e., 1.77 GHz). This further depicts the gain of 2.92 dB in the zero degree at the antenna front-end and the gain of 5.29 dB at the antenna back-end. The higher gain in the back-end was caused by the dielectric properties of the material that was selected as the background material in the modelling and simulation.

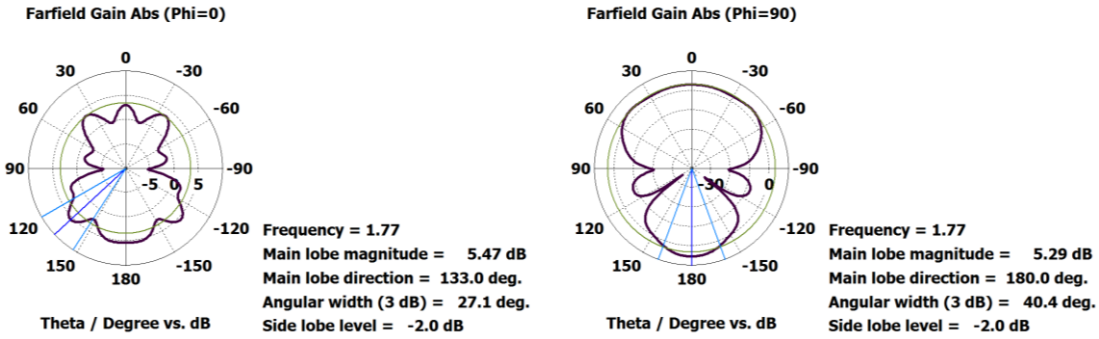

(a): H-plane polar radiation pattern at 1.7 GHz. (b): E-plane polar radiation pattern at 1.7 GHz.

Fig 4. 65: H and E-plane field polar radiation patterns in the resonant regions.

In order to improve the directivity of the design, [14] has proposed to utilize a sheet of graphene in the lower- and upper-flare extensions of the antenna to reduces the SLLs and hence to increase the directivity. In this regard, a thin, flexible, and magnetically loaded silicone microwave absorbing material sheet (i.e., ECCOSORB FGM-40) was selected to employ as part of the high-performance design of the proposed antenna. Hence, the dielectric properties of this sheet was measured using the open-ended probe method and loaded into the software-based modelling of the system. The measured dielectric properties of this absorber sheet can be found in Figs. 3.20 (a) and (b). Based on the measured data, the absorber sheets were modelled in the CST software and have been attached to both the lower- and upper-outer extended flares of the antenna. These parts are the locations of the ridges, which the EM wave is propagating through, as in Fig. 4.66.

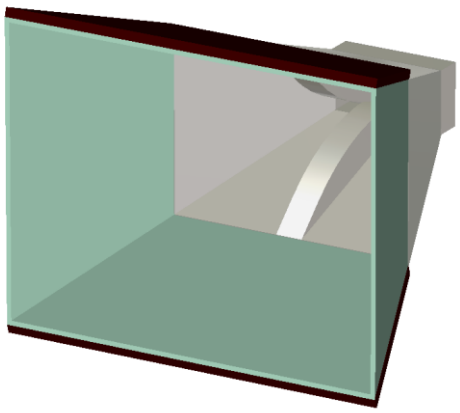

Fig 4. 66: Extended PDRH antenna (with the absorber) immersed in the mixture, as the proposed background material for the EM modelling.

Moreover, Fig. 4.67 (b) shows that the effects of the absorber on the frequency of operation is negligible, due to a minor frequency shift for the first large resonant point ~20 MHz, and a slight increase in the bandwidth ~10 MHz.

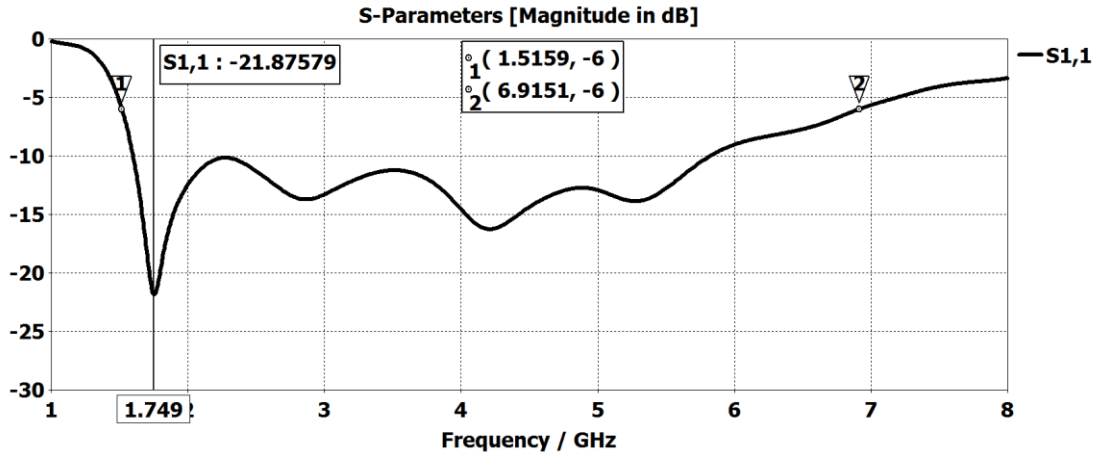

Fig 4. 67: Simulated S_{11} when the absorber sheet attached to the upper and lower flare of the extended PDRH antenna.

Fig. 4.68 represents the maximum gain over the frequency of the interest (1-8 GHz) for the design with the absorber attached to it that was generated by the software. The results indicates more or less the same gain over the frequency as the design with no absorber.

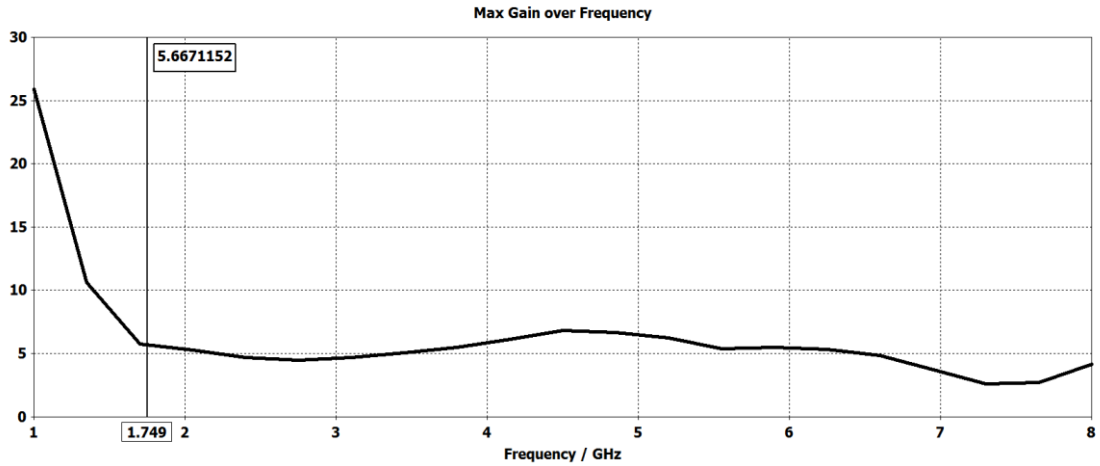

Fig 4. 68: Maximum gain over the frequency range of 1 to 8 GHz for the design when the absorber sheet attached to the upper and lower flare of the extended PDRH antenna generated.

Moreover, the H and E far-field radiation patterns represents a significant effect on the directivity and gain of the antenna, as in Fig. 4.69. The antenna gain increased to 5.39 dB, and the SLLs reduced, exhibiting an improved directivity of the main lobe, compared with the case without the absorber.

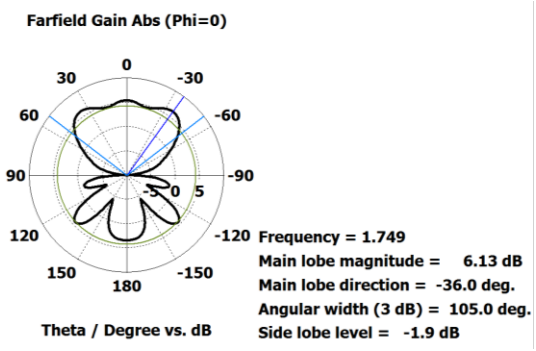

(a): H-plane polar radiation pattern at 1.7 GHz.

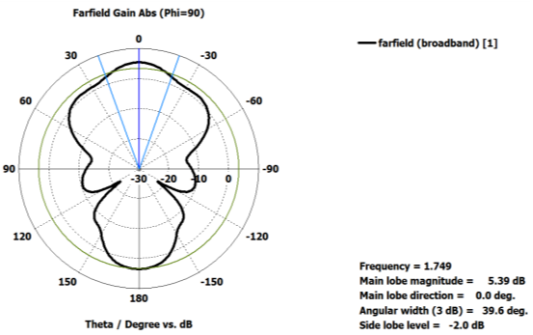

(b): E-plane polar radiation pattern at 1.7 GHz.

Fig 4. 69: H and E-plane field polar radiation patterns in the resonant regions.

4.1.3.10. EXTENDED EDRH ANTENNA DESIGN IN THE MIXTURE OF PARAFFIN AND TITANUIM OXIDE:

After more literature review on the materials with high permittivity and low conductivity, to replace the liquid oil with an alternative solid material due to unsuitability of using a liquid for the system, paraffin is purposed as better solution in this section to be replaced with the liquid oil. The paraffin was chosen as preliminary material due to the advantages this material has such as solubility, flexible fixed shape, and low conductivity compared to others. The measured dielectric properties of the paraffin, shown in Figs. 3.19 (a) and (b) presents the low conductivity as well as not high permittivity at the frequency of 3.1 GHz (ε_r~2.16 & σ~0.003).

In order to increase the permittivity of the paraffin, it was mixed with the r-TiO_2 that has a high permittivity and low conductivity. However, the conductivity of the mixture may increase to some extent compared to r-TiO_2 conductivity, but the conductivity is still in the acceptable range, which does not disturb the wave propagation.

The centre frequency of 3.1 GHz is chosen for the proposed system based on the tissue penetration capability, and the required antenna bandwidth that increases the range resolution. Consequently, the dielectric properties of the materials were measured in the frequency range of 1 to 8 GHz. The ideal Three portions of the r-TiO_2 (60g) was mixed with two portions of the paraffin (40g) in the liquid form at 70ºC and left to cool down. This has produced the white solid shape material, with the measured dielectric properties, using the open-ended probe method in the range of 1–8 GHz; as shown in Figs. 3 (a) and (b). The measured permittivity of the mixture is more than twice as the paraffin with a slightly higher conductivity at the frequency of 3.1 GHz (ε_r~5.4 & σ~0.004). The proposed medium for the developed antenna has a permittivity of 5.4 at 3.1 GHz;

therefore, the impedance of the medium can be defined using (4-1a, b) as 160.75 ohms; i.e., reduced by less than half compared to the free-space case.

The *E*- and *H*- planes dimensions of the elliptical design filled with the dielectric material were determined by the equations presented in the seminal antenna textbook [3]. The antenna design based on the defined parameters in the pyramidal design. Furthermore, it is optimised, in order to operate within the desired frequency of operation as set in the software shown in Table 4.1.

Table 4. 1. Antenna parameters dimensions.

Section Name	**Size (mm)**	**Section Name**	**Size (mm)**	**Section Name**	**Size (mm)**
Waveguide (Inside)	$r_w \times r_h \times l$ 12×6×6	Back (Outside)	$r_w \times r_h \times l$ 14×8×7	Flare (Inside)	$r_w \times r_h \times l$ 27×19×40
Waveguide ridges	w×l×h 6×4×4.7	Backspace (Inside)	r_b 5	Flare ridges	w×l 6×42.72
Waveguide ridges gap	h 2.5			Extended Flare	$\mathbf{r_w \times r_h} \times l$ 42×32×40
Connector diameters	r_c 0.4699	Connector heights	r_h 30		

Figs. 4.70 presents the modelling of the proposed antenna based on the measured mixture of the material data (i.e., paraffin and r-TiO_2) loaded into the software as new material by using the user dispersion option, as well as the time-domain transient solver.

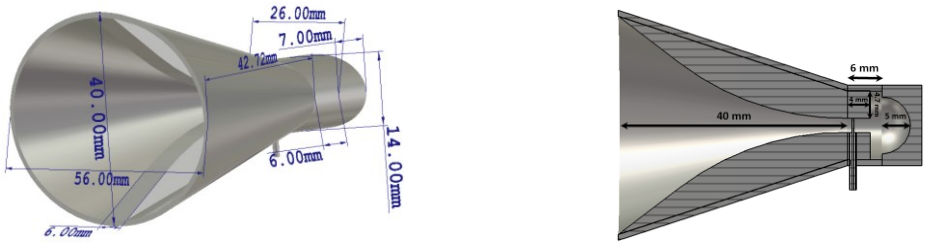

(a): Outside view perspective (b): Inside view perspective

Fig 4. 70: Modelled EDRH antenna, with the aperture dimensions.

In order to achieve the objective of the system, which is to locate the antenna in the EM far-field region for the propagation of the plane-wave, and furthermore to produce a delay for avoiding the overlapping issue.

The optimal approach is to extend the outer aperture of the antenna to the defined length so the scanning tissue area is placed in the far-field region. This might have added more

complexity to the fabrication and realization of the device, with the increased cost, but on the other hand, it has made the antenna more stable in its operation, and mostly free of any destructive interference signals and noise.

In addition, equations (4-1a, b) have been used to define the design wavelength followed by the far-field distance of the system (i.e., d_f). The wavelength is calculated as 74 mm and is obtained based on the operating frequency of 3.1 GHz, and the measured material permittivity properties.

The far field distance was also calculated according to equations (4-1a, b), which are defined based on the obtained wavelength (λ) and largest section of the design dimension (i.e., D). The wavelength of this design can be defined by equation (4-1a) and is calculated to be $\lambda = 64\ mm$ and the far-filed distance defined by (4-1b) is calculated to be $d_f = 91\ mm$.

The high-dielectric EDRH antenna extended with the pyramidal aperture length of 40 mm, based on equations (4-2a, b), in order to maintain the primary design antenna objectives, as shown in Fig. 4.71.

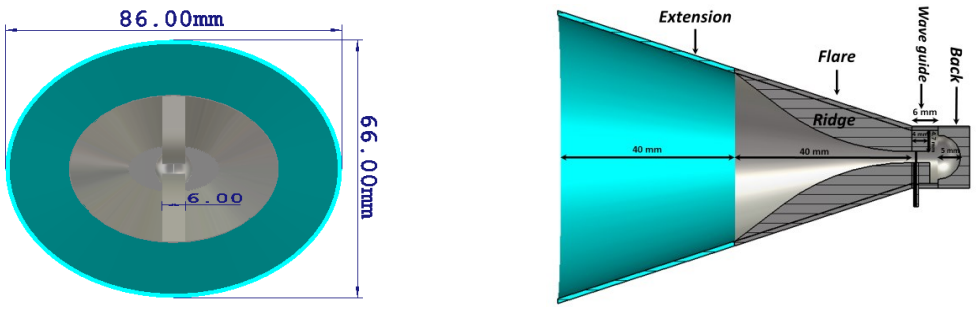

(a): Outside view perspective (b): Inside view perspective

Fig 4. 71: Aperture dimensions of the modelled extended EDRH antenna.

The developed mixed material was chosen as the background material in the CST software, to evaluate the antenna performance inside the dielectric medium effectively.

As such, the primary figures of merit for the evaluation of the proposed antenna, including the reflection coefficients based on the scattering (S)-parameters, gain, and EM radiation patterns, have been obtained and further shown in Figs. 4.72 (a) to (d).

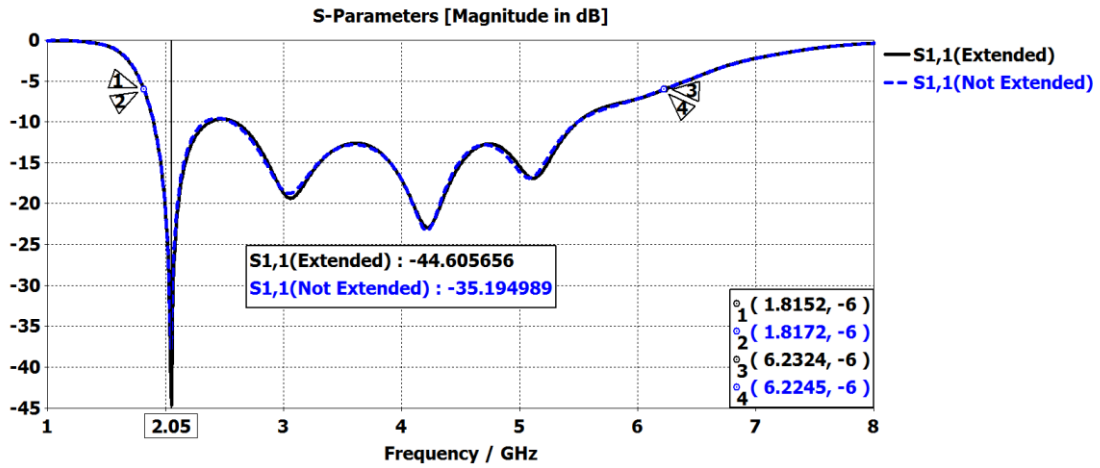

Fig 4. 72: Simulated S_{11} when the antenna is inside the proposed material.

The extended EDRH antenna design dimensions in the mixture are shown in Fig 4.71. Moreover the reflection coefficient (i.e., S_{11}) results for the antenna obtained and shown in Fig. 4.72 presents the wide operating bandwidth of 4.4 GHz from 1.82 to 6.22 GHz, taking –6 dB as a reference. Where in the extended design, the results represent the slight increased bandwidth to 4.41 GHz at –6 dB point. The -6 dB is in line with other biomedical application [15]. The design was optimized to operate at (-10 dB) to account for worst-case scenarios

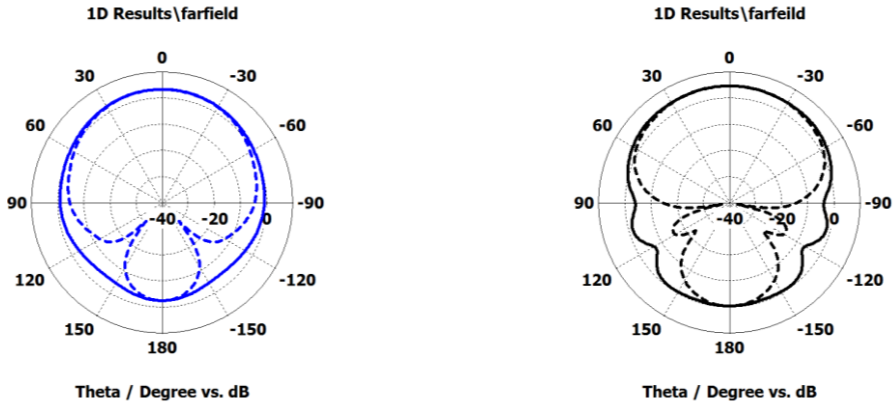

(a): Antenna Design (b): Extended Antenna Design

Fig 4. 73: H-plane polar (solid line) and E-plane polar (dashed line) far-field radiation patterns of the antennas, at the 3.1 GHz frequency with -6 and -5.2 dB sidelobe levels.

In addition, Figs. 4.73 shows the polar radiation patterns, in the magnetic and electric field direction (Phi = 0º & 90º) at the antenna front-end that demonstrates slight SLLs. Where in the extended design, the results represent an increase in directivity as well as the SLLs at 3.1 GHz in the magnetic and electric field direction at the antenna front-end.

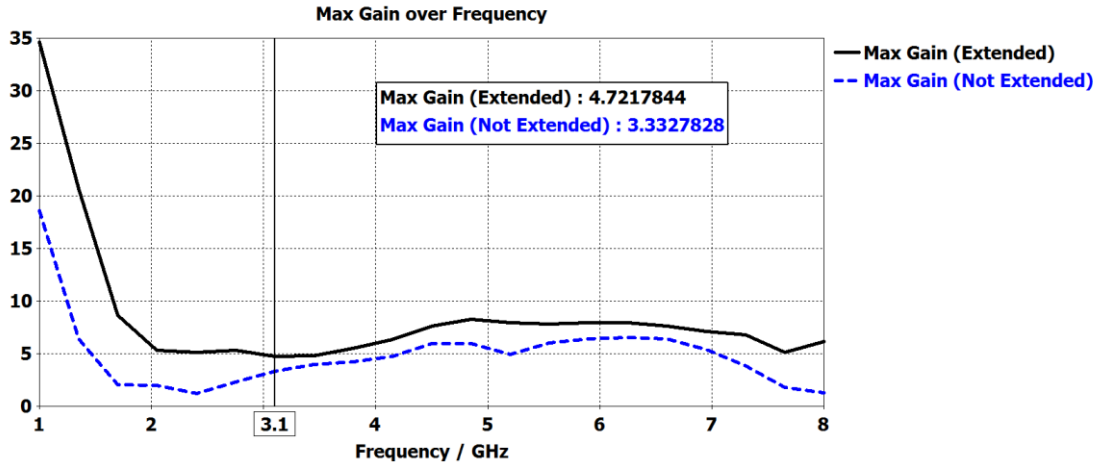

Fig 4. 74: Gain over the frequency range of 1 to 8 GHz for both the EDRH and extended EDRH designs.

Fig. 4.74 presents the gain of the design over the operating frequency range (i.e., 1 to 8 GHz). This further depicts the minimum gain of 1.2 dB at 2.4 GHz and the maximum gain of 6.5 dB at 6.25 GHz for the EDRH antenna design. Where in the case of extended design, depicts significant increase in the gain over the operating frequency with a minimum gain of 4.72 dB at 3.1 GHz and maximum gain of 8.26 dB at 4.85 GHz compare to the design with no extension.

4.1.4. DRH ANTENNA IMPEDANCE MATCHING

The impedance matching is an important parameter in any antenna design. If an antenna is not matched most of the energy will reflect back when it is exited from the connector into the design structure. This is important in the design such as the horn antenna design filled with high dielectric. Therefore, the design was partially tested to check the operation of the design in each independence section.

4.1.4.1. IMPEDANCE MATCHING IN THE WAVEGUIDE

Previously in this Chapter, the concept of impedance matching for the DRH antenna design based on the ridges and the tappers design dimensions were employed using the equations (3-4 a to d) in Chapter 3. In this part of the thesis, to support the equations given, the simulation results were generated to demonstrate the design matching within the waveguide section of the antenna design [4].

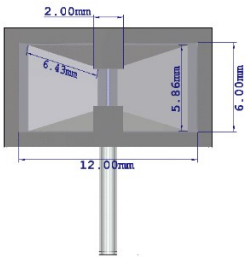

(a): Front view perspective

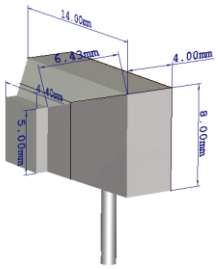

(b): Back view perspective

Fig 4. 75: DRH waveguide design dimensions using the ideal high dielectric (41).

Figs. 4.75 represented the DRH waveguide design section filled with the created ideal material with the permittivity of 41 and the conductivity of 0.1S/m. Two ports were placed, one at connector point and one to the outer aperture of the waveguide, in order to represent the impedance matching of this part of the horn design [16].

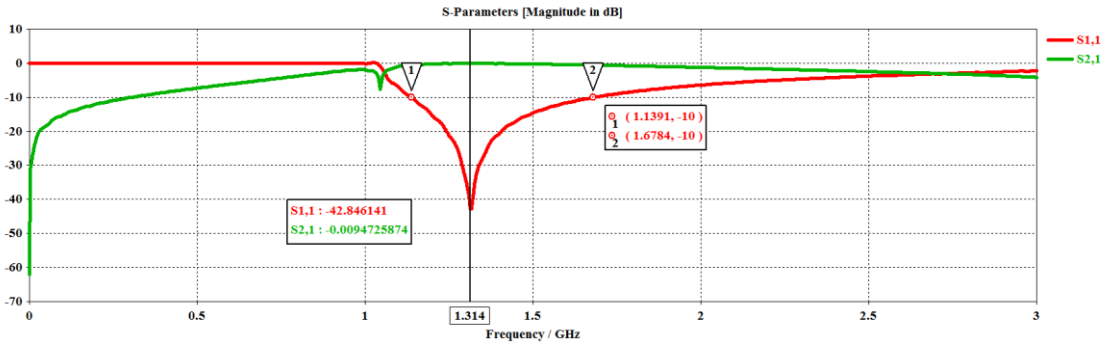

Fig 4. 76: S_{11} graph over the frequency range of 0 to 3 GHz.

S_{11} graph shown in Fig. 4.76, represents that the waveguide has the acceptable operation within the frequency range of 1.14 to 1.68 GHz that is almost 500 MHz of bandwidth. The S_{11} graph drops below −10 dB point and the S21 is nearly zero that represents; this part of the antenna operates well in response to impedance matching.

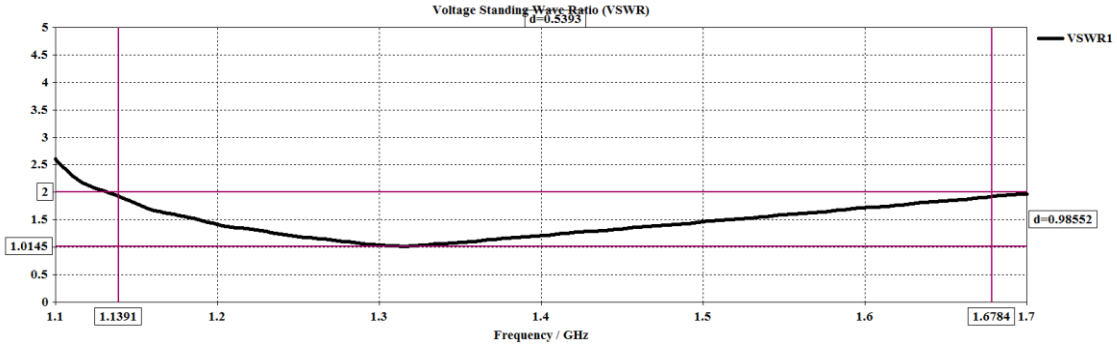

Fig 4. 77: Voltage standing wave ratio (VSWR) graph at the operating frequencies of 1.139 to 1.67 GHz.

Fig. 4.77 represents the VSWR graph, which indicates that this part operates well in the interested frequency range (1.14-1.68GHz), as the graph stays below 2 within the given frequency range.

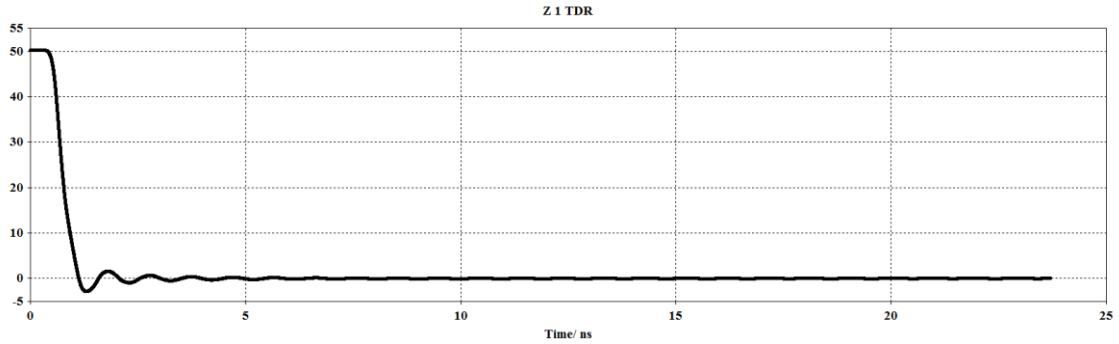

Fig 4. 78: Time domain refectory (TDR) graph at zero to 25ns time.

The time domain refectory (TDR) graph shown in Fig. 4.78 above represent the smooth transaction of the energy over the time of 0 to 25 ns from the impedance of 50 to 0 ohms. This explain the matching capability of the design.

4.1.4.2. IMPEDANCE MATCHING IN CONNECTION PIONT

In this section, the error that can be produced during the fabrication process are analysed. Such as, when the antenna was designed in the ideal environment within the software (CST Studio) with no air gap. An air gap between the core of connector and the ceramic can be developed in the fabrication processes, which can be investigated here.

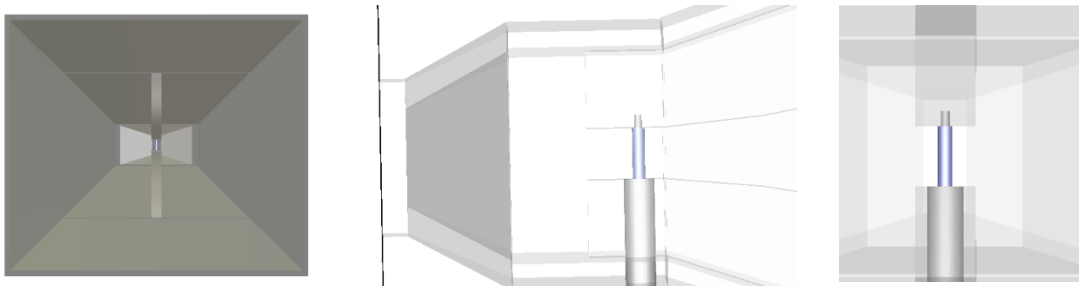

(a): Front view (b): Inside view (c): Back view

Fig 4. 79: the air gap created around the connector of the antenna design with the ceramic environment.

In order to justify the errors that can be added to the design during the fabrication process; air gap with a thickness of 0.5 mm was created around the core of the design shown in Fig. 4.79. The background material was chosen as the real ceramic by creating the environment using measured data.

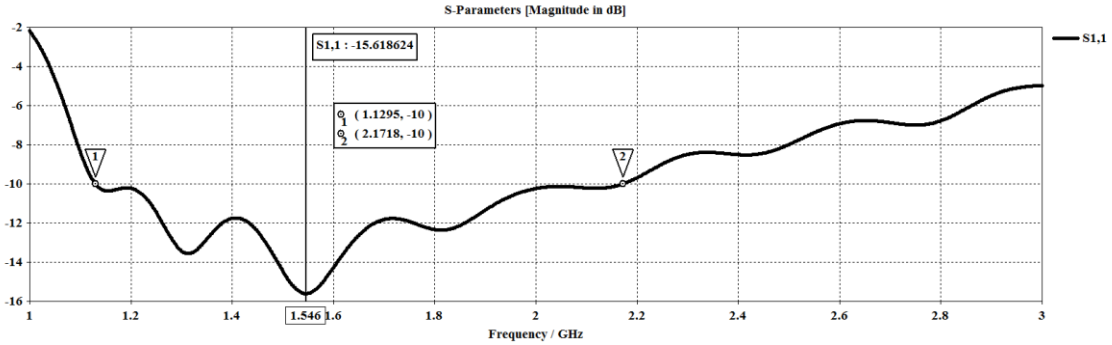

Fig 4. 80: S_{11} graph in the frequency range of 1 to 3 GHz.

Fig. 4.80 represents the S_{11} graph, which compares to the previously design results that does not have any air gap and presented in the section 4.2.3.3, generates two resonant frequencies, which shifted slightly to a higher frequency and marginally shorter bandwidth. Moreover, there is a considerable shift on the magnitude that can be related to the design gain.

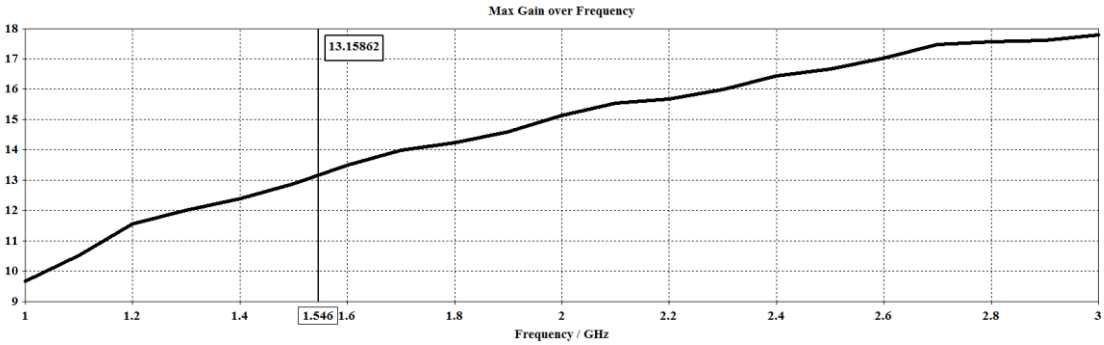

Fig 4. 81: Gain of the design over the frequency range of 1 to 3 GHz.

The gain of the design over the frequency range of 1 to 3 GHz represented in Fig. 4.81, does not demonstrate many changes that indicates the air gap in the design does not have much effect on the gain performance of the design.

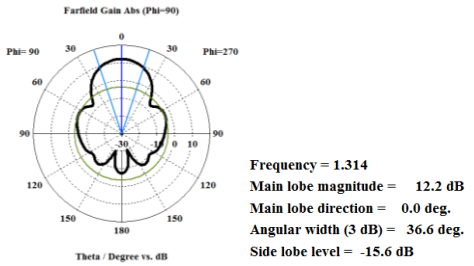

(a): E-plane polar pattern at 1.3 GHz.

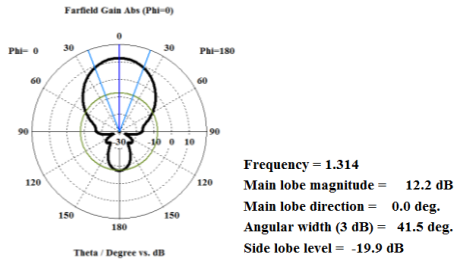

(b): H-plane polar pattern at 1.3 GHz.

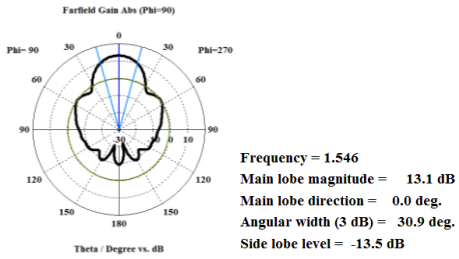

(c): E-plane polar pattern at 1.5 GHz.

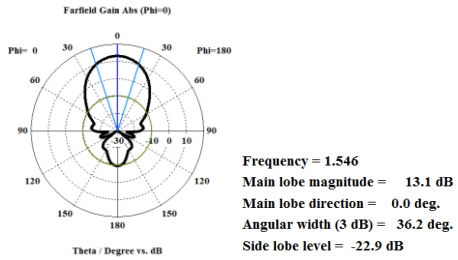

(d): H-plane polar pattern at 1.5 GHz.

Fig 4. 82: E and H field polar radiation patterns in the resonant regions.

The polar radiation patterns at the resonant frequencies indicate not much change on the SLLs, as well as directivity of the design with air gap, compared to the one with no air gap. Therefore, the results show, the air gap does not have a great effect on the functionality of the design.

4.2. DESIGNS COMPARISON

In this section, Table 4.2 is generated containing all the designs and their specification.

Table 4. 2. Different DRH designs with their specifications.

Name DRH antenna	*Surrounding Medium (ε_r)*	*Shape*	*Size (cm)*	*Bandwidth (GHz)*	*Operating frequencies*	*Gain (dB) at lowest resonant*
Initial P	1 (free space)	pyramidal	10	2.56	2.94 – 5.5	7.5 at 3.16 GHz
Improved P	1 (free space)	pyramidal	10	3.67	2.83 – 6.5	7.7 at 3.22 GHz
Initial high dielectric P	41 (σ=0.1 S/m)	pyramidal	4	0.49	1.17 – 1.66	7.26 at 1.45 GHz
Improved high dielectric P	41 (σ=0.1 S/m)	pyramidal	4	0.5	1.12 – 1.62	7.65 at 1.43 GHz
Guided P	41 (σ=0.1 S/m)	pyramidal	4	0.71	1.69 – 2.4	9.76 at 1.86 GHz
Elliptical	41 (σ=0.1 S/m)	Elliptical	3.5	1.03	1.61 – 2.64	10.39 at 2.04 GHz
Extended P	41 (σ=0.1 S/m)	pyramidal	6.8	0.9	1.3 – 2.2	12.08 at 1.58 GHz
Extended E	41 (σ=0.1 S/m)	Elliptical	9.8	0.82	1.07 – 1.89	12.25 at 1.35 GHz
Extended P	VLF-440 (ε_r=29)	pyramidal	8.3	1.08	1.09 – 2.17	12.77 at 1.47 GHz
Extended E	VLF-440 (ε_r=29)	Elliptical	7	1.08	1.09 – 2.17	11.73 at 1.17 GHz
Skin-Matched (SM)	VLF&TiO_2(ε_r=44)	pyramidal	3.8	0.64	1.45 – 2.09	10.72 at 1.68 GHz
Extended SM P	VLF&TiO_2(ε_r=44)	pyramidal	6.8	0.89	1.41 – 2.3	15.22 at 1.75 GHz
Skin-Matched (SM)	VLF&TiO_2(ε_r=44)	Elliptical	3.8	0.91	1.09 – 2	30.3 at 1.47 GHz
Extended SM E	VLF&TiO_2(ε_r=44)	Elliptical	9.8	0.7	1.1 – 1.8	35.3 at 1.32 GHz
Extended P	Distilled water (ε_r=79.5)	pyramidal	9.8	0.59	1.12 – 1.71	−3.6 at 1.28 GHz
Extended P	Deionised water (ε_r=77.9)	pyramidal	9.8	0.6	1.13 – 1.73	−2.35 at 1.3 GHz
Extended P	Oil& TiO_2 (ε_r=5.26)	pyramidal	8.8	5.2	1.6 – 6.8	5.7 at 1.76 GHz
Extended P	Paraffin& TiO_2 (ε_r=5.4)	pyramidal	8.8	4.39	1.81 – 6.2	5.7 at 2.05 GHz

By analysing the Table 4.2, the antenna designs using the skin-matched ceramic (mixture of VLF-440 and TiO_2) is the most compact design that has highest gain; however, fabrication procedure is complex and costly. Concerning, the designs low-permittivity designs (mixture of TiO_2 with oil and paraffin), these designs have wider bandwidth and the fabrication cost is low compare to the ceramics, but the gain is relatively low that would be result of mismatched. The designs with different type of water (distilled and deionised) is not satisfactory due to the high conductivity values of these waters and therefore the energy absorption within the medium that push the gain of design to negative. Finally, free space designs suffers from the parameters such as being compact in the frequency interest region and mismatching issue, which cause most of the energy reflected from the tissue.

4.3. CHAPTER SUMMARY

This Chapter consists of different types of a DRH antenna designs and simulation results within the different mediums (Free Space, water, skin matched ceramic, mixture of an oil and TiO_2, and mixture of paraffin and TiO_2) with different bandwidths and centre frequencies. The Chapter's summary can be outlined as:

- DRH antenna was selected as premium design for the system due to its large bandwidth, directivity, gain and impedance matching capability.
- First two DRH antennas were designed in the free space having the large bandwidth and gain. However, the designs were operated in the higher frequencies than the system needs due to the penetration depth as well as enormous pulse reflection due to the permittivity differs from free space (1) to the defined skin medium (i.e. 40-45).
- Different DRH antennas were designed in the ideal dielectric constant of 41 and almost the centre frequencies of 1.5 and 1.8 GHz and the best design was selected for the real ceramic data.
- Pyramidal and elliptical DRH antennas were selected as a prime designs and were modified to operate in the real ceramic design, which had permittivity of 30 at the selected centre frequencies of 1.5 and 1.8 GHz.
- The extension for the antenna designs were purposed to locate the antenna in the far field region with respect to the scanning tissue part of the body in order to generate a plane wave propagating through the monitoring area.
- Different liquid such as distilled, deionised water and their mixture with other detergent and glycerol were proposed to ease the fabrication, but due to the substantial conductivity of water, the pulse energy was absorbed within the antenna design.
- Dielectric measured linseed oil was chosen based on its low conductive; the permittivity of the oil was increased by mixing the r-TiO_2 with the oil. Moreover, PDRH antenna was designed for the mixture and the absorber sheet added to increase the directivity at the low frequencies of interest.
- Paraffin was selected based on the ability to turn to the required shape, as it turns to liquid form at 70°C and turns back into the solid form at normal temperature. Paraffin was mixed with the r-TiO_2 to increase the permittivity. The EDRH antenna was designed to operate within the mixture at the frequency of interest.

- Impedance matching functionality was investigated at the waveguide section of the design, which presents acceptable functionality.
- The fabrication error such as air gap between the ceramic and the core of the connection was inspected in a simulation that illustrates not a great impact on the design parameters.

REFERENCES (CHAPTER 4)

[1] A. R. Mallahzadeh, A. A. Dastranj, and H. R. Hassani, "A novel dual-polarized double-ridged horn antenna for wideband applications," *Prog. Electromagn. Res. B*, vol. 1, pp. 67–80, Jan. 2008.

[2] U. Schwarz, R. Stephan, and M. A. Hein, "Miniature double-ridged horn antennas composed of solid high-permittivity sintered ceramics for biomedical ultra-wideband radar applications," *in Proc. IEEE APSURSI*, pp. 1–4, Toronto, ON, Canada, Jul. 2010.

[3] C. A. Balanis, "Antenna theory - a review," *Proceedings of the Ieee*, vol. 80, pp. 739-805, Jan 1992.

[4] R. Mallahzadeh and A. Imani, "Double-ridged antenna for wideband applications," *Progress in Electromagnetics Research-Pier*, vol. 91, pp. 273-285, Jan. 2009.

[5] S. I. Latif, D. F. Tapia, D. R. Herrera, M. S. Nepote, S. Pistorius, and L. Shafai, "A directional antenna in a matching liquid for microwave radar imaging," *Int. J. Antennas Propag.,* vol. 2015, Nov. 2015, Art. no. 751739.

[6] S. Sarjoghian, Y. Alfadhl, and X. Chen, "Compact ultra-wideband double-ridged horn antennas for medical imaging," *in Proc. Loughborough Antennas Propag. Conf. (LAPC),* pp. 1–4, Loughborough, U.K., Nov. 2016.

[7] B. Jacobs, J. W. Odendaal, and J. Joubert, "An improved design for a 1–18 GHz double-ridged guide horn antenna," *IEEE Trans. Antennas Propag*., vol. 60, no. 9, pp. 4110–4118, Sep. 2012.

[8] N. Z. Tenigeer, J.-H. Qiu, P.-Y. Zhang, and Y. Zhang, "Design of a novel broadband EMC double ridged guide horn antenna," *Prog. Electromagn. Res. C*, vol. 39, pp. 225–236, May 2013.

[9] D. T. Al-Zuhairi *et al.,* " Characterizing horn antenna signals for breast cancer detection," *Can. J. Elect. Comput. Eng.,* vol. 41, no. 1, pp. 8-16, Apr. 2018.

[10] U. Schwarz, M. Helbig, J. Sachs, R. Stephan, and M. A. Hein, "Design and application of dielectrically scaled double-ridged horn antennas for biomedical UWB radar applications," *in Proc. IEEE Int. Conf. UltraWideband (ICUWB)*, pp. 150–154, Vancouver, BC, Canada, Sep. 2009.

[11] F. S. Di Clemente, R. Stephan, and M. A. Hein, "Ultra-wideband miniaturised high permittivity-matched antennas for biomedical diagnostic," *7th Eur. Conf. on Antennas and Propag. (Eucap)*, pp. 2896-2899, Gothenburg, Sweden, Apr. 2013.

[12] S. I. Latif, D. Flores-Tapia, S. Pistorius, and L. Shafai, "Design and performance analysis of the miniaturised water-filled double-ridged horn antenna for active microwave imaging applications," *Microw. Antennas Propag.,* vol. 9, no. 11, pp. 1173-1178, Agu. 2015.

[13] S. Latif, S. Pistorius, and L. Shafai, "A double-ridged horn antenna design in canola oil for medical imaging," *in 2nd Int. Conf. Advances in Elect. Eng. (ICAEE)*, pp. 421–424, Dec. 2013.

[14] H. Balegh, B. A. Arand, and L. Yousefi, "Side lobe level reduction in horn antennas using graphene," *in 24th Iranian Conf. Elect. Eng. (ICEE)*, pp. 1937-1941, Shiraz, Iran, May 2016.

[15] S. Latif, S. Pistorius, and L. Shafai, “A double-ridged horn antenna design in canola oil for medical imaging,” in 2nd Int. Conf. Advances in Elect. Eng. (ICAEE), pp. 421–424, Dec. 2013.

[16] M. A. Saed, “Broadband CPW-FED planar slot antennas with various tuning stubs,” *Progress in Electromagnetics Research-Pier,* vol. 66, pp. 199-212, Jan. 2006.

CHAPTER 5

5. ABDOMINAL FAT MEASUREMENT SYSTEM

In this Chapter, the system behaviour will be evaluated using various DRH antenna designs in different material on the modelled human tissue (studied in Chapter 3 and 4). Moreover, the hardware components would be needed to finalise the system hardware design were considered base on availability.

5.1. SYSTEM DESIGN ANALYSIS

The system will be evaluated using different time domain approaches such as the reflected pulse, TDR and reflection coefficient, employed by various research groups in the similar systems [1, 2]. The system operation was investigated when the proposed antenna was located on the modelled tissue in order to measure the fat thickness. Modelled tissue is comprised of 2 mm skin, a large amount muscle, and a layer of fat with thickness varying from 10 to 40 mm, in 5 mm increasing steps.

5.1.1. SYSTEM ANALYSIS USING THE FREE SPACE DRH ANTENNA DESIGNS

Two PDRH antennas designed in free space in section 4.2.1.2 both benefiting from wide bandwidth, and other designs that were developed within different high dielectric materials will be individually applied and analysed in the system. Moreover, the tissue modeled previously is placed in the far field distance in front of the antennas, the GP is transmitted to the tissue, reflected pulse is recorded, and analysed based on the time of arrival and amplitude reduction of received pulse. Furthermore, the system is evaluated when it operates at different centre frequency and bandwidth (1 and 3.5 GHz), to assess the effect of penetration depth and range resolution in the system performance.

5.1.1.1. WIDE BANDWIDTH DESIGN IN FREE SPACE PERFORMANCE IN THE SYSTEM

In a design with wide bandwidth, a GP with the centre frequency of 3.3 GHz and bandwidth of 1GHz (2.83−3.83) was generated using CST software as presented in Fig. 5.1. The created pulse was transmitted using the antenna to the modelled tissue and the reflected pulses were captured and analysed.

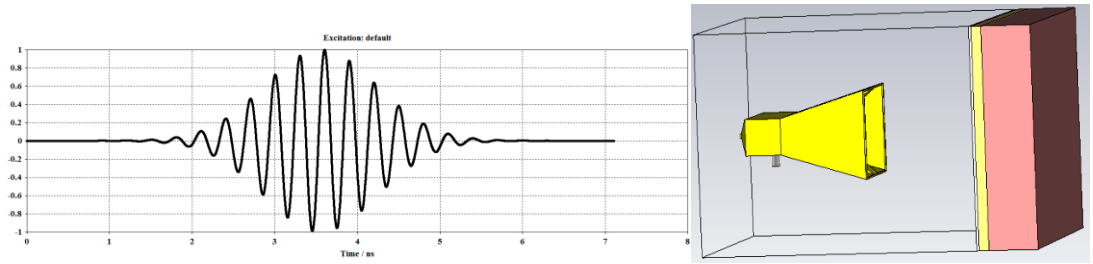

Fig 5. 1: Modelled tissue placed in front of the antenna and the GP was generated and transmitted using CST signal excitation.

The impulse response is a common method applied in systems with time domain results. There is possibility of acquiring information such as location and type of a medium by impulse responses using the methods such as S_{11}, TDR and Group delay. Fig. 5.2 represents the transmitted and reflected pulses in free space, when the modelled tissue was in the far-field region of the designed antenna in the time domain. In addition, the reflected pulses were studied, in terms of time, amplitude and shape.

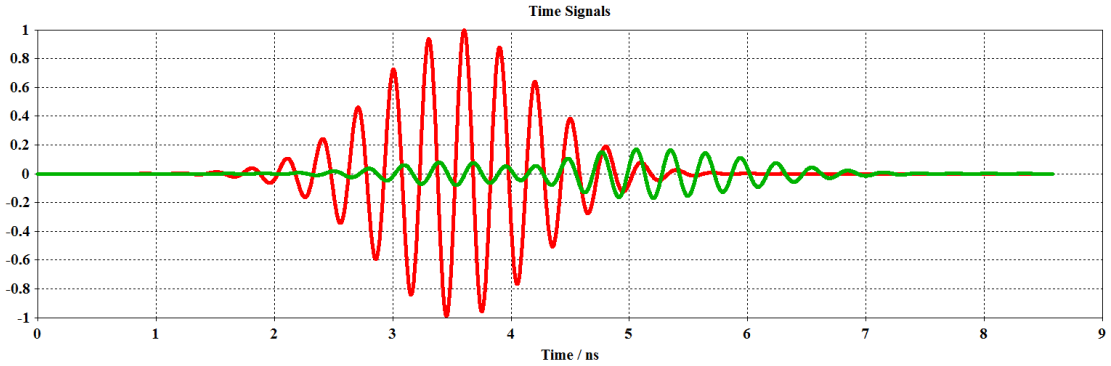

Fig 5. 2: Transmitted (red) and reflected (green) pulses from the antenna to the tissue located in the far field region.

Furthermore, the acquired information were assessed, in the frequency and time domains, when the thickness of the fat layer in the modelled tissue was changed from 10 to 40 mm of 5 mm steps based on the abdominal fat thickness in humans. Fig. 5.3 represents the generated reflection coefficient response in the frequency domain using CST software.

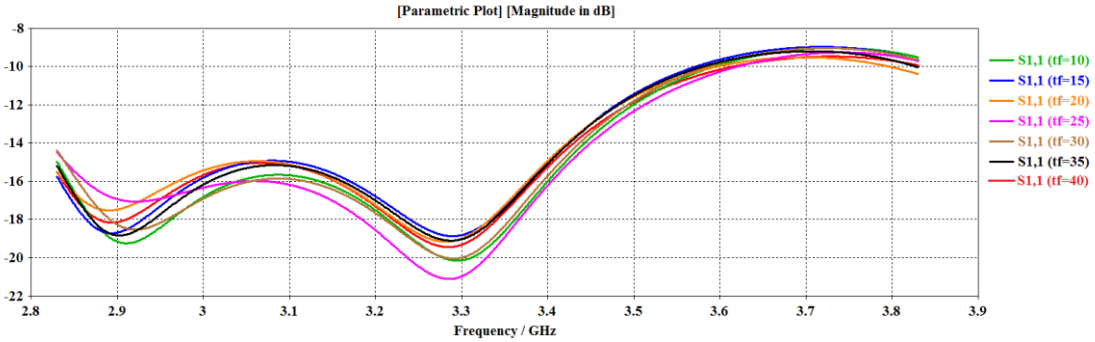

Fig 5. 3: Generated return loss, when fat thickness varies from 10 to 40 mm with 5 mm iteration.

The S_{11} graphs shown in Fig. 5.3, demonstrates non-uniform behaviour in terms of the magnitude, time and shape when the tissue modelled with different fat thickness scenarios (i.e. change of fat thickness from 10 to 40 mm) were employed in the system. These cannot be easily interpreted in anyway refer to the inconstant changes of amplitude and time. Therefore, the next step was to observe the time domain graphs to define the changes in amplitude and time difference for fat thickness changes.

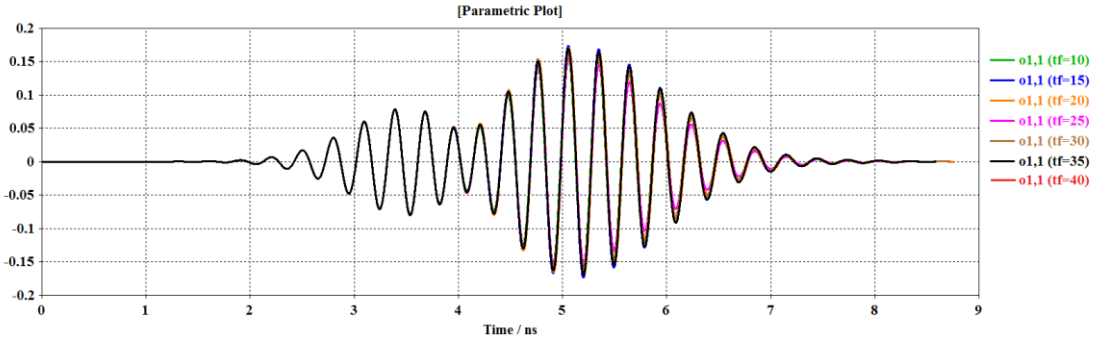

(a)

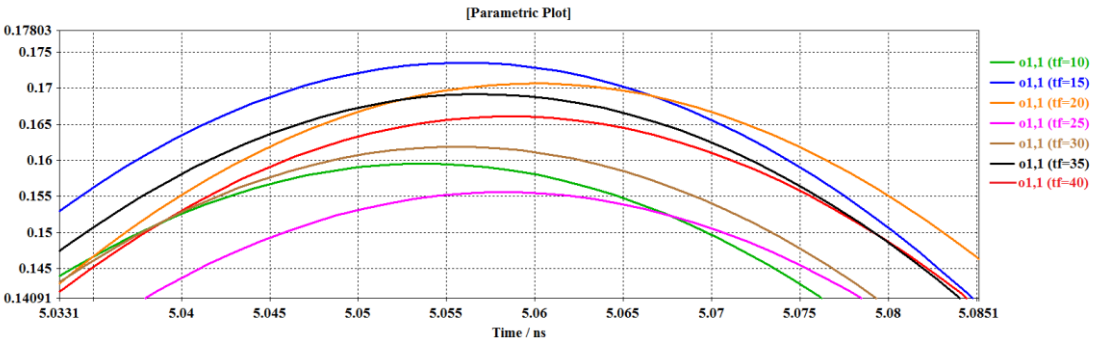

(b)

Fig 5. 4: Generated reflected pulse when the fat thickness varies from 10 to 40 mm with 5 mm iteration.

Fig. 5.4 presents the generated reflected pulses in time domain when the fat thickness of the modelled tissue changed from 10 to 40 mm in 5 mm steps. Moreover, analysing the reflected pulses in different fat scenarios indicates that there is no constant change in relation to the time shifting, amplitude of the pulse, which was expected due to the signal overlapping issue.

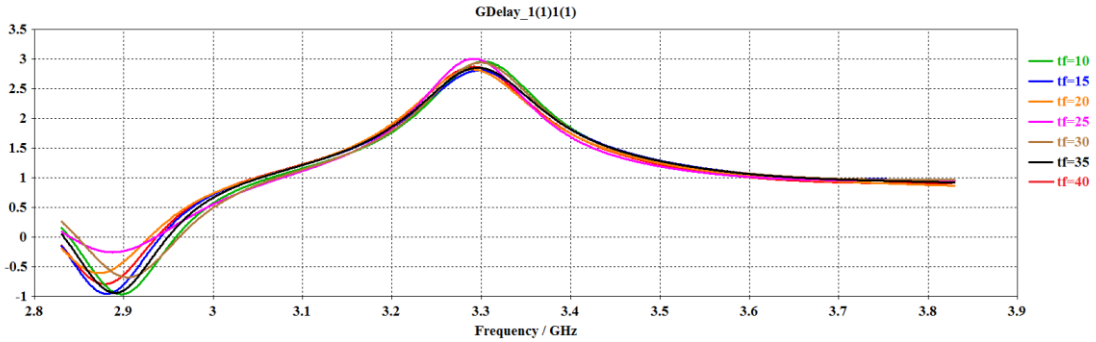

Fig 5. 5: Group delay when the fat thickness varies from 10 to 40 mm with 5 mm iteration.

In addition, the group delay and TDR graphs were generated for different fat thicknesses and are shown in Fig. 5.5 and Fig. 5.6 respectively. Fig. 5.5 represents the group delay and demonstrates constant change of time for thicknesses from 10 to 20 mm, and start lagging thereafter, which could be resulted by overlapping.

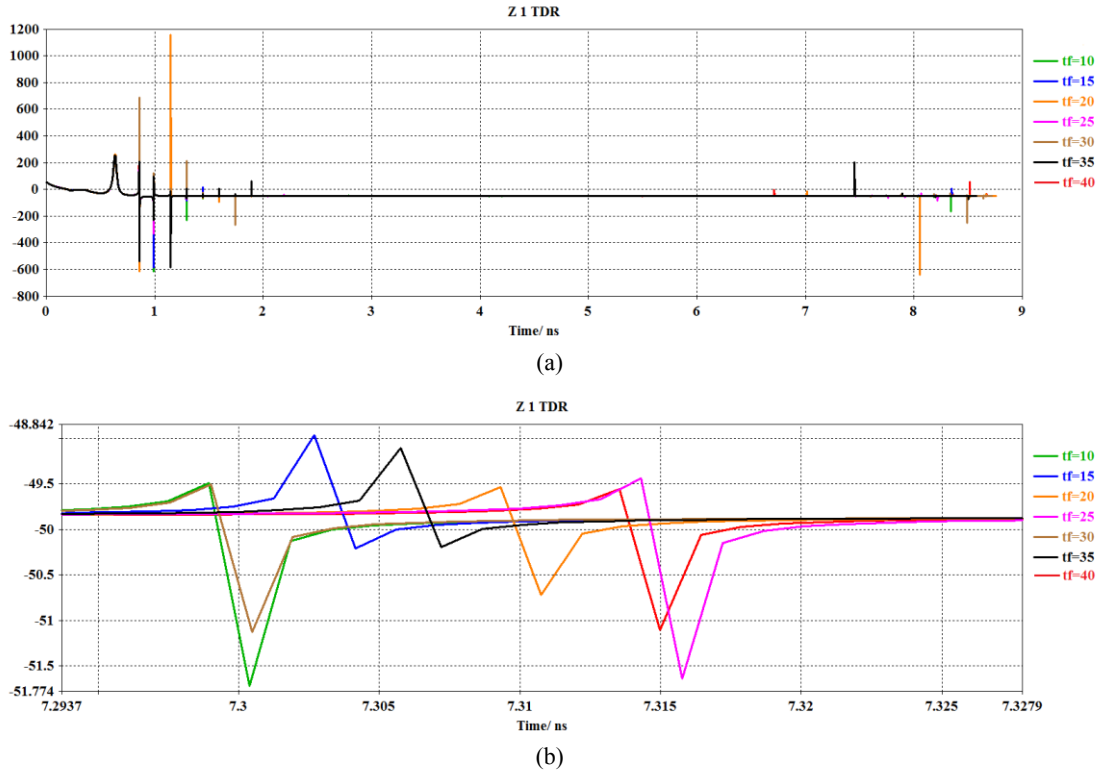

Fig 5. 6: TDR results when the fat thickness varies from 10 to 40mm with 5 mm iteration.

Figs. 5.6 represents, the generated TDR for different fat layer thicknesses from 10 to 40 mm. The results indicate a constant shift in time for fat thicknesses of 10 to 25 mm; however, when the thickness increased to 30 mm, signal shifted back to the same position where the thickness was 10 mm with another cycle of time starting over. According to the time domain results, the measurement of the fat thickness using the antenna in free space, indicated that the system was unable to determine the fat thickness in the required region. In addition, the generated results clarified that the antenna design and the pulse were not suitable for the system. Furthermore, it is worth studying the specific absorption rate (SAR) of the EM energy inside the medium for the different scenarios of fat thicknesses. To define and gain understanding of the absorption rate parameter inside the medium, when the permittivity is known, and the conductivity can be defined by equation (5−1);

$$\sigma = \frac{\alpha}{\pi f}\sqrt{\frac{\alpha^2}{{\mu_0}^2} + \frac{\omega^2 \varepsilon_0 \varepsilon_r}{\mu_0}} \qquad \text{Eq. (5−1)}$$

where α is attenuation coefficient, ε_r is relative permittivity, μ_0 is magnetic permeability of free space, and f is frequency. In addition, the SAR of an electric field inside a medium can be defined by equation (5−2);

$$SAR = \int \frac{\sigma(r)|E(r)|^2}{\rho(r)} dr \qquad \text{Eq. (5-2)}$$

where, SAR is a function of the electrical conductivity (σ, measured in Siemens/meter), the induced E-field from the radiated energy (i.e. E, measured in Volts/meter), and the mass density of the tissue (i.e. ρ, measured in kg/cubic-meter). The SAR is calculated by averaging technique (i.e. integrating) over a specific volume (typically a 1-gram or 10-grams area) [3]. Figs. 5.7 and 5.8, illustrate the induced E-field radiation energy that is being absorbed by each layer through the medium. Fig. 5.7 represents the case, when the modelled tissue has a fat layer with thickness of 10 mm, where Fig. 5.8 demonstrate the case, for 40 mm fat layer.

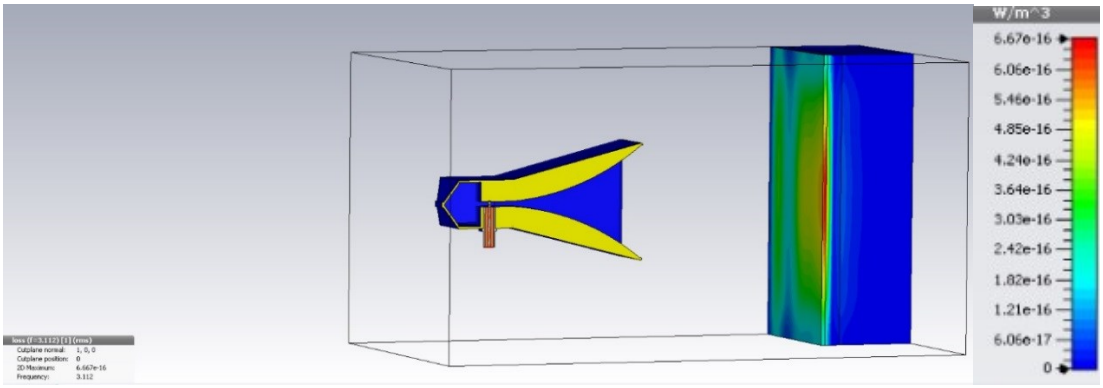

Fig 5. 7: The SAR radiation when there is a fat layer with 10mm thickness presented in the modeled tissue.

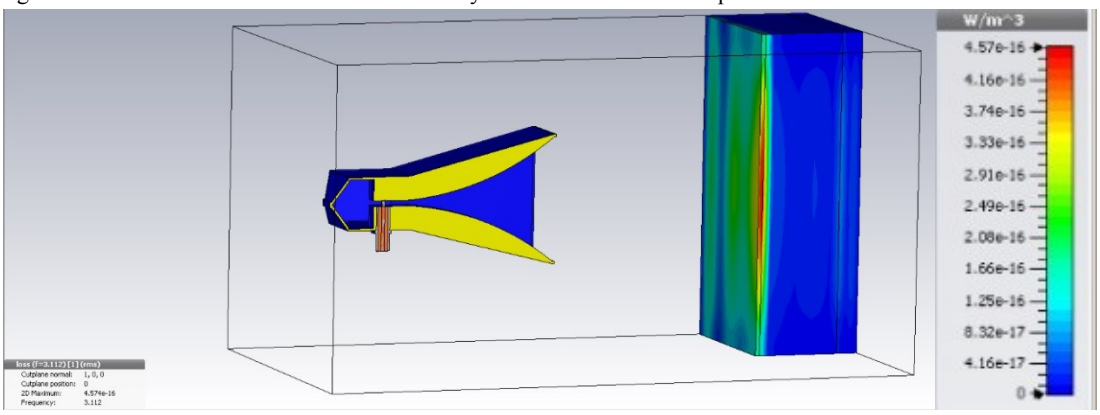

Fig 5. 8: The SAR radiation when there is a fat layer with 40mm thickness presented in the modeled tissue.

Figs 5.7 and 5.8 represent an insignificant amount of the penetration in both cases where the modelled tissue had fat thicknesses of 10 and 40 mm, however, it can be observed that minor amounts of energy has been penetrated through the medium, which proves the system has minor operation functionality. Defining the equation (5−2), there are two elements that have more impact on the radiation pattern; the first element is electrical

conductivity, which increased slightly from one tissue type to another, and second and more important element is mass density that can change significantly from one type to another. Each tissue type has an approximate mass density, which makes the simulation more vulnerable in terms of the outcome results. Finally, based on the analytical and simulation results, the system would not be able to determine the fat thickness and therefore there is need of a wider bandwidth to satisfy the range resolution and lower centre frequency to satisfy required penetration through the medium.

5.1.1.2. IMPROVED SYSTEM DESIGN IN FREE SPACE

In this section, the improved design in free space was employed in the system and a GP with the centre frequency of 3.21 GHz and bandwidth of 3.66 GHz (2.83−6.49 GHz) was generated using CST-MWS as shown in Fig. 5.9. In addition, the pulse has been transmitted using the designed antenna to the tissue model and the reflections were recorded for further investigation.

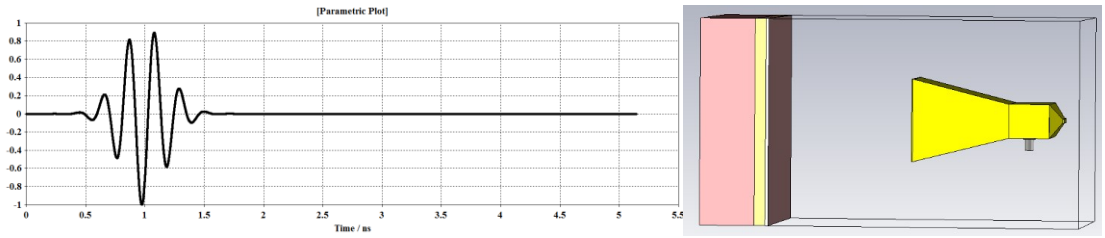

Fig 5. 9: The tissue placed in front of the antenna and the GP was generated and transmitted using CST signal.

The thickness of fat layer changed from 10 to 40 mm with 5 mm steps and the responses were generated and saved for each case individually for further analysis.

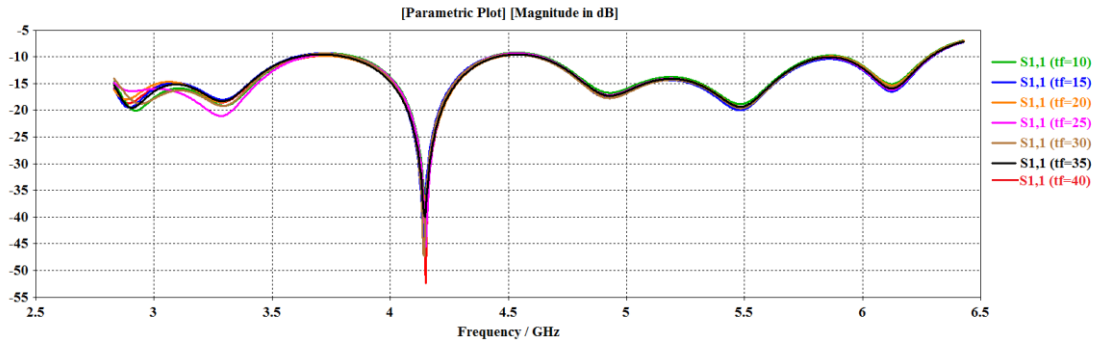

Fig 5. 10: Captured S_{11} for the Reflected Pulse when the fat thickness varies from 10mm to 40mm.

Fig. 5.10 represents the S_{11} graphs of the system for different fat thicknesses. The results specify non-constant changes regarding the magnitude and the frequency shifting as it was expected. The next stage is to consider the time domain results and check if the meaningful information can be acquired from the results.

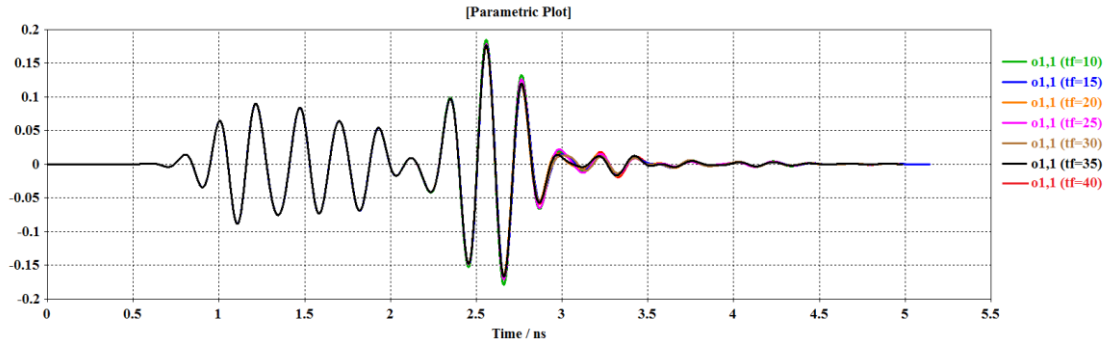

(a)

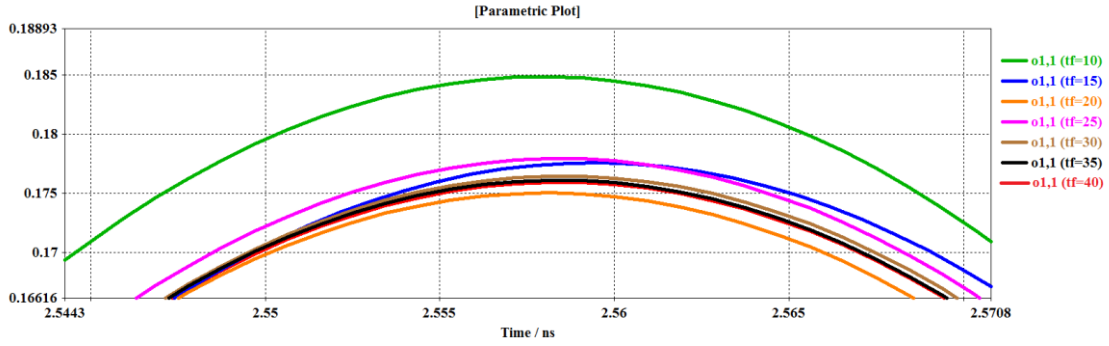

(b)

Fig 5. 11: Captured Reflected Pulse when the fat thickness varies from 10mm to 40mm.

Figs. 5.11 shows the reflected pulses generated for different fat thicknesses from 10 to 40 mm. Comparing the results, there are no regular changes concerning amplitude or time shifting. This proves that the system is not operating due to low penetration in the modelled tissue and the large reflection was generated result of the mediums mismatched.

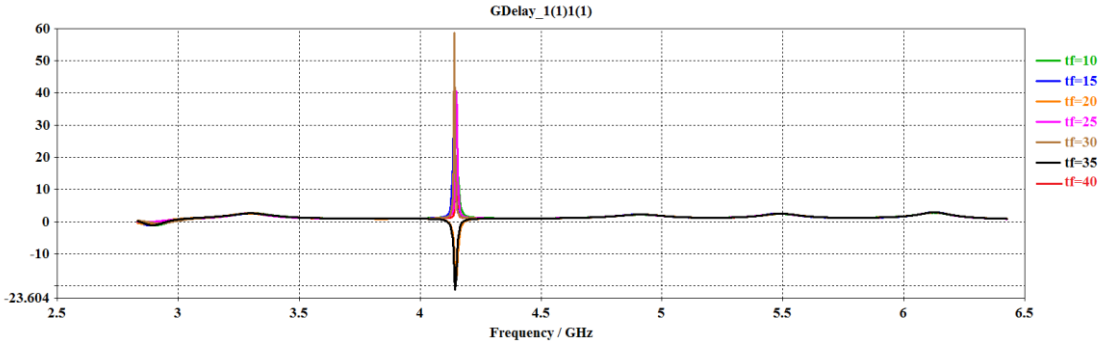

Fig 5. 12: Group delay graph results generated when the fat thickness varies from 10 to 40 mm with 5 mm iteration.

The group delay graph shown in Fig. 5.12 proves the irregularity in each case also the concept of over-lapping results. The overall results have verified that the results have been corrupted base on their unknown behavior and therefore one of the important parameters (e.g. range resolution or penetration depth) for the pulse is not sufficient for correct measurement of fat layer. Therefore, a new idea of habitation of a horn antenna to

the materials with the close permittivity to the human tissue will present in the next section.

5.1.2. SYSTEM ANALYSIS USING DRH ANTENNA DESIGNS IN HIGH DIELECTRIC MATERIAL

Following more research and looking through different techniques that can improve the system performance by minimising the large reflection from the skin results of the mediums mismatch, and overlapping the pulse results of the range resolution. New concept was introduced to design the antenna in a material with a high permittivity close to the human skin (40−45). Refer to equation (2-13), the required bandwidth and therefore the range resolution for the pulse could be defined to enable the system to detect a small object. That part of the equation, which involves with the speed of the pulse in the free space, worth it to be paid more attention to, especially when the antenna was embedded in high dielectric materials. This means, the speed of pulse in free space can be reduced by embedding the antenna in the high permittivity materials that has a permittivity close to the skin's permittivity and therefore better matching can be achieved. This not only can compact the antenna and therefore the system, it also can reduce the first large reflected signal that was produced due to mismatching issue, which must be removed through complex signal processing technique. Table 5.1 illustrates the required bandwidth for the pulse and therefore range resolution when it is operating inside a medium with a high permittivity close to the human skin.

Table 5. 1: The human tissue thickness and related bandwidth required for detection in the skin's environment.

Tissue types	***Thickness (mm)***	***Required Bandwidth(GHz)*** $\geq v_s / 2\Delta R$
Skin	2	11.71
Fat	16	1.46
Muscle	30	0.78

Table 5.1 demonstrates that by reducing c (speed of light) to v_s (speed of signal transfer through skin like medium), the required bandwidth to have premium resolution would reduce significantly. By putting the antenna into the material with the permittivity close to the skin's permittivity (40-45) we reduce the large reflected pulse from the skin, generated due to mismatches in the medium.

The technique has its own limitation such as putting an antenna in such a medium that may have high conductivity has great effect on the antenna operation and the transmitted signal. This can reduce the gain, radiation pattern and signal power considerably but it is worthy to try the technique and to eliminate the critical limitations such as using high dielectric ceramic in the design that has low conductivity. Hence, based on previous research, and the retrieved results, we are directed to the choice of embedding the antenna in the medium with a high dielectric constant close to the human skin's permittivity. This reduces the size, large reflections resulting mismatched and required bandwidth improving the range resolution. Therfore, a WB antenna is proposed for the system that should have following features to satisfy the project requirements:

- It should have centre frequency of less than 3 GHz to penetrate better through the modelled human based on skin depth issue.
- It should have a minimum bandwidth of 500 MHz to be able to satisfy the range resolution.
- It should have small dimensions, as it should be able to locate on the body and use in the compact system.
- The developed antenna should be designed in the material that has the permittivity close to human skin (40-45) as well as low conductivity.

Based on the considerations given above, the PDRH antenna designed in the previous section has been redesigned to satisfy the given specifications. With the use of mathematical equations in Balanis textbook [4], the minimum size for the aperture of horn was found to be 40 mm for centre frequency of less than 3 GHz; however, by reducing the centre frequency the bandwidth may be effected also but this can be addressed later. More study on penetration depth as well as the range resolution suggest that the centre frequency of 1.45 GHz is the optimum frequency for the system to be able to scan the modelled tissue. Table 5.2 shows the dielectric properties, loss tangent, and wavelength and penetration depth of each tissue layers at 1.45 GHz frequency using equation (2−10).

Table 5. 2: Penetration depth related parameters of three type of the modelled human tissue.

Tissue Name	Frequency (GHz)	Conductivity (S/m)	Relative Permittivity	Loss tangent	Wavelength (mm)	Penetration depth (mm)
Skin Dry	1.45	1.054	39.5	0.330	32.4	32.1
Skin Wet	1.45	1.066	44.5	0.297	30.6	33.6
Fat	1.45	0.066	5.4	0.153	88.8	186.1
Muscle	1.45	1.164	54	0.267	27.8	33.8

Table 5.2 suggests the applicable penetration depth through each employed tissue modelled at 1.45 GHz centre frequency. In addition, the antenna was redesigned based on the operating centre frequency in the CST software and the defined parameters to get the best performance.

5.1.3. NEAR AND FAR FIELD EFFECTS ON THE SYSTEM

In order to identify the location for the antenna with respect to the monitoring area, the designed antenna was located in three different regions in front of the modelled tissue (near, middle, far field regions). The concept of placing the antenna in the far-field region of the monitoring area was developed to generate a plane wave and a delay. The concept can address the overlapping issue that occurs when the antenna is used as a transceiver. However, the concept can be ignored in the application where the antenna is not being employed as a stand-alone transceiver. In addition, a GP with low and high centre frequencies of 1.2 and 1.7 GHz were generated and transmitted through the modelled tissue using the CST software, which is shown in Fig. 5.13.

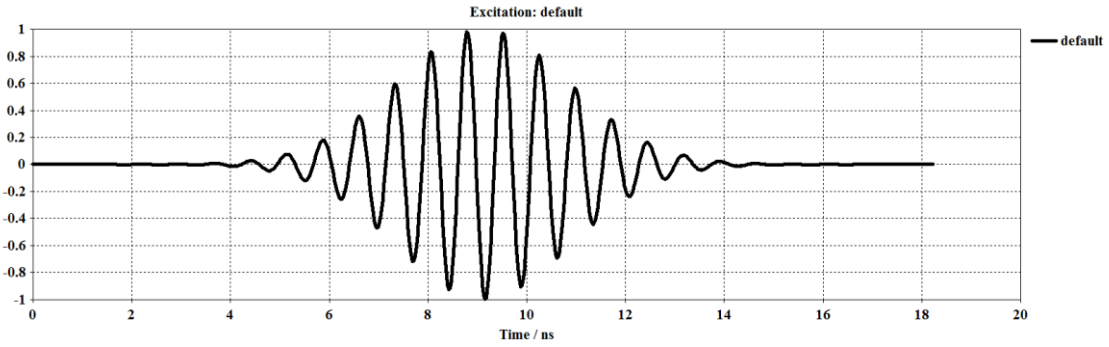

Fig 5. 13: The GP with lower and higher frequencies ($\boldsymbol{f_l = 1.2\ GHz, f_h = 1.7\ GHz}$).

In order to be able to identify where is the best location to place the antenna against the modelled tissue, the previously defined equations (5−3a, and b) were applied here again, which determines the near and far field distance.

$$\lambda = {}^{c}/_{f\sqrt{\varepsilon_r}} = \frac{3\times10^8}{1.45\times10^9\times\sqrt{41}} = 32.3mm \qquad \text{Eq. (5−3a)}$$

$$d_f = 2 \times D^2/_{\lambda} = \frac{2\times32^2}{32.3} = 63.4mm \qquad \text{Eq. (5−3b)}$$

Where λ the wavelength, c is the speed of light, f is the centre frequency, ε_r is the permittivity of the material that the antenna embedded in, d_f is the distance of the modelled tissue from the antenna and D is the biggest dimension of the aperture of the antenna. By applying the defined parameters of the design in the equations (5−3a, and b);

the far field distance for the design was determined to be 63.5 mm. This means if the SMA connection of the antenna where the pulse is excited from has distance from the tissue less than the defined distance the antenna is located in the near field. Otherwise, the antenna is located in the far field of the monitoring area.

Far field theory is defined that in the far field region an E and M field are orthogonal to each other, a plane wave will be generated that propagates efficiently in this area and therefore better response can be retrieved by the system. This means by locating the monitoring area in the far field region of the antenna hawse have to take into account that the extra distance in the medium will absorb some amount of energy to get to the scanning medium. Therefore, three cases of modelling (Near, Meddled and Far field regions) were proposed here to verify the best location where the antenna should be placed with respect to the monitoring area to provide the best response. Moreover, as the antenna embedded in the ideal high dielectric material that has the permittivity of 41 and conductivity of 0.1-S/m, the far field distance will be reduced and therefore the antenna structure. In the first case, the modelled tissue was located in the near field region of the antenna that shown in Fig. 5.14 and the response was analysed.

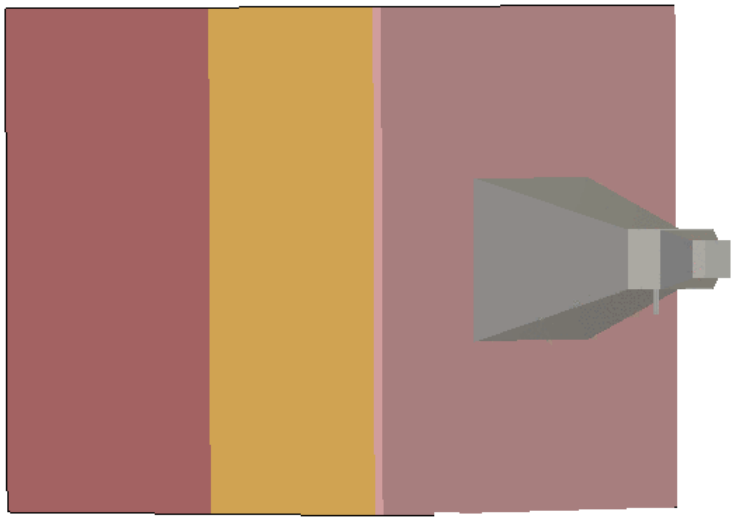

Fig 5. 14: PDRH antenna filled with ideal high dielectric placed on the modelled tissue in the nearfield region.

The pulse transmitted to the modelled tissue for different fat thicknesses from 15 to 40 mm and the time domain results were generated using the CST studio software as shown in Fig. 5.15.

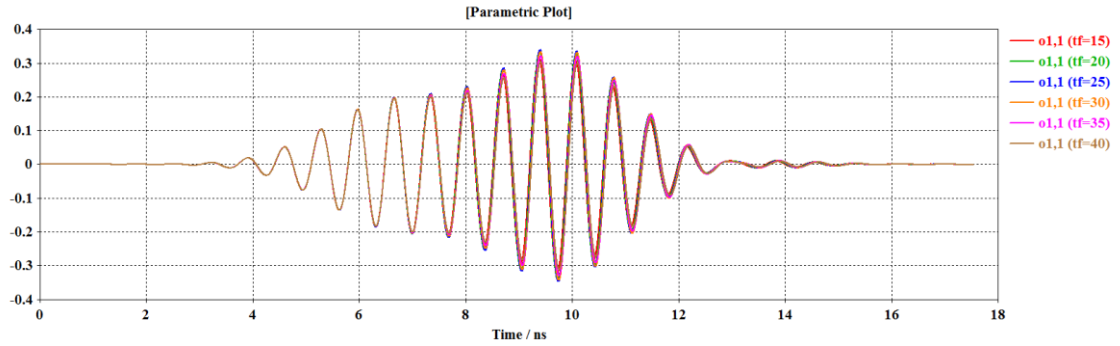

(a)

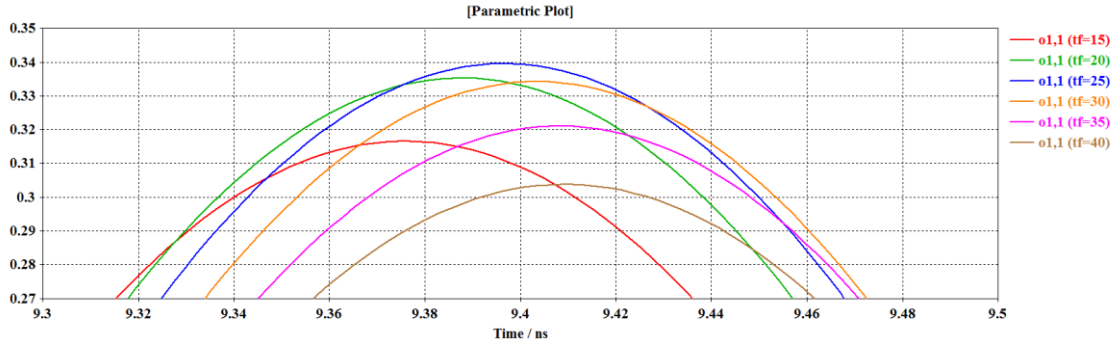

(b)

Fig 5. 15: Reflected pulses for the case when the modelled tissue placed in the near-filed region and consists of the fat layer with thicknesses of 15 to 40 mm with 5-mm thickness iteration.

Figs. 5.15 represents the reflected pulses in the time domain when the fat thickness changes from 15 to 40 mm in steps of 5 mm. As it can be observed, the reflected pulse amplitude is overlapped, which forced the first two thicknesses (15 and 20 mm) to drop below the amplitude of the rest. Regarding the pulses time delay, they show constant changes approximately as expected.

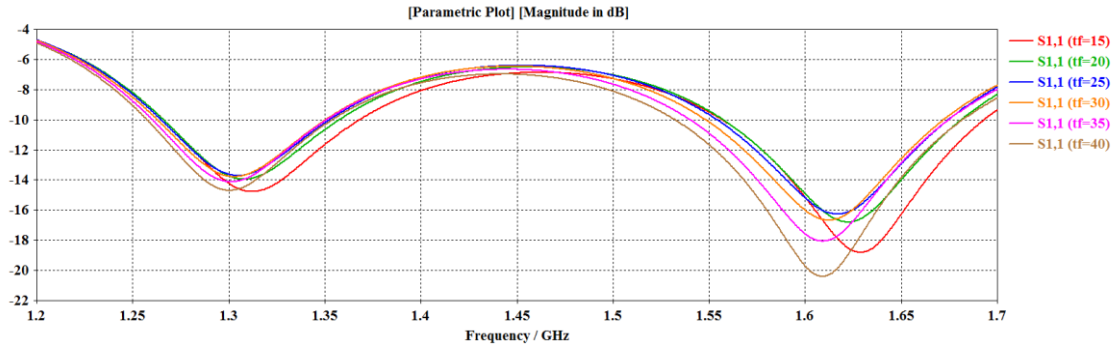

Fig 5. 16: S_{11} results for the case when the modelled tissue placed in the near-filed region and consists of the fat layer with thicknesses of 15 to 40 mm with 5-mm thickness iteration.

Fig. 5.16 represents the S_{11} graph for the same scenarios and indicates the results based on the magnitude and frequency shift for the first two cases (15 and 20 mm), which are lagging behind from other cases indicating the overlapping issue.

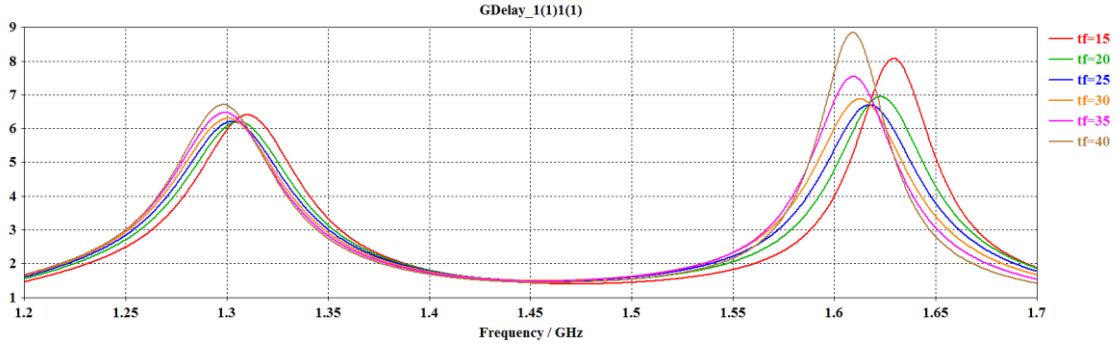

Fig 5. 17: Group delay results for the case when the modelled tissue placed in the near-filed region and consists of the fat layer with thicknesses of 15 to 40 mm with 5-mm thickness iteration.

The group delay graph for different cases are generated in Fig. 5.17 that indicates the overlapping concept with reference to the frequency shift in the x-axes and time delay in the y-axes of the graph.

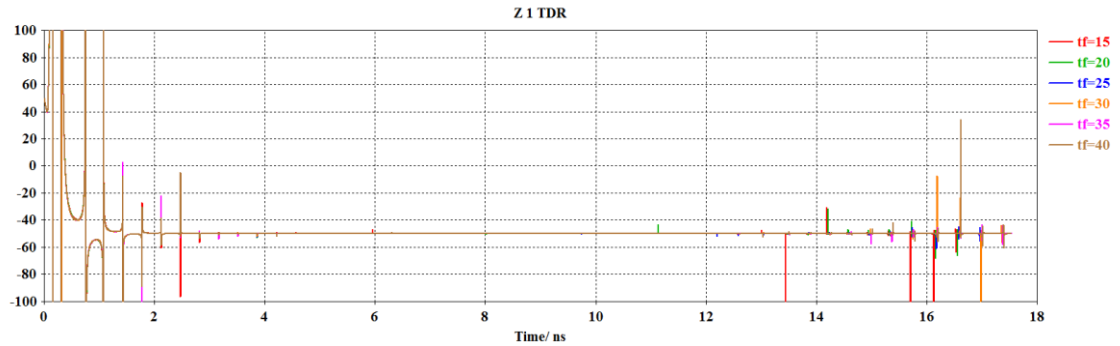

(a)

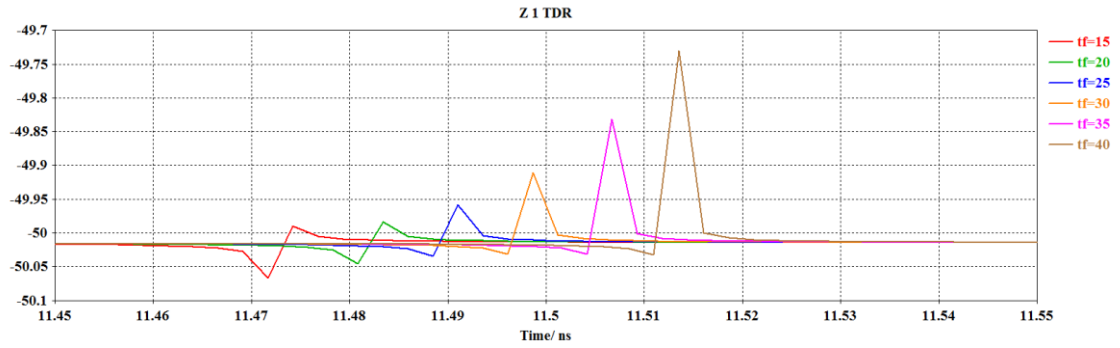

(b)

Fig 5. 18: TDR results for the case when the modelled tissue placed in the near-filed region and consists of the fat layer with thicknesses of 15 to 40 mm with 5-mm thickness iteration.

Fig. 5.18 represents the time domain reflectometry (TDR) graph of the system with respect to the modelled tissue where the fat thickness changed from 15 to 40 mm with steps of 5 mm. The results represent the overlapping in the early stage of the time that can be retrieved from the later time that is shown in the Fig. 5.18 (a).

In the improved case, the modelled tissue was located at the same distance found by calculation and defined as a middle field. Fig. 5.19 represents the antenna was located

30 mm apart from the outer aperture of the designed antenna that means 63 mm apart from the excitation point (the core of SAM connector). The WB pulse was generated and transmitted to the modelled tissue with different fat thicknesses and the reflected pulses were captured and analysed in the time domain.

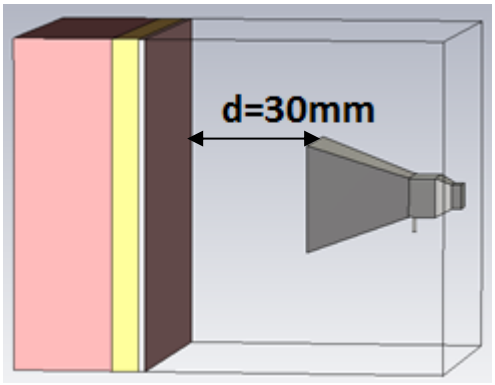

Fig 5. 19: PDRH antenna filled with ideal dielectric (41) placed 30-mm apart from the tissue in the transition region.

The approach was to change the fat thickness and record the reflection parameters to be able to verify the concept, which was to measure the fat with different thicknesses. The sweep of five times were generated in the software for the fat thickness parameters from 10 to 40 mm and results were recorded and presented in Fig. 5.20.

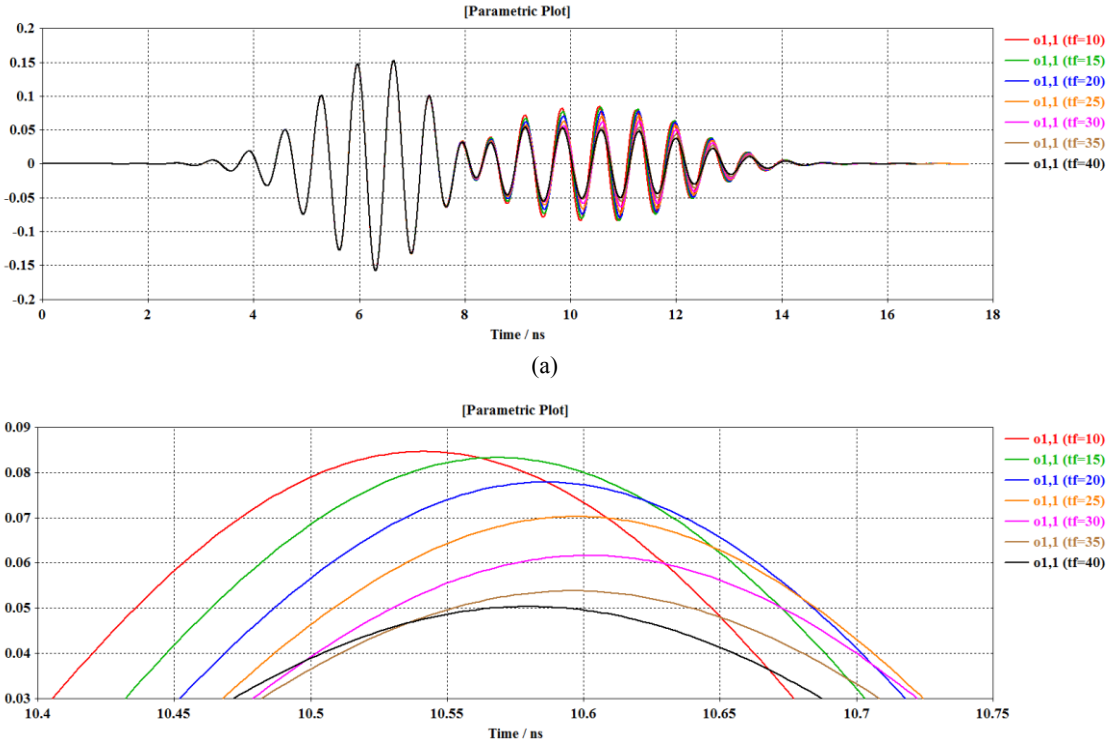

Fig 5. 20: Reflected pulses when the antenna placed 30 mm apart in transition region from the modelled tissue and the fat layer sweep from 10 to 40 mm with 5-mm iteration.

Fig. 5.20 represents the reflected pulses in the time domain for different cases when the fat thickness has changed from 10 to 40 mm. The results demonstrate the amplitude reduction of the reflected pulse as it was expected, the time delay for the reflections can verify that the system is operating based on changing parameters; however, the first case is still lagging by small amount.

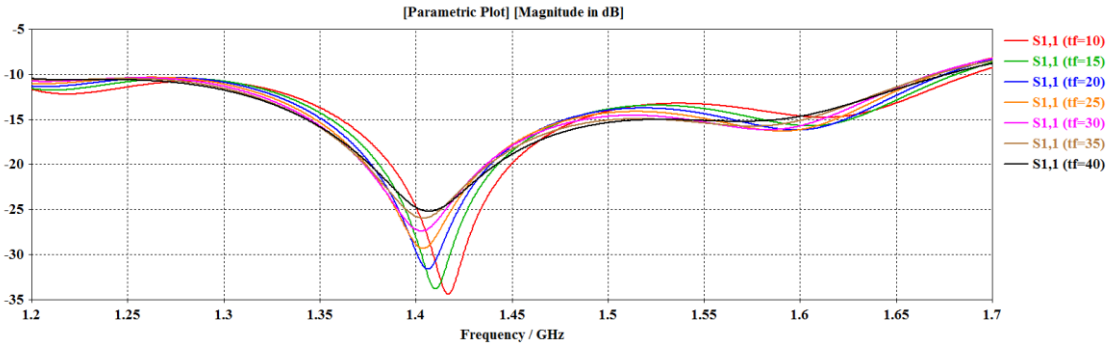

Fig 5. 21: S_{11} results for the case when the modelled tissue placed in the transition region and consists of the fat layer with thicknesses of 10 to 40 mm with 5-mm thickness iteration.

Fig. 5.21 illustrates frequency response of the system and shows constant changes of the magnitude and shift of frequency from one case to another at the centre frequency of 1.45 GHz, which proves the concept of the measurement for the fat layer thickness with a minor lagging to the first case.

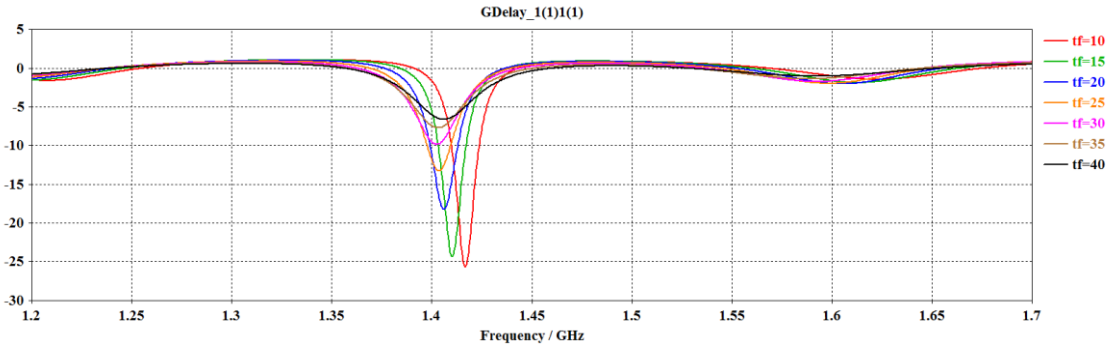

Fig 5. 22: Group delay results for the case when the modelled tissue placed in the transition region and consists of the fat layer with thicknesses of 10 to 40 mm with 5-mm thickness iteration.

Finally, the group delay that retrieved from the time domain results is represented in Fig. 5.22 and the delays of the reflected pulses for different cases when the thickness of the fat layer alters from 10 to 40 mm illustrates constant changes excluding with the first case (10 mm). This verifies the system operation based on the simulated results with minor shift to the first case.

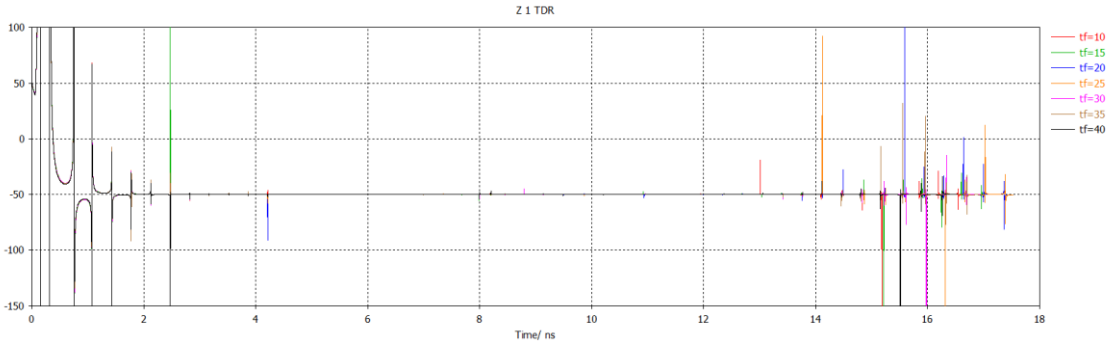

(a)

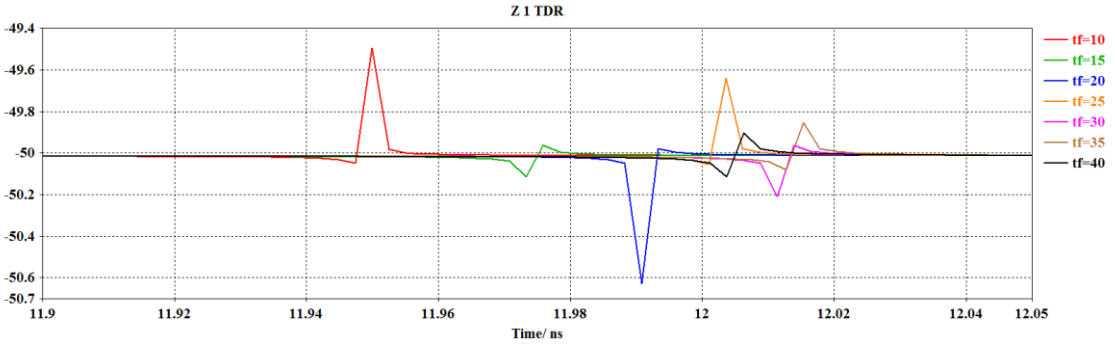

(b)

Fig 5. 23: TDR results for the case when the modelled tissue placed in the transition region and consists of the fat layer with thicknesses of 10 to 40 mm with 5-mm thickness iteration.

The TDR graphs shown in Fig. 5.23 presents the time delay in each case where the fat thickness changes in the earlier was sequential as the overlapping had occurred in the last case due to the middle field distance for the system that placing the tissue far off by 30 mm more than the first case.

In the third and final case, the modelled tissue was placed 60 mm from outer aperture of the antenna, which means more than 90 mm from the excitation point of the design. Fig. 5.24 represents the modeled tissue in front of the designed antenna and 60 mm to stay well beyond the far field region.

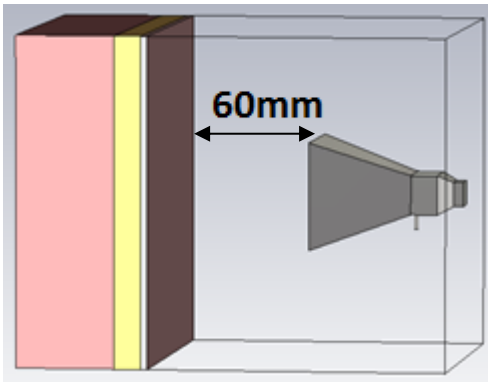

Fig 5. 24: PDRH antenna filled with ideal high dielectric (41) placed 60 mm apart from the tissue in far-field region.

Fig. 5.24 illustrates the tissue model (2 mm Skin, 10 mm Fat, and 40 mm muscle) that has been located 60 mm from antenna permitted to transmit the pulse, receive the reflection pulse, and analyse it. The approach was taken to change the fat thickness and record the reflection parameters to be able to prove the concept, which was to detect the fat with different thicknesses. The sweep of five times has been generated for the fat thickness parameter of 10 to 40 mm and the results have been recorded as is shown in Figs. 5.25.

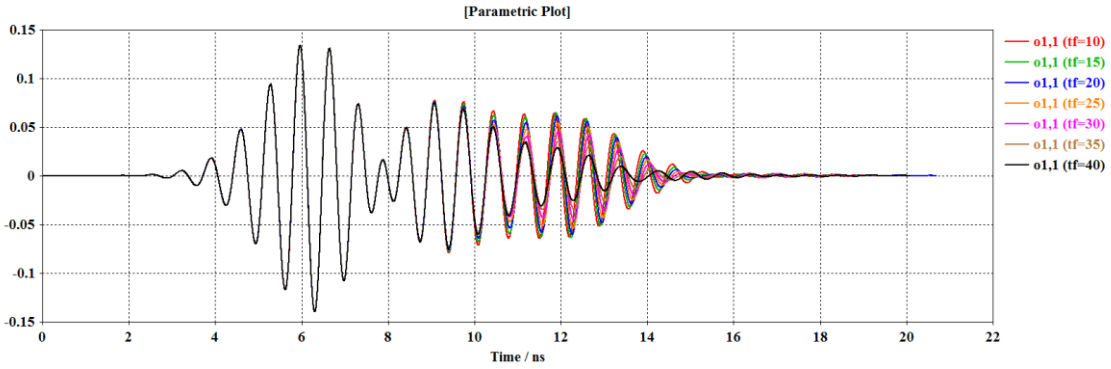

(a)

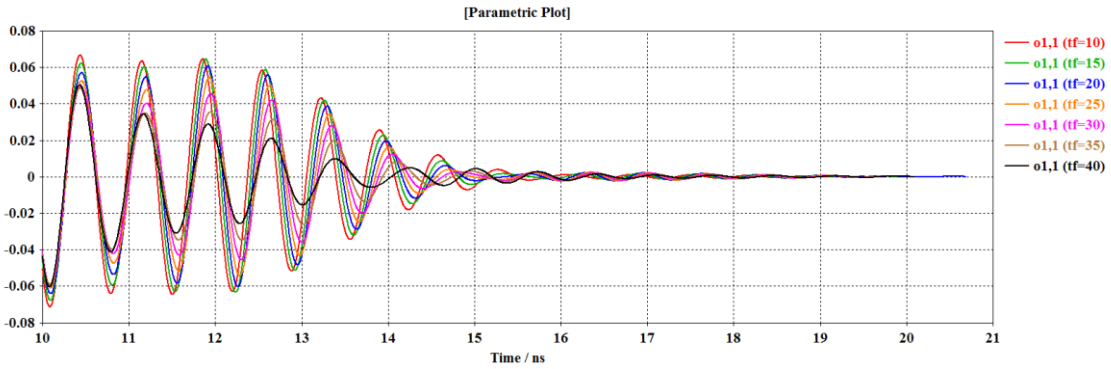

(b)

Fig 5. 25: Reflected pulses when the antenna placed 60 mm apart in the far-filed region from the modelled tissue and the fat layer sweep from 10 to 40 mm with 5-mm iteration.

Fig. 5.25 presents the reflected pulse in the time domain from different cases when fat thickness changes from 10 to 40 mm with steps of 5 mm. The results demonstrates a constant decrease in the amplitude of the reflected pulse for each case, which were expected and a constant time delay for each reflection that verifies premium operation for the system with reference to the different fat thickness.

In addition, comparing these far-field results, to the near-field results, we observe that there is decrease in the amplitude of the reflected pulse, which was expected. Because, the prior pulse always gets to the muscle earlier than others do, which means the pulse

penetrates in the muscle and the energy gets absorbed after that point, and no more reflection is expected refer to the unlimited muscle layer designed in the tissue modelled.

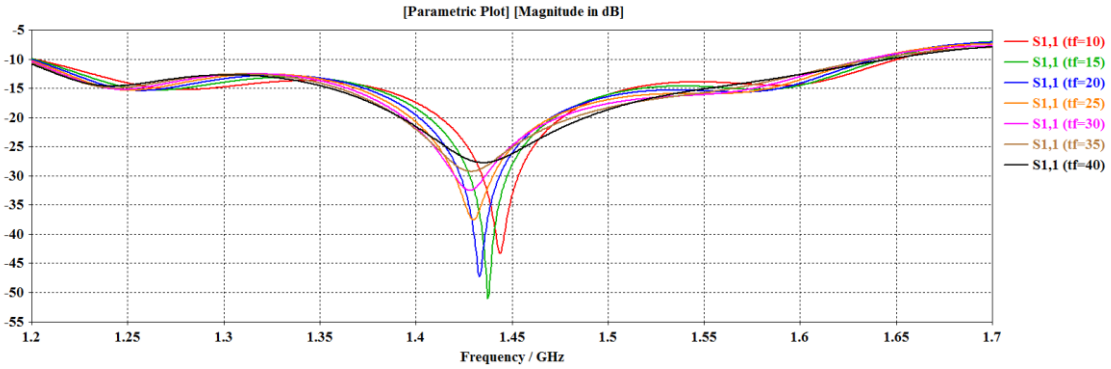

Fig 5. 26: S_{11} results for the case when the modelled tissue placed in the far-field region and consists of the fat layer with thicknesses of 10 to 40 mm with 5-mm thickness iteration.

Fig. 5.26 represents the S_{11} results of the system that verifies the magnitude and frequency shift changes with regularity within the interested region at the chosen centre frequency (1.4-GHz).

This verifies that the concept of measuring fat layer with different thicknesses using magnitude changes based on the absorption and reflection has been evaluated in the specific point and may differs in the higher frequencies.

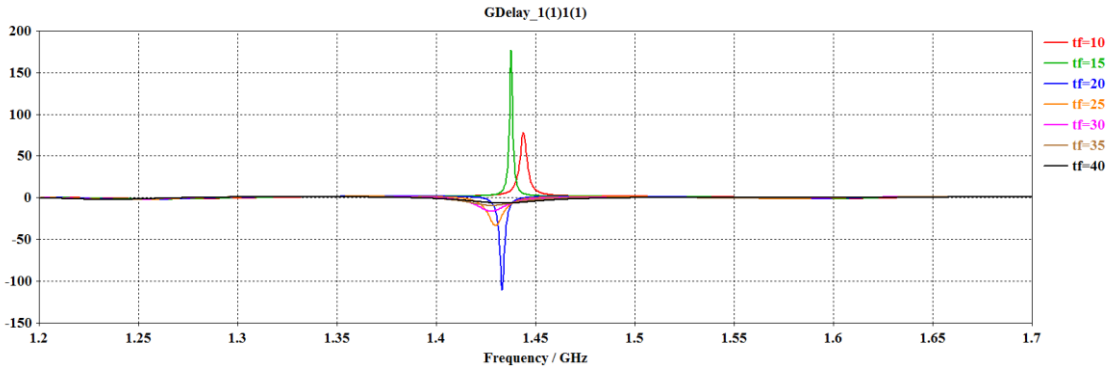

Fig 5. 27: Group delay results for the case when the modelled tissue placed in the far-field region and consists of the fat layer with thicknesses of 10 to 40 mm with 5-mm thickness iteration.

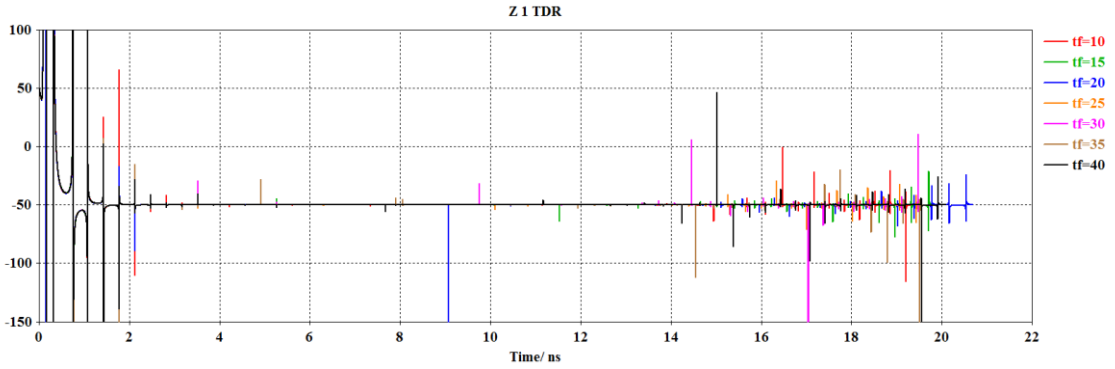

(a)

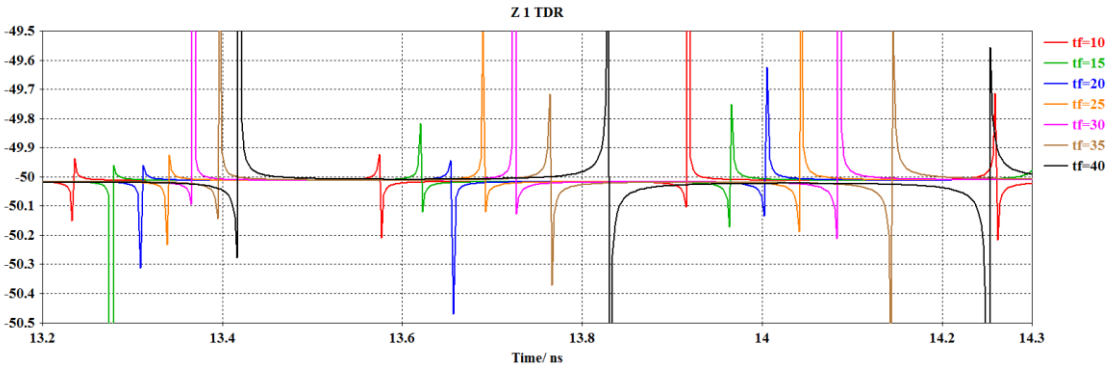

(b)

Fig 5. 28: TDR results for the case when the modelled tissue placed in the far-field region and consists of the fat layer with thicknesses of 10 to 40 mm with 5-mm thickness iteration.

Figs. 5.27, 5.28 illustrate the group delay and the TDR response of the system for each case at the chosen centre frequency for different the fat thicknesses. It shows the results are in agreement with expected received time, which can be defined as following.

The traveling time of reflected pulse must be found first to be able to define the pulse repetition time (PRT). However, defining the traveling time has a direct relation to the distance to the medium and the speed of the pulse within the medium that can be defined by the equation (5−4).

$$t = \frac{d}{v} \qquad \text{Eq. (5−4)}$$

in which , t represents the time taken for the pulse to travel from the transmitter to the target and reflected back to the receiver, d is the distance from the transmitter to a target and back to the receiver end, found by equation (5−6), and finally v is the velocity of the wave in the medium.

The distance of the excitation point to the medium can be found using equation (5−5):

$$d = 2\frac{l}{sin\theta} \qquad \text{Eq. (5−5)}$$

Where l represents the distance and θ is the angle of the pulse from/to the transmitter/receiver to the target. Moreover, the wave velocity can be defined by equation (5−6).

$$v = \frac{c}{\sqrt{\varepsilon_r}} \qquad \text{Eq. (5−6)}$$

Where v is the velocity of the wave in the specific medium, $c \cong 3 \times 10^8\, {}^{m}/_{s}$ is the velocity of the wave in free space (the same as light) and ε_r is the relative permittivity of the medium in a specific frequency.

Table 5. 3: Time taken for a pulse to transmit from one end of the mediums and reflected back to the same end.

Tissue types	Speed within the medium - V(m/s)	Thickness - l (mm)	Time taken to transmitt and reflect back - t (ns)
ceramic	0.046×10^9	201	$t_m = 4.3$
Skin	0.046×10^9	4	$t_s = 0.085$
Fat	0.129×10^9	20	$t_f = 0.15$
Fat	0.129×10^9	10	$t_f = 0.077$

Table 5.3 illustrates the time taken for the pulse to travel through each medium, based on their chosen approximate thicknesses. The calculation provides the time taken for the pulse to travel from the antenna port inside the high dielectric ceramic material to the modelled tissue and reflected back through the medium to the antenna port.

This means that the pulse must travel almost 105 mm to pass through the dielectric, which takes app. 4.3 ns. Moreover, travelling through the skin with the thickness of 2 mm will add up around 0.085 ns to overall travelling time, 0.15 ns for 10 mm of the fat thickness and further 5 mm steps fat thicknesses, which was added each time initiate the time of around 0.077 ns. Furthermore, there is delay inside the port itself, which is negligible and not being taken into the account.

Using Table 5.3, by adding the three last columns that represent the traveling time of the pulse from the port to the termination of the fat tissue layer in the first case, considering only 10 mm fat thickness, the travelling time can be determined by equation (5−7) and is shown in Fig. 5.29:

$$t = t_{muscle} + t_{skin} + t_{fat} = 4.3 + 0.085 + 0.15 = 4.535 \text{ ns} \quad \text{Eq. (5−7)}$$

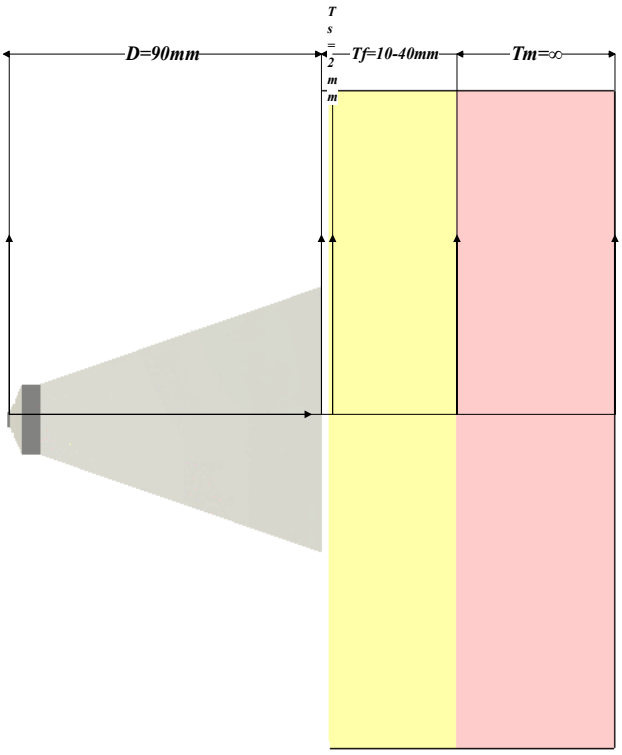

Fig 5. 29: Length of the antenna and thickness of the modeling tissue layers.

For initiating, the second case forward where 5 mm thickness of the fat will be adding to the fat layer, there is need of adding 0.077-ns to the time (t) that was defined by equation (5−7). Furthermore, the pulse itself has its own time taken to be generated based on its wide bandwidth and shifted frequency that is modulated with sign wave, which should be added to the delay initiate previously to be able to retrieve the pulse completion time into the system. Furthermore, there is need to generate a graph and equation that can be used to translate the results into a meaningful measurement of the fat layer thickness, to generate this graph, following processes were taken:

The first step is to save and transfer the reflection pulses from different cases where the fat thickness changed from 10 to 30 mm with steps of 5 mm individually. This can be determined by generating each case separately in a new project and saving the reflected pulse from the modelled tissue and transferring the data into the MATLAB software for further analysis. Fig. 5.30 represents reflected pulses for the different cases when the fat layer not presented and scenarios when the fat layer has a thickness of 10 to 30 mm with steps of 5 mm. Furthermore, for the case when the modelled tissue has not been presented, the energy has been absorbed within the high dielectric ceramic environment in the early stage of the time. Where as in the cases when the modelled tissue has been located in front of the antenna and specially the cases with a thicker fat layer, the energy has been

absorbed in much later time. When the conductivity of the embedded environment of the antenna is high and therefore the absorption rate parameter plays a critical role.

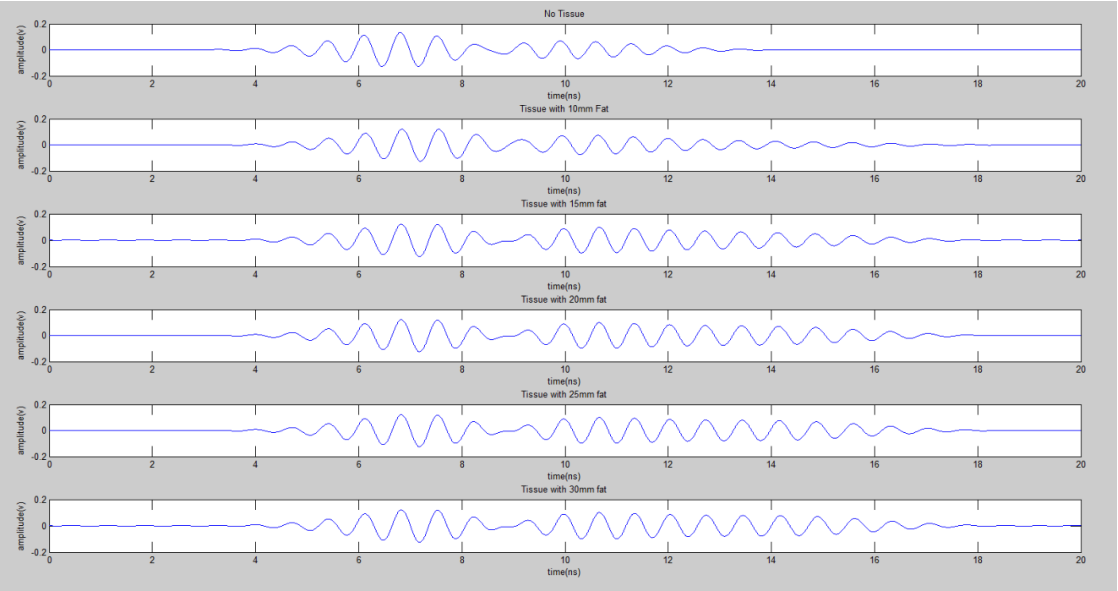

Fig 5. 30: The reflected pulse recorded in the case there is no tissue presented and in the cases when the tissue presented and thickness of fat layer differs from 10 to 30 mm by adding 5-mm fat to the fat layer of the each cases.

The next step was, to subtract all the five cases with different fat thickness from the case where there was no tissue presented in the designed system, to eliminate the effect of the antenna and the environment from the system.

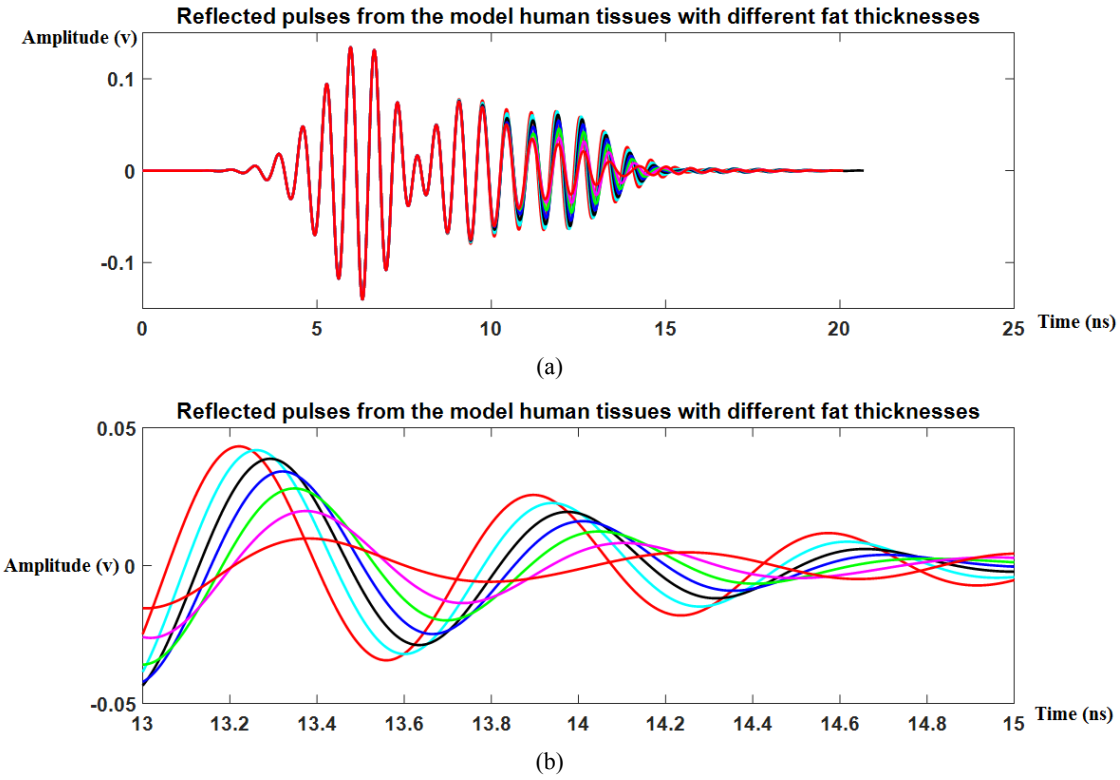

Fig 5. 31: The subtracted reflected pulse from the five cases thickness of fat differs from 10mm to 30mm by adding 5mm fat to each case from the case where the tissue was not present.

The amplitude and time shift in the highest point of the reflected pulses are shown in Fig. 5.31 which highlights a gradual increase of the amplitude as it was expected and time shifting which explains the time delays that have been added to each case as the thickness of the fat increase by 5 mm rapidly. In the following step, the results taken from the MATLAB were recorded in the Microsoft Excel (ME) and amplitude and time graphs were generated as shown in Fig. 5.32.

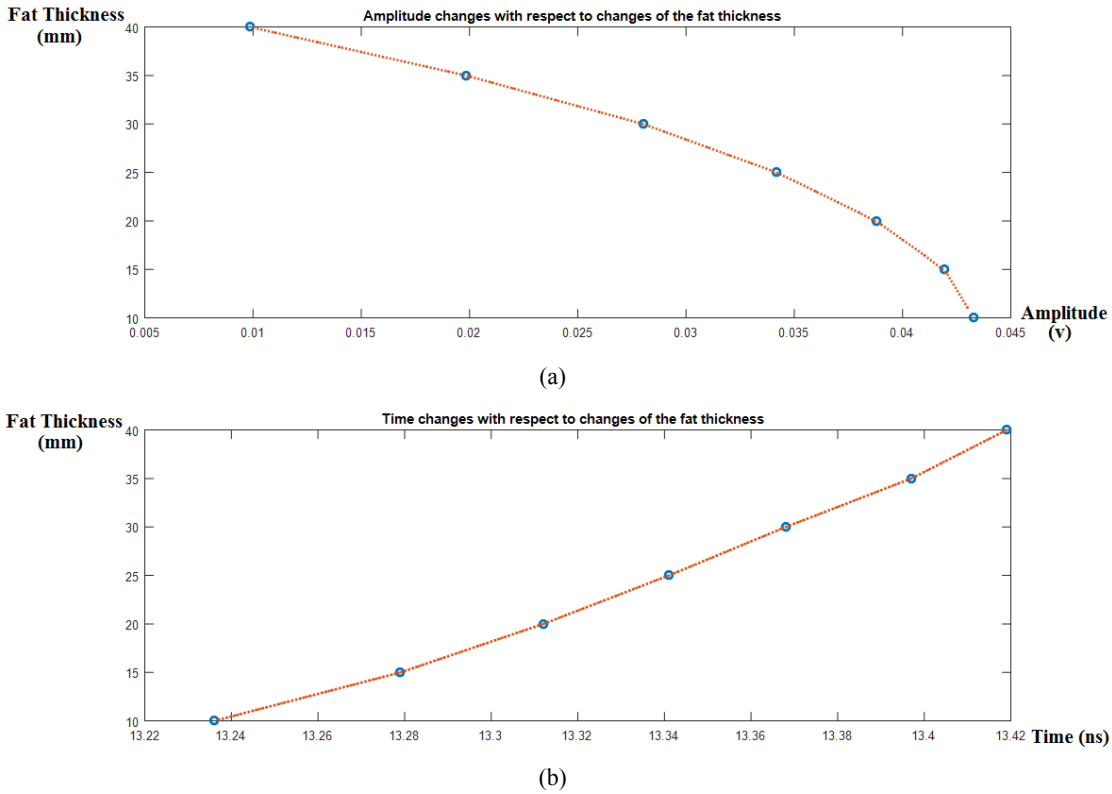

Fig 5. 32: Reflected pulses highest amplitude and related time of a chosen window time of 13 to 13.5 ns for different fat thickness cases (10 to 40 mm).

Fig. 5.32 presents the estimated table values of the (a) amplitude and (b) time shifting in the different cases where the fat layer is differing from 10 to 40 mm with steps of 5 mm. The highest pick of the chosen window time (13 to 13.5 ns) were recorded using the MATLAB graph shown in Fig. 5.31.

In addition, the graphs shown in Fig. 5.32 can be employed to generate an equation to predict the unknown thickness of the fat layer based on the amplitude and time of the reflected pulse. The method was applied to determine the thicknesses of few predefined cases to validate the method in the simulation that shows the approximate confirmed results, which verifies the system operation [5, 6].

5.1.4. THE SYSTEM METHODOLOGY

This section is focuses on the methods used by the system to extract information from the reflected pulses captured by the system for different fat thicknesses (15-40 mm). First step is to separate the reflected pulse from the conjunction of the fat layer with the muscle layer from the entire reflected pulses. To be able to assign a section of the reflected pulse to conjunction of the fat and muscle layers, which in fact should be the second big reflected pulse in the entire reflected pulses, the traveling time should be calculated.

5.1.4.1. TRAVELING TIME

The multilayers human tissue model has different specifications not only in terms of electric properties but also in terms of the thickness of each layer, which causes generation of several echoes traveling time specific to each layer in the system. The traveling time of the reflected pulse should be determined in order to be able to define the PRT. However, traveling time has a direct relation to the distance where the pulse is echoed by a medium. The equations (5-5 to 5-7) will be used again to define the velocity and time taken for the pulse to travel in each of these mediums.

Table 5. 4: Travelling time calculation for the pulse in the medium.

Environments	**Connector**	**Antenna**	**Skin**	**Fat**
Materials	**Teflon**	**Ceramic**	**Human Skin**	**Human Fat**
Relative Permittivity (ε_r)	2.1	41	41	10
Length (mm)	10	91	2	10
Velocity (m/s)= $c/\sqrt{\varepsilon_r}$	207019668	46852128	46852128	94868330
Time (ns)= $2l/v$	0.096	3.884	0.085	0.2

Start of triggering for the monitoring window was selected based on the minimum size of the fat layer and the end time can be defined for the case having larger amount of fat. The total traveling time from the excitation point of connector up to the conjunction point of the fat layer with muscle layer was calculated to be 4.26 ns in Table 5.4. The rise time starting point, which is 2 ns, should be added to the time that comes to 6.26 ns.

This gives the starting time of the scanning for the selected reflected pulse. The highest amplitude after the start scanning window time is selected as inspection point of the selected pulse, but this may alter a bit depending on the fat thickness.

5.1.4.2. REFLECTION BASED METHOD

This system operates based on the Reflection and the TDR techniques, which have been used previously by researchers [7, 8]. This technique first monitors the reflected pulse based on expected traveling time and then collects the highest amplitude point within the monitoring time. The result then is inserted into the equation, which is defined based on the data, retrieved for different fat thicknesses. The TDR technique is used alongside with the reflection technique in order to increase the accuracy of the system. The monitoring window has been calculated and set to 7 to 10 ns for the reflected pulse from the conjunction of fat with muscle layer. The highest amplitude wave has been selected, and the time and amplitude have been recorded for different fat thickness from 15 to 40 mm.

Table 5. 5: The highest amplitude of the reflected pulse from the fat to muscle conjunction.

Thickness (mm)	*Amp (v)*	*Amp_diff (v)*
15	0.195	x
20	0.196	0.0117
25	0.185	0.0187
30	0.166	0.0213
35	0.145	0.0212
40	0.123	

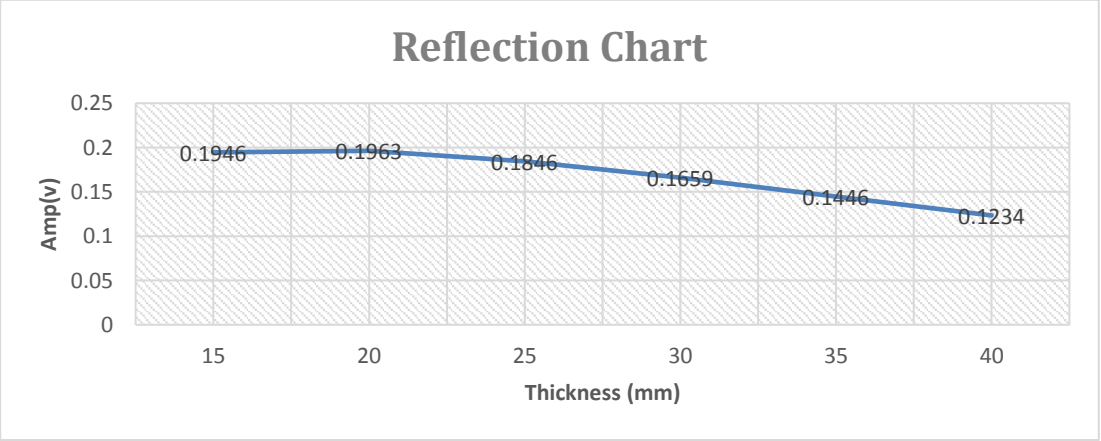

Fig 5. 33: Amplitude data generated from the reflected pulse based on different fat thickness (15 - 40 mm).

The graph in Fig. 5.33 has been plotted based on the amplitude of highest point in the monitoring window time. As it is noticed in the first point, there is a small shift in the simulation, which is caused by the far field constraint and can be ignored. An equation generated by the MATLAB software can describe the data and can be used to estimate the thickness based on given amplitude shown in Fig. 5.34.

Linear model Poly2:

$$f_1(x) = p_1x^2 + p_2x + p_3 \qquad \text{Eq. (5–8)}$$

Coefficients (with 95% confidence bounds):

p_1 = -1152 (-3398, 1093), p_2 = 102.6 (-617.4, 822.6), p_3 = 44.69 (-11.7, 101.1)

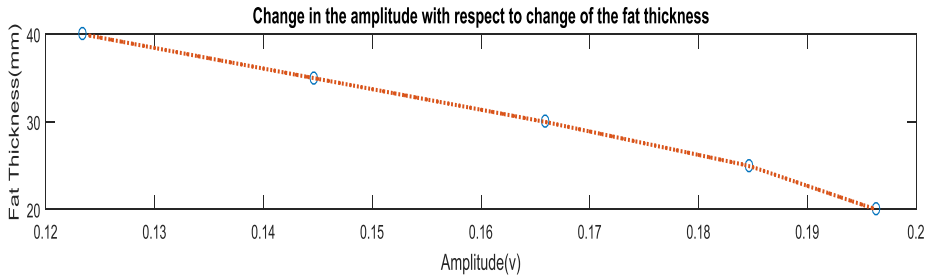

Fig 5. 34: The MATLAB graph generated for amplitude change based on fat thickness change from 20 to 40 mm.

Fig. 5.35 represents the S_{11} graph, for different fat layers from 15 mm to 40 mm, and demonstrates the stability in system operation against frequency. The S_{11} graph proves that the pulse has better consistency in lower frequencies compared to high frequencies where there would be less penetration depth.

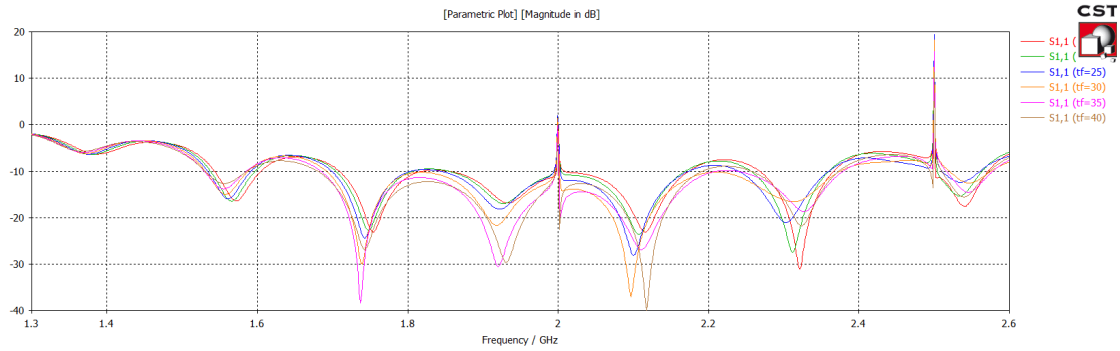

Fig 5. 35: Generated S_{11} graph for the tissue model when the fat layer thickness changes from 15 to 40 mm.

The time domain refectory (TDR) graph has been generated using the CST software, the TDRs have been investigated in terms of highest amplitude reflected pulse, for all cases where the fat thickness was changing in steps of 5 mm and results are shown in Fig. 5.36.

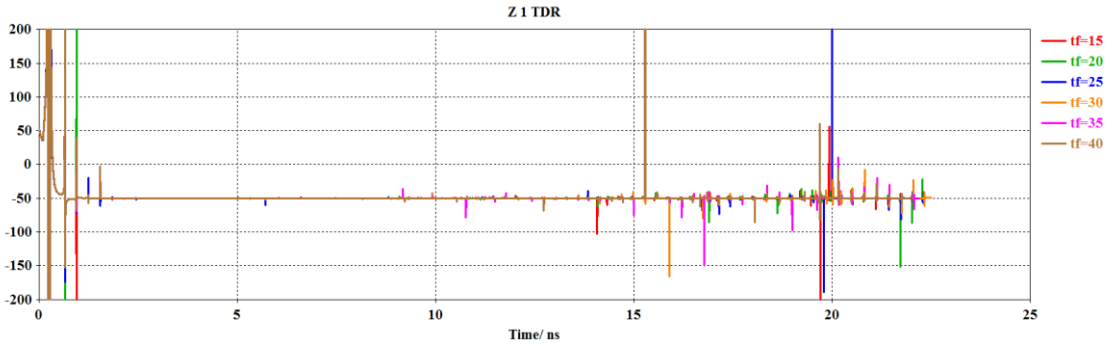

(a)

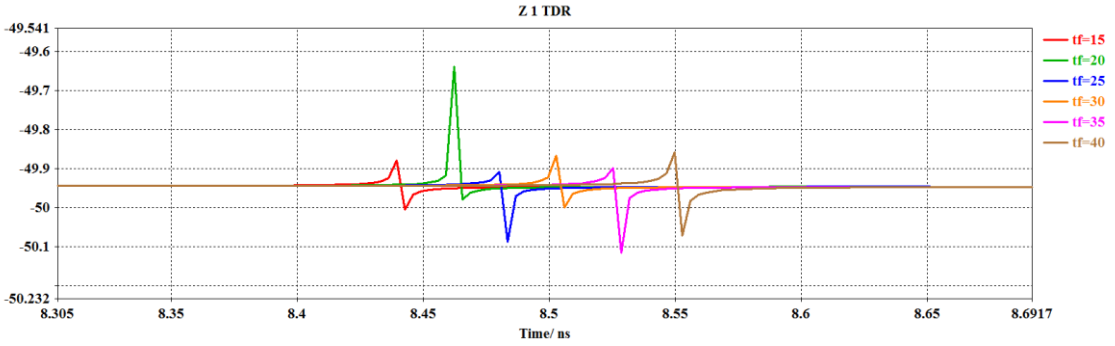

(b)

Fig 5. 36: Generated the TDR graph using the predefined widow for the time of arrival for the pulse for different cases where the fat thickness changes.

The monitoring window has been selected based on the relaxation time of the reflected pulse. The results were recorded in a Table and a graph was generated for time delay for different fat thicknesses from 15 to 40 mm. Results are presented in Table 5.6, Fig. 5.37.

Table 5. 6: The time of the highest amplitude of the TDR graph when the reflected pulse was received from different cases when the fat thickness iterates from 15 to 40 mm.

Thickness (mm)	***Time(ns)***	***Time_diff (ns)***
15	8.4394	x
20	8.4623	0.023
25	8.4804	0.018
30	8.5028	0.0224
35	8.5254	0.023
40	8.5497	0.024

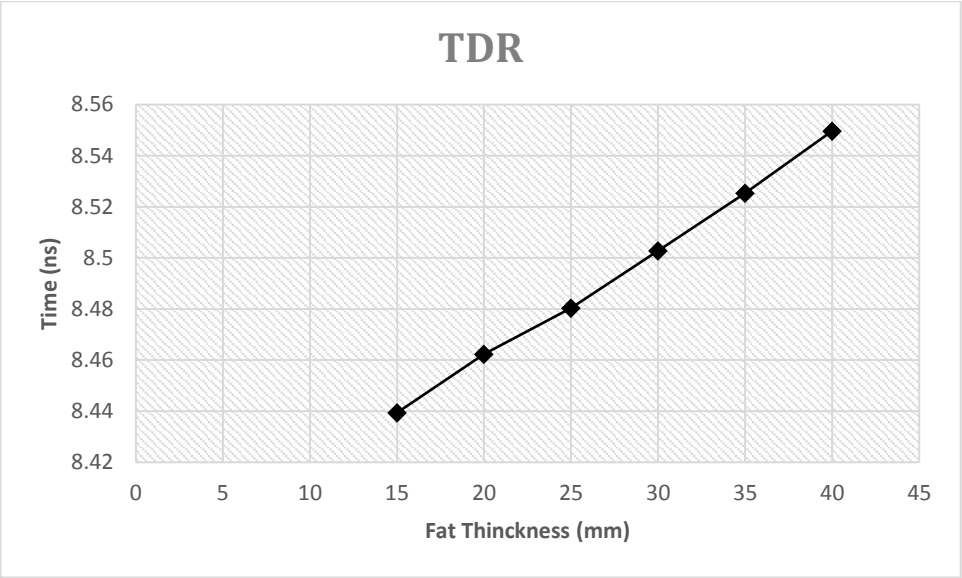

Fig 5. 37: Generated graph regards to the time difference for the cases when the fat thickness iterates from 15 to 40 mm.

Fig. 5.37 represents the time delay occurred for different fat thicknesses, which can be used later in the system design to measure the fat thickness. An equation was generated using the MATLAB software, which is used to determine any fat thicknesses base on the TDR method. A good consistency of time delay concerning the fat thickness can be observed in the simulation result shown in Fig. 5.38. This justifies why, the method is chosen by researchers and widely being used in the system.

Linear model Poly2:

$$f_2(x) = p_1x^2 + p_2x + p_3 \qquad \text{Eq. (5–9)}$$

Coefficients (with 95% confidence bounds):

p_1 = -156.9 (-999.5, 685.8), p_2 = 3313 (-1.336e+04, 1.999e+04),

p_3 = -1.74e+04 (-9.99e+04, 6.511e+04)

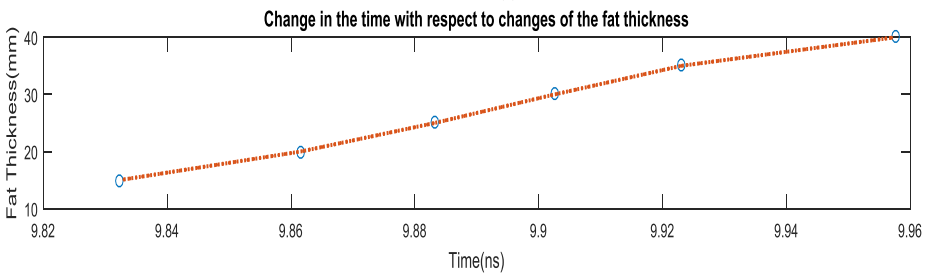

Fig 5. 38: The Mat-Lab graph generated for the time change based on fat thickness changes from 15 to 40 mm.

The TDR results shown in the Fig. 5.38 represent the time reflection pulses dealy for different fat thicknesses from 15 to 40 mm. The results can be used to determine fat thickness in the system. Both the reflection pulse and the TDR response can be used in the system to increase the accuracy of the system.

5.1.5. SYSTEM ANALYSIS USING THE DRGH ANTENNA DESIGNS WITHIN IDEAL HIGH DIELECTRIC

In this section, the system operation is investigated for the case when the DRGH antenna is embedded in an ideal high dielectric (41) to measure the fat thickness of the modelled tissue, which was designed and tested in Chapter 3. The design advantages from wider bandwidth compared to the previous PDRH antenna design are better range resolution and high centre frequency that results less penetration depth. A GP with the 700 MHz bandwidth ($f_l = 1.7\ GHz$ & $f_h = 2.4\ GHz$) was generated using the CST software as shown in Fig. 5.39.

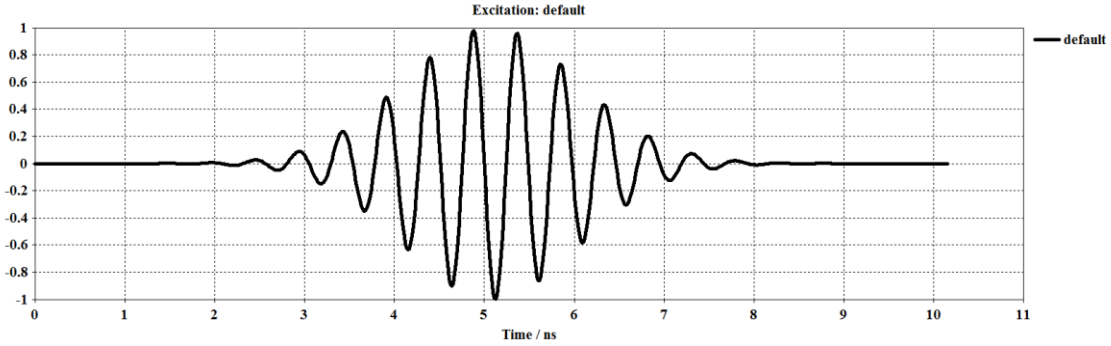

Fig 5. 39: A GP with the lower and higher frequencies of ($\boldsymbol{f_l = 1.7GHz, f_h = 2.4GHz}$) generated using the CST-MWS software.

To be able, to recognize w here the best place to locate the tissue concerning the delay needed to avoid overlapping and move close to the far field region. The calculations were obtained to compute for far-field region, which was defined previously.

$$\lambda = {}^{c}/_{f\sqrt{\varepsilon_r}} = \frac{3\times10^8}{1.8\times10^9\times\sqrt{41}} = 26mm \qquad \text{Eq. (5–3a)}$$

$$d_f = 2 \times D^2/_{\lambda} = \frac{2\times32^2}{26} = 78mm \qquad \text{Eq. (5–3b)}$$

Refer to the parameter's definitions determined using the predefined equations (5–3a, b), the minimum antenna length should be 78 mm. Therefore, the antenna was placed 85 mm apart from the modelled tissue to be close to the far field region of the antenna and getting better response from the system.

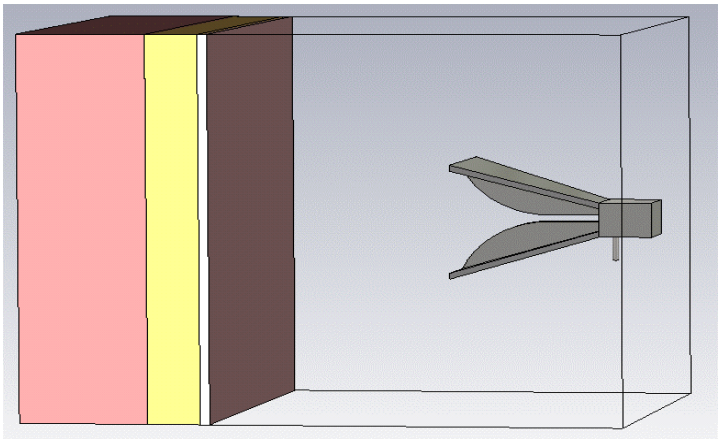

Fig 5. 40: Modelled tissue placed in front of the DRGH antenna, 85 mm apart in the antenna far-field region.

Fig. 5.40 represents how the DRGH antenna was placed in front of the modelled tissue with distance of 85 mm apart. The simulation results will be generated for five sweeping points, where the thickness of the fat increasing from 15 to 40 mm with 5 mm steps.

The created GP was transmitted through the antenna to the modelled tissue and reflected pulses were generated using CST-MWS software for further analysis. The centre frequency for the design was selected as 1.8 GHz considering the antenna operated frequency and penetration depth parameter required for the system.

Table 5.7 illustrates the dielectric properties, loss tangent, and wavelength and penetration depth defined for each tissue types in 1.8 GHz frequency based on equation (2−10).

Table 5. 7: Dielectric properties and penetration parameters of three type of human tissues employed in the modelled tissue.

Tissue Name	Frequency (GHz)	Conductivity (S/m)	Relative Permittivity	Loss tangent	Wave -length (mm)	Penetration depth (mm)
Skin Dry	1.8	1.185	38.8	0.304	26.4	28
Skin Wet	1.8	1.232	43.8	0.280	24.9	28.80
Fat	1.8	0.078	5.1	0.146	71.8	157
Muscle	1.8	1.341	53.5	0.226	22.60	29.2

The parameters determined in Table 5.7 for different tissue types with their dielectric properties, suggest that employing the pulse with a 1.8 GHz centre frequency, there would be applicable penetration depth through the modelled tissue.

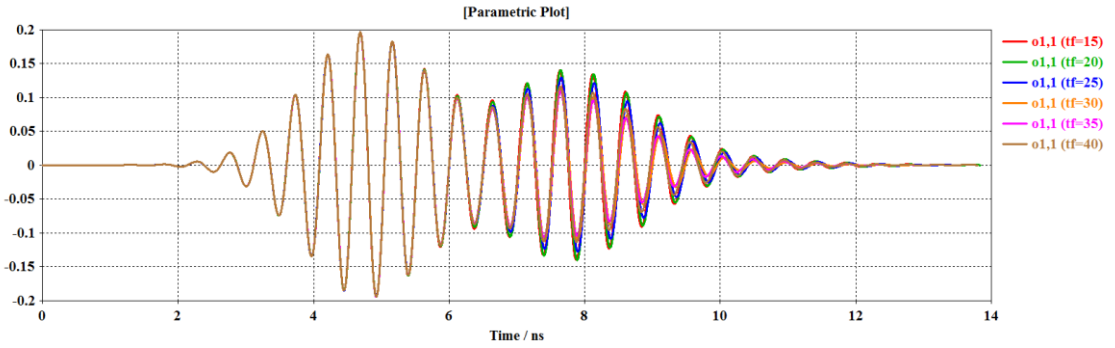

(a)

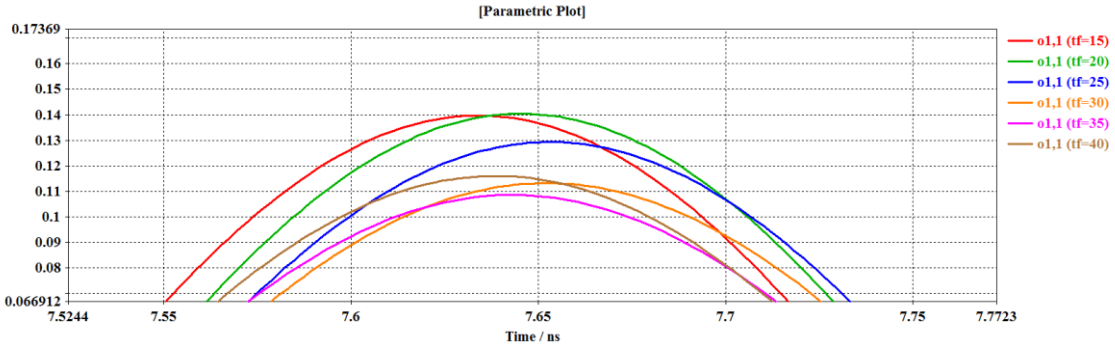

(b)

Fig 5. 41: Reflected pulses from the modelled tissue in the case where the fat layer thickness changes from 15 to 40 mm with thickness iteration of 5 mm.

Fig. 5.41 represents changes in amplitude for different fat thicknesses of 15 to 40 mm with 5 mm steps, which indicates an increase in the first two steps followed by a sudden reduction of amplitude in next four steps and increase of last step. The first two amplitude increase could be expected while increasing the fat thickness, but sudden changes in amplitude can be explained as the pulse should be very weak by the time hitting the muscle layer in the last case (t_f = 40-mm).

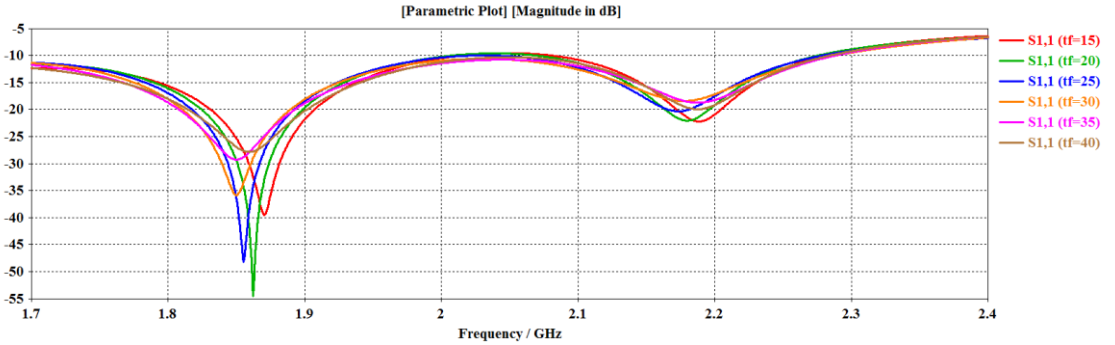

Fig 5. 42: S_{11} results of the modelled tissue in the case where the fat layer thickness changes from 15 to 40 mm.

The S_{11} results represented in Fig. 5.42, demonstrates the magnitude changes and shifting of the frequencies that can be clarified from the chosen screening window (i.e. 1.8 to 1.9 GHz) from the lowest magnitude. This indicates same behaviour as reflected pulses for

different cases and do not behave in repetitive manner in the higher and lower frequency range for different fat thickness.

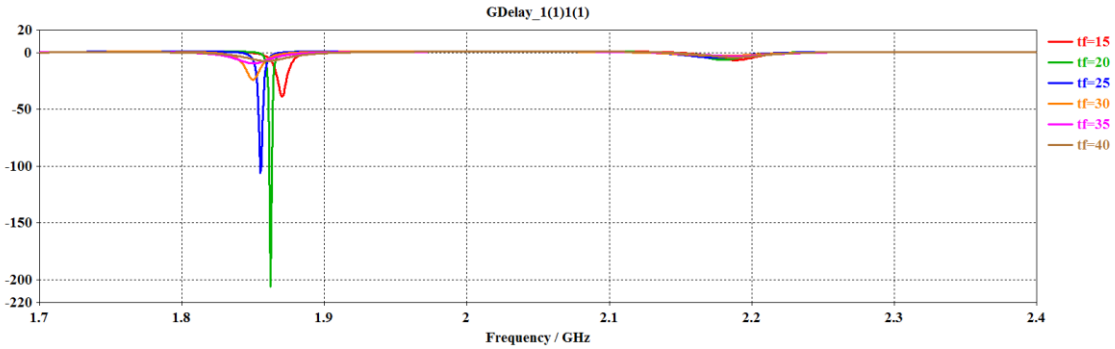

Fig 5. 43: Group delay results generated for the modeled tissue in the cases where the thickness fat layer changes from 10 to 40 mm with the thickness of 5-mm iteration.

Fig. 5.43 represents the group delay of the transmitted pulses for different thickness of the fat layer from 15 to 40 mm. The results represents irregular changes for the lowest and highest thickness, and regularity in other thicknesses, which was expected.

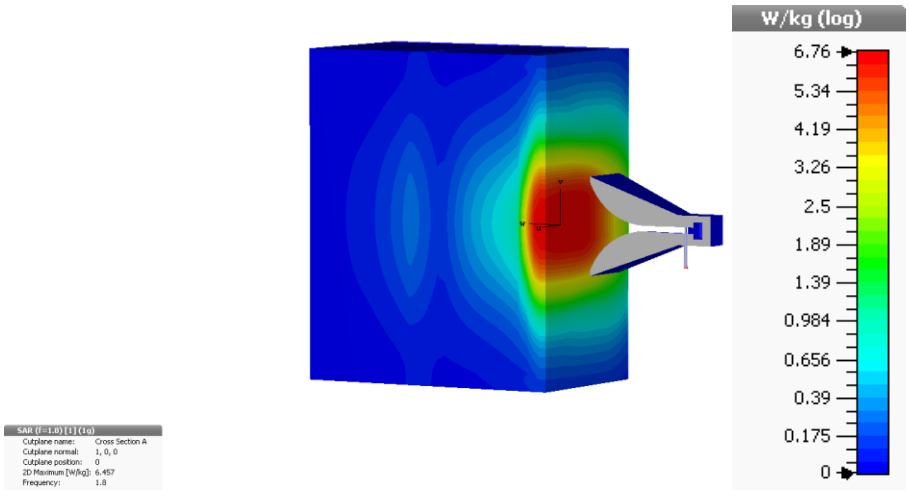

Fig 5. 44: SAR results of the modeled tissue generated in the case where the fat layer thickness is 10 mm.

Finally, by analysing the SAR of the wave propagation through the medium with fat layer thickness of 10-mm that (Fig. 5.44), it can be proved that the pulse strength is poor with respect to the penetration through the modelled tissue compare with previous PDRH designs. This can be the reason why it cannot illustrate good results in the first and last cases. The next approach was to redesign the antenna to increase the bandwidth without increasing the size, different approaches such as corrugation was studied, which makes the design more complex. The new design was studied, which was to make the pyramidal shape into the elliptical cylinder shape. The EDRH antenna had increased the bandwidth to double the previous pyramidal design that may improve the system operation.

5.1.6. SYSTEM ANALYSIS USING THE EXTENDED EDRH ANTENNA IN HIGH DIELECTRIC MIXTURE OF PARAFFIN AND TITANUIM OXIDE

The EDRH type of antenna has been selected by various research groups for biomedical applications to monitor inside the human body. This antenna attracts the attention of many other engineers and researchers in the radar field, due to its advantages such as large bandwidth, high gain/directivity, and matching capability. These important principles make this type of antenna an efficient solution, as compared with the other bidirectional types, such as Vivaldi, bowtie, and wire helix. Considering these advantages, the antenna suffers from some disadvantages, such as high fabrication cost due to the shape complexity, and a large aperture for the low-frequency applications (2–6 GHz). Using the low frequency for such an application that aims to scan the human body is a crucial demand due to the penetration depth factor. The antenna with an extension was successfully designed in Chapter 4 and embedded with the dielectric mixture of the paraffin with the r-TiO_2 has been employed in this section, to analyse the system behavior before proceeding to the experimental part of the system. A human abdominal tissue consisting of 2 mm skin, 10 mm fat and infinite muscle, with width and height of 100 mm were constructed in CST software and the extended EDRH antenna was placed in front of the modeled tissue as presented in Fig. 5.45. The UWB GP with the given bandwidth was generated using the CST software. The pulse later was transmitted to the tissue modeled and the reflected pulse was recorded.

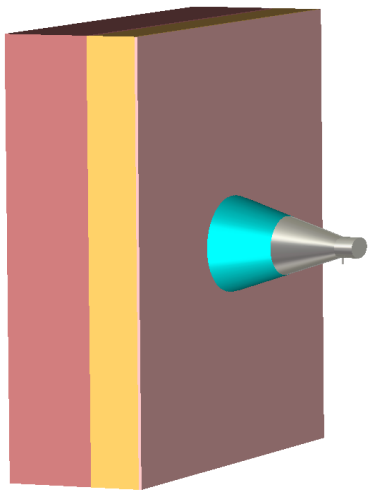

Fig 5. 45: The extended EDRH antenna filled with the ceramic placed on the tissue modeled.

Moreover, the measured dielectric properties of the mixture in the frequency region, has been loaded into the software using the new material dispersion, as shown in Fig. 5.46.

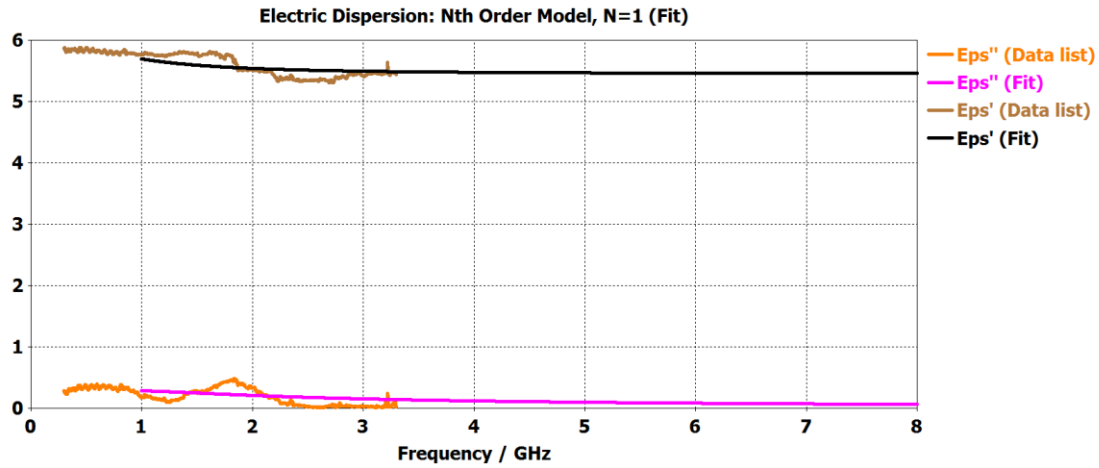

Fig 5. 46: Measured dielectric properties of the mixture has been loaded into the CST software.

The next step was to check the reflection coefficient of the antenna design when it has been located on the modelled tissue when the fat layer has thickness of 35 mm (assumed to be the obese case), which was modelled and generated using the CST-MWS software and shown in Fig. 5.47.

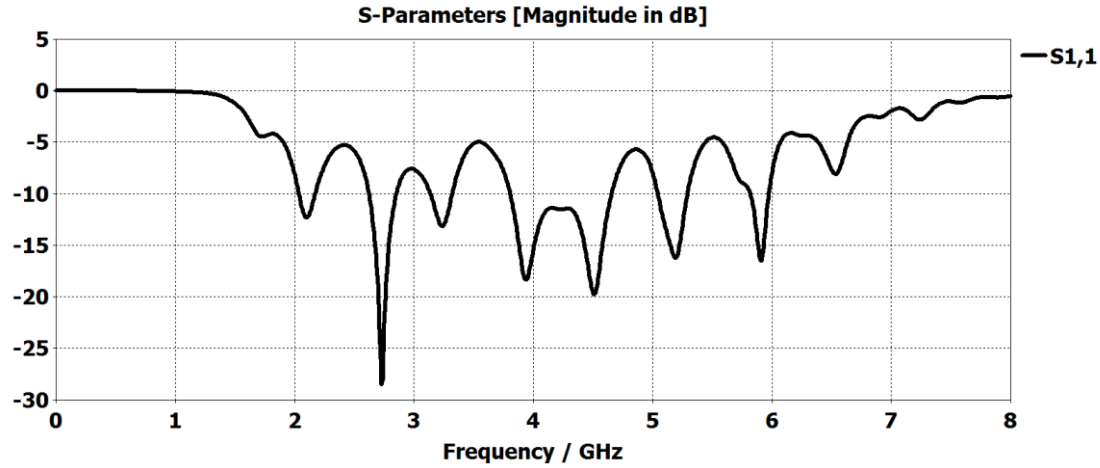

Fig 5. 47: S_{11} for the extended EDRH antenna filled with the ceramic placed on the tissue modeled.

The reflection coefficient of the antenna when was placed on the modelled tissue presented in Fig. 5.40. The antenna operation point was selected at –5 dB, which was defined by the researcher as acceptable operating point in the on body medical application [9]. This confirms the antenna operating bandwidth of approximately 4 GHz that was deepen at around 1.9 GHz frequency. The GP with the bandwidth of 1 GHz (1.9–2.9 GHz) was generated using the CST software as shown in Fig. 5.48. The pulse will be used to transmit to the tissue and the reflected pulse will be recorded for further analysis.

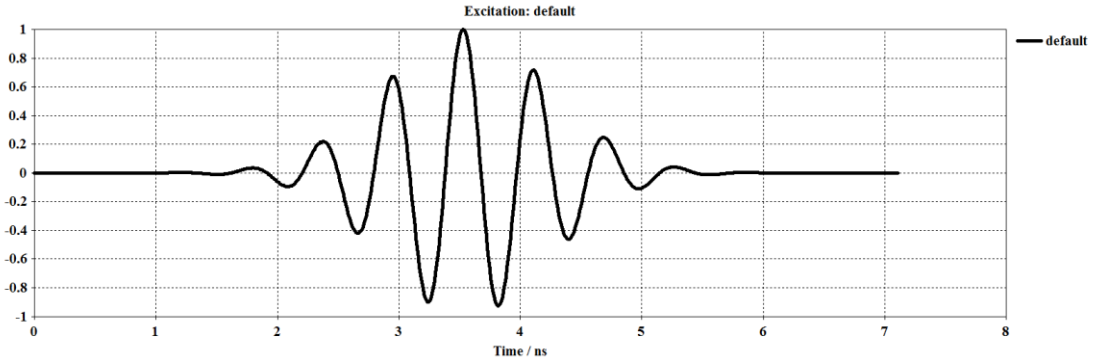

Fig 5. 48: Generated a GP with 1GHz bandwidth (1.2-2.2GHz).

The pulse transmitted to the tissue modeled in five sequences, where in each sequence, the thickness of the fat layer was changing from 15 mm to 40 mm with steps of 5 mm, and the reflected pulse for each case were recorded as is represented in Fig. 5.49.

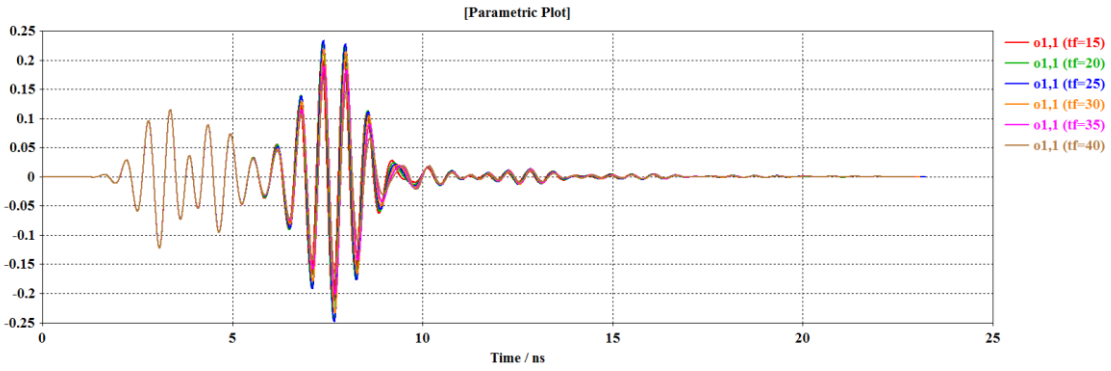

(a)

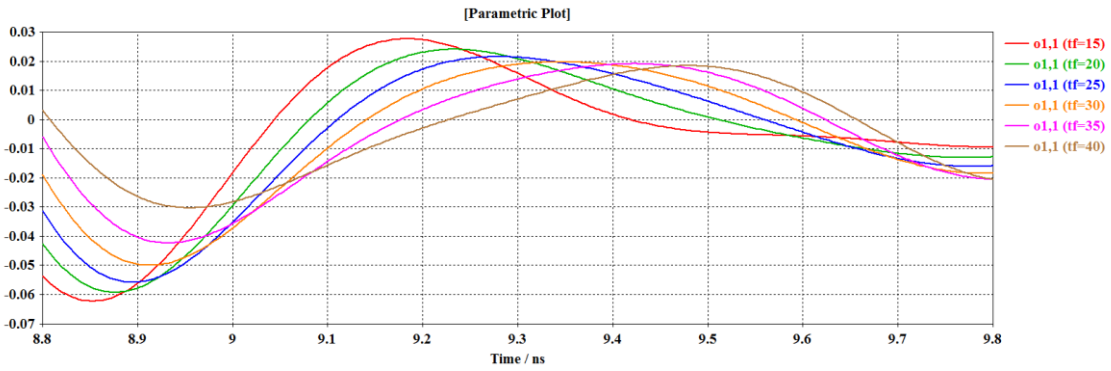

(b)

Fig 5. 49: Reflected pulses when the fat layer thickness changed from 15 to 40 mm with an iteration of 5-mm.

The window selected on the reflected pulses based on the calculated traveling time represents a decrease in the amplitude and time shift of each case in a repetitive manner.

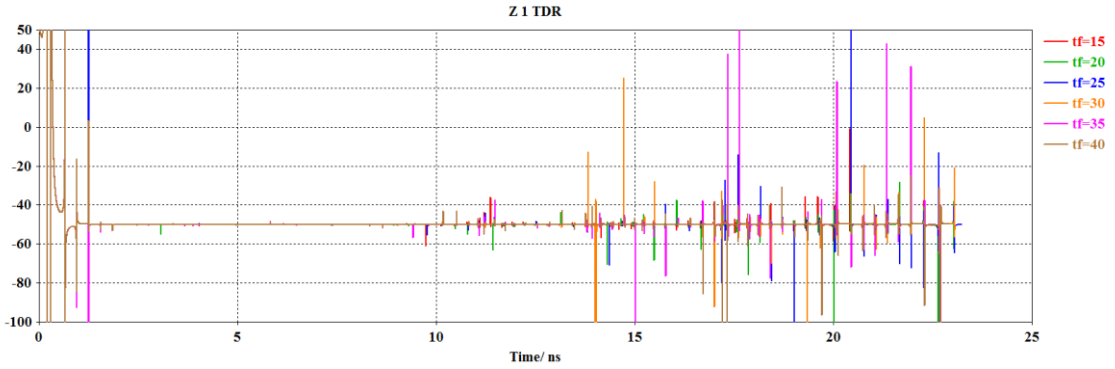

(a)

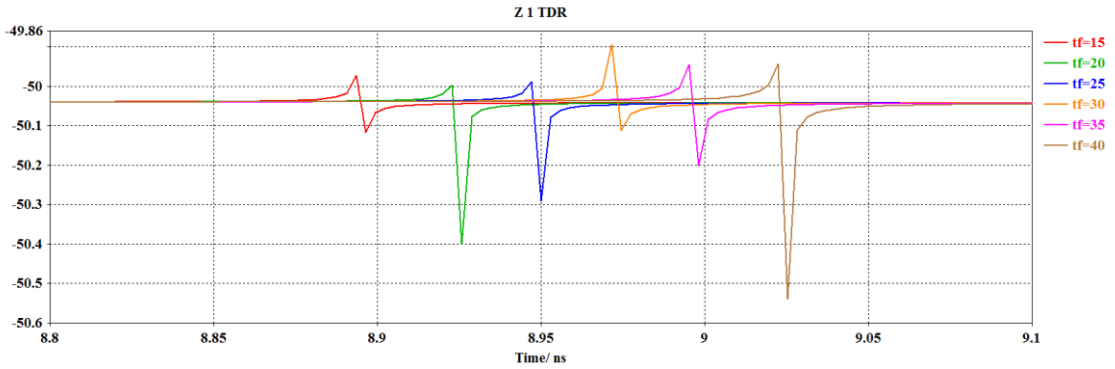

(b)

Fig 5. 50: The TDR graph when the fat layer thickness changed from 15-40mm with an iteration of 5mm.

The TDR graph that is represented in Fig. 5.50, demonstrates the reflected pulses in the monitoring area where the reflection of the last layer that was 40mm expected to arrive. The results show the continuous time difference between each case. In the next stage of the system behaviour, the tissue model that consists of two layers, including 2-mm skin and infinite muscle, has been redeveloped, assuming there is no fat existing in this specific area. Fig. 5.51 shows the stage, presenting the proposed antenna filled with the mixture material placed on the modelled forearm tissue.

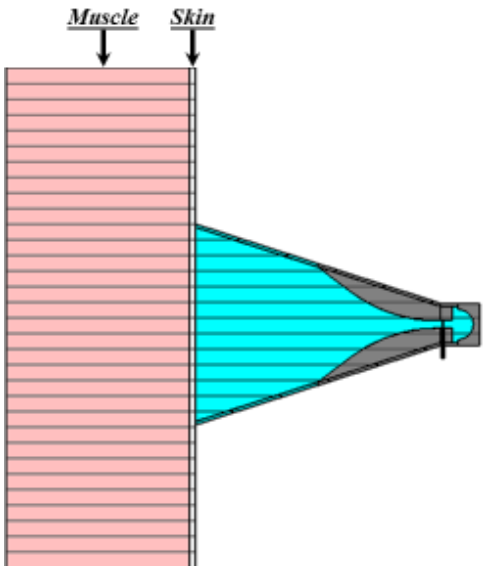

Fig 5. 51: Proposed EDRH antenna, which has been located on the modelled forearm tissue.

The reflection coefficient results are obtained for a frequency range up to 8 GHz; assumed as a calibration point shown in Fig. 5.52. These results demonstrate a frequency shift of 140 MHz in the spectrum of interest, compared with the case where the modeled tissue was not present as shown in Fig. 5.47, but still obtaining the same bandwidth of 4 GHz.

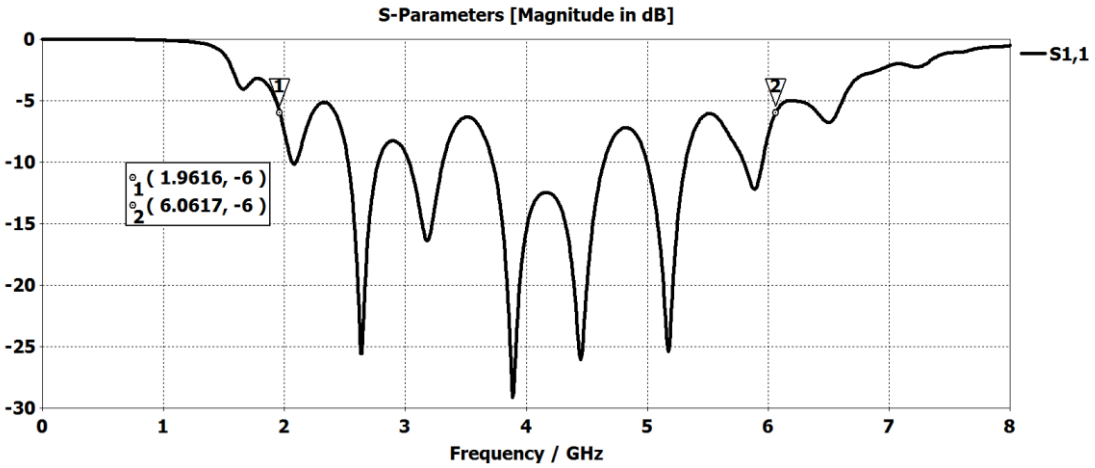

Fig 5. 52: Simulated S_{11} of the antenna, when the fat layer does not exist.

Fabrication of the complex 3D-printed EDRH antenna requires an 3D printer using a metal (copper and aluminium) or plastic (polyethylene and acrylonitrile butadiene styrene), and some modification to the design, such as cutting the antenna symmetrically to two parts prior to printing, and attaching them back together, as in Fig. 5.53 (a) [10-12].

The Stratasys Objet30 Prime 3D printer has been used to print the prototype with a resolution of 100 μm. The prototype has been realized with a clear finish, and the supportive material that was removed by rinsing the prototype using pressurized water. The cost of a Vero clear transparent polyethylene is ~ 650 USD per kg [13].

Hence, the cost of the Vero material including the support material used to 3D print the prototype is less than 50 USD. Hence, the Objet30 printer, offers cost-effective solutions for 3D printing small complex antenna structures with a high resolution. In addition, the printed EDRH antenna is painted with a silver conductive paint with acceptable conductivity [13] to the extended part.

In addition, the antenna was connected to a 50-ohm cable SMA connector with an outer dimension of 1.19 mm fed and glued to the lower- and upper-ridges of the antenna, as shown in Fig. 5.53 (b). The two sections of the antenna then glued together, and the glued area was painted and finally filled with the prepared high-dielectric mixture. During this

process, it was placed upside down to remove any remaining bubble gaps produced during the mixing and filling process; i.e., Fig. 5.53 (c).

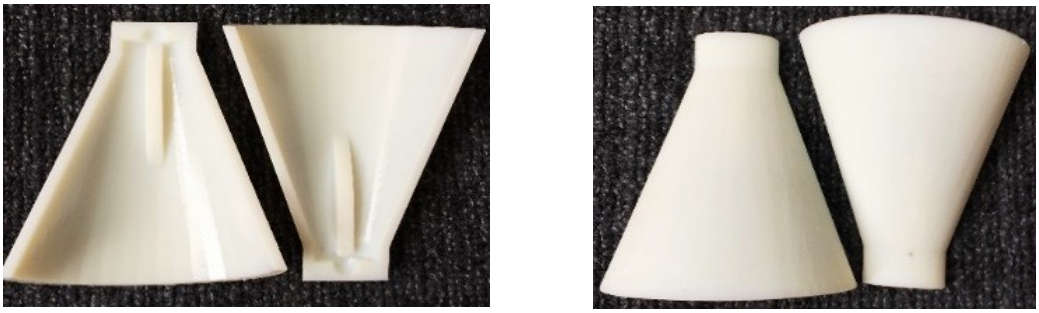

(a). 3D-printed EDRH antenna using the polyethylene material.

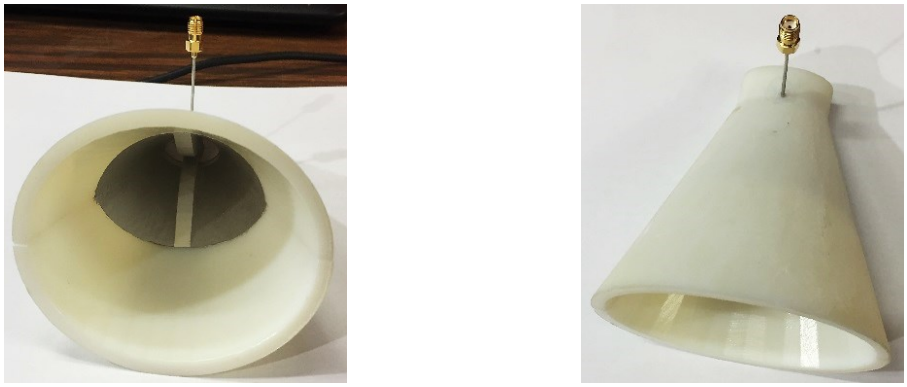

(b). 3D-printed EDRH antenna, as conductive-painted and fed with a semi-ridged SMA connector.

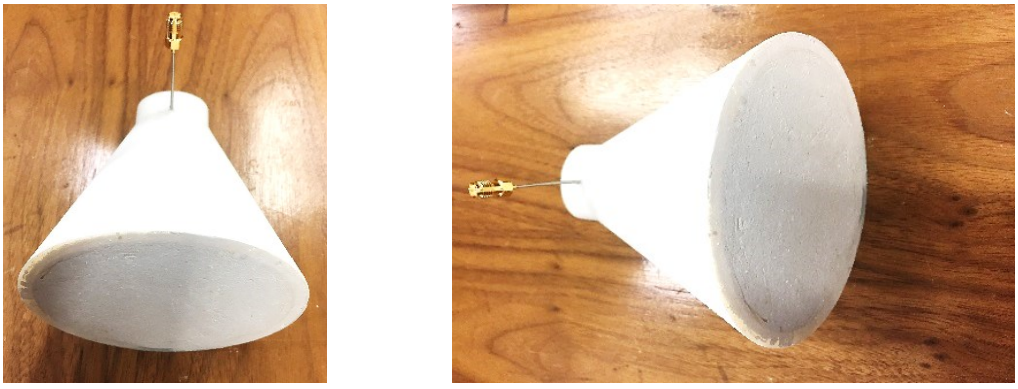

(c). 3D-printed EDRH antenna, filled with the high-dielectric mixture.

Fig 5. 53: Fabrication process of the 3D-printed EDRH antenna.

The forearm of the body is selected as the equivalent tissue to the modeled tissue in the simulations, with regards to the non existance of the fat layer. The flexible coaxial cable is utilised to connect the antenna to the VNA and was calibrated to remove the cable effects using the Ecal calibration kits. The fabricated antenna filled with the dielectric mixure was placed on the forearm location of the human arm and is shown in Figs. 5.54.

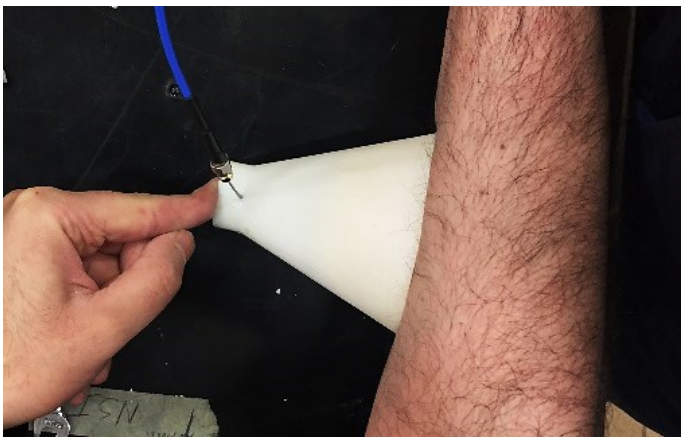

Fig 5. 54: The 3D-printed antenna placed on the arm for the calibration.

The reflection coeffeint results have been obtained and compared with the simulations at the first resonance point below –6 dB (chosen to be the operating point for this antenna), which refers to the on-body biomedical applications, as shown in Fig. 5.55 [9]. The comparisons shows a frequency shift of 0.4 GHz, to the higher band, and an increase of –3.39 dB in the magnitude at the first large resonance. This was expected due to the different effects and errors, such as the fabrication process, experimental environment, and human errors can build up to the real data compared to the simulated data. It should be noted that the air gap between the antenna and body can be reduced using the semi-solid mixture (e.g., oil and r-TiO_2) and have same dielectric constant that has removed the effect of the air gap in the real experiment. This novel method of implementing a materials-filled antenna system can be deployed in the other biomedical applications that aim to scan inside the human body, such as in the abdominal fat measurement [14].

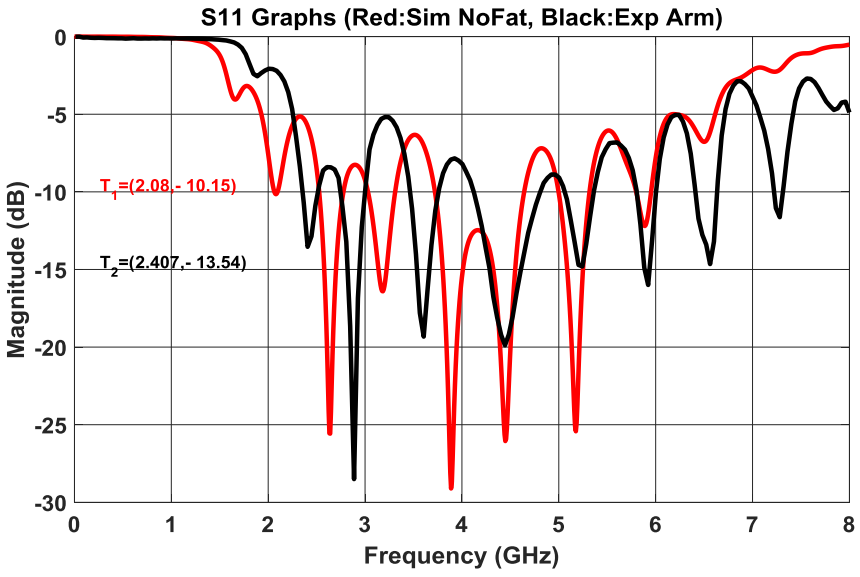

Fig 5. 55: The red plot depicts the simulations; i.e., no fat case; and the black plot shows the measured results obtained based on the arm's case.

5.1.7. SYSTEM ANALYSIS USING THE 3D EXTENDED PDRH ANTENNA IN DIELECTRIC MIXTURE

In this part, the extended PDRH antenna was filled with the high dielectric mixture of the linseed oil and the r-TiO_2 that will be used to determine the fat thickness of the modelled tissue. To prove the system operation, a liquid medium was modelled consisting of oil and water and the system was tested and analysed.

5.1.7.1. SYSTEM EVALUATION USING A LIQUID MODEL

A liquid model which consists of two layers of distilled water and linseed oil has been proposed, in replacement of the fat and muscle in the human tissue model, and a thin layer of skin was ignored, to approximately evaluate the performance of the system before utilizing it in the developed model.

The centre frequency of 1.8 GHz is also chosen to monitor the system. The dielectric properties of both the measured liquids using the discussed open-ended probe technique was shown in Chapter 3. The antenna is placed on the liquid model, where the thickness of the oil layer is zero at first, and is then increased from 10 to 30 mm, in steps of 10 mm as in Figs. 5.56.

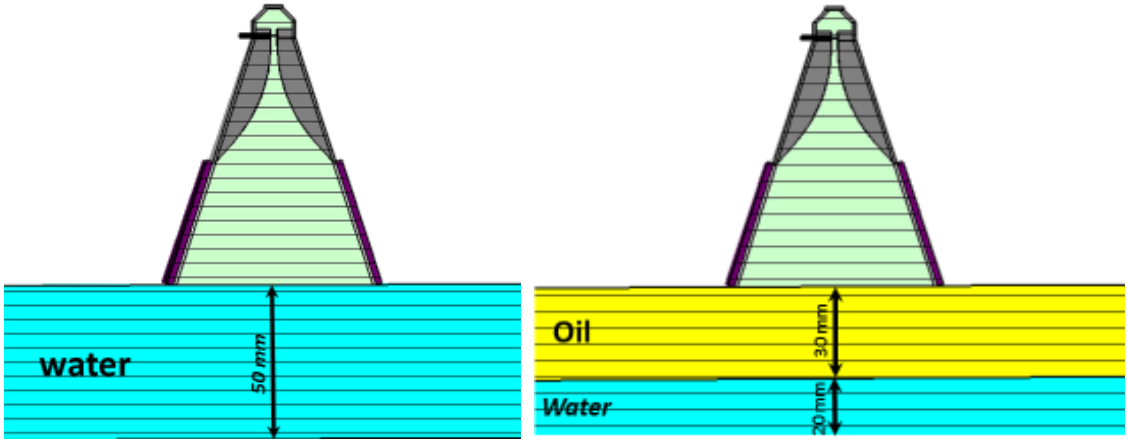

(a) The distilled water. (b) The oil layer with thicknesses of 10 to 30 mm.

Fig 5. 56: Modeling of the developed PDRH antenna, which was placed on both liquid models.

The reflection coefficients for both cases was generated using the CST software and presented in Figs. 5.57 (a) and (b).

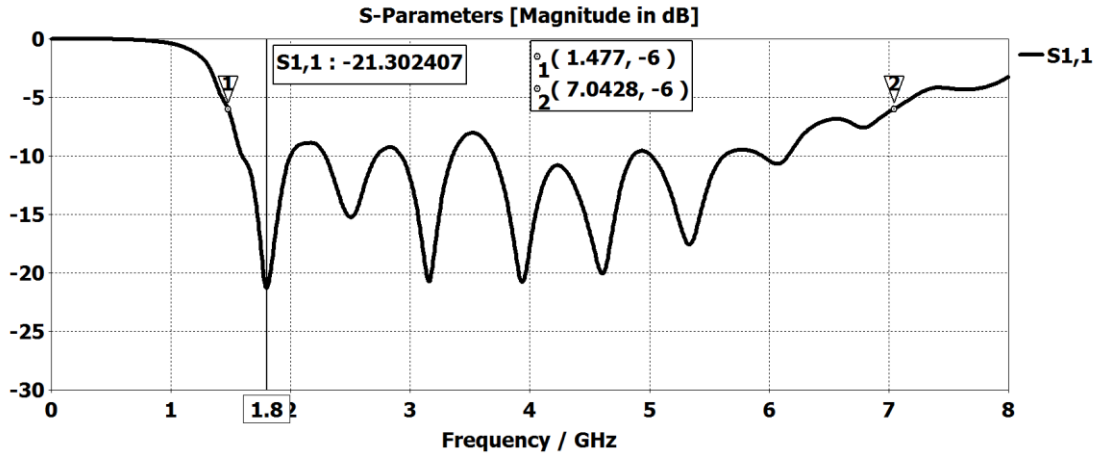

(a): Simulated S_{11} results of the antenna, when it has been placed in the distilled water.

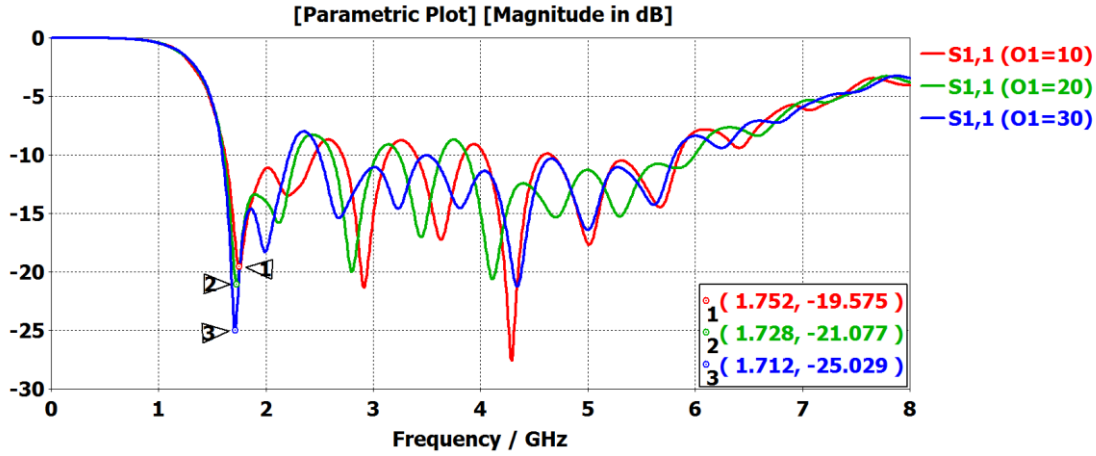

(b): Simulated S_{11} when the oil layer thickness changes from 10 to 30 mm, with an iteration of 10-mm.

Fig 5. 57: Simulated return loss results for both cases when the oil does not exist, and the oil thickness iterates.

The method was developed to employ the highest magnitude of the first deepest point in reflection coefficient close to f_c = 1.8 GHz. The first S_{11} measurement has been chosen for the case when only water exists, that is deployed to initiate the system calibration, as in Fig. 5.57 (a). Followed by a set of scenarios when the oil thickness changes, and markers have pointed out the changes in magnitude at the largest transition close to the frequency of interest, as in Fig. 5.57 (b). Table 5.8 is generated from the highest magnitude point of the interested region for different scenarios, and a graph and an equation have been generated, as shown in Fig. 5.58. This is obtained from the experimental data, to relate the rate of change of magnitude to the oil thickness.

Table 5. 8: Difference in the frequency and magnitude at the first large transition point, with a reference to the oil thicknesses.

Oil Thickness (mm)	Frequency (GHz)	Magnitude (dB)
10	1.752	–19.575
20	1.728	–21.077
30	1.712	–25.018

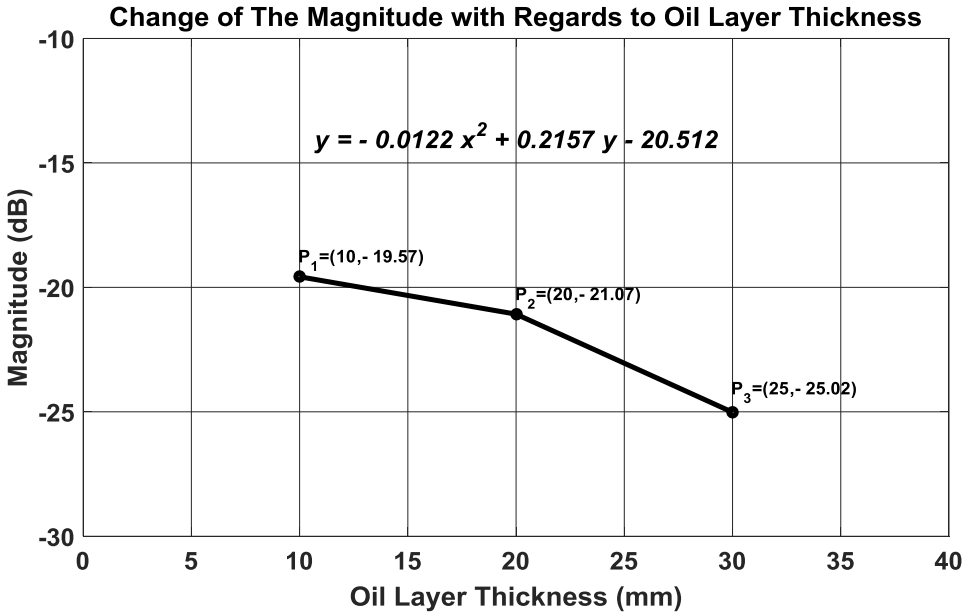

Fig 5. 58: Generated graph and equation based on the simulated S_{11} data, presenting the rate of change in magnitude, when the oil layer thickness iterates from 10 to 30 mm in the first large transition.

5.1.7.2. SYSTEM EVALUATION USING AN ABDOMINAL TISSUE MODEL

In the next stage, the tissue model that consists of three layers; i.e., 2 mm skin, 15–30 mm fat, and infinite muscle; has been thoroughly developed in the software. This has been conducted to present the abdominal tissue and the antenna filled with the material mixture, which is placed on this tissue model, as shown in Fig. 5.59.

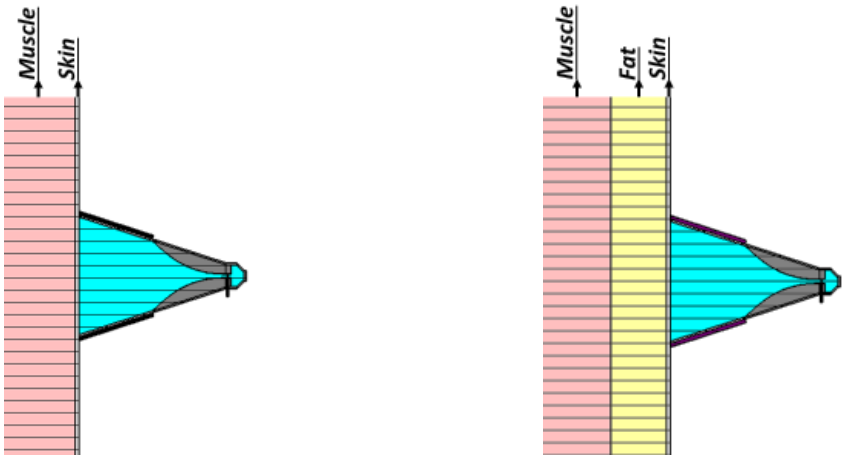

(a) The tissue without the fat layer (b) The tissue with the fat layer.

Fig 5. 59: Modelling of the developed PDRH antenna, when the antenna was placed on both tissue modelled.

Moreover, the dielectric properties of the material in the desired frequency region, which was already measured, has been also loaded into the software using the new material dispersion, as shown in Fig. 5.60.

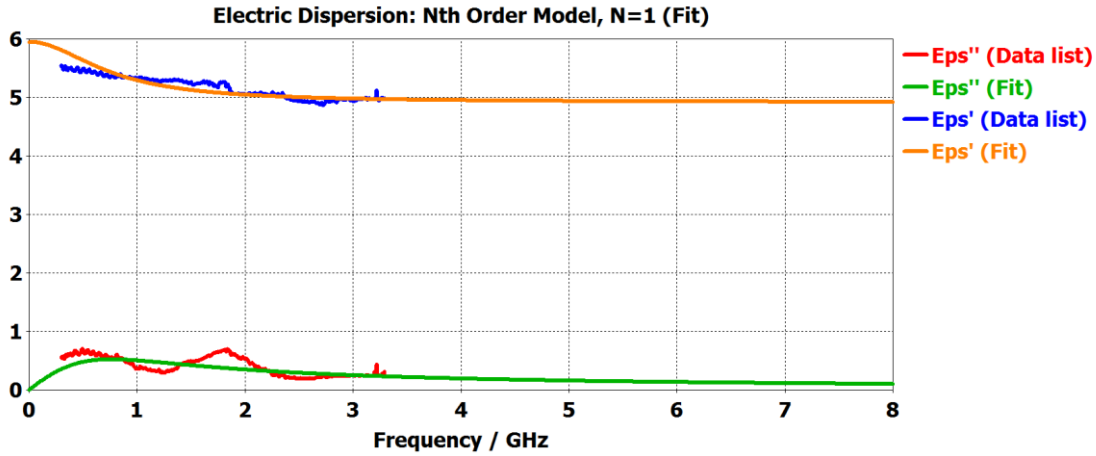

Fig 5. 60: Measured properties of the mixture loaded into the software.

Furthermore, the high-dielectric material-filled PDRH antenna was placed on the tissue model without fat layer, and the S_{11} results are obtained for a very low frequency range up to 8 GHz that is assumed as a calibration point as shown in Fig. 5.61.

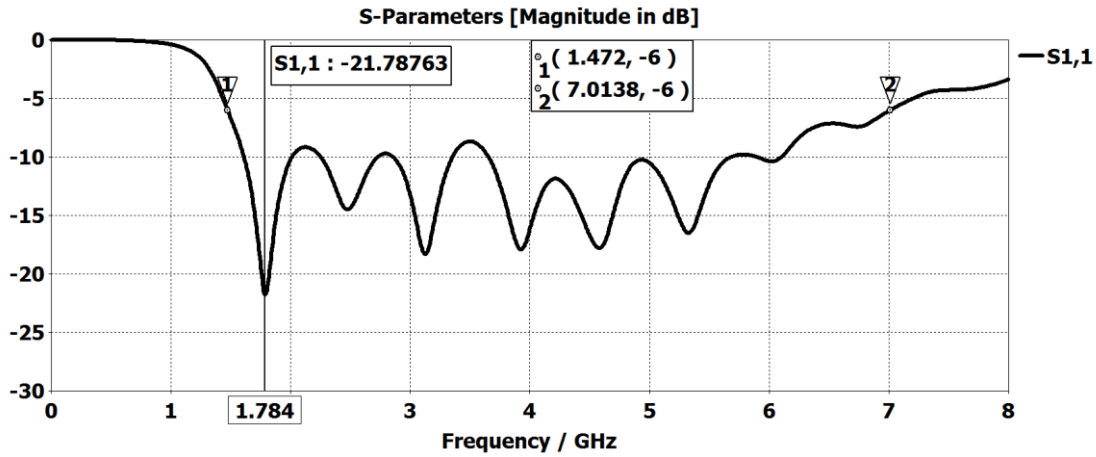

Fig 5. 61: Simulated S_{11} of the antenna, when the fat layer does not exist.

The fat layer increases from 15 to 30 mm in steps of 5 mm and the results have been captured and depicted in Fig. 5.62.

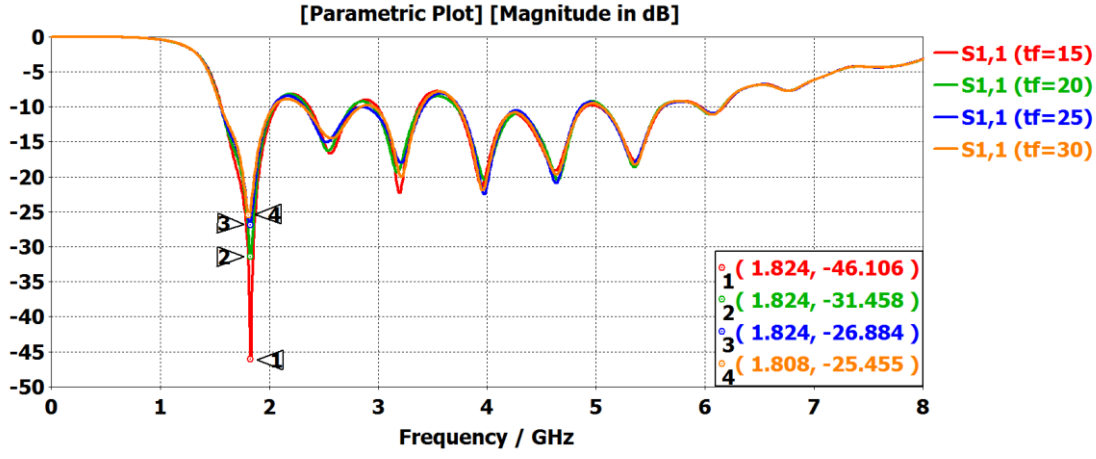

Fig 5. 62: Simulated S_{11} when the fat layer thickness changes from 15 to 30 mm, with an iteration of 5-mm.

The results demonstrate a constant change in the magnitude at the first large transition with respect to the thickness of the fat layer, as in Table 5.9. Fig. 5.63 also shows a generated graph and an equation based on the data collected from the magnitude difference at the first large transition point, when the thickness of the modelled tissue fat layer changes from 15 to 30 mm. The generated equation would be used in order to accurately predict the fat layer based on the measured data [14, 15].

Table 5. 9: Difference in frequency and magnitude at the first large transition point, with reference to the fat thicknesses.

Fat Thickness (mm)	Frequency (GHz)	Magnitude (dB)
15	1.824	–46.108
20	1.824	–31.458
25	1.824	–26.884
30	1.808	–25.455

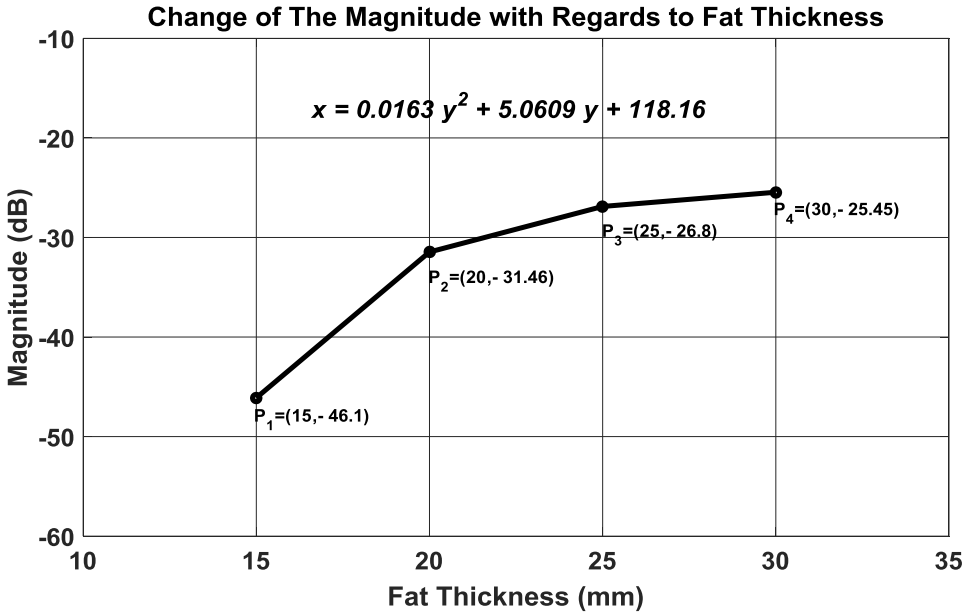

Fig 5. 63: Generated graph and equation based on the simulated S_{11} data, presenting the rate of change in magnitude, when the fat layer thickness iterates from 15 to 30 mm in the first large transition.

5.1.7.3. ANTENNA FABRICATION, REALIZATION

Fabrication of the 3D printed PDRH antenna requires an in-house 3D printer, and some modification to the design, such as cutting the designed antenna symmetrically to two parts before the printing, and allocating a screw spacing on the side edges, to attach them together, as in Fig. 5.64 (a). Also, the printed PDRH antenna has been painted with a silver conductive paint, up to the extended part of the design. In addition, the antenna is connected to a 50-ohm semi-ridge cable SMA connector with an outer dimension of 1.19 mm fed and glued to the antenna's lower- and upper-ridges, as in Fig. 5.64 (b) [16]. The antenna is filled with the titanium oxide mixture, and it has been placed upside down to

remove any remaining bubble gaps produced during the mixing and filling process, i.e., Fig. 5.64 (c).

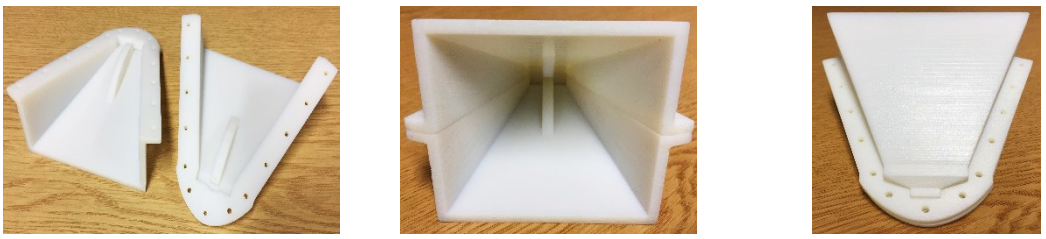

(a): The 3D-printed PDRH antenna using the polyethylene material.

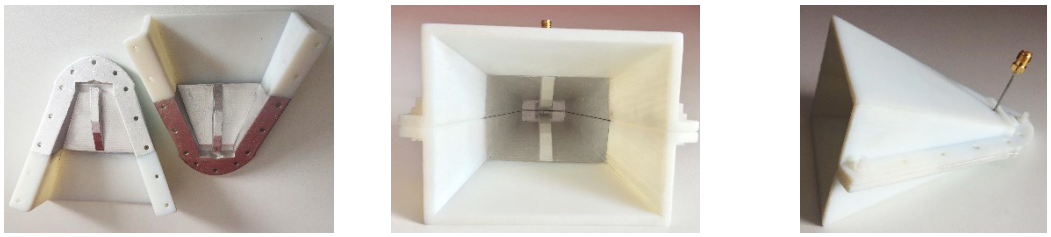

(b): The 3D-printed PDRH antenna conductive-painted and fed with a semi-ridged SMA connector.

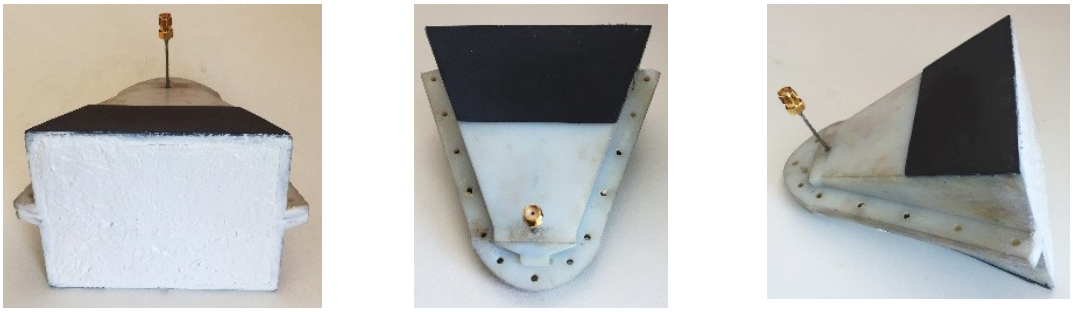

(c): The 3D-printed PDRH antenna filled with the high-dielectric material and the absorbers are glued to lower and upper-extended flares.

Fig 5. 64: Fabrication of the PDRH antenna filled with high dielectric mixture of the oil and the r-TiO_2.

5.1.7.4. EXPERIMENTAL SYSTEM EVALUATION USING LIQUID MODEL

A two-layer liquid model consisting of distilled water and linseed oil has been assembled, to prove the concept of the system operation, which was to measure the oil thickness in the two-layer model. The antenna is also connected to the VNA using a coaxial cable that is calibrated using the ECal. The antenna is placed on top of the modelled liquid layers and the reflection coefficient is measured and saved for different liquid modelled scenario, to define a mathematical calibration and measurement method based on the retrieved data. In the first scenario, the antenna has been accurately placed on the distilled water, using a prepared setup, as shown in Fig. 5.65.

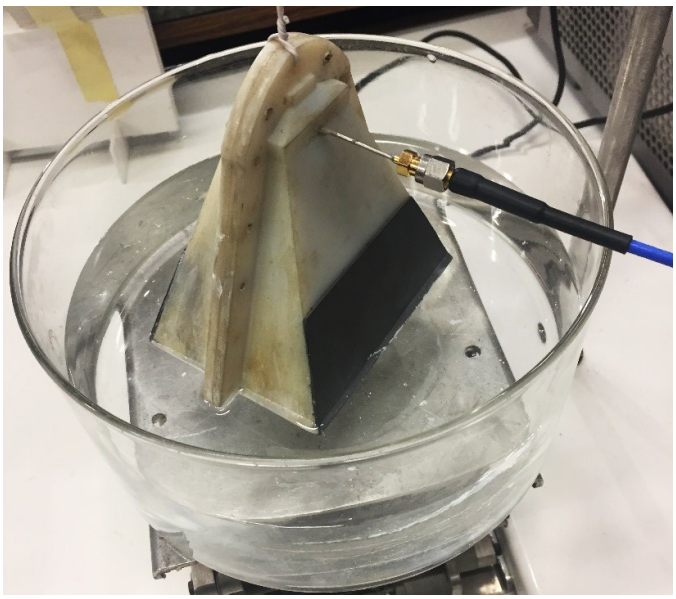

Fig 5. 65: The prepared measurement setup, presenting the antenna placed on the distilled water for the experiment.

In addition, the reflection coefficient is generated by the VNA and is stored. The next part of the experiment was focused on adding the linseed oil to the container to increase the oil thickness to 10 mm thickness, followed by saving and plotting the S_{11} values.

The process is repeated for 20 mm and 30 mm oil thicknesses, and the generated data are stored for the analysis, which has been shown in Fig. 5.66.

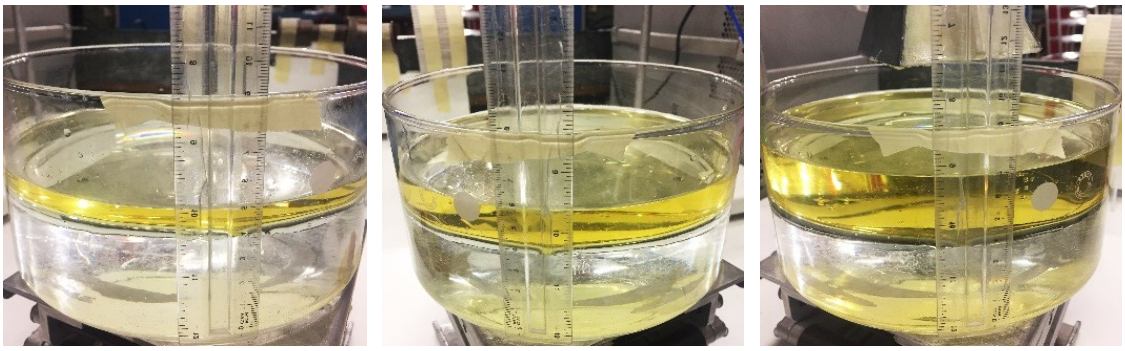

Fig 5. 66: The prepared setup of the developed liquid model, for different oil thicknesses of 10 to 30 mm for the experiment.

The experimental magnitude of the first large transition point close to fc = 1.8-GHz of the water is depicted in Fig. 5.67.

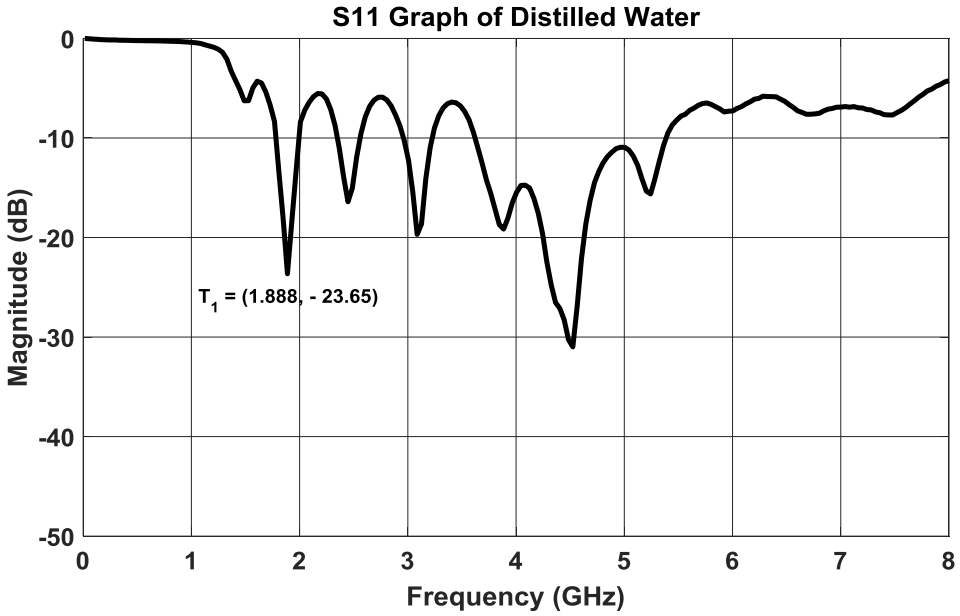

Fig 5. 67: Measured S_{11} results of the antenna on the distilled water.

The measured results have been compared with the simulations to determine the difference value, which refers to the difference between the simulation and experimental environments. This value for the magnitude has been found to be around 2.35 dB. The procedure, namely the calibration process, has been deployed, to subtract the value from the measured results compared with the simulated results. The measured S_{11} results for different oil layers have been shown in Fig. 5.68.

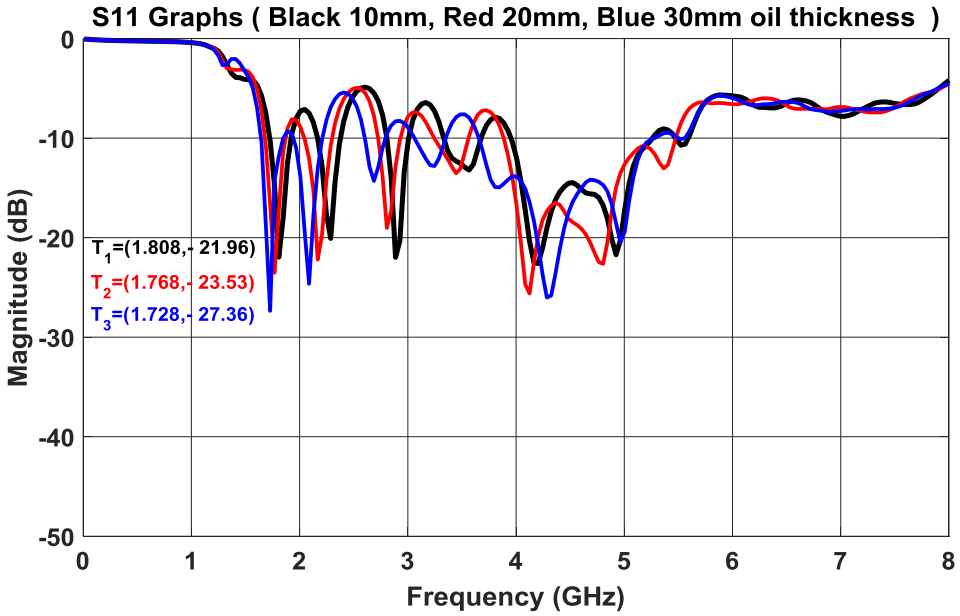

Fig 5. 68: Measured S_{11} results of the antenna for three developed cases, when the oil thicknesses changed to 10, 20, and 30 mm.

This is effectively used to predict the first large transition points of the simulations, by simply subtracting the magnitude rate. This has proved the output performance of the system based on both the numerical and measured results. This has shown that there is a negligible difference introduced into the system that can be the result of human errors.

5.1.7.5. ANTENNA MEASUREMENTS ON A REAL HUMAN TISSUE

The proposed method presented previously has been employed, to calibrate the system, followed by the measurement of the abdominal fat. Hence, the system has been calibrated using an area of the human body, where there is none or a small amount of fat, such as the arm and the results has been compared to the simulation results with the same scenario ((i.e., No fat layer exists model), as shown in Fig. 5.69.

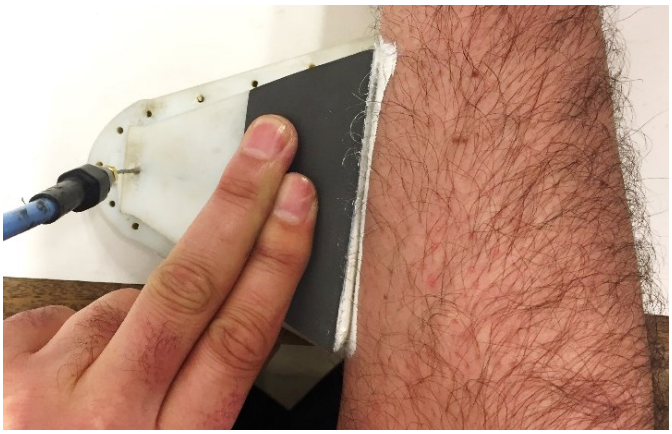

Fig 5. 69: The developed antenna placed on the arm for the calibration.

The results exhibit a slight shift in magnitude and frequency, compared to the simulations, as can also be seen in Fig. 5.70. This minor difference could be due to the differences that may have been added to the system, during the experimental stage, as opposed to the error-free simulation environment. It should be noted that the air gap between the antenna and the body has been also eliminated by using the semi-solid mixture, which has removed the effect of the air gap in the real experiment.

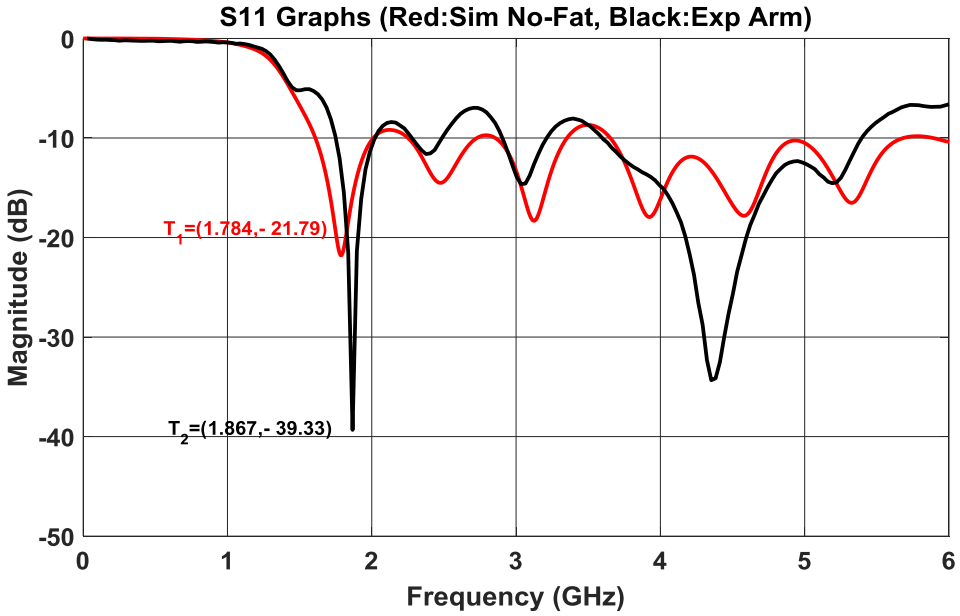

Fig 5. 70: The red plot presents the simulations (i.e., no fat case), and the black plot shows the measurements, obtained based on the arm case.

In addition, the antenna has been placed on the abdominal area of the human body that had an unknown amount of fat, as presented in Fig. 5.71.

Fig 5. 71: The antenna placed on the abdominal for the fat measurement.

The S_{11} results have been obtained based on the measurements on the body, and further compared with the measured results of the case based on the arm, as shown in Fig. 5.72.

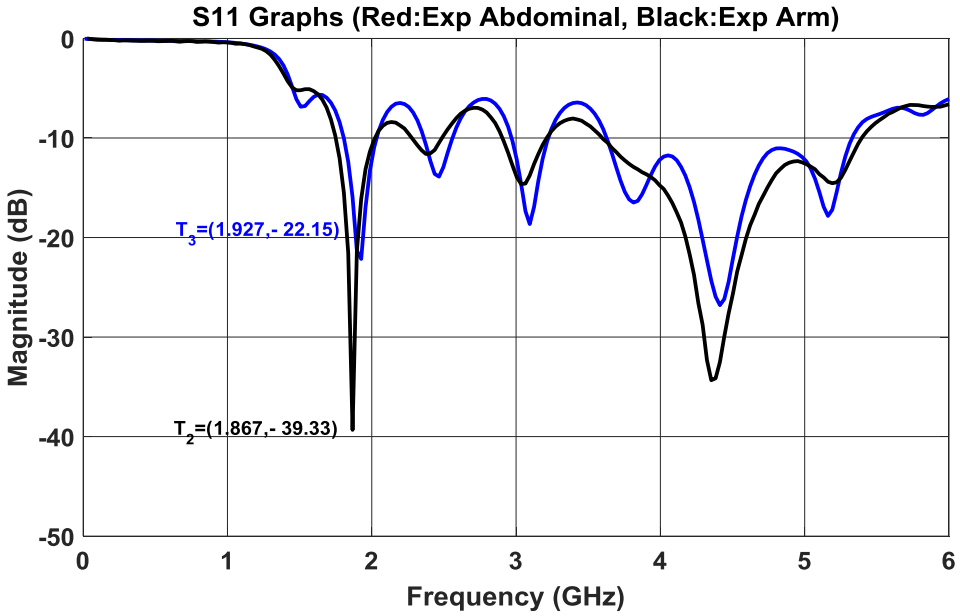

Fig 5. 72: The blue plot refers to the measured abdominal case, and the black plot refers to the measured arm case.

In addition, the change in the magnitude at the highest point of the first large transition for the abdominal fat has been stored and calibrated using the simulations, to calculate the estimated amount of the fat in the abdominal area. The highest point of the first large transition for the arm has been recorded at the frequency of 1.867-GHz, with the magnitude of –39.33 dB. In the abdominal case, these values are changed to 1.927-GHz with the magnitude of –22.15 dB.

The developed method to calculate the estimated thickness of the oil layer has been used in this case, to accurately predict the fat thickness. The first stage was to calibrate the measured magnitude of the first large transition point at the frequency of interest, according to the simulation results given in Table 5.9. By subtracting both the measured and simulated magnitude values, the value has been further determined as –17.54 dB.

This value is then added to the measured abdominal value to determine the magnitude value (i.e., –39.69 dB) of the real tissue, with respect to the simulations. This value has been used in the equation in Fig. 5.63, to determine the fat thickness as 13.86 mm.

5.1.7.6. SYSTEM ERROR ANALYSIS

Mean value: For a data set, the arithmetic mean, also called the mathematical expectation or average, is the central value of a discrete set of numbers: specifically, the sum of the values divided by the number of values presented in equation (5-10) [17].

$$\text{Mean } (\bar{x}) = \frac{1}{N}\sum x_i \qquad \text{Eq. (5-10)}$$

In statistics, the standard deviation (SD) is a measure that is used to quantify the amount of variation or dispersion of a set of data values shown in equation (5-11) [16].

$$\text{Standard Deviation (SD)} = \sqrt{\frac{\sum_{i=1}^{N}(x_i-\bar{x})^2}{N-1}} \qquad \text{Eq. (5-11)}$$

The mean value and standard deviation were determined using the equations (5-10&11) for all different scenarios, where the thickness of the oil was altered from 10 to 30 mm and presented in Table 5. 10.

Table 5. 10: Definition of the mean value and standard deviation for the liquid modelled case.

Oil Thickness (mm)	*Simulated Magnitude (dB)*	*Measured Magnitude (dB)*	*Subtraction(dB) (Measured-Simulated)*	*Mean Value ($\bar{x}$) (dB)*	*Difference of Subtraction & Mean (dB)*	*Standard Deviation (SD) (dB)*
10	-19.575	-21.96	-2.385	-2.393	0.008	0.046
20	-21.077	-23.53	-2.453	-2.393	-0.059	0.046
30	-25.018	-27.36	-2.342	-2.393	0.051	0.046

$$\text{Diff Value} = \bar{x} \pm \text{SD} = -2.393 \pm 0.046 \qquad \text{Eq. (5-12)}$$

$$Error = \frac{\text{SD}}{\bar{x}} = \frac{0.046}{2.393} = 0.019 \approx 2\% \qquad \text{Eq. (5-13)}$$

The system error was calculated using the equations (5-12&13) and defined to be within ±1 mm thickness that was determined as substantial for such a system.

5.2. SYSTEM HARDWARE DESIGN

In this section, all mathematical equations needed to analyse and evaluate the behavior of the GP transmitted by the antenna (horn antenna) through the human abdominal tissue (HAT) model as shown in Fig. 5.73 were obtained.

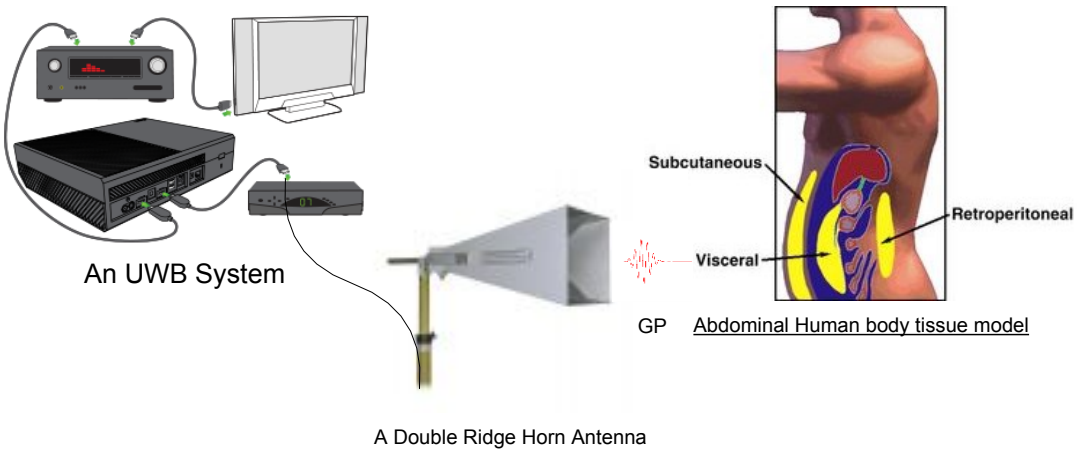

Fig 5. 73: A WB Fat Detection System.

The WB Fat Detection System shown in Fig. 5.73 consists of a WB system, A DRH antenna, and a HAT model. A number of techniques have been used by researchers to extract the information from the reflected pulse such as TDR, amplitude and phase-based methods. The horn antennas will be regarded as a transceiver to transmit the Gaussian pulse (generated by a WB pulse generator) and capture reflected pulse from each layer. The captured pulses will be amplified, filtered, converted to digital format, and finally will be transferred to a Laptop to be analysed and an image of the area of interest will be created using the existing method. As the aim of the system is to detect and measure the place and thickness of the fat layer in the model, there would be a need for wide investigation to be done on the pulse, which will be transmitted through the suitable antenna design in the system. There are some calculated parameters mathematically defined to illustrate the pulse behavior during transmission and reflection period, which is, get premeditated in this section before we intend to move to simulation and finally practically test the system. A brief description produced for the system in following helps to understand the hardware components and their operation in the system concisely;

The system consists of three major components: a computer, WB hardware system and a horn antenna. The horn antenna has been selected in this system based on its specific capability of high gain and directivity compared to the other antenna design. The WB hardware subsystem consists of more elements; here some of its major components will

be mentioned to provide an overview of the whole system that should take care of during this project. UWB signal generator: the signal generator should be used later in the project to be able to generate the pulse that was chosen based on the system operation. However, it should be remembered that using expensive and huge signal generators is in contradiction with the system's needs in terms of designing and building a small and cheap pulse generator that can generate the pulse. An ADC and FPGA device will be chosen to be used for signal data processing, as an incoming reflected signal to the system, which is analogue, should be converted to digital before being able to analyse the data received from the antenna in an FPGA device. A VNA has all these components built in but as the system should work independently from other expensive and big equipment, there is a need to design our hardware separately. Some small components used in the hardware will be mentioned here such as Voltage Control Oscillator (VCO), Power Amplifier (PA), Low Noise Amplifier (LNA) and Band Pass Filter (BPF). These will be discussed and designed later in the project. The operation of the system will be briefly discussed in this part, to give an overview of what the system is supposed to do; The first stage is to generate the pulse using a signal generator and mix it with a sine wave to adjust the bandwidth to the required pulse bandwidth. Following generating the pulse, the LNA and the PA will be used to amplify the pulse and finally transmit it through the switch with the horn antenna to the modeled tissue. The next step is to capture the reflected pulse by the receiver horn antenna. The pulse should be amplified, separated from other components such as noise by the filter process, and finally converted from analogue to digital data using the ADC. The data then will be sent to the FPGA device for sampling and data acquisition and transferred to a laptop to construct the image as it is shown in Fig. 5.74 [18].

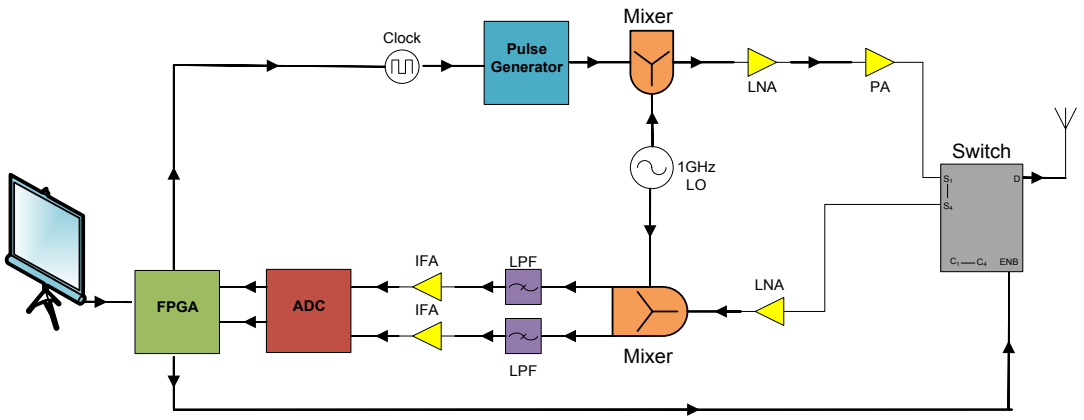

Fig 5. 74: a WB Fat Detection System component [17].

5.2.1. SYSTEM HARDWARE DESIGN BASED ON LAB COMPONENTS

In order to be able to prove that the simulation results are correct and the results in real environment will have an approximately same outcome, the practical measurement has to be performed and the results should be compared. The first part of the hardware in this project is in fact the antenna, which should be placed on the tissue to transmit and receive a WB pulse in order to be able to analyse the reflected pulse as it is shown in Fig. 5.75.

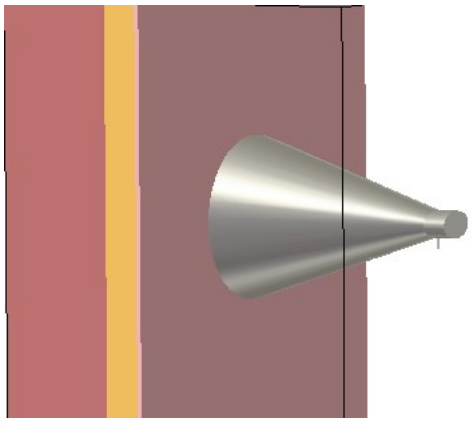

Fig 5. 75: Double ridged horn antenna filled with a ceramic with a high permittivity.

The next important step is to check the required components to create the hardware and their availability in the lab to practically transmit a WB pulse and capture the reflected pulse in cases of different fat thickness. The reflected pulses from each case where the fat thickness in the modeled tissue is changed from 10 mm to 30 mm in steps of 5mm, the results are recorded and analysed. The components available in the antenna lab can be used to construct the hardware to demonstrate the abdominal fat measurement as follows. The first steps in the hardware set up is to produce a WB pulse that requires a WB signal generator with a Local Oscillator (LO) or a Voltage Control Oscillator (VCO) to sweep the pulse to the frequency of interest.

The in-house picosecond pulse generator (model 10060A as shown in Fig. 5.76), is capable to generate a periodic rectangular pulse of 100 ps to 10 ns in the period of 10 μs up to 1 sec.

Fig 5. 76: Model 10060A Programmable Pulse Generator.

The in-house radio frequency (RF) continuous wave (CW) generator, which is enabled to generate CW signal from 20 MHz up to 40 GHz is illustrated in Fig. 5.77.

Fig 5. 77: RF sweep CW generators (0.020 – 40 GHz).

Both wave generators can be connected to the high-performance Marki mixer shown in Fig. 5.78 that works in the frequency range of 1 MHz to 6 GHz, to mix the WB pulse with the CW and produce an intermediate frequency (IF) for the generated WB pulse. The IF modulated pulse can be defined by equation 1 as follows:

$$f(t) = \begin{bmatrix} sin2\pi f_c t & pT \le t \le pT + \tau \\ 0 & pT + \tau \le t \le (p+1)T \end{bmatrix}$$

Where p is the period, T is the signal repetition period, τ is the signal duration and f_c is the centre frequency.

Fig 5. 78: The T3-03 is a high-performance mixer featuring LO/RF from 1 MHz to 6 GHz.

After the WB pulse has been generated, a 10 dB directional coupler will be used to divide and distribute the pulse power as shown in Fig. 5.79. The generated pulse that transmitted through port1 will divide the 75% of transmitted power directly to port 2 and 25% of the signal power will appear on coupled port 3 for monitoring where the port 4 is isolated. The directional coupler circuit diagram and actual component have chosen as is shown in Figs. 5.79 and 5.80.

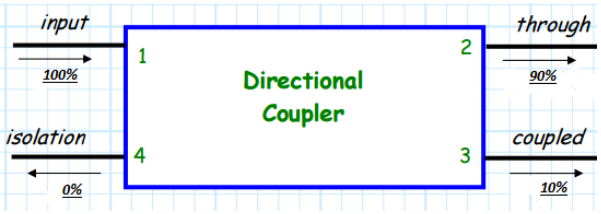

Fig 5. 79: The block diagram of the 10 dB directional coupler in transmitting and receiving condition.

Fig 5. 80: C0825-06 Coupler SMA 0.8-2.5 GHz 6dB VSWR 1.2.

The high gain block amplifier used in this step of the design is amplify the pulse before transmission. This improves the detection of reflected pulse and benefits the noise filter.

Fig 5. 81: The 23 dBm P1dB, 50 MHz to 4 GHz, Gain Block Amplifier, 26 dB Gain, 35 dBm IP3, 5 dB NF, SMA.

The next step is to transmit the pulse and to capture the reflected pulse, for this section of the hardware set up, there is need of a circulator to redirect the reflected pulse to a data analyser for further analysis. Fig. 5.82 demonstrates an SMA circulator, which operates in 1-2 GHz frequency band.

Fig 5. 82: CF1020 Circulator 1-2Ghz VSWR 1.35 S Steel SMA 50Watts.

The next step of the hardware set up that needs to tackle is remove the noises were added to the reflected pulse, a Low Noise Amplifier (LNA) component is suggested, as reflected pulse will attenuate result of passing through the channel and mix with some noise in the channel. The CBLU1033213 Broadband LNA, which can cover the bandwidth of 0.1-3 GHz with a gain of 32 dB and noise figure as low as 1.3 dB as is shown in Fig. 5.83 and will be used during the experiment.

Fig 5. 83:CBLU1033213 Broadband low noise amplifier (0.1-3GHz).

Finally, the serial data logger/analyser LeCroy SDA1100 shown in Fig. 5.84 will be connected to the directional coupler to check the transmitted pulse as well as capturing the reflected pulse to save and later being compared by other scenarios where the fat thickness alters.

Fig 5. 84: Serial Data Logger/Analyser LeCroy SDA11000 (maximum sampling rate: 40 Gbit/sec).

The abdominal fat measurement system consists of all components has been illustrated in Fig. 5.85. The system can be improved by adding a power amplifier (PA), and a switch to increase the power level and switch for send a pulse at each operating time and wait to receive the reflected pulse before transiting the next pulse for the comparison and accuracy. The components were all selected based on the technical requirements and cost.

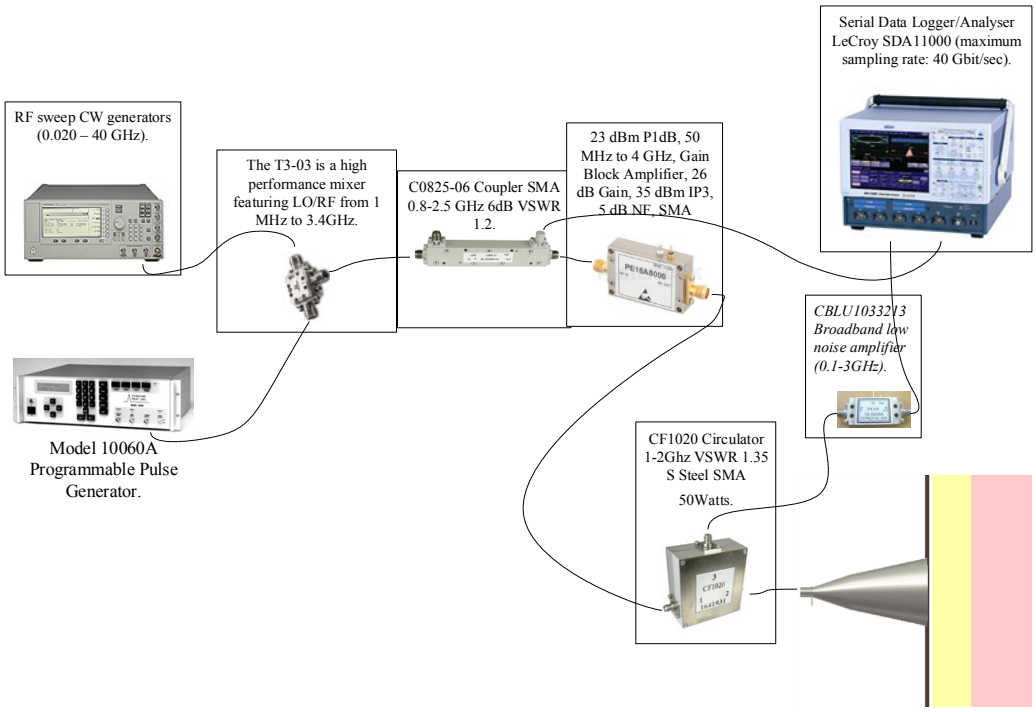

Fig 5. 85: WB reflected based abdominal fat measurement system set up.

5.3. ELIMINATING SYSTEM ERRORS

The built-in errors during the design development and implementation can create great side effect on the operation of the system. These errors should be considered in each stage and eliminate their effect on the system. Therefore, in this section, the solutions considered to eliminate some of these side effects has been presented.

In this section, the gaps between the antenna and the human skin when the antenna is attached to the body for the system measurement were analysed. These gaps can produce the errors as well as the dry skin and wet skin may differ in permittivity by some amounts refer to the person to another can add another error to the system. Both errors can be minimised by applying a gel to the skin before the system touch the skin. The technique not only eliminates the gap between the device and the skin, furthermore, it can minimised the error caused by the skin dielectric properties difference, due to different dryness conditions of one person to another. The detergent and food liquid solutions such as Triton 100, Polysorbate 20, glycerol and xylitol can be mixed with the distilled water to increase the permittivity to 40 as mentioned in Chapter 3 of this thesis.

5.4. CHAPTER SUMMARY

The system was analysed based on the time domain techniques when the tissue consists of skin, fat, and muscle modeled in the CST studio and the antenna was placed in the far-field region from the tissue. The fat thickness iterated from 10 to 40 mm and the time domain results were analysed respectably.

- In the first phase, the WB DRH antenna that was designed in free space and was placed in front of the model tissue. Two cases were obtained where the pulses with short (1GHZ) and wide (3.6GHz) bandwidth was generated and transmitted and reflected time results were analysed when the fat thickness changed from 15 to 40 mm. The results describe the overlapping issue in both cases. However, in the first case, it was more severe, and the reflected pulse combines with the vast bulk reflection from the skin, which makes the second pulse that comes from fat layer more difficult to retrieve.
- In the second phase, the DRH antenna was designed in the background material that had a permittivity of 41 and conductivity of 0.1S/m and was placed in front of the modeled tissue at different distances (attached, near and far field). The results describe the best results with the less overlapping issue can be retrieved when the antenna was placed in far-field region of the tissue.
- Next and third phase was to use the reconfigured design for the dielectric ceramic that was characterised in Chapter 3. The PDRH and EDRH antennas were designed using ceramic data and with the extension to determine the reflected pulse and the TDR graph.
- The extended EDRH antenna filled with a mixture of the linseed oil and r-TiO_2 were designed and fabricated using 3D printing method, and the reflection coefficient of the antenna on the arm was investigated.
- The extended PDRH antenna filled with a mixture of paraffin and the r-TiO_2 were designed, fabricated and employed in the system to identify the fat thickness using the reflection coefficient method. The system operation was first tested and approved on the liquid modelled of the oil and water to identify the oil thickness.
- The fourth phase was to define the hardware components based on the lab availability that should be used in future for the hardware system design.
- Fifth phase was to investigate the errors developed during the design process such as air gap between the transmitter and the modeled tissue and use matching gel to eliminate the air gap as well as matching the environment.

REFERENCES (CHAPTER 5)

[1] E. Taoufik, S. Nabila and B. Ridha, "The reflection of electromagnetic field by body tissue in the UWB frequency range," *IEEE International Radar Conference*, pp. 1403-1407, Washington, DC, USA, May. 2010.

[2] M. Strackx *et al.,* "Measuring material/tissue permittivity by UWB time-domain reflectometry techniques," *Int. Sympo. Applied Scie. in Biomed. and Communica. Techs. (ISABEL)*, Rome, Italy, Nov. 2010.

[3] D. Oloumi, P. Boulanger, A. Kordzadeh, and K. Rambabu, "Breast tumor detection using UWB circular-SAR tomographic microwave imaging," *in Proc. 37th Annu. Int. Conf. IEEE Eng. Med. Biol. Soc. (EMBC)*, pp. 7063-7066, Milan, Italy, Aug. 2015.

[4] C. A. Balanis, "Antenna theory - a review," *Proceedings of the Ieee,* vol. 80, pp. 739-805, Jan 1992.

[5] S. Sarjoghian, Y. Alfadhl, X. Chen, "A novel wide-band reflection-based system for measuring abdominal fat in humans," *in URSI Commission B Int. Symp. on Electromagnetic Theory (EMTS)*, Aug. 2016.

[6] D. T. Al-Zuhairi, J. M. Gahl, A. M. Abed, and N. E. Islam, "Characterizing horn antenna signals for breast cancer detection," *Can. J. Elect. Comput. Eng.*, vol. 41, no. 1, pp. 8-16, Apr. 2018.

[7] A. Cataldo, G. Cannazza, E. De Benedetto, and N. Giaquinto, "Experimental validation of a TDR-based system for measuring leak distances in buried metal pipes," *Progr. Electromagn. Res.*, vol. 132, pp. 71–90, Dec. 2012.

[8] E. Laloy, J. A. Huisman, and D. Jacques, "High-resolution moisture profiles from full-waveform probabilistic inversion of TDR signals," *Journal of Hydrology,* vol. 519, pp. 2121-2135, Nov. 2014.

[9] S. Latif, S. Pistorius, and L. Shafai, "A double-ridged horn antenna design in canola oil for medical imaging," in 2nd Int. Conf. Advances in Elect. Eng. (ICAEE), pp. 421–424, Dec. 2013.

[10] B. Zhang, Y.-X. Guo, H. Sun, and Y. Wu, ''Metallic, 3D-printed, k-bandstepped, double-ridged square horn antennas,'' *Appl. Sci.,* vol. 8, no. 1, pp. 33–39, Dec. 2017.

[11] S. Wirth, I. L. Morrow, and I. Horsfall, "Fabrication procedure and performance of 3D printed X-band horn antenna," *in Loughborough Antennas & Propagation Conference,* pp. 4, Jan. 2018.

[12] S. Lee *et al.,* "Robust design of 3D-printed 6-18 GHz double-ridged TEM horn antenna," *in Applied Sciences*,Vol. 8, p. 1582, Sep. 2018.

[13] S. Alkaraki *et al.,* "Performance comparison of simple and low cost metallization techniques for 3D printed antennas at 10 GHz and 30 GHz," *IEEE Access*, vol. 6, pp. 64261–64269, Nov. 2018.

[14] S. Sarjoghian, Y. Alfadhl, and Xiaodong Chen, "A novel wide-band reflection-based system for measuring abdominal fat in humans," *in URSI Int. Symp. Electromag. Theory (EMTS)*, pp. 586–589, Aug. 2016.

[15] S. Rashid *et al.,* "3D Printed UWB Microwave Bodyscope for Biomedical Measurements," *in IEEE Antennas and Wireless Propagation Letters,* Vol. 99, PP. 1-1, Feb. 2019.

[16] S. Rashid *et al.*, "3-D Printed UWB Microwave Bodyscope for Biomedical Measurements," *in IEEE Antennas and Wireless Propagation Letters*, vol. 18, no. 4, pp. 626-630, April 2019.

[17] G. Douglas, Altman, and J. Martin Bland. "Standard deviations and standard errors" *british medical journal (Clinical research ed.),* vol. 331,pp. 903, Oct. 2005.

[18] Y. Wang, “UWB Pulse Radar for Human Imaging and Doppler Detection Applications,” *Phd Thesis*, Electrical Engineering, University of Tennessee, 2012.

CHAPTER 6

6.1. DISCUSSION

The defined equations and mathematical results, produced in Chapter 2 of this thesis, indicate that in order to design a WB abdominal fat measurement system, which satisfies the objectives of the project, several important factors need to be addressed such as the penetration depth, range resolution and antenna structure. The first two of these factors were discussed in detail, and a frequency range of 1 to 3 GHz with a minimum bandwidth of 500 MHz were found to satisfy the system needs.

Regarding the antenna design, it seems that a DRH antenna may meet the system requirements, but designing such an antenna to operate in free space and at such high frequencies requires the antenna to be quite big in size. Therefore, the option of designing an antenna for operation in a medium with high permittivity (close to the skin's permittivity) was considered. This choice has many advantages such as reduction in antenna size and cost, and also it considerably reduces the strength of the first large reflection from the skin. Hence, this option have resulted in a compact system with better performance.

However, as the greatest amount of the pulse energy will be absorbed within the high permittivity material, this technique has the undesirable drawback that it will reduce the penetration depth. The solution to overcome the shallow penetration depth would be to reduce the center frequency and therefore to increase the system penetration depth.

In fact there is a trade-off between these factors (i.e. penetration depth and range resolution); improving one, would deteriorate the other. In this project, an optimal point for this trade-off has been investigated. Therefore, the system was named as WB system and not a UWB system, since UWB is specified to operate within the UWB range (3.1−10.6 GHz).

Regarding range resolution requirements, the simulation results using CST software, generated for the purpose of finding the required bandwidth indicated that a horn antenna with minimum bandwidth of 500 MHz is required to satisfy the system's resolution criterion. In addition, the simulation results verified the validity of equation (2-9), and so proved that the range resolution does play a critical role in one-dimensional models.

Therefore, A DRH antenna for use in free space with bandwidth of 460 MHz, which operate at the centre frequency of 3.1 GHz was designed and developed (using the CST software). Then modelled tissue was placed in front of the antenna and the system was run to analyse different fat thicknesses. The results proved that the system can not distinguish the tissue with different fat thicknesses based on the amplitude reduction and time shifting methodologies.

The same procedure on the new design embedded in a high dielectric material with a higher centre frequency of 1.8 GHz proved that for thicknesses of fat layer larger than 30 mm the pulse amplitude is lagging from all consistence cases when the fat thickness is less than 30 mm. This proves that with increasing the bandwidth, the range resolution has been increased and therefore the system is operating successfully.

The pyramidal and elliptical DRH antennas with the extension were further designed and proposed for this application. The extension was added to the design to satisfy the far field region phenomena in order to separate and identify the reflections and increase the gain and directivity of the antenna designs.

The linseed oil and paraffin were selected due to their low conductivities and were mixed with the r-TiO_2 to increase the permittivity. These high dielectric mixtures were embedded into the designs to reduce the magnitude of reflections from the skin. The antenna designs were fabricated using polyethylene material using an in-house 3D printing method and were painted with the high conductivity paint.

In addition, a semi-ridge cable SMA connector was used to connect the source signal to each designed antennas, finally, each horn antenna was filled with the mixture. Both designed antennas were used to measure the fat thickness, and the results verified that the pyramidal shape has better performance. This proves it has the better penetration depth due to the design's lower centre frequency.

The reflection coefficient and TDR results for the reflected pulse were generated in the simulation to relate the tissue fat thicknesses to the energy loss and the time delay of the system. Concerning the demands for equipment needed to perform each technique, the reflection coefficient technique was selected for the experiment because of the equipment availability. This technique was employed first on the liquid modelled (oil and water) and then on the real human tissue, and the technique provided measurement of the fat thickness with ±1 mm error margin.

6.2. CONCLUSION

Comprehensive investigation on the available systems and techniques to measure the abdominal fat and their advantages and disadvantages, motivates the use of the WB technique. The WB technique satisfies evaluation criteria based on specified factors such as penetration depth and range resolution. The pulse parameters such as a centre frequency within the range of 1 to 3.5 GHz and minimum bandwidth of 500 MHz were specified as the optimal frequency for the premium system operation.

The abdominal modelled tissue was designed using the real abdominal tissue specification such as dielectric parameter values and using realistic thicknesses of each tissue type. To transmit a pulse into the modelled tissue, an antenna that operates at the pulse centre frequency and within the specified bandwidth is required. Therefore, the DRH antenna was proposed here, due to its wide bandwidth and high gain and directivity as well as its matching capability.

The main concern of this type of antenna is bulky size and structure when designed for the frequency range of interest. Therefore, a method of immersing the antenna in a high dielectric material was proposed to enable reduction of the antenna's size and reduce the large reflections caused by mismatching. Different dielectric materials were examined for selecting the best material with high permittivity and low conductivity.

Among all, the barium based VLF-440 ceramic, linseed oil, and paraffin where chosen because of their low conductivity. The oil and paraffin were mixed with a concentrated portion of the anatase r-TiO_2, using a best available mixer creating less bubbles, to increase the permittivity of the filler material.

The pyramidal and elliptical DRH antenna were designed and an extension was added to each design to locate the antenna in the far field region of the scanning area. Different time domain methods such as the pulse reflection were investigated for the purpose of determining the fat thickness of the modelled tissue.

The reflection coefficient method was used successfully to measure the thickness (10 to 40 mm) of fat on the modelled tissue in the simulation, and also in the experiment with measurement error within ± 1 mm.

6.3. NOVELTIES

The main contributions of this work can be summarized as follows:

1. The proposed pyramidal and elliptical DRH antenna has a shape that is not only suitable for the finalized system, but it has also improved the operational parameters such as directivity, gain, and bandwidth compared to the similar types of horn antenna.

2. The extension was proposed and added to the antenna in order to keep the antenna in the far-field region of the monitoring area. This will eliminate signal overlap issues in the case of using the antenna as a transceiver in a system and also isolate the internal area of the design to some extent, and also cause the wave propagating into the medium to be closer to a plane wave. In addition, an absorber sheet was added to the designs that improve the designs' directivities and further insulates the internal structures.

3. The wide range of dielectric materials with low conductivities was proposed to miniaturize the design and reduce the reflection within the system. The proposed different materials have advantages such as ease and low cost to manufacture into the required shape, and also have high permittivity close to that of the human skin.

4. The dielectric properties of the materials were measured within the frequency range of interest (0.3 – 3.3 GHz) using the open-ended high-temperature probe and results were confirmed by other methods such as the resonant cavity method.

5. The reflection coefficient technique was selected and applied to the system to measure the abdominal fat thickness in both the simulation and in experiment, and the technique proved the system operation with an accuracy within ±1 mm.

6.4. FUTURE WORK

For future work of the project, following actions may be considered:

- To fabricate the antenna design using the modified skin's permittivity matched ceramic, which involves processes such as compressing, sintering, milling and machining of the ceramic sample. In addition, the ceramic sample that was cut to the required shape will be painted using highly conductive silver paint, and finally connected to the SMA connector for experimental test. This involves antenna characteristic measurements and placing the antenna on the known fat thickness of abdomen for the calibration. Furthermore, proving successful operation of the system requires to measure the unknown thickness of abdominal fat for different individuals.
- To order the hardware components that were purposed in the final part of Chapter 5, to produce the system design and enable the user to take advantage of the antenna designs within the hardware to be built. This enables the user to take advantage of different types of techniques such as reflected pulse, TDR and group delay to measure the abdominal fat.

Moreover, in order to improve the performance of the system, some of the important key points are summarized as follows:

- Different pulses may be considered and the optimal pulse for this application in terms of centre frequency, shape, and bandwidth can be investigated.
- Different techniques such as reflected pulse, group delay and return loss may be used to extract information such as the location and the type of tissue.
- Two and three-dimensional techniques for reconstructing the image based on the acquired information may be considered.
- A hardware system that can generate, transmit, receive and analyse the reflected pulse can be designed and produced.